RICE UNIVERSITY

Characterizing Engineered Nanomaterials: From Environmental, Health and Safety Research to the Development of Shaped Nanosphere Lithography for Metamaterials

by

Zuzanna A. Lewicka

A THESIS SUBMITTED

IN PARTIAL FULFILLMENT OF THE

REQUIREMENTS FOR THE DEGREE

Doctor of Philosophy

APPROVED. THESIS COMMITTEE:

Vicki L. Colvin, Kenneth S. Pitzer-Schlumberger Professor of Chemistry and Professor of Chemical & Biomolecular Engineering

Frank K. Tittel, Professor, Electrical and Computer Engineering

Michael S. Wong, Professor, Chemical & Biomolecular Engineering and Chemistry

HOUSTON, TEXAS

MAY 2012

ABSTRACT

Characterizing Engineered Nanomaterials: From Environmental, Health and Safety Research to the Development of Shaped Nanosphere Lithography for Metamaterials

by

Zuzanna A. Lewicka

In this thesis two issues in nanotechnology have been addressed. The first is the comprehensive characterization of engineered nanomaterials prior to their examination in toxicology and environmental studies. The second is the development of a method to produce nanostructure arrays over large areas and for low cost.

A major challenge when assessing nanomaterial's risks is the robust characterization of their physicochemical properties, particularly in commercial products. Such data allows the critical features for biological outcomes to be determined. This work focused on the inorganic oxides that were studied in powdered and dispersed forms as well as directly in consumer sunscreen products. The most important finding was that the commercial sunscreens that listed titania or zinc oxide as ingredients contained nanoscale materials. Cell free photochemical tests revealed that ZnO particles without any surface coating were more active at generating ROS than surface coated TiO_2 nanoparticles. These studies make clear the importance of exposure studies that examine the native form of nanomaterials directly in commercial products.

The second part of this thesis presents the development of a new method to fabricate gold nanoring and nanocrescent arrays over large areas; such materials have

unique optical properties consonant with those described as metamaterials. A new shaped nanosphere lithography approach was used to manipulate the form of silica nanospheres packed onto a surface; the resulting array of mushroom structures provided a mask that after gold evaporation and etching left either golden rings or crescents over the surface. The structures had tunable features, with outer diameters ranging from 200 to 350 nm for rings and crescent gap angles of ten to more than a hundred degrees. The use of a double mask method ensured the uniform coverage of these structured over 1 cm^2 areas. Experimental and theoretical investigations of the optical properties of the arrays revealed the optical resonances in the infrared region. Finally, in the course of developing the nanorings, etch conditions were developed to deposit large area arrays of polystyrene nanodoughnuts with diameters from 128 to 242 nm. These non-conductive structures provide an ideal template for further attachment of magnetic of optically emissive nanoparticles.

TABLE OF CONTENST

LIST OF FIGURES VII

LIST OF TABLES XIX

Chapter 1 Introduction to nanomaterial characterization needs for environmental health and safety 1

1.1 Engineered nanomaterials - general overview 1

1.2 Occurrence of engineered nanoparticles in the environment 5

1.3 Effects of nanoparticles on organisms 6

1.4 Nanoparticle physicochemical characteristics of relevance for toxicology 10

1.5 The special case of sunscreens 12

1.5.1 Regulatory policy as related to sunscreens 13

1.5.2 Photocatalytic activity of TiO_2 and ZnO nanoscale particles 13

1.5.3 Health effects of nanoscale titania and zinc oxide 14

1.5.4 Materials derived from consumer products and their photochemical behavior 16

Chapter 2 Strategies for physicochemical characterization of commercial nanomaterials for environmental and health studies 19

2.2 Best practices for characterization of nanoparticles in dry solid form 19

2.2.1 Methods for nanoparticle characterization 20

2.2.2 Commercial, dry materials for characterization and experiments 24

2.2.3 Results from the characterization of dry powder nanomaterials 25

2.2.4 Conclusion 42

2.3 Interlaboratory comparison of the size and surface charge measurements of nanoparticles prior to biological impact assessment 44

2.3.1 The International Alliance for NanoEHS Harmonization 44

2.3.2 Procedures and methodology 45

2.3.3 Results and discussion 48

2.4 The structure, composition and dimensions of TiO_2 and ZnO nanomaterials in commercial sunscreens 60

2.4.1 Materials and methods 60

2.4.2 Results and discussion 64

2.4.3 Conclusion 80

Chapter 3 The photochemical behavior of sunscreen pigments 81

3.1 Materials and methods 82

3.1.1 Dichlorofluorescein fluorescence 83

3.1.2 Luminol chemiluminescence 84

3.1.3 POBN and DMPO electron paramagnetic resonance spectroscopy 85

3.1.4 Congo red decolorization 87

3.1.5 Comparative investigation of photocatalytic properties of ZnO and TiO_2 materials 88

3.2 Results and discussion 89

3.2.1 Dichlorofluorescein and luminol tests: evaluation of ROS production by sunscreen emulsions 89

3.2.2 Spin trapping of hydroxyl radicals 92

3.2.3 Congo red dye decolorization test 100

3.2.4 ZnO vs. TiO_2 – comparative investigation of photocatalytic properties 104

3.3 Conclusion 107

Chapter 4 The optical properties and existing fabrication methods for ring and crescent-shaped nanostructures.....110

4.1 Optical properties of gold nanorings and nanocrescents 111

4.1.1 Plasmonics as a way of understanding nanorings and nanocrescents..... 111

4.1.2 The case of metamaterials..... 117

4.1.3 Metamaterials designs..... 120

4.1.4 Techniques for metamaterials fabrication..... 126

4.2 Nanosphere lithography for the production of nanorings and nanocrescents arrays 128

4.3 Polystyrene nanodoughnuts arrays fabricated by nanosphere lithography . 132

Chapter 5 Fabrication of two-dimensional gold nanostructures arrays by shaped nanosphere lithography 135

5.1 Materials and methods 136

5.1.1 Substrate preparation and monolayer of polystyrene spheres formation..... 136

5.1.2 The shaping of polystyrene sphere form and diameter..... 137

5.1.3 Formation of gold nanostructures 138

5.1.4 Characterization methods..... 140

5.1.5 A simulation study of nanorings and nanocrescents arrays 142

5.2 Results and discussion 143

5.2.1 A close-packed array of polystyrene spheres..... 143

5.2.2 Annealed and etched polystyrene masks 150

5.2.3 Structures fabricated by sputtering and electron beam evaporation 154

5.2.4 Nanorings and nanocrescents formation 159

5.2.5 Control over nanorings and nanocrescents features 164

5.2.6 Optical properties of nanorings and nanocrescents 168

5.3 Conclusion 175

Chapter 6 Fabrication of two-dimensional polymer nanodoughnuts by nanosphere lithography 177

6.1 Materials and methods 178

6.1.1 The formation of nanodoughnuts arrays 178

6.1.2 Characterization methods 179

6.2 Results and discussion 180

6.3 Conclusion 192

Conclusion 193

References 196

LIST OF FIGURES

Figure 1.1.1 Schematic representations of various forms of nanomaterials, which include nanoparticles, nanotubes, and nanoplates 2

Figure 1.1.2 Trend for size-dependent reactivity change of a material as the particle transitions from macroscopic (bulk-like) to atomic 3

Figure 1.1.3 Percentage of scientific papers addressing the hazard of carbon-based materials, metal oxides, metals and semiconductor nanoparticles 4

Figure 1.1.4 Recommended minimum physical and chemical parameters for characterizing nanomaterials on toxicology studies 11

Figure 2.2.1 Digital images of as-received ST01_TiO_2, T-Avo_TiO_2, Umicore_CeO_2 and Aldrich_Fe_xO_y samples 26

Figure 2.2.2 Secondary electron images of ST01_TiO_2, T-Avo_TiO_2, Umicore_CeO_2 and Aldrich_Fe_xO_y samples obtained at low (5,000x) and high (50,000x) magnification levels, showing: the degree of agglomeration/aggregation in the ‘as-received powders’ 27

Figure 2.2.3 TEM images and size histograms of ST01_TiO_2, T-Avo_TiO_2, Umicore_CeO_2 and Aldrich_Fe_xO_y samples 29

Figure 2.2.4 High magnification image of T-Avo_TiO_2 sample 29

Figure 2.2.5 N_2 adsorption-desorption isotherms for STO1_TiO_2 (A) and T-Avo_TiO_2 (B) samples 33

Figure 2.2.6 Digital images of ST01_TiO_2, T-Avo_TiO_2, Umicore_CeO_2 and Aldrich_Fe_xO_y samples before (upper row) and after degassing at 200^oC prior BET analysis (lower row)..... 34

Figure 2.2.7 X-ray diffraction pattern of ST01_TiO_2 and Umicore_CeO_2..... 35

Figure 2.2.8 EDS spectra of ST01_TiO_2 and Umicore_CeO_2 37

Figure 2.2.9 XPS wide scan spectrum (A) and high resolution XPS spectrum of Ti2p and O1s regions for sample T-Avo_TiO_2 (B and C) 39

Figure 2.2.10 XPS C1s scans for samples ST01_TiO_2 and T-Avo_TiO_2..... 40

Figure 2.2.11 Thermo-gravimetric analysis curves for analyzed metal oxides 41

Figure 2.3.1 Partners and collaborators participated in IANH. 45

Figure 2.3.2 Three repeat DLS measurements on two aliquots (A and B) of Silica IRMM-304. Hydrodynamic diameter from all six measurements was 43.37 ± 0.87 and polydispersity index was 0.13 ± 0.02..... 52

Figure 2.3.3 Three repeat DLS measurements on two aliquots (A and B) of Ceria Umicore D246 gently transferred to the tube to DLS cuvette. Hydrodynamic diameter from all six measurements was 158.97 ± 4.23 and polydispersity index was 0.19 ± 0.01 53

Figure 2.3.4 Three repeat DLS measurements of Ceria Umicore D246 obtained after the sample was vigorously shaken. Hydrodynamic diameter from three measurements of the same aliquot was 1920.67 ± 81.13 nm..... 54

Figure 2.3.5 Three repeat DLS measurements of Ceria Umicore D246 obtained for two aliquots (A and B) sonicated for 30 min using batch sonicator. Hydrodynamic diameter from all six measurements was 1947.17 ± 203.35 and polydispersity index was 0.57 ± 0.12..... 54

Figure 2.3.6 The phase plots for Polystyrene BL-PS (A) and Silica IRMM-304 (B) 56

Figure 2.3.7 Hydrodynamic diameters measured for Silica IRMM-304 (A), Polystyrene BL-PS (B), Ceria Umicore D246 (C) and Ceria Umicore D246-sonicated (D). 57

Figure 2.3.8 Zeta potential measurements obtained on Polystyrene BL-PS 58

Figure 2.4.1 Photographs of the labels on the sunscreen 05 (A) and 07 (B) 66

Figure 2.4.2 SEM images of ‘as-provided’ sunscreens and TEM images of ‘diluted’ samples..... 67

Figure 2.4.3 SEM images at low magnification level (1,000x) for the ‘as-provided’ samples (00-08)..... 68

Figure 2.4.4 SEM images at high magnification level (50,000x) for the ‘as-provided’ samples (00-08)..... 69

Figure 2.4.5 X-ray diffraction patterns of ‘as-provided’ sunscreens and industrial nanopowders. 72

Figure 2.4.6 TEM images of the ‘diluted’ samples (00-07) and the particles obtained from companies (T-Avo, T-Eco, Z-Cote)..... 74

Figure 2.4.7 Particle distribution histograms. 76

Figure 2.4.8 EDS analysis of TiO_2 pigments ‘extracted’ from sample 02 and T-Eco (A), and ZnO pigments ‘extracted’ from sample 04 and Z-Cote (B) 78

Figure 2.4.9 High resolution TEM images of coated TiO_2 (T-Avo, A and T-Eco, B) and uncoated ZnO (Z-Cote, C) nanopowders 79

Figure 3.2.1 DCFH fluorescence (A) and luminol chemiluminescence (B) of sunscreen emulsions before and after 5 min of UVA irradiation 90

Figure 3.2.2 The EPR spectra of spin trapped radicals obtained by 5 min UVA irradiation of samples 00, 01, 02, 04, 05, 06, 07 dispersions containing POBN. 93

Figure 3.2.3 The EPR spectra of spin trapped radicals obtained by 5 min UV irradiation of extracted inorganic particles from sunscreen samples 00, 01, 02, 03, 04, 05, 06, 07. . 94

Figure 3.2.4 The EPR spectra of spin trapped radicals obtained by irradiation (5 min) of sample 06 dispersion containing DMPO (lower spectrum), and DMPO/EtOH (upper spectrum) 95

Figure 3.2.5 Concentration of DMPO-OH adduct generated during 1 (P25 and Z-Cote) and 5 min (all other samples) of UVA irradiation, normalized to the active ingredient weight (TiO_2 or ZnO) 97

Figure 3.2.6 UV-Vis absorption spectra of (A) Congo red aqueous solution and (B) sample 06 and Congo red aqueous suspension monitored during a 60-min UVA

irradiation time. Bottom pictures show the color change of the solutions before and after the 60-min illumination..... 101

Figure 3.2.7 Experimental data of decolorization of Congo red (CR) dye in the presence of sunscreen extracts (samples 00-02, 04-07),..... 102

Figure 3.2.8 Photodegradation of Rose Bengal under UVA irradiation for five cycles: (A) Z-Cote, (B) P25 commercial powders. 105

Figure 3.2.7 Photostability of Z-Cote and P25 nanopowders..... 107

Figure 4.1.1 Simulated local-electric field amplitude distribution of a nanoring of 60 nm radius..... 112

Figure 4.1.2 Sketch of the charge distribution of the first three resonances of metal nanocrescents (A-C) and the closed ring (D)..... 115

Figure 4.1.3 Extinction spectra for varying crescent opening 116

Figure 4.1.4 Dielectric permittivity and magnetic permeability diagram..... 118

Figure 4.1.5 Calculated images of a metal rod in the glass filled with liquid of n =1.3 (A) and the liquid with a negative refractive index of n = −1.3 (B)..... 119

Figure 4.1.6 Microwave frequency metamaterial that consists of a two-dimensional periodic array of copper split ring resonators and wires, fabricated by a shadow mask/etching technique on glass circuit board 120

Figure 4.1.7 Metamaterials with $\mu < 0$ (A) and $\varepsilon < 0$ (B); a periodic structures composed of split ring resonators (A) and thin infinite wires (B) 121

Figure 4.1.8 Illustration of the analogy between a conventional LC circuit (A) and the single SRRs (B). (C) An electron micrograph of a typical SRR fabricated by electron-beam lithography 124

Figure 4.1.9 Progress in metamaterial operating frequency over the past decade..... 125

Figure 4.2.1 Schematic diagrams of single-layer (A) and double-layer (B) nanosphere masks and the corresponding nanoparticles arrays (C and D)..... 129

Figure 4.2.2 Changes in the mask morphology obtained by deforming the colloid particles by RIE etching (A-C) for 6 min (A) 14 min (B), and 20 min (C); and annealing (D-F) via 1, 2, 4 microwave exposures..... 130

Figure 5.1.1 Digital pictures of Minilock-Phantom III plasma RIE system from Trion Technologies with closed (A) and open (B) RIE chamber and schematic representation of RIE process in the chamber 138

Figures 5.1.2 Schematic view of the sample without the solid mask (A), with one-side solid mask (B) and double-side solid mask (C)..... 139

Figure 5.1.3 Sketch of the gold nanostructures geometry indicating the diameter ‘d’ of the mushroom, the gap opening ‘α’ of the nanocrescents, the maximum nanostructure width ‘w’, outer ‘d_o’ and inner ‘d_i’ diameters of the nanorings..... 141

Figure 5.2.1 Digital picture of polystyrene spheres assembled onto glass substrate (A) and SEM images obtained at 5,000x (B) and 20,000x (C) magnification levels of defects in polystyrene monolayer such as blank spots and multilayers caused by cluster of polystyrene particles. The solution was not filtered before applying to the substrate.... 143

Figure 5.2.2 The aqueous colloidal solution of polystyrene spheres obtained from Bangs Laboratories (A) and DLS analysis of the polystyrene beads obtained from this company and labeled as (B) 400 nm and (C) 250 nm 144

Figure 5.2.3 Digital pictures of 30µl drop of suspension of 400 nm polystyrene spheres on RCA1 cleaned (A) and untreated (B) glass substrates..... 145

Figure 5.2.4 Schematic representations of drop drying (A), floating on an interface (B) and spin coating (C) methods of assemble of polystyrene spheres (PS). 146

Figure 5.2.5 SEM images obtained at 500x (A, D, G), 5,000x (B, E, H), and 20,000x (C, F, I) magnification levels of polystyrene spheres assembled onto substrates by drop drying (A-C), floating on an interface (D-F) and spin coating (G-I) methods 148

Figure 5.2.6 SEM images of polystyrene spheres patterns obtained by spin coating method at 1,000 (A), 2,000 (B) and 3,000 rpm (C) and digital image of the substrate covered by uniform polystyrene spheres monolayer 148

Figure 5.2.7 A digital image of 1 cm^2 silicon wafer piece covered by polystyrene beads (A) and digital optical microscope images of polystyrene beads assembly in the middle part of the sample (B) at the sample edge (C) and the corner (D). 149

Figure 5.2.8 SEM images of PS 400 nm masks on Si surface before annealing (A, D) and annealed at 105°C for 30 min (B, E) and 60 min (C, F). 150

Figure 5.2.9 SEM Images of the polystyrene spheres 400 nm (A-D) and 250 nm (E-H) before (A, E) and after Ar/O_2 plasma etched for 30 sec (B, F), 45 sec (C, G) and 60 sec (D, H) 151

Figure 5.2.10 SEM 45 deg view images of untreated, closely packed polystyrene monolayer (A); 15 sec (B) and 30 sec (C) Ar/O_2 plasma treated monolayer; the dependence of the polystyrene diameter on the Ar/O_2 plasma treatment time for 400 (black line) and 250 nm (red line) polystyrene spheres suspensions purchased from Bangs Laboratories (D); 152

Figure 5.2.11 Schematic side view of the mushroom structure (A) and SEM images obtained at tilt angle of 45 deg of the collapsed spheres formed after 30 sec Ar/O_2 plasma etching of 400 nm polystyrene beads (B) 153

Figure 5.2.12 SEM micrographs (A, D) and AFM amplitude (B, E) and height (C, F) images showing the difference in shape of nanostructures fabricated by sputtering (A-C) and evaporation of 40 nm of gold through 400 nm unmodified polystyrene spheres monolayer 155

Figures 5.2.13 SEM images obtained at 50,000x (A) and 120,000x (B) magnification levels of gold nanoparticle array formed using a double-layer mask of 400 nm PS 156

Figure 5.2.14 SEM images of periodic gold nanoparticles arrays formed by sputtering (A-C) and evaporation (D-E) of 40 nm of gold through unmodified masks of 400 nm PS (A-D) and masks annealed for 30 min (B, E) and 60 min (C, F) at 105^{o}C..... 157

Figure 5.2.15 SEM images of arrays of (A) round nanoparticles with no pattern and (B) nanoholes 158

Figure 5.2.16 SEM images obtained at tilt angle of 45 deg showing schematic flow of the fabrication of an array of gold nanorings..... 160

Figure 5.2.17 SEM images and corresponding structure size distribution histograms of collapsed spheres covered with sputter deposited gold film of thickness 40 nm (A and D), sample after 120 sec argon plasma etching (B and E) and the gold nanorings achieved after removal of the spheres by using an adhesive tape (C and F) 161

Figure 5.2.18 SEM (A, B) and EDS (C) images of gold nanorings array fabricated by sputter depositing of 20 nm gold film onto a monolayer of collapsed spheres with a diameter of 220 nm and argon plasma etching for 60 sec 161

Figure 5.2.19 SEM images presenting uniformity of the samples fabricated by depositing gold film of thickness 40 nm onto a monolayer of the collapsed spheres followed by argon plasma etching without the solid mask (A-B), in a presence of one-side solid mask (D-E) and double-side solid mask (G-I). SEM analysis was carried out at the top left part (A, D, G), in the middle (B, E, H) and at the bottom right part of the sample (C, F, I). 163

Figure 5.2.20 The dependence of nanostructures dimensions on polystyrene spheres diameters (A and B) and the solid mask thickness (C and D). 164

Figure 5.2.21 SEM images of the nanostructures fabricated by sputter depositing of 40 nm (A) and 20 nm (B) gold films onto collapsed spheres with a diameter of 200 nm... 165

Figure 5.2.22 AFM analysis of the nanorings and the nanocrescent, showing section (A) and height (B) of the nanorings fabricated by sputter depositing 40 nm of gold followed by 120 sec argon plasma etching; height (C) of the nanorings fabricated by sputter depositing 20 nm of gold followed by 60 sec argon plasma etching; section (D) and height (E) of the nanocrescents fabricated by sputter depositing 40 nm of gold followed by 150 sec argon plasma etching and height (F) of the nanocrescents fabricated by sputter depositing 20 nm of gold and 90 sec argon plasma etching 166

Figure 5.2.23 SEM images of nanorings produced by sputter depositing (A) and evaporating (B) of 40 nm gold film onto a monolayer of collapsed spheres with a diameter of 300 nm. 167

Figure 5.2.24 SEM images of the nanostructures fabricated by sputtering gold film of 40 nm onto a monolayer of collapsed spheres with diameter of 300 nm (A) and etching with argon plasma for 90 sec (B), 120 sec (C) and 150 sec (D) 168

Figure 5.2.25 SEM images of the nanostructures with geometrical parameters as follows: (A) $\alpha = 206 \pm 10^{o}$, $d = 324 \pm 9$ nm, $w = 41 \pm 5$ nm; (B) $d_o = 351 \pm 7$ nm, $d_i = 246 \pm 8$ nm; (C) $d_o = 308 \pm 7$ nm, $d_i = 201 \pm 9$ nm. 169

Figure 5.2.26 Experimental measurements performed by using FTIR microscopy (A) and FTIR spectroscopy (B) for nanocrescents array for c-polarized (dotted line) and u-

polarized (solid line) beam and measured UV-VIS-NIR extinction spectra of nanorings arrays. 169

Figure 5.2.27 Numerical simulations for nanocrescents (A) and nanorings (B) arrays which were obtained using the actual parameters of the fabricated nanostructures presented in Figure 5.2.25 172

Figure 5.2.28 Gap opening (α) dependent excitation spectra of gold nanocrescents with geometrical parameters: d = 333 nm; w = 46 nm; h = 35 nm 173

Figure 5.2.29 Diameter (d) dependent excitation spectra of gold nanocrescents with geometrical parameters: $\alpha = 158^{o}$; w = 46 nm; h = 35 nm 174

Figure 6.2.1 SEM images obtained at tilt angle of 45 degrees showing the change in morphology of polystyrene spheres after argon plasma etching. (A) SEM image of 400 nm close-packed polystyrene beads monolayer assembled on a silicon wafer, (B) polystyrene beads treated by argon plasma for 90 sec, (C) sample after immersion in tetrahydrofuran for thirty minutes and (D) the same sample after sonication for five minutes. 180

Figures 6.2.2 Digital images (A-C) and SEM images (D-F) of 1 cm^2 silicon wafer pieces covered by 400 nm polystyrene spheres (A, D) and samples after argon plasma etching for 60 sec (B, E) and 90 sec (C, F) 181

Figure 6.2.3 Effect of solvent treatment on bulk polystyrene. Digital images of piece of polystyrene foam food container introduced into tetrahydrofuran (A), after 2 sec in tetrahydrofuran (B) after 10 min in methanol (C). 183

Figure 6.2.4 SEM images obtained at a tilt angle of 45 deg and 50,000 magnification levels of (A) untreated, (B) 60 sec and (C) 90 sec plasma treated polystyrene beads immersed in tetrahydrofuran for 30 min 183

Figure 6.2.5 SEM studies on the effect of solvent on formation of polystyrene nanodoughnuts. SEM images of samples after immersion in tetrahydrofuran (A), toluene (B) and methanol (C) 184

Figure 6.2.6 Tilted-view SEM image (A) of nanodoughnuts array with some undetached domes and top-view SEM images (B and C) of underside of the domes 185

Figure 6.2.7 XPS survey scans and C 1s spectra of untreated and argon plasma treated polystyrene beads assembled on silicon wafer as well as nanodoughnuts array 186

Figure 6.2.8 Raman spectra from (A) 400 nm spin coated polystyrene beads on a silicon substrate; (B), (C), (D) polystyrene beads etched with argon plasma for 30, 60 and 90 sec, respectively. 188

Figure 6.2.9 AFM analysis of the polystyrene nanodoughnuts array on silicon substrate fabricated using 400 nm polystyrene beads, showing phase (A), amplitude (B) and topography (C) 190

Figure 6.2.10 SEM images of nanodoughnuts arrays fabricated using 400 nm (A, B) and 250 nm polystyrene beads (C). 191

LIST OF TABLES

Table 2.2.1 Instrumentation for characterization of nanoparticles in dry solid form 20

Table 2.2.2 Source of nanomaterials with specifications provided by the manufacturer . 25

Table 2.2.3 Characterization of nanoscale pigments 36

Table 2.2.4 Elemental composition of nanoparticles..... 38

Table 2.3.1 Refractive indexes for samples used in the calculation of hydrodynamic diameters from DLS measurements in round robin testing 48

Table 2.3.2 The results from DLS and pH measurements for IRMM-304, PS-BL, not sonicated Umicore D246 and sonicated Umicore D246 samples..... 50

Table 2.4.1 Identification of nanoscale pigments in studied sunscreens 65

Table 2.4.2 Characterization of nanoscale pigments 70

Table 3.1.1 Types of tests and samples used in photoactivity study 83

Table 3.2.1 Particle characterization and their properties in Rose Bengal degradation ... 99

Table 3.2.2 Output of ROS for the sunscreen samples..... 108

Chapter 1 Introduction to nanomaterial characterization needs for environmental health and safety

This chapter provides an overview of the current exposure and toxicity evaluation of engineered nanomaterials. A special emphasis in this review is the prior work on the best practices for nanomaterial physicochemical characterization as it relates to the biological and toxicological activity of nanoparticles.

1.1 Engineered nanomaterials - general overview

Nanotechnology has been defined by the ASTM (the American Society for Testing and Materials) as follows:

'A term referring to a wide range of technologies that measure, manipulate, or incorporate materials and/or features with at least one dimension between approximately 1 and 100 nanometers (nm). Such applications exploit the properties, distinct from bulk/macroscopic systems, of nanoscale components' [1].

Nanoscale materials (or nanomaterials) have been described as any materials having one or more dimensions from approximately 1 to 100 nm [1, 2]. These can be naturally occurring (e.g. volcanic ash), incidentally produced (e.g. diesel exhaust particles) or intentionally made. Of most relevance to this work is the latter classification: manmade (engineered or manufactured) nanoscale materials designed with specific properties (e.g.: mechanical, optical, electrical and/or magnetic) that differ from those of bulk materials. Nanomaterials can exist in various forms: nanoplates, nanorods, nanotubes or nanoparticles as presented in Figure 1.1.1. According to BSI (The British Standards Institution) nanoplates are objects having a nanoscale order thickness while

having two other external dimensions significantly larger; nanorods have two similar external dimensions in the nanoscale and the third dimension significantly larger; nanotubes are hollow nanorods; while nanoparticles are defined as particles with all three dimensions within the nanoscale [2].

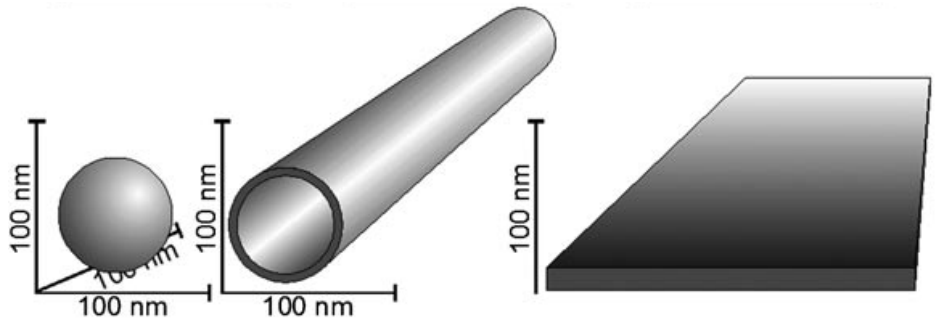

Figure 1.1.1 Schematic representations of various forms of nanomaterials, which include nanoparticles, nanotubes, and nanoplates. Adapted from [3]

Nanoscale materials are often lighter, stronger, and more reactive than bulk materials and thus find many socially beneficial applications in areas as diverse as medicine and aerospace [3, 4]. One size-dependent property that often motivates the generation of nanoscale materials is the surface area. As the size of a material decreases, the ratio of surface molecules/atoms to total molecules/atoms increases exponentially [5]. Greater surface area means larger fraction of molecules/atoms available for chemical reaction which increases nanomaterials surface reactivity as presented in Figure 1.1.2 [6]. This translates into improved physical, chemical and biological properties and allows creating superior devices. Other size-dependent properties may arise from the

confinement of electronic excitations, or the enhanced cooperativity of magnetic spins in solids of low dimensions [7, 8].

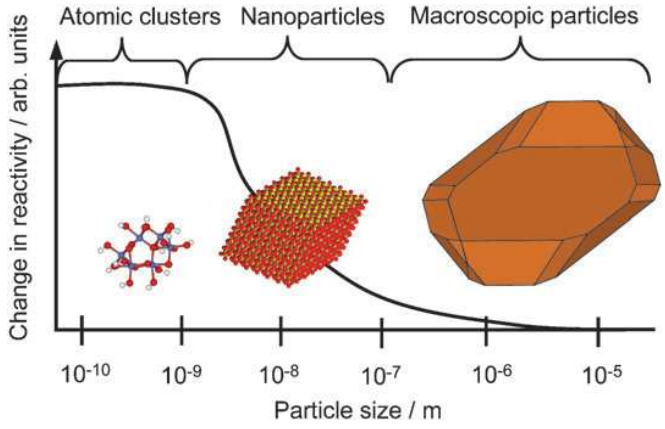

Figure 1.1.2 Trend for size-dependent reactivity change of a material as the particle transitions from macroscopic (bulk-like) to atomic; Adapted from [6].

Given their many unique and size-dependent properties, it is not surprising that their use in consumer products is increasing rapidly [9, 10]. In 2009, the Project on Emerging Nanotechnologies (PEN) inventory identified over one thousand nanotechnology-based consumer products on the market from over twenty-four countries, including the US, China, Canada, and Germany [10]. The largest group of products (605 products) was within the health and fitness category, which included cosmetics, clothing, personal-care products, sporting goods, sunscreens, air and water filters. However, the database has not been updated since August 2009 due to run out of the funding for the PEN inventory [10, 11]. Therefore, presented in PEN numbers of consumer products

having engineered nanomaterials is only a portion of nanotechnology-enabled products currently on the market.

As their use has expanded to include many applications that bring them into contact with people and the environment, significant questions have been raised about their possible biological and environmental interactions [12, 13]. As noted by Simkó and Mattsson 'A risk can be deduced from exposure data together with the hazard assessment' that results after exposure [14]. This exposure and hazard frame has dominated the development of the study of nanomaterial risk. Different nanomaterials have been the subject of varying levels of risk-based analysis. These types include carbon-based materials such as fullerenes and carbon nanotubes; metal oxides nanoparticles and rods (iron oxide, cerium oxide, titanium dioxide, silicon dioxide, etc); metals (gold and silver), as well as semiconductor nanoparticles or so-called quantum dots (typically cadmium sulfide and cadmium selenide) [15]. Interestingly, a literature analysis reveals that of these materials the metal oxide and carbon-based systems have been the most examined (Figure 1.1.3).

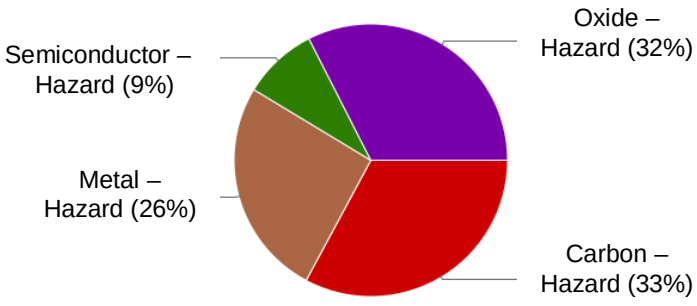

Figure 1.1.3 Percentage of scientific papers addressing the hazard of carbon-based materials, metal oxides, metals and semiconductor nanoparticles between years 1960 and 2012 [16].

1.2 Occurrence of engineered nanoparticles in the environment

As the number of consumer products containing engineered nanoscale particles grows, so will the chance of environmental exposure to wide range of organisms [17]. For example, it has been estimated that in the United States, based on the reported market size for suncare products, approximately125 tons of nanoscale TiO_2 and ZnO ultraviolet (UV) blocking agents are used (and released) in commercial products every year [18]. Nanoscale TiO_2 and ZnO particles are used in sunscreens because they do not scatter visible light as their larger counterparts and appear transparent when applied to the skin [19, 20]. Furthermore, Handren et al. estimated upper and lower bound annual United States production quantities for five classes of engineered nanomaterials: titanium dioxide (TiO_2), silver (Ag), cerium oxide (CeO_2), carbon nanotubes (CNTs) and fullerenes, that range from 7800 – 38,000 tons/yr for TiO_2; 2.8 – 20 tons/yr for Ag; 35 – 700 tons/yr for CeO_2; 55 – 1101 tons/yr for CNTs; and 2 – 80 tons/yr for fullerenes [21]. These estimates were done based on data from academic publications, professional reports, company web sites, production process patents, and personal communication with company representatives. The fact that such information was not readily available reflects the lack of labeling and reporting standards for consumer products that contain nanoscale materials.

Nanoparticles can enter the environment either during the manufacture, use or disposal of such nano-containing products; studies of fate and transport have concluded that the natural sinks for nanoparticles are soil or water [22, 23]. So far, no measurements of engineered nanoparticles in the environment have been able to quantify trace concentrations of these materials [17]. However, some have found qualitative evidence

that nanoscale pigments do find their way into the solid waste generated in wastewater treatment plants [24]. However, absent better quantitative analytical tools for environmental exposures much of the information about exposure has been derived from relatively coarse grained environmental exposure models [25, 26].

To complicate the study of exposure even further, a growing body of research focuses on the fact that nanoparticles can change drastically their behavior and physical characteristics as the move through the environment [27-29]. Changes in physicochemical properties such as surface charge and size can drastically modify environmental fate and transport. Guzman et al. showed that mobility of nanoscale materials in aqueous environment is dependent on size of nanoparticles. They reported that zero point charge (ZPH) of TiO_2 nanoparticles changed with the size and the aggregation state increased as the pH of the solution approached the ZPH [30]. On the other hand, Labille et al. studied the aging and fate of a TiO_2 nanoscale particles recommended by manufacturer (BASF Chemical Company) as sunscreen pigments and discovered that after contact with water, TiO_2 nanocomposite dispersed and formed stable suspension available to the microorganisms [31].

1.3 Effects of nanoparticles on organisms

Once released into the environment, nanomaterials will interact with organisms. Environmental engineers have studied how nanomaterials affects model organisms such as algae, daphnia magna, zebrafish, bacteria or crustacean from an aquatic ecosystem [32-36]. The results indicate that nanoparticles may have ecotoxicological effects which depend sensitively on the size, shape, surface coating and crystalline form of the particles

[34, 37]. Recently, there have been also studies performed on terrestrial organisms such as the nematode Caenorhabditis elegans [38, 39]. Wang et al. have not observed significant difference in toxicity between nano (TiO_2 - 50 nm, ZnO - 20 nm) and bulk materials (> 200 nm) for example. But, as is the case with many studies, there was a significant difference between the particle compositions as a function of size. On the other hand, Roh et al. demonstrated a relationship between the diameter of TiO_2 nanoparticles and their impact on nematodes. Smaller sized titania (7 nm) had a more negative impact on C. elegans fertility and survival than larger sized zinc oxide (20 nm). These kinds of inconsistencies in the nanotoxicology literature are more of the exception than the rule. Most analyses of the data suggests that direct comparisons between studies is a challenge because the form of nanomaterial properties (size, shape, degree of agglomeration, chemical and catalytic) that contribute to ecotoxicity were not appropriately defined [40]. Thus, studies of nanoscale titania can be different in their conclusions because the specific forms of nanoscale titania examined can be different.

Human toxicity studies, with a main focus on exposures to workers, are concerned with dispersion and uptake from air, as well as uptake through ingestion and skin penetration [5, 15]. Nanoparticles deposition in the body after inhalation and the factors influencing the fate of inhaled nanomaterials can be found in review by Yang et al. [41]. For example, Kreyling et al. showed that about 1% of iridium particles (15 and 80 nm) inhaled by rats accessed the systemic circulation and deposited material in organs such as liver, spleen, heart, and brain [42]. Moreover, 15 nm particles were deposited at a rate far greater than 80 nm particles. Furthermore, translocation of carbon nanoparticles into the brain via olfactory nerve system has also been reported [43]. Metal oxide nanoparticles

such as TiO_2 entered the brain through olfactory bulb, as well. In the presence of TiO_2 particles the level of malondialdehyde (MDA), which is a marker of oxidative stress was elevated and the ultrastructural changes of neurons in the hippocampus were observed [44]. Moreover, Wang et al. noticed differences in responses on central nervous system to anatase TiO_2 particles versus the rutile titania with lower risk potential for the second ones. In summary, different types of inhaled nanoparticles can translocate into the liver, brain and other organs through blood vessels and the central nervous system. This exposure can produce acute and chronic changes within cells and organisms. Less data is available about dermal contact and ingestion [3, 45].

Once exposed to the human body, a central and still unanswered question is the rate at which nanoparticles are cleared or degraded. A review discussing the nanoparticle interaction with living systems has recently been done by Lu et al. [46]. One model anticipates that should nanoparticles find their way into the body, they would be marked with proteins as foreign agents and consumed by phagocytes (immune cells) [47]. After delivery to the lymph nodes they could be biodegraded into biologically safe components if their constituent material was itself non-toxic. Phagocytosis is a basic defense mechanism against exogenous substances. However, if particles are very stable and difficult to metabolize within the body, they could reside in the body for long time periods and unknown health effects may occur.

In the past few years many investigators have been developing *in vitro* model systems using both human and animal cells to simplify the study of the cellular response to nanoparticles [48]. While, *in vitro* testing provides a limited view of the responses of only the cell types being tested, it is quick, relatively inexpensive, and allows evaluation

of specific mechanisms of action [49]. Although nanoparticle-induced cytotoxicity has been reported by several groups, the exact mechanism for toxicity is not well understood [50-52]. Nonetheless, studies point to a nanoparticle-enhanced generation of reactive oxygen species (ROS) that may result in oxidative stress, inflammation, and consequent damage to proteins, membranes and DNA [53 , 54].

Lewinski et al. who reviewed cytotoxicity of carbon-, metal- and semiconductor-based nanoparticles concluded that different data has been published about cytotoxicity due to differences in experimental procedures as well as differing nanoparticle properties [50]. Incomplete characterization, lack of protocols and calibration standards in nanoparticle characterization will result in inconsistent and unreliable toxicity data. For example, in one study multiwall carbon nanotubes were reported to be toxic and cause a decrease in mitochondrial membrane potential [55], whereas another study reported that these nanotubes were nontoxic [56]. The uncertainties and inter-study inconsistencies are likely caused by variations in nanoparticle characteristics and experimental procedures.

As physicochemical properties can influence on toxicological endpoints, their determination is necessary for the interpretation of experimental studies [27, 49, 57, 58]. There is no doubt that nanoscale particles can in some forms be biologically reactive and lead to cell damage; what is less clear is whether these cell culture effects are apparent in animal systems [59]. In addition, the risk of any potentially toxic substance is not only a function of hazard but also chance of exposure. However, lack of exposure data for humans and the environment limits the effective risk assessment of commercially available nanomaterials [9, 60].

1.4 Nanoparticle physicochemical characteristics of relevance for toxicology

Nanomaterial properties that form the foundation of their use in produces may also prove harmful to organisms under certain circumstances. This broad hypothesis certainly needs refinement, with a specific focus on which physicochemical properties of nanomaterials are the most important in defining their hazard [27, 52, 59, 61, 62].

To date, no specific regulation for nanomaterials at the international level exists. The International Standards Organization (ISO) published nanotechnology terminology in 2008 as an outcome of ISO/TC 229 Nanotechnologies: ISO/TS 27687 'Nanotechnologies - Terminology and definitions for nano-objects - Nanoparticle, nanofibre and nanoplate' [63]. This international organization continues its work in developing effective regulation for nanotechnology-related products including 'guidance on physicochemical characterization of engineered nanoscale materials for toxicologic assessment' (ISO/DTR 13014), but writing new rules takes time; hence it will take some time before new standards are completed [63].

A minimum set of parameters that accounts for the most important and identifiable nanomaterial characterization in nanotoxicity studies was discussed and proposed at the Woodrow Wilson International Center for Scholars in Washington DC, 2008 [64]. Although there is some variability across the list of ideal properties, most authors agree with the minimum characterization set presented in Figure 1.1.4 [27, 61, 64, 65]. Definitions of nanoparticle characteristics and techniques suitable for their measurements were described in [27, 66].

Recommended Minimum Physical and Chemical Parameters for Characterizing Nanomaterials on Toxicology Studies

What does the material look like?

• Particle size/size distribution

• Agglomeration state/Aggregation

• Shape

What is the material made of?

• Overall composition (including chemical composition and crystal structure)

• Surface composition

• Purity (including levels of impurities)

What factors affect how a material interacts with its surroundings?

• Surface area

• Surface chemistry, including reactivity, hydrophobicity

• Surface charge

Overarching considerations

• *Stability*—how do material properties change with time (dynamic stability), storage, handling, preparation, delivery etc? Include solubility, and the rate of material release through dissolution.

• *Context/Media*—how do material properties change in different media; i.e. from the bulk material to dispersions to material in various biological matrices?
("as administered" characterization is considered to be particularly important)

• *Where possible, materials should be characterized sufficiently to interpret the response to the amount of material against a range of potentially relevant dose metrics, including mass, surface-area and number concentration."*

Figure 1.1.4 Recommended minimum physical and chemical parameters for characterizing nanomaterials on toxicology studies. Adapted from [64].

Characterization of nanoscale particles should begin with the study of as-received samples which are often shipped as dry powders [66]. Although this primary characterization is useful, particularly for ensuring batch similarity, powder studies alone are incomplete. It is vital to investigate properties of nanomaterials when they are dispersed in the media used for toxicity studies. Some material properties, like chemical composition and crystal structure, are the same in both dry and dispersed phases. However, the composition of the fluid in which nanoparticles are dispersed may affect their agglomeration state, surface charge and reactivity [59, 65]. Also, many of these changes can be slow to occur and thus samples dispersed in fluids may change over a period of time. Ideally, physicochemical studies should be completed at various time points throughout any biological studies to account for these possible effects [27]. In addition to dry powders and dispersions, nanomaterials are also formulated for consumer products in solid composites (e.g. clay particles in car bumpers) or emulsions (e.g. oxide nanoparticles in sunscreens).

1.5 The special case of sunscreens

In sunscreens, the size-dependent optical properties of TiO_2 and ZnO nanoparticles make them transparent at visible wavelengths; thus, when applied to the skin they form clear films as opposed to white, cloudy applications. Moreover, both materials have very strong absorbance and scattering at UVB and UVA wavelengths (290 – 320 and 320 – 400 nm, respectively) which makes them effective at protecting skin from the ultraviolet radiation present in sunlight [20, 67-69].

1.5.1 Regulatory policy as related to sunscreens

In the United States, product labeling regulations have specifically addressed the issue of pigment size in the list of suncare ingredients. Briefly, manufacturer's need only list the chemical composition rather than the diameter, form or crystalline structure of the pigment. Historically, micronized titania and zinc oxide particles have been used in sunscreens for decades. Because of their large size they scatter visible light and produced a white and chalky appearance when applied. When manufacturer's began to shrink the particle size of these inorganic pigments, the US Food and Drug Administration (FDA) reviewed their requirements for labeling of personal care product ingredients. They ruled in 1999 that 'micronized' titania and zinc oxide was an appropriate terminology for sunscreen pigments and that it was not necessary to specify whether pigments were truly nanoscale [70]. As a result, consumers do not know when the products they are using contain nanoscale materials.

1.5.2 Photocatalytic activity of TiO_2 and ZnO nanoscale particles

While the label may not convey the particle size of sunscreen pigments, this does not mean that such information is irrelevant. Over the past decade the size-dependent biological characteristics of these materials has been of increasing interest to scientists and policymakers alike [53, 71-78]. One specific area of concern has been the native photocatalytic activity of sunscreen pigments. While they are effective at absorbing ultraviolet light, some forms of both titania and zinc oxide are also effective at transforming their photoexcitations into surface reactive species that generate highly oxidizing products. As a result, in addition to suncare products, nanoscale TiO_2 also is of

interest in the ultraviolet mediated oxidation of organic pollutants and wastewater contaminants [72-76]. These applications rely on the ability of TiO_2 nanoparticles to form reactive oxygen species (ROS) such as hydroxyl (OH·), superoxide (O_2·), hydroperoxy (HOO·) radicals, and hydrogen peroxide (H_2O_2) when excited with ultraviolet (UV) lights [79-82]. Critical for these remediation examples is the observation that the generation of ROS by certain forms of nanoscale titania is catalytic: a single particle of titania can generate many hundreds of ROS species under constant ultraviolet illumination [52]. While less studied, nanoscale ZnO materials also can catalyze the photooxidation of organic species in water, and may be more efficient photocatalysts than TiO_2 [83-90]. However, since zinc oxide is more soluble than titania the lifetime of these materials is more limited than titania for some applications; however, when applied to the skin the materials should be stable for months.

1.5.3 Health effects of nanoscale titania and zinc oxide

Reactive oxygen species are generally acutely toxic to living systems because they rapidly react with many cell components (e.g. DNA, proteins and lipids) and lead to cell damage [91-93]. In light of their interest as photocatalytic materials, it is not surprising that toxicology studies have shown that TiO_2 and ZnO nanoparticles have an adverse effect on cellular function when illuminated by UV light. Some studies have shown that TiO_2 nanoparticles are toxic only in the presence of UV light [94, 95], while other studies have shown that in the presence of UV irradiation the toxicity is higher than in the dark [96-100]. ZnO nanoparticles have also shown DNA damage in cultured

human fibroblast under the influence of UV light and photocatalytic effect on human sperm and lymphocytes [99, 101-103].

Whether these acute cell effects are relevant to a product applied to skin depends in part on whether the particles translocate across the dermis; studies of these pigments appear to indicate that for healthy and intact skin, nanoscale materials do not penetrate the dermis but can end up in hair follicles, sweat glands, or skin folds [104-109]. However, at the seaside, where sunscreens are more likely to be used, the action of sun, water and sand can irritate or even harm the skin by hydration, IR irradiation, peeling or inflammation and in consequence enhance its permeability [110]. Furthermore, recent studies demonstrated that the state of skin can have significant effects on its barrier performances [5, 111-113]. Therefore, there is still uncertainty on skin penetration of sunscreen zinc oxide and titanium dioxide nanoparticles under a variety of real-life conditions. Moreover, to fully assess the toxicological impact of sunscreen nanoparticles future studies will need to focus on the potential for ROS generation by TiO_2 and ZnO nanoparticles lodged in hair follicles [108]. In addition to the potential photocatalytic effect on cells, ZnO and TiO_2 nanoparticles may cause loss of the ultraviolet protection efficacy of sunscreens, due to the enhanced photo-oxidative degradation of organic sunscreen components [114].

Also important in understanding the connection between chemical and biological reactivity are the physicochemical characteristics such as particle size and surface area, crystal structure, surface chemistry and particle aggregation/agglomeration tendency. For example, photochemical reactivity is quite sensitive to the phase composition of TiO_2 with rutile materials being orders of magnitude less chemically reactive than equivalently

sized anatase systems and this trend is reflected in short-term in-vitro cell toxicology studies [71, 115]. Additionally, chemical reactivity of nanoscale oxides can be reduced by modifying surfaces with inert inorganic materials such as silica (SiO_2) and alumina (Al_2O_3), and/or by doping with manganese or vanadium [114, 116-120]. Due to the great variety of different nanoparticle forms of TiO_2 and ZnO that exhibit different chemical behaviors, it is difficult to generalize the potential ROS generation capacity of inorganic pigments used in sunscreens [121].

1.5.4 Materials derived from consumer products and their photochemical behavior

FDA regulations do not require that labels provide information about the diameter, form or photoactivity of inorganic sunscreen ingredients [70]; therefore, consumers and researchers have little information about what people are exposed to. Much of the work presented here is aimed at filling this knowledge gap. Specifically, the following chapters describe the study of sunscreen pigments derived from products, as well as pure powdered oxides that are highly similar to derived pigments. Compared to studies of model titania and zinc oxide pigments, there has been comparatively little systematic study of the properties of pigments derived from commercial products.

Hidaka et al. showed that ZnO pigments extracted from commercially available in Japan sunscreen products, when illuminated by UV, caused DNA plasmids strand breaks via the generation of ROS [101]. The same pigments were also photoactive toward degradation of phenol. The similar effect of methylene blue dye rapid photodegradation by sunscreen-isolated- zinc oxide pigments (uncoated, dimethicone coated and mixtures of ZnO and TiO_2 particles) was presented by Rampaul et al. [118]. In the area of the

potential hazard of sunscreen pigments ZnO has been less studied than TiO_2 [122]. Titania is more commonly used photocatalysts than ZnO, and as a result there has been more concern for this material. DNA damage induced by TiO_2 nanoparticles extracted form sunscreens was first noted in 1997 by Dunford et al. [123]. Then, Rampaul et al. found that some TiO_2 particles isolated from sunscreens caused significant cellular damage to cultured human skin and other animal epithelium cells [118]. Recently, Buchalska et al. tested photoreactivity of TiO_2 sunscreen components toward degradation of azur B and oxidation of α-terpinene and showed high efficiency of singlet oxygen formation [124].

These studies largely relied on 'pure' pigments; it is possible that the other consituents in suncreens may modify or augment the nanoparticle effects. The full sunscreen, including TiO_2 pigments, have also been tested toward the formation of oxygen- and carbon-centered radicals with spin trap electron paramagnetic resonant (EPR) spectroscopy by Brezova et al.. They concluded that some sunscreens generated ROS [80]. These observations were confirmed by Barker at al., who showed that sunscreens containing titanium dioxide and zinc oxide nanoparticles were the primary cause of the rapid corrosion of paint surfaces on steel roofing via the production of reactive oxygen species [125].

A central challenge in assessing the risk of inorganic pigments used in sunscreens has been the great diversity of material types present: both titania and zinc oxide are used, often in different sizes and forms, with different surface coatings and possibly distinct crystal structures. To address any specific hazards of nanoscale materials require identification of their characteristics, e.g. size, shape and surface area. Only

comprehensive characterization of nanoscale materials for toxicology assessment would allow some identification of the potential dangers of nanoparticles. Ultimately, the data may enter a public access ‘nanoparticle safety database’, which in addition to materials type e.g. ZnO, will contain their characteristics (e.g. size, shape) and the results of toxicity tests. Then, by asking a specific question ‘e.g. how hazardous are ZnO nanoparticles of certain size and form’ the database will provide the result of an experiment that was done on the safety of these specific materials [11].

The characterization of the nanomaterials can be complicated, time consuming and expensive. However, it is vital to define exactly what manufacturers, consumers and the environment are exposed to during production, application and release of nanomaterials [29]. Therefore, in Chapter 2 and Chapter 3 of this thesis strategies for physicochemical characterization of commercial nanomaterials for environmental and health studies are presented.

Chapter 2 Strategies for physicochemical characterization of commercial nanomaterials for environmental and health studies

A selection of methods potentially suitable for nanoparticle characterization in powdered form is presented in the first part of this chapter. Then, the results from round robin test that investigated hydrodynamic size and zeta potential of nanoparticle dispersions are shown. Finally, analytical techniques for the detection and physicochemical characterization of nanoparticles in commercially available sunscreen formulations are described.

2.2 Best practices for characterization of nanoparticles in dry solid form

There are a minimum number of physical and chemical parameters that must first be characterized before nanoparticle interactions with biological systems are evaluated. Scanning and transmission electron microscopes can produce high resolution images of nanoparticles attached on appropriate substrates either in powdered form or evaporated as dilute films; these methods permit the dimensions, shape and form (e.g. agglomerated or isolated) to be directly visualized. Energy dispersive x-ray spectroscopy identifies and quantifies the elemental composition of the sample, often in similar sample formats to that used for electron microscopies. Other methods require powdered samples such as BET (Brunauer, Emmett, Teller) surface area analysis and x-ray diffraction (XRD). BET provides a quantitative measure of the specific surface area of the nanoparticles. XRD can determine the crystallinity and crystal structure of nanomaterials; also, for materials with dimensions below 20 nm the line widths of diffraction peaks can provide a measure of the grain size. X-ray photoelectron spectroscopy (XPS) uses the emission of core

photoelectrons to determine the chemical oxidation state of atoms at the nanoparticle surface. Combustion and thermal analysis of powders by thermo-gravimetric analysis (TGA) is complementary to XPS, and provides a quantitative measure especially of carbon bound to nanoparticle surfaces. A summary table of these methods if provided in table 2.2.1 and detailed information about each one follows this table.

2.2.1 Methods for nanoparticle characterization

Table 2.2.1 Instrumentation for characterization of nanoparticles in dry solid form

Technique / Instrument	**Information**
SEM-EDS (scanning electron microscopy energy dispersive spectroscopy) FEI Quanta 400F Field Emission Scope	Particle size distributions, shape, morphology, aggregation state and overall elemental composition
TEM (transmission electron microscopy) JEOL 1230 high contrast Transmission Electron Microscope	Particle size distributions, shape, morphology and aggregation state,
BET (Brunauer-Emmett-Teller) Quantachrome Autosorb 3B Surface Analyzer	Specific surface area, porosity, average diameter of particles
XRD (X-ray diffraction) Rigaku D/MAX Ultima II diffractometer	Crystal structure, crystallite size
XPS (X-ray photoelectron spectroscopy) Quantera x-ray photoelectron spectroscopy scanning microprobe	Surface elemental composition and in some cases oxidation state
TGA (thermo-gravimetric analysis) Q-600 Simultaneous Thermo-Gravimetric Analyzer	Quantitative analysis of carbonaceous surface species

SEM/EDS (Scanning electron microscopy/energy dispersive spectroscopy)

Samples for SEM/EDS characterization were prepared by mounting powders on SEM aluminum stubs (Electron Microscopy Sciences, Hatfield, PA) using double-sided adhesive tabs (Ted Pella Inc, Redding, CA) and sputter-coating with a conductive layer of gold (~ 20 nm). SEM and EDS were obtained using a FEI Quanta 400F Field Emission Scope equipped with Secondary Electron (SE) and a liquid nitrogen cooled Energy Dispersive X-Ray spectroscopy (EDS) detector (EDAX Genesis) with a working distance of 10 mm and a spot size setting of 4. For a good signal in high vacuum mode an accelerating voltage of 30 kV was used. In a typical imaging experiment, samples were imaged at randomly selected locations at magnification levels: 1,000x, 5,000x, 20,000x, 50,000x and 100,000x. EDS analysis was obtained at the 1,000x magnification level.

TEM (Transmission electron microscopy)

TEM samples were prepared by inserting a TEM grid (300-mesh copper/carbon grid, Ted Pella, Inc.) into the dry powder using tweezers to hold the grid. The grid was then flipped over to remove large agglomerate of particles and placed in the TEM for imaging. TEM images were obtained on a JEOL 1230 high contrast Transmission Electron Microscope (HC-TEM), employing an accelerating voltage of 80 kV. Size evaluation of particles are based on the analysis of a large number of particles, generally $N > 100$, for the best statistical results [126]. Therefore, for each sample, multiple images were collected to obtain a statistically significant population of more than one hundred particles. Both, width and length (the longest axis) for all the particles were defined manually using Image-Pro Plus 5.0 (Media Cybernetics) [127, 128].

BET (Brunauer-Emmett-Teller) specific surface area and BJH (Barrett-Joyner-Halenda) pore size analysis

Surface area and pore size analysis were carried out on fully automated Quantachrome Autosorb 3B Surface Analyzer. For measurements, powder samples were weighted and introduced into the glass cells (6 mm, small bulb), obtained from Qantachrome Instruments (Florida, USA). The material was heated under vacuum to the acceptable temperature for the materials (200^oC) for several hours to remove surface adsorbed contaminants. Then, the prepared sample was cooled with liquid nitrogen and analyzed by measuring the volume of N_2 gas adsorbed at specific pressures. The surface area and pore size was calculated automatically using Autosorb 3 software program. The average surface area and standard deviation were obtained by duplicate measurements. Assuming that the particles have a spherical shape with a smooth surface and are the same size, the surface area can be related to the average particle size by the equation $D_{BET} = 6000/(\rho \cdot SSE)$ (in nm), where D_{BET} is the average diameter of a spherical particle, SSE represents the measured surface area of the powder in m^2/g, and ρ is the theoretical density in g/cm^3 ($\rho_{TiO2} = 4.0\ g/cm^3$, $\rho_{CeO2} = 7.3\ g/cm^3$, $\rho_{FexOy} = 5.0\ g/cm^3$).

XRD (X-ray diffraction)

XRD samples were prepared by directly applying powder onto a Zero Background Holder and pressing to level the surface of the sample with the edge of the holder. The X-ray diffraction pattern was recorded on a Rigaku D/MAX Ultima II diffractometer equipped with monochromated CuKα radiation, employing a sampling width of 0.05^o, scan speed of 0.35^o/min and ranges from 20 to 85^o. Each spectrum was

taken using a voltage of 40 kV and a current of 40 mA. The crystallite size (D_{XRD}) of nanopowders was determined from the XRD patterns of the most intense peaks according to the Scherrer equation with correction for instrumental broadening: $D_{XRD} = K (\lambda / \beta \cos \theta)$, $\beta = (\beta^2_{measured} - \beta^2_{instrument})^{1/2}$, where K is a constant equal 0.89, λ the X-ray wavelength equal to 0.154 nm, $\beta_{measured}$ and $\beta_{instrument}$ are the full widths at half-maximum (FWHM) height of the most intense peak of the sample and that of the standard sample, respectively. A compound LaB_6 from National Institute of Standards and Technology was used as standard for calculating the full widths at half maximum of the instrumental line profiles. The FWHM values were calculated automatically from profile-fit peaks using the Jade 9 program.

XPS (X-ray photoelectron spectroscopy)

The XPS sample was prepared by pressing a nanoparticle into the surface of a piece of indium foil (0.5 x 0.5 cm). The indium foil with sample was then loaded onto a sample holder designed for XPS measurements. A Quantera x-ray photoelectron spectroscopy scanning microprobe was used in collecting the XPS data; the takeoff angle was 45^o, and a 114.8 W monochromatic Al x-ray source was applied for all the measurements. The power of the x-rays was 40.0 W. The spot size diameter was 200 μm, and a pass energy of 140.0 eV was used for survey scans (low resolution) and 26.0 eV for Ti2p, Ce3d, Fe2p, O1s, C1s elemental scans (high resolution). The binding energy was referenced to the C1s line at 284.8 eV which occurs from adventitious hydrocarbon (C-H bond) found on the sample holder and XPS instrument.

TGA (Thermo-gravimetric analysis)

Thermo-gravimetric analysis was performed on a Q-600 Simultaneous Thermo-Gravimetric Analyzer from TA Instruments. Nanoparticle samples (2 - 4 mg) were placed in platinum pans and heated to 130°C under an argon atmosphere followed by a 20 minute soak at constant temperature to remove any remaining solvent. The samples were then subjected to a heating gradient of 10°C/min to 1000°C.

2.2.2 Commercial, dry materials for characterization and experiments

The dry materials used in this research include titanium dioxide (TiO_2), cerium oxide (CeO_2) and ion oxide (Fe_xO_y) purchased from commercial sources. Two samples: ST01_TiO_2, and Umicore_CeO_2 were purchased form Ishihara Corporation (San Francisco, CA) and Umicore Nanomaterials (Belgium, Europe), respectively, by Centre for BioNanoInteractions (CBNI) at University College Dublin and were shipped to Rice University for analysis. Samples: T-Avo_TiO_2 and Aldrich_Fe_xO_y were obtained directly by Rice University from EMD Chemicals, Inc. (Hawthorne, NY) and Sigma-Aldrich (Milwaukee, WI), respectively. The information provided by manufacturers (obtained from technical data sheets and websites) is summarized in Table 2.2.2 [129-132].

Table 2.2.2 Source of nanomaterials with specifications provided by the manufacturer

Nanomaterial	**Source**	**Specifications**
ST01_TiO_2,	Ishihara Corporation San Francisco, CA, USA	White powder Anatase TiO_2 95 % D_{XRD} 7 nm SSA 320 m^2/g
T-Avo_TiO_2	EMD Chemicals Inc Hawthorne, NY, USA	White powder Rutile TiO_2 75 – 82 % PPS < 20 nm SiO_2 coating 13 – 20 % SSA 40 – 90 m^2/g
Umicore_CeO_2	Umicore Nanomaterials Belgium, Europe	Cubic CeO_2 D_{BET} 10 – 40 nm SSA 20 – 85 m^2/g
Aldrich_Fe_xO_y	Sigma-Aldrich Milwaukee, WI, USA	Nanopowder, spherical Ion (II, III) oxide ≥ 98 % PPS_{TEM} < 50 nm SSA >60 m^2/g

Abbreviations: D_{XRD} –crystallite size, SSA – BET specific surface area, PPS – primary particle size, D_{BET} –average diameter calculated from SSA;

2.2.3 Results from the characterization of dry powder nanomaterials

As discussed previously, to fully determine which physical properties of nanomaterials are most important for determining their toxicity it is vital to have standard, precise and accurate methods for physicochemical characterization. To develop such methods, four commercially available metal oxide nanopowders were evaluated for their particle size, size distribution, agglomeration or aggregation, shape, composition, surface

chemistry, purity, surface area, crystal structure and crystallite size. This information was derived from a battery of tests that provided redundant information, thereby validating and also constraining the various approaches.

The appearance of the as-received samples to the naked eye is illustrated in Figure 2.2.1. ST01_TiO_2 and T-Avo_TiO_2 were white powders. Umicore_CeO_2 and Aldrich_Fe_xO_y samples had light yellow and dark brown colors, respectively.

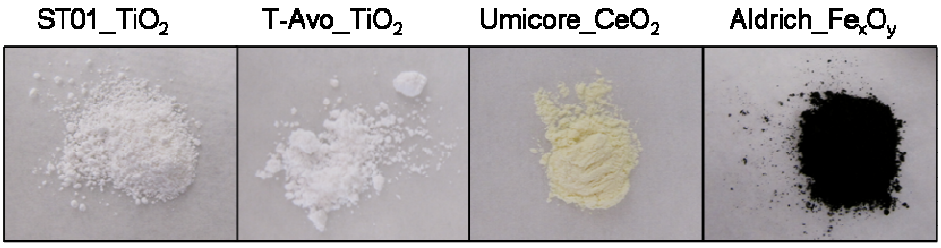

Figure 2.2.1 Digital images of as-received ST01_TiO_2, T-Avo_TiO_2, Umicore_CeO_2 and Aldrich_Fe_xO_y samples

Electron microscopy analysis

Electron microscopy is widely used for the visualization of nanomaterials. All samples were analyzed with SEM and TEM to determine size, observe shape and agglomeration/aggregation state. SEM images obtained at low magnification level (5,000x), showed that samples ST01_TiO_2, Umicore_CeO_2 and Aldrich_Fe_xO_y formed loose agglomerates with wide size distributions and dimensions that in some cases exceeded 10 µm. The difference between agglomeration and aggregation has been the subject of some debate in the nanotoxicology community; generally accepted practice holds that agglomerated nanoparticles are usually attracted to each other by relatively weak Van der Waals interactions. As a result the material can be redispersed in solution,

often requiring some sonication, under ambient conditions. Aggregated nanoparticles are generally much more difficult to break up as they are held together by stronger electrostatic or hydrogen bonding forces. Distinguishing among aggregation and agglomeration in microscopic images is thus challenging; the only guide is that agglomerates are often less dense while aggregates compare much more compact. Based on this, we refer to these materials as agglomerates and emphasize the need to develop more quantitative measures of the degree of nanoparticle association [133]. To make this point throughout the presentation, the term 'cluster' will be used to describe an assemblage of particles in an image without reference to the degree of association.

T-Avo_TiO_2 consisted of clusters with sizes below 10 µm. Some of the individual nanoparticles forming the clusters are visible in higher magnification SEM images (50,000x). The exact diameter of these features is right at the limit of detection for this instrument, which is about 20 nm.

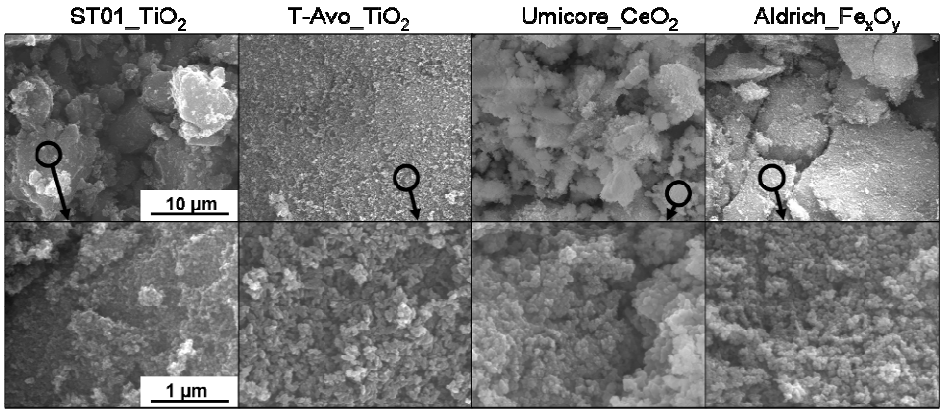

Figure 2.2.2 Secondary electron images of ST01_TiO_2, T-Avo_TiO_2, Umicore_CeO_2 and Aldrich_Fe_xO_y samples obtained at low (5,000x) and high (50,000x) magnification levels, showing: the degree of agglomeration/aggregation in the 'as-received powders'

The resolution available in TEM makes it possible to unambiguously confirm that the larger clusters seen in SEM are actually made from a number of much smaller nanoscale particles (see Figure 2.2.3). Different magnifications were used to image the primary size of the particles. Because of the edges of the nanoparticles were often touching, it was not possible to use automated image analysis to determine the primary particle size. For this reason, the particle dimensions were defined manually. A length and width measurement was recorded only if clear edges of the particle were apparent along both axes of the particles. Assuming a normal distribution, with typical sampling sizes of more than one hundred particles, the error in these average dimensions should be less than 10 % [134].

The histograms of the primary particle sizes obtained from TEM analysis are shown in Figure 2.2.3. Relatively narrow particle size distribution was measured for the spherical particles present in sample ST01_TiO_2 (d = 5.4 ± 0.8 nm). T-Avo_TiO_2 particles were needle-shaped with a length of 28.2 ± 8.9 nm. Aldrich Fe_xO_y nanoparticles were predominantly spherical (d = 23.4 ± 9.4 nm) while umicore_CeO_2 nanoparticles shapes varied from particle to particle with a very broad size distribution (d = 21.1 ± 9.4 nm). A summary of the dimensions of these samples found from TEM are presented in Table 2.2.3. TEM imaging at higher magnification (see Figure 2.2.4) further revealed a nonuniform coating layer on T-Avo_TiO_2 particles.

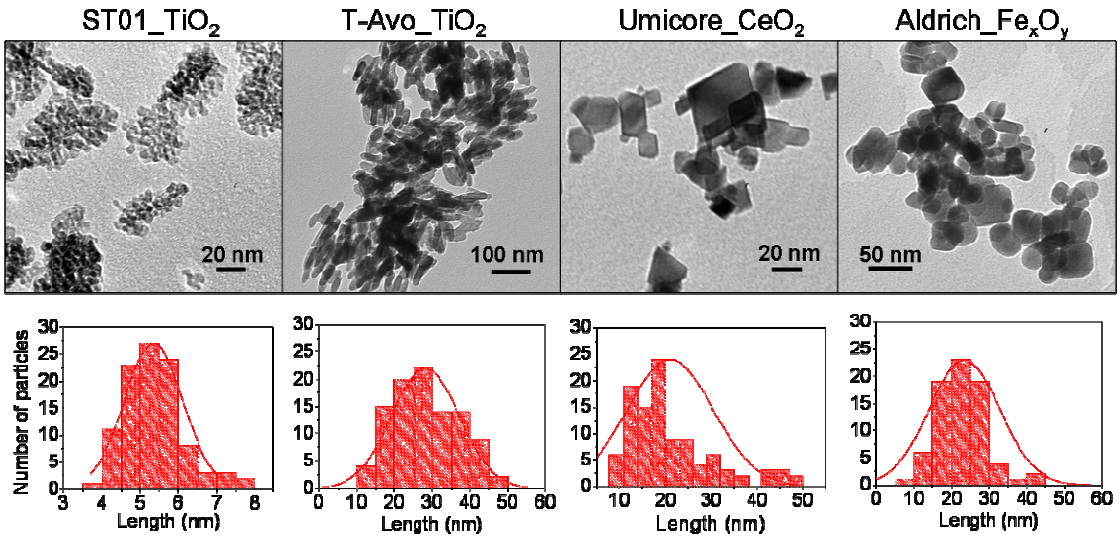

Figure 2.2.3 TEM images and size histograms of ST01_TiO_2, T-Avo_TiO_2, Umicore_CeO_2 and Aldrich_Fe_xO_y samples

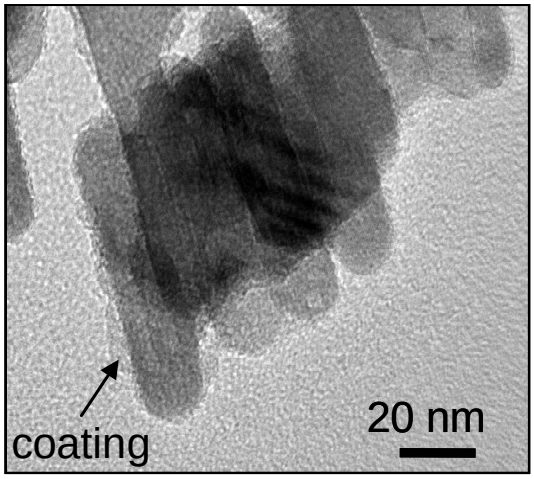

Figure 2.2.4 High magnification image of T-Avo_TiO_2 sample

While electron microscopy analysis can be time consuming and expensive, it is perhaps the best way to evaluate primary particle size/size distribution, shapes and surface coating. Its limitation is that it cannot fully determine the agglomeration or aggregation state of nanoparticles directly in suspension; these 'net' sizes are the physical

dimensions that are the most important for biological interactions. The agglomeration or aggregation state is likely to differ depending on whether particles are measured as powders (as seen in Figure 2.2.4) or found via other methods such as light scattering in dispersions in water or other relevant biological media [135]. This issue is also important for airborne exposures. Furthermore, depending on the interparticle interactions, groups of particles that are effectively agglomerated in one medium could become dissociated in other kinds of biological fluids. In this instance, it will be the primary particles rather than their associates that will be of relevance to an interpretation of toxicity data. Clearly, new analytical tools and validation experiments are required to fully address the complex questions surrounding nanoparticle association and dissociation in biologically relevant media (cell culture media, dosing solution, aerosol, etc.).

In spite of its importance, no vendors report the as-prepared agglomeration or aggregation state or their powders. One high magnification SEM image of Umicore_CeO_2 nanoparticles is available on the Umicore website which clearly shows objects much larger than the primary particle sizes, suggesting association of the nanoparticles. One TEM image of clustered, rather than single primary T-Avo_TiO_2 particles can also be found on the company website. However, the image is too low of resolution to reveal the surface coating material and too high of magnification level to measure particle agglomerate size.

Vendors often report the dimensions of the primary nanoparticles in powders, but this information can be difficult to interpret as the methods used to measure primary particle sizes are rarely provided. Depending on the method the meaning of the primary particle ‘size’ can be very different; for example EMD Chemicals, specifies T-Avo_TiO_2

as less than 20 nm but it is not clear if that is primary particle size, cluster size, or grain size as may be determined via x-ray diffraction. Others may use a different technique other than TEM to get the particle size (Umicore_CeO_2 D_{BET} 10 – 40 nm or ST01_TiO_2 D_{XRD} 7 nm). Alternative techniques, such as the mean particle size calculated from BET surface area or crystallite size from XRD line broadening of selected reflections reflect assumptions that can lead to a systematic error in the definition of particle size. Sigma-Aldrich does not report a specific diameter for the oxide particle size (e.g. only that it is < 50 nm) and do not reveal information about number of analyzed particles thereby making an estimate of the precision impossible. Vendor information alone is neither reliable nor sufficient for toxicity studies. Independent research is required in order to thoroughly analyze received samples.

Surface area and pore size analysis

The surface area is a physicochemical parameter considered to be of central importance to nanoparticle toxicity because, as the particle size decreases, its surface area to volume ratio increases; hence a greater portion of nanoparticle surface atoms or molecules being available to react with other matter [66]. It might be assumed that larger surface area leads to more toxicity. It has even been demonstrated that particles of the same substance but of a different surface area exhibit the same toxicity when the dose is expressed in terms of net surface area as opposed to mass or number of particles [136-139]. However, other studies have questioned this hypothesis because nanomaterial toxicity is a matter of several physicochemical parameters only one of which is surface area [140, 141].

The specific surface areas (SSA) of the as-purchased samples were found to range from 34.2 ± 0.7 m^2/g for Umicore_CeO_2 to 275.3 ± 19.7 m^2/g for ST01_TiO_2. If these particles are assumed to be spherical, the equivalent particle size can be calculated from the SSA. The equivalent particle diameter so calculated was 24.1 ± 0.5 nm for Umicore_CeO_2 powder and 5.4 ± 0.4 nm for ST01_TiO_2. The equivalent particle diameters of all analyzed samples were in excellent agreement with the TEM examination of primary particle sizes (see Table 2.2.3), indicating that these particles were loosely agglomerated. If the primary particles formed strong agglomerates (due to strong bonds between particles), they would result in lower SSA and larger values of sizes calculated by the BET method [142, 143].

While the surface areas of all four powders measured in this lab were within the broad ranges reported by the manufacturer; a more quantitative comparison was only possible with two of the commercial materials. The surface areas of T-Avo_TiO_2 and Umicore_CeO_2 powders reported by manufacturers were 40 to 90 m^2/g and 20 to 85 m^2/g, respectively; these ranges encompass our own data, but their existence suggests batch to batch variation. In contrast, the producers of ST01_TiO_2 and Aldrich_FexOy did provide more quantitative surface areas that were in both cases higher than these laboratory values (14 % and 32 %, respectively). This systematic error may result from batch to batch variability in the manufacturing of nanoparticles; alternatively, a difference in procedures that were applied during BET measurements could also account for errors in this value.

BET analysis was also used to determine porosity of metal oxide nanoparticles. An example of the adsorption-desorption isotherms of the STO1_TiO_2 and T-Avo_ TiO_2

samples are presented in Figure 2.2.5 A and B. For all samples, within a wide pressure range, isotherms corresponded to type II (IUPAC classification). Type II isotherms are representative of nonporous materials. However, isotherms of STO1_TiO_2 (Figure 2.2.5 A) and Umicore_CeO_2 were not reversible and at high relative pressures exhibited a type H3 hysteresis loops which has been attributed to the open spaces within the agglomerates [144]. Pore analysis has not been reported by manufacturers, even if the porosity of nanoparticles significantly increases the surface area. This factor may be one reason SSA measured in this laboratory is lower than that reported by some manufacturers.

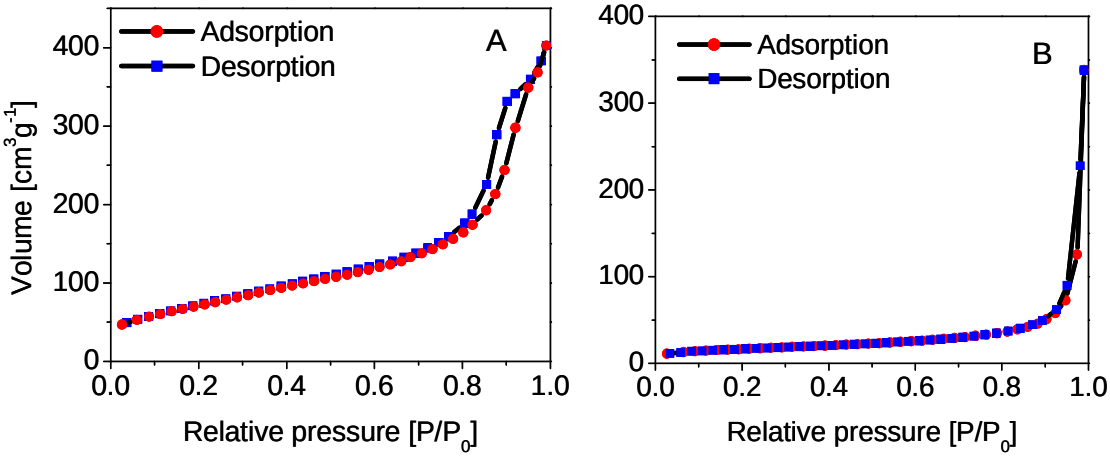

Figure 2.2.5 N_2 adsorption-desorption isotherms for STO1_TiO_2 (A) and T-Avo_TiO_2 (B) samples

It is also important to note that degassed at 200^{o}C for 7 h prior BET analysis ST01_TiO_2 sample changed appearance from white to grey as presented in Figure 2.2.6 which may suggest the presence of impurities in this sample, or possibly the reduction of the titania to a less reduced form.

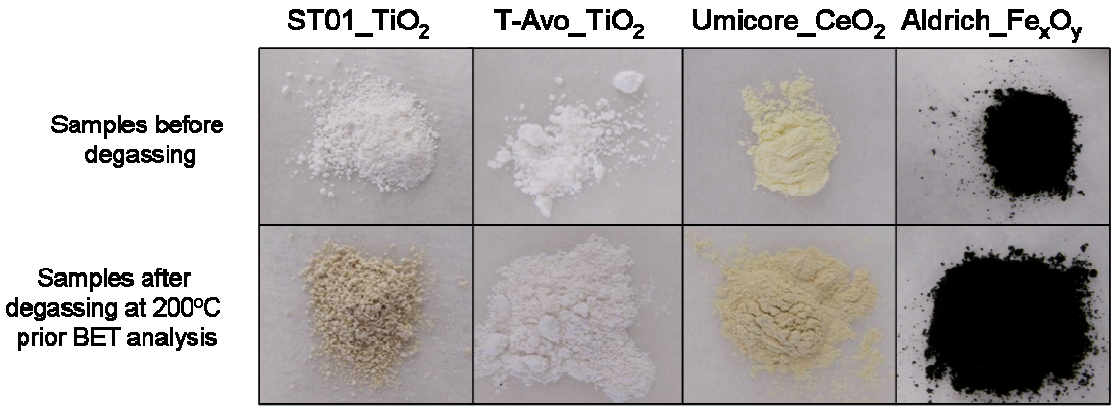

Figure 2.2.6 Digital images of ST01_TiO_2, T-Avo_TiO_2, Umicore_CeO_2 and Aldrich_Fe_xO_y samples before (upper row) and after degassing at 200^{o}C prior BET analysis (lower row)

XRD (X-ray diffraction)

The crystalline form also determines the toxicity of nanoscale material. For example, the two most important polymorphs of titania, rutile and anatase, display different photocatalytic activities with anatase acting as a stronger photocatalyst than rutile [145]. Studies have shown that this chemical activity of anatase TiO_2 translates into an increase in biological activity [44, 71].

XRD patterns obtained for ST01_TiO_2 and Umicore_CeO_2 samples are presented in Figure 2.2.7. These patterns were used to identify the crystal phase and estimate crystallite sizes of analyzed samples. Pure-phases TiO_2 anatase and rutile were found in samples ST01_TiO_2 (Figure 2.2.7 A) and T-Avo_TiO_2, respectively. The cerium oxide nanoparticles crystallized in the cubic fluorite structure (Figure 2.2.7 B). The magnetite phase was identified in Aldrich_Fe_xO_y though it is very difficult to distinguish magnetite

from the more oxidized maghemite in x-ray diffraction. These crystal structures agreed well with those reported by the nanoparticle producers.

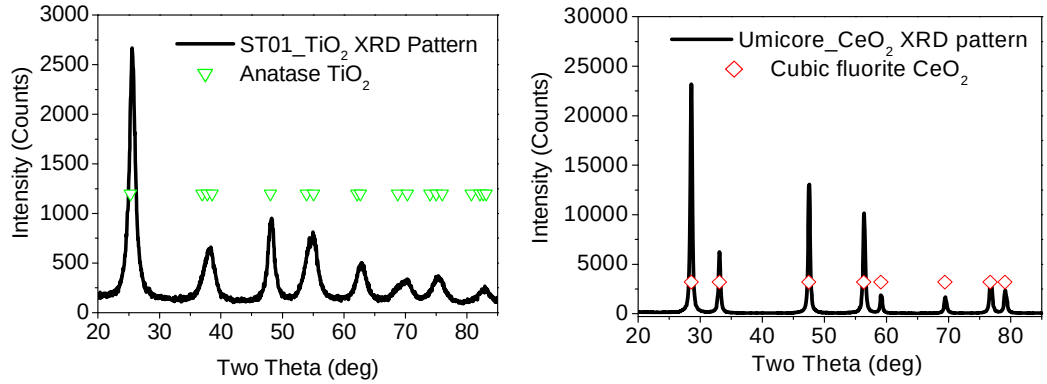

Figure 2.2.7 X-ray diffraction pattern of ST01_TiO_2 and Umicore_CeO_2

Furthermore, the crystallite size for ST01_TiO_2, T-Avo_TiO_2, Umicore_CeO_2 and Aldrich_Fe_xO_y was estimated from the full width at half-maximum by the Scherrer equation after subtracting the instrumental broadening. ST01_TiO_2 peaks appeared broader in comparison to all the other XRD patterns, indicating smaller particles. The crystallite size calculated from Scherrer equation for ST01_TiO_2 was 6.7 nm; this value agreed with the number reported by Ishihara Corporation (7 nm). The crystallite sizes for all analyzed samples are presented in Table 2.2.3 and are in good agreement with TEM and BET results.

Table 2.2.3 Characterization of nanoscale pigments

Sample name	W_{TEM} [nm]	L_{TEM} [nm]	D_{XRD} [nm]	D_{BET} [nm]	SSA [m^2/g]	Crystal structure
ST01_TiO_2	3.9 ± 0.7	5.4 ± 0.8	6.7	5.4 ± 0.4	275.3 ± 19.7	Anatase
T-Avo_TiO_2	13.8 ± 2.8	28.2 ± 8.9	18.8	26.5 ± 0.6	56.6 ± 1.3	Rutile
Umicore_CeO_2	16.0 ± 7.4	21.1 ± 9.4	25.5	24.1 ± 0.5	34.2 ± 0.7	Cerianite
Aldrich_Fe_xO_y	17.6 ± 7.8	23.4 ± 9.4	22.3	29.0 ± 1.5	41.5 ± 2.0	Magnetite

Abbreviations: W_{TEM} and L_{TEM} – average width and length determined from TEM analysis, D_{XRD} – crystallite size, D_{BET} – average diameter calculated from SSA (BET specific surface area)

Elemental analysis by energy dispersive x-ray spectroscopy (EDS)

Energy dispersive x-ray spectroscopy (EDS) was used to confirm the elemental composition of particles and to detect any impurities that may be present (see Table 2.2.4). Example of EDS spectra obtained for T-Avo_TiO_2 and Umicore_CeO_2 are presented in Figure 2.2.8. ST01_TiO_2 and T-Avo_TiO_2 samples both contained Titanium as expect (≥ 30 wt %). EDS also found that T-Avo_TiO_2 contained silicon (Si 9 wt %). The major elements in Umicore_CeO_2 and Aldrich_Fe_xO_y samples were Ce and Fe, respectively. A higher amount of carbon was present in ST01_TiO_2 (36 wt %) and Umicore_CeO_2 (20 wt %) as compared to T-Avo_TiO_2 (8 wt %) and Aldrich_Fe_xO_y (6 wt %), which may indicate the presence of residual surfactant or dispersion additive in these samples. Such impurities could have a drastic impact on studies of toxicity.

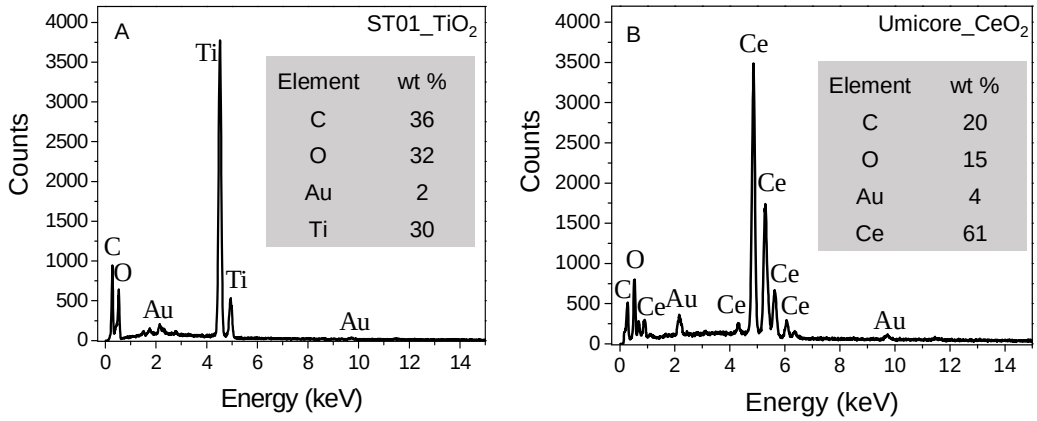

Figure 2.2.8 EDS spectra of ST01_TiO_2 and Umicore_CeO_2 (Au element results from sputter coating the SEM stub)

The impurities in the sample rather than the primary material structure, may be responsible for the biological effects; hence it is essential to accurately control the chemical parameters of each nanomaterial tested in toxicity studies. For example, Pulskamp et al. showed that impurities associated with the commercial nanotubes caused toxicity in cells [55]. Nanomaterial may be contaminated during the preparation process by more toxic, surface-adsorbed surfactants, for example used to control size and shape of the particles [146]. To further elaborate on the nanoparticle surface composition, this laboratory turned to x-ray photoelectron spectroscopy (XPS).

Table 2.2.4 Elemental composition of nanoparticles

Sample	**EDS analysis (wt %)**	**XPS analysis (wt %)**
ST01_TiO_2	C (36), O (32), Ti (30), Au (2)	C (16), O (62), Ti (22)
T-Avo_TiO_2	C (8), O (32), Ti (46), Si (9), Au (5)	C (3), O (68), Ti (12), Si (17)
Umicore_CeO_2	C (20), O (15), Ce (61), Au (4)	C (28), O (52), Ce (20)
Aldrich_Fe_xO_y	C (7), O (18), Fe (71), Au (4)	C (12), O (71), Fe (17),

X-ray photoelectron spectroscopy (XPS)

Particle surface coating plays important roles in determining the toxicity because of its direct contact with the biological systems. Studies on a number of commercial formulations of TiO_2 particles indicate that different surface treatments can influence the pulmonary toxicity [147]. Surface coating can render noxious particles non-toxic while less harmful particles can be made highly toxic. For example, in the case of TiO_2 nanoparticles silica is often used to block access to the titania surface in a solution environment, and consequently reduce its reactivity [114, 148].

The results from XPS surface elemental analyses for all samples are reported in Table 2.2.4. They are comparable with EDS analysis and confirmed that elemental composition of samples was consistent with TiO_2, SiO_2, CeO_2 and Fe_xO_y. Moreover, XPS confirmed the presence of a SiO_2 surface coating for T-Avo_TiO_2 sample and carbon-containing constiuents in samples ST01_TiO_2 and Umicore_CeO_2. An example of an wide scan XPS and high resolution spectra for Ti2p and O1s regions are presented in Figure 2.2.9.

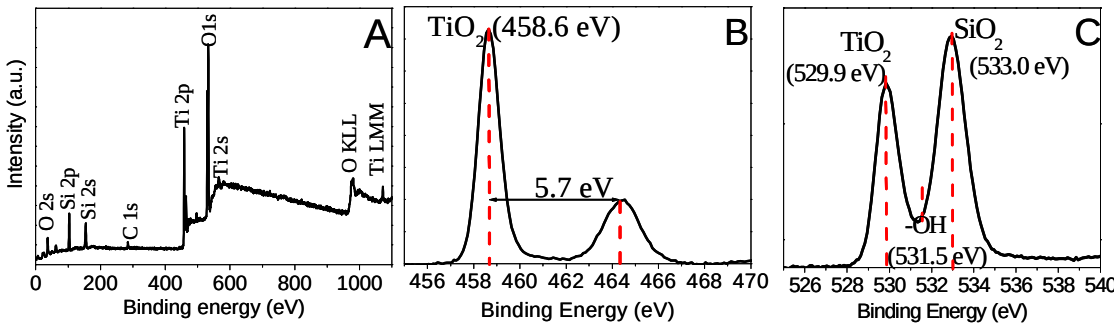

Figure 2.2.9 XPS wide scan spectrum (A) and high resolution XPS spectrum of Ti2p and O1s regions for sample T-Avo_TiO_2 (B and C)

High resolution XPS spectra of Ti2p, Ce3d and Fe2p regions provide the best information about the chemical state, particularly the oxidation state, of surface atoms. Figure 2.2.9 B shows an example of the high resolution XPS spectrum of Ti2p obtained for sample T-Avo_TiO_2. The Ti2p data obtained for both samples T-Avo_TiO_2 and ST01_TiO_2 indicated that titanium element mainly existed as the chemical state of Ti^{4+} on the basis of values reported in the literature [149, 150]. Umicore_CeO_2 exhibited a complex spectrum that consisted of the Ce3d XPS spectrum of a Ce^{4+} compound (six structures) and Ce^{3+} species (four structures). Characteristic peaks of CeO_2 were at 882.6 eV and 916.7 eV. Small lines appeared also at 886.7 eV and 903 eV that characterize Ce^{3+} oxide [151]. The Fe2p XPS spectrum for sample Aldrich_Fe_xO_y pointed toward the existence of two oxidation states of Fe^{2+} and Fe^{3+}. The $2p_{3/2}$ photoelectron peaks were observed around 710 eV for Fe^{2+} and 711 eV for Fe^{3+}[152].

Peak fitting of the O1s peak into two signals generated a good fit to the experimental total peak for samples ST01_TiO_2, Umicore_CeO_2 and Aldrich_Fe_xO_y. The main signals for these samples were attributed to the TiO_2 (529.9 eV), CeO_2 (529.4 eV) and Fe_xO_y (529.7 eV), respectively. The second peak at 531.5 eV corresponded to OH.

The O1s peak for T-Avo_TiO_2 (see Figure 2.2.9 C) was fitted to three peaks centered at 533.0 eV 529.9 and 531.5 eV that indicated the presence of SiO_2, TiO_2 and OH [150, 152-154]. Therefore, XPS confirmed presence of SiO_2 surface coating for T-Avo_TiO_2 sample.

XPS investigations revealed also that the surface of samples ST01_TiO_2 and Umicore_CeO_2 were covered by carbon-containing contaminants. These data were in good agreement with EDS (Table 2.2.4). The X-ray photoelectron spectra of C1s for samples ST01_TiO_2 (Figure 2.2.10), Umicore_CeO_2 and Aldrich_Fe_xO_y were curve-fitted with three peak components having binding energies at about 284.8, 286.4 and 288.8 eV. These peaks may be attributed to the species C-H, C-O and C=O, respectively, and indicate a certain amount of carbon impurities [150]. XPS results for T-Avo_TiO_2 (Figure 2.2.10) showed no evidence for the existence of C=O species.

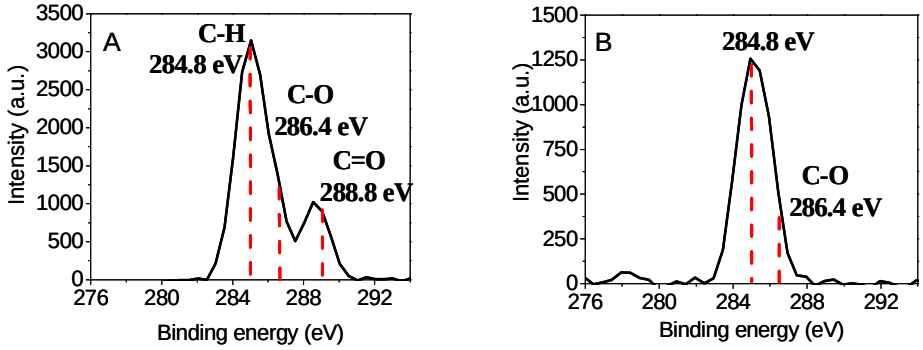

Figure 2.2.10 XPS C1s scans for samples ST01_TiO_2 (A) and T-Avo_TiO_2 (B)

XPS is among one of the most common analytical methods used in determining the chemical composition of a nanoscale particle's surface. However, in this study surface composition of nanoscale particles was confirmed with the analysis of TGA data.

Thermo-gravimetric analysis (TGA)

Thermo-gravimetric analysis of metal oxide particles was performed to quantitatively analyze for the amount of carbon in the sample; to do this, it heats the sample under conditions that oxidize the carbon thereby allowing for the determination of the amount (weight loss) and type (desorption temperature) of carbon. Figure 2.2.11 shows weight loss under heating for all samples. No significant loss in weight was observed for sample Aldrich_Fe_xO_y in temperature range 100 – 1000^{o}C. ST01_TiO_2 and Umicore_CeO_2 has relatively small changes in weight between 150 – 300^{o}C (3 % and 1 %, respectively) consistent with organic carbon. A mass loss of 2.5 % for T-Avo_TiO_2 took place between 250 – 500^{o}C. No significant weight loss was apparent above 500^{o}C for these samples. The weight loss in the temperature range of 150 – 500^{o}C can be attributed to the removal of physisorbed and chemisorbed water and residual organics. For T-Avo_TiO_2 the silica coating began to decompose above 400^{o}C [155, 156].

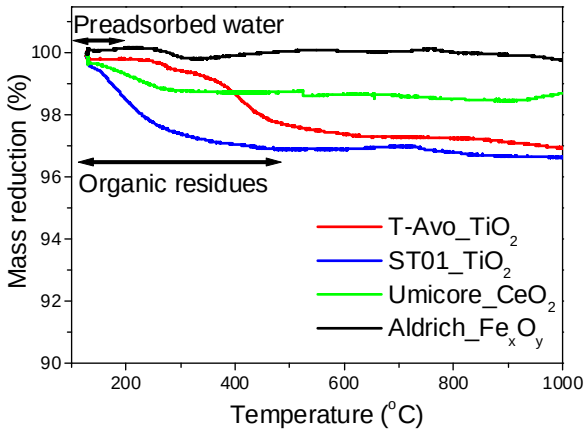

Figure 2.2.11 Thermo-gravimetric analysis curves for analyzed metal oxides

Some carbon constituents, either intentionally incorporated or accidental impurities, are present in two of the four samples studied: ST01_TiO_2 and Umicore_CeO_2. Data from EDS, XPS and TGA all point to the existence of organic carbons. As the manufacturers are not willing to share the details of their preparation or stabilization chemistry, an exact identification of the material is not possible. However, its presence suggests that carbon-content could be an important variable to account for when studying the toxicity of commercial nanoscale powders. Ideally, for environmental and health studies samples should be free from any adventitious solvents or precursors used in their production. Such toxic impurities can drastically change the response of cells and organisms to these materials. For example, for nickel ferrite particles coated with oleic acid prepared by the polyol method, the cytotoxicity significantly increased when one or two layers of oleic acid were deposited as compared to prepared without oleic acid impurities [157].

2.2.4 Conclusion

This section of the thesis presents detailed characterization of four metal oxide nanopowders (ST01_TiO_2, Umicore_CeO_2, T-Avo_TiO_2 and Aldrich_Fe_xO_y) obtained from chemical companies (Ishihara Corporation, EMD Chemicals Inc, Umicore Nanomaterials and Sigma-Aldrich). Since no single parameter has yet been identified as being responsible for nanomaterial toxicity, it is best to measure a set of physical and chemical parameters. Presented here are methods for evaluation of the primary particle size and size distribution, shape, aggregation state, specific surface area, porosity, crystal structure, crystallite size, overall and surface elemental compositions. This information

generally was derived from multiple parallel techniques including scanning and transmission electron microscopy, Brunauer-Emmett-Teller surface area analysis, x-ray diffraction, energy dispersive x-ray spectroscopy, x-ray photoelectron spectroscopy and thermo-gravimetric analysis.

Each of the samples used in this study had different physicochemical properties. In some cases, the parameters of nanoscale materials reported by the manufacturers were different than the actual measurement. For example, surface areas of ST01_TiO_2 and Aldrich_Fe_xO_y reported by the manufacturers differed from our measurements by 14% and 32%, respectively. Researchers should confirm before studies these fundamental parameters so as to ensure their data can be adequately compared to other laboratories. Accurate characterization of nanoparticles is necessary because information provided by manufacturers can be incomplete due to batch-to-batch variability. Also, as shown here the best information results when a variety of techniques are employed. Each provides complementary information that can both validate and further inform the complete understanding of the material. Finally, while not addressed in this section, to fully support toxicity studies analytical methods are needed for the form of nanomaterials directly in the medium of interest, ideally at very different time points in a biological study. The next section centers on this complex issue and evaluates the hydrodynamic size and surface charge (zeta potential) of nanoparticle dispersions.

2.3 Interlaboratory comparison of the size and surface charge measurements of nanoparticles prior to biological impact assessment

The purpose of this section is to present results from an international interlaboratory test (round robin test) that investigated the reproducibility of the measurements of nanoparticle hydrodynamic size and zeta potential. Each laboratory followed a standard protocol for sampling handling and measurement methods. The results of round robin test for nanoparticle hydrodynamic size distribution and zeta potential are presented by Roebben et al. [158]. Here, a report of Rice University's findings in dynamic light scattering (DLS) measurement for determining the size distribution and zeta potential of three samples delivered by Centre for BioNano Interactions at University College Dublin (UCD) and Institute for Reference Materials and Measurements (IRMM) will be described and compared with data obtained by other collaborators that participate in The International Alliance for NanoEHS Harmonization (IANH).

2.3.1 The International Alliance for NanoEHS Harmonization

Reproducibility of the measurements of nanoparticle properties is necessary to obtain meaningful data in nanotoxicity studies. Such reliable data is essential for the investigation of nanoparticle hazards. The International Alliance for NanoEHS Harmonization chaired by Prof. Kenneth Dawson (Centre for BioNano Interactions at University College Dublin) performed round robin test on hydrodynamic size and zeta potential for gold, silica, polystyrene, and ceria nanoparticles [158]. '*The International Alliance for NanoEHS Harmonization is an interdisciplinary alliance of scientific experts,*

themselves currently active in all aspects of this arena, drawn from Europe, Japan and the United States that seeks to establish reproducible approaches for the study of nanoparticle hazard' [159]. Institutions participated in the IANH are presented in Figure 2.3.1. The Center for Biological and Environmental Nanotechnology at Rice University (Houston, TX) is one of the IANH collaborators that participated in round robin tests on hydrodynamic size and zeta potential.

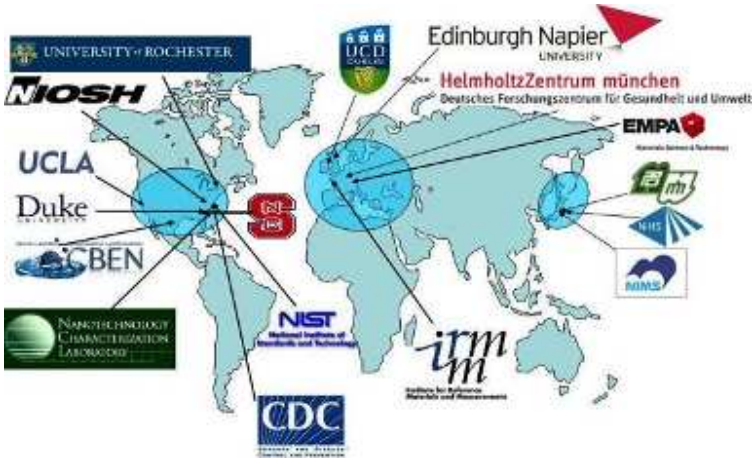

Figure 2.3.1 Partners and collaborators participated in IANH. Adapted from [159]

2.3.2 Procedures and methodology

This section outlines the procedures that Rice University used in the dynamic light scattering (DLS) and zeta potential analyses of silica, polystyrene, and ceria nanoparticles. The goal of these measurements was to determine

i) hydrodynamic diameter from three (consecutive) measurements on two aliquots

ii) pH of the samples

iii) zeta potential

Materials

Three samples were delivered to Rice University Houston, TX from Centre for BioNanoInteractions (CBNI) at University College Dublin (UCD) and the Institute for Reference Materials and Measurements with instruction for DLS tests on nanoparticle suspensions and a Microsoft Excel spreadsheet for reporting the results. The package sent from UCD contained 10 ml of 0.05 mg/ml suspension of aggregated cerium oxide (CeO_2) nanoparticles stabilized in nitric acid at pH 4. This sample was coded as Umicore D246. The primary CeO_2 particle size calculated from the specific surface area measured using the BET method was 30 nm. However, this sample did not consist of single particles but aggregates whose sizes ranged between 100 nm and 200 nm. The second sample, here coded as BL-PS, contained 10 ml of 0.05 mg/ml amine-modified 60 nm polystyrene nanoparticle suspension [160]. These two samples were shipped in foam boxes with 3M Freeze Watch and Thermax thermal sensors attached. The package from IRMM contained a Quality Control Material IRMM-304 in amber glass ampoule that consisted of 9 ml of 43 ± 3 nm silica (SiO_2) nanoparticles suspended in an aqueous solution [161].

Sample characterization protocol

The IANH DLS test protocol was distributed electronically to all ten collaborators that participated in round robin testing of nanomaterials. The list of round robin test participants is presented by Roebben et al. [158]. The IANH DLS test protocol was created based on a previously existing NIST-NCL protocol [162]. Besides the summary of provided materials, the characterization protocol included information about sample

handling and storage, instructions for opening glass ampoule with silica nanoparticles, and guidelines for material testing and data reporting.

The participants were asked to store SiO_2 nanoparticles at room temperature and the other two samples, CeO_2 and PS, at 4^oC before testing them. If the samples were subjected to freezing temperatures participants should ask for a new set of samples. The protocol for sample characterization specified that silica and polystyrene nanoparticles should be analyzed as received without sonication, dilution or filtration. The sample with ceria nanoparticles was divided and 5 ml aliquot was tested as received and the other half after 30 min sonication in a Fisher Scientific bath sonicator (FS6; power 40W). For each sample three measurements were performed on two aliquots, resulting in six data points.

Before DLS analysis, the pH of the samples was measured using ACCUMET AB15 pH-meter equipped with Accumet Combi pH/ATC polypropylene probe. The pH-meter was calibrated before use. The hydrodynamic diameters of nanoparticles were determined by a Zetasizer Nano ZS (Malvern, Herrenberg, Germany) in polycarbonate cuvettes (Sarstedt AG & Co., Nürnberg,Germany) under backscattering conditions of 173° and using the cumulants method. The instrument was powered up 30 minutes in advance of measurement to allow the laser to stabilize. 0.75 ml of the sample was loaded into DLS cuvette using a syringe. The cuvette was capped to prevent dust contamination and evaporation of the solution. To prevent air bubbles, the cuvette was examined visually before placing on the cuvette holder. Air bubbles may cause false signal reflection that lead to an incorrect particle size distribution. The DLS measurements were performed at 25^oC. The refractive index and viscosity of suspending medium (H_2O) used during DLS analysis were 1.33 and 0.89 cPa (for 25^oC), respectively. Refractive indices for all

samples used in the calculation of hydrodynamic diameters from DLS measurements are given in Table 2.3.1. Three repeat DLS measurements on two aliquots of IRMM-304, PS-BL, not sonicated Umicore D246 and sonicated Umicore D246 were performed.

Table 2.3.1 Refractive indexes for samples used in the calculation of hydrodynamic diameters from DLS measurements in round robin testing

Material	**Refractive Index**
Silica IRMM-304	1.46
Polystyrene BL-PS	1.58
Ceria Umicore D246	2.31

2.3.3 Results and discussion

Shipping and storing the samples

One package with silica nanoparticles (IRMM-304) and the second one with cerium oxide (Umicore D246) and polystyrene nanoparticles (BL-PS) were sent from Institute for Reference Materials and Measurements (IRRM) and University College Dublin (UCD), respectively on the 4th of February, 2009, via DHL and delivered to Rice University, Houston, TX, two days later. The samples from UCD were shipped in styrofoam box with 3M Freeze Watch and Thermax thermal sensors attached. Both sensors show no color indication, which suggested that the samples were not exposed to freezing temperatures.

Storage and shipping the samples is extremely important to ensure quality data in interlaboratory research. Problems due to delay in receiving the samples and

inappropriate storage can result in sample damage. The sample shipping procedure was discussed with IANH collaborators before sending the samples to round robin test participants. It was concluded that samples could be shipped in polypropylene tubes, or glass scintillation vials if they were adequately wrapped/secured. If a bottle contains liquid, it is also necessary to surround the cap with an additional barrier such as parafilm or tape to prevent any leaked material from coming into contact with people or surfaces. Then, samples should be placed in styrofoam boxes, card board boxes or padded envelopes where there is bubble wrap inside. If sample is temperature sensitive the thermal sensors, for example 3M Freeze Watch or Thermax should be used.

DLS measurements of hydrodynamic diameter

Samples delivered by UCD and IRMM were used for dynamic light scattering (DLS) measurements to obtain hydrodynamic size and zeta potential. Prior to DLS measurement pH measurements of IRMM-304, PS-BL, not sonicated Umicore D246 and sonicated Umicore D246 samples were performed. The results from DLS and pH experiments are presented in Table 2.3.2 in requested by INAH format.

Table 2.3.2 The results from DLS and pH measurements for IRMM-304, PS-BL, not sonicated Umicore D246 and sonicated Umicore D246 samples

Sample name	**Run number**	**Size (nm)**	**PDI**	**pH**	**Zeta potential (mV)**
Silica IRMM-304	1	44.13	0.111	9.08	NA
	2	42.81	0.108		
	3	42.58	0.108		
Silica IRMM-304	4	44.72	0.148		NA
	5	43.30	0.158		
	6	42.69	0.133		
Polystyrene BL-PS	1	61.20	0.073	7.71	33.7
	2	59.57	0.098		
	3	59.49	0.111		
Polystyrene BL-PS	4	59.56	0.126		32.5
	5	60.08	0.147		
	6	59.00	0.102		
Ceria Umicore D246	1	165.7	0.183	4.4	NA
	2	160.0	0.207		
	3	158.2	0.190		
Ceria Umicore D246	4	158.1	0.183		NA
	5	159.3	0.183		
	6	152.5	0.167		
Ceria Umicore D246 - sonicated	1	2078	0.517	4.94	NA
	2	1999	0.694		
	3	2080	0.393		
Ceria Umicore D246 - sonicated	4	2127	0.623		NA
	5	1784	0.706		
	6	1615	0.492		

Abbreviations: NA – Not available, PDI – Polydispersity index, Size – hydrodynamic diameter

DLS measurements showed that Silica IRMM-304 and Polystyrene BL-PS were nearly monodisperse with a polydispersity index (PDI) less than 0.2 and Hydrodynamic diameter (d) 43.37 ± 0.87 nm for SiO_2 and 59.82 ± 0.76 nm for polystyrene nanoparticles. Ceria Umicore D246 consisted of aggregates with 158.97 ± 4.23 nm in size that were dispersed in the solution and larger aggregates (~ 1000 nm), which were not visual and settled to the bottom of the tube.

Dynamic light scattering (DLS) is a fast method for characterizing the size of nanoparticles in solution. This technique involves monochromatic light, interacting with particles undergoing Brownian motion in a fluid. The particles in a solution undergo movement that is caused by the fluid molecules. The motion is size dependent (e.g. larger particles, move slower through the fluid) and results in a shift in the frequency of incident light (Doppler shift). Larger particles, which have lower velocities, cause lower frequency shifts and smaller particles that rapidly move through the fluid cause the higher frequency shift. Therefore, measuring the frequency shift provides movement of the particles and their size distribution. DLS measurements of Silica IRMM-304 and Polystyrene BL-PS samples indicated a narrow size distribution. Figure 2 shows the uniform nature of silica nanoparticles with a hydrodynamic diameter within 42.5 – 44.2 nm.

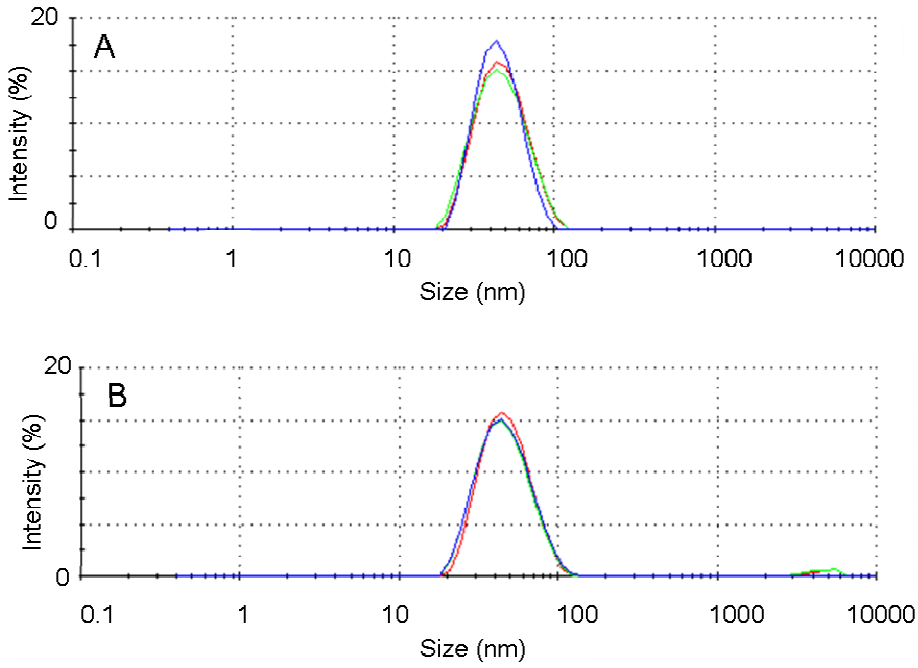

Figure 2.3.2 Three repeat DLS measurements on two aliquots (A and B) of Silica IRMM-304. Hydrodynamic diameter from all six measurements was 43.37 ± 0.87 and polydispersity index was 0.13 ± 0.02

Ceria Umicore D246 was tested as received and after 30 min sonication in Fisher Scientific bath sonicator. This sample was divided into two equal parts just after delivery. The first half of the sample was tested without sonication. 0.75 ml of the solution was gently transferred from the tube to the DLS cuvette using a syringe. Then, the second aliquot was transferred from the same tube and DLS measurement was repeated. The DLS spectra from these two experiments are presented in Figure 2.3.3. Untreated Ceria Umicore D246 consists of aggregates with sizes 158.97 ± 4.23 and PDI of about 0.2. However, when the rest of this sample (3.5 ml) was vigorously shaken and 0.75 ml was transferred to DLS cuvette for next measurement, the DLS spectra significantly changed (see Figure 2.3.4). The large aggregates that settled at the bottom of the tube redispersed

in solution after manual hand shaking. This observation of the importance of even minor disturbances in the determination of aggregate sizes underscores the limitations of DLS in accurately measuring the dimensions of aggregates or agglomerates larger than several microns. At these sizes, particles are large enough to settle under gravity in minutes.

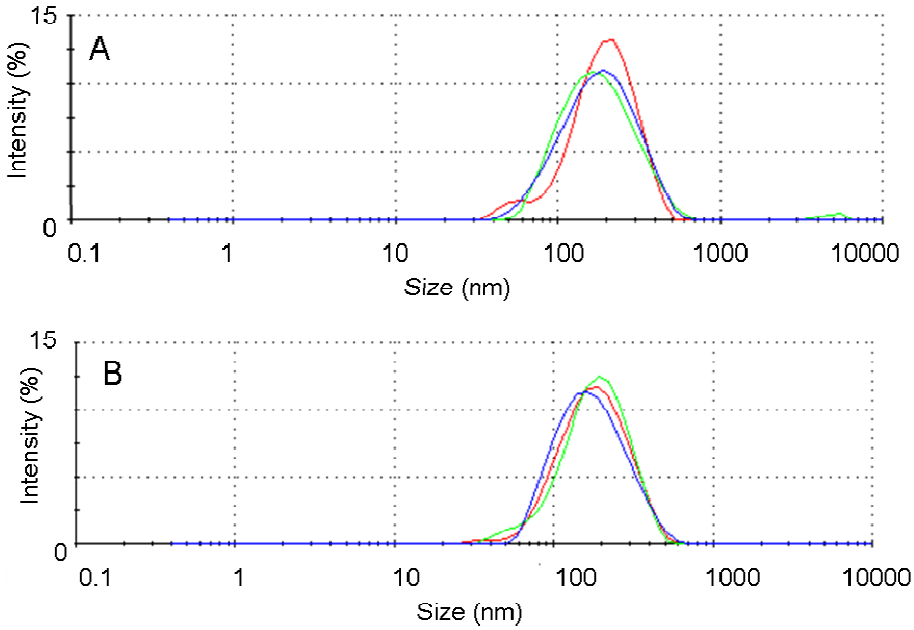

Figure 2.3.3 Three repeat DLS measurements on two aliquots (A and B) of Ceria Umicore D246 gently transferred to the tube to DLS cuvette. Hydrodynamic diameter from all six measurements was 158.97 ± 4.23 and polydispersity index was 0.19 ± 0.01

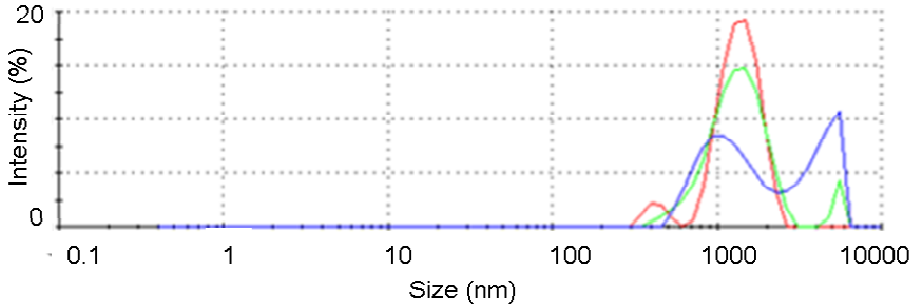

Figure 2.3.4 Three repeat DLS measurements of Ceria Umicore D246 obtained after the sample was vigorously shaken. Hydrodynamic diameter from three measurements of the same aliquot was 1920.67 ± 81.13 nm.

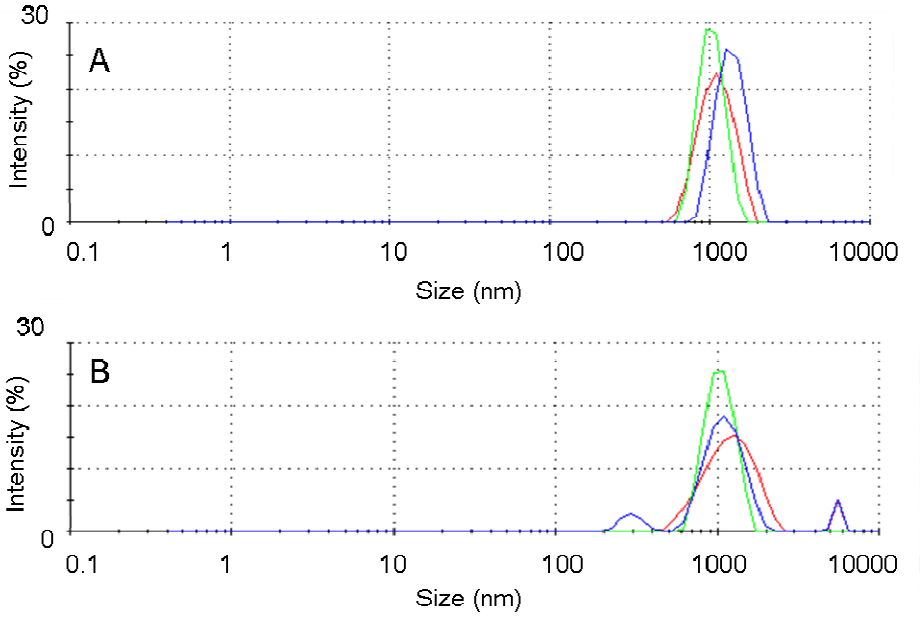

Figure 2.3.5 Three repeat DLS measurements of Ceria Umicore D246 obtained for two aliquots (A and B) sonicated for 30 min using batch sonicator. Hydrodynamic diameter from all six measurements was 1947.17 ± 203.35 and polydispersity index was 0.57 ± 0.12

The presence of large scale aggregates in Ceria Umicore D246 sample was confirmed by conducting an experiment with sonicated sample (see Figure 2.3.5). Sonication clearly redispersed aggregates that had settled to the bottom of the tube.

pH and zeta potential measurements

DLS measurement of nanoparticle hydrodynamic diameter can be used as a method for monitoring the stability of nanoparticle solution. When the stability of the nanoparticles is changing aggregates may form, and the DLS determined hydrodynamic diameter increases. The quality of nanoparticle dispersion can also be determined by directly measuring the zeta potential, which is dictated both by nanoparticle interactions and solution pH. Particles suspended in deionized aqueous solution will repel each other and resist the formation of aggregates when their zeta potential will in be large, above +30 mV or below -30 mV [163]. We confirmed that Polystyrene BL-PS nanoparticles formed stable solutions and for pH 7.7 their zeta-potential became +33.1 mV. The phase plot obtained with BL-PS sample was excellent. The plot had alternating slope with time followed by a smooth positive peak (see Figures 2.3.6 A). We did not report zeta potential for Silica IRMM-304 and Ceria Umicore D246 because of the poor data quality. Low quality data could be due to sample or electrode degradation or incorrect position of the zeta cell that results in no electrode contact phase plots (see Figures 2.3.6 B), making tests results unreliable [164].

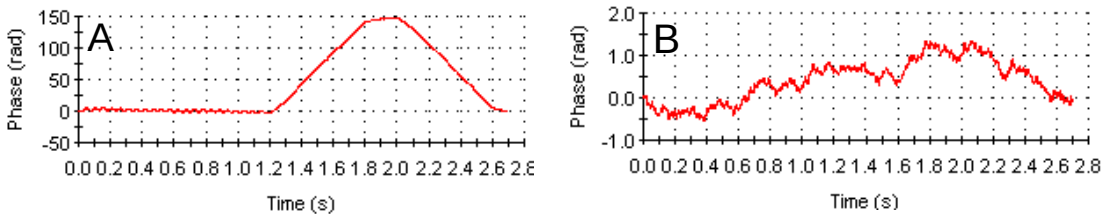

Figure 2.3.6 The phase plots for Polystyrene BL-PS (A) and Silica IRMM-304 (B)

Comparison of DLS measurements with data obtained by other IANH collaborators

The values of hydrodynamic diameters obtained for Silica IRMM-304 and Polystyrene BL-PS samples matched well between all laboratories (see Figures 2.3.7 A and B). A difference of only 2% was found between ten laboratories for both Silica IRMM-304 and Polystyrene BL-PS samples. However, for aggregated samples, Ceria Umicore D246, the difference between round robin participants for non-sonicated sample was 23%. After sonication, our results and data reported by laboratory 4 did not match with the others (see Figures 2.3.7 D).

The major reason for the differences seen in data obtained for sonicated ceria nanoparticles could be difference between equipment used for sonication, sample containers and test volumes. The list of sonicators used by round robin participants and the different power levels operated were presented in [158]. Roebben et al. concluded that the existing best practices to produce a homogeneous dispersion should be further tested when used in toxicity studies because sonication caused variation in inter-laboratory replicability [158]. Furthermore, polydisperse samples, such as Ceria Umicore D246 that consisted of nanoparticle aggregates require characterization technique to be improved because factors such as polydispersity and aggregation increased variation in DLS data. Silica IRMM-304 and Polystyrene BL-PS samples are nearly monodisperse

nanoparticles. As a result, the laboratories could agree well on their basic dimensions and surface characteristics. Therefore, the INAH DLS test protocol can be applied to the characterization of nearly monodisperse nanoparticles dispersions in ecotoxicity studies.

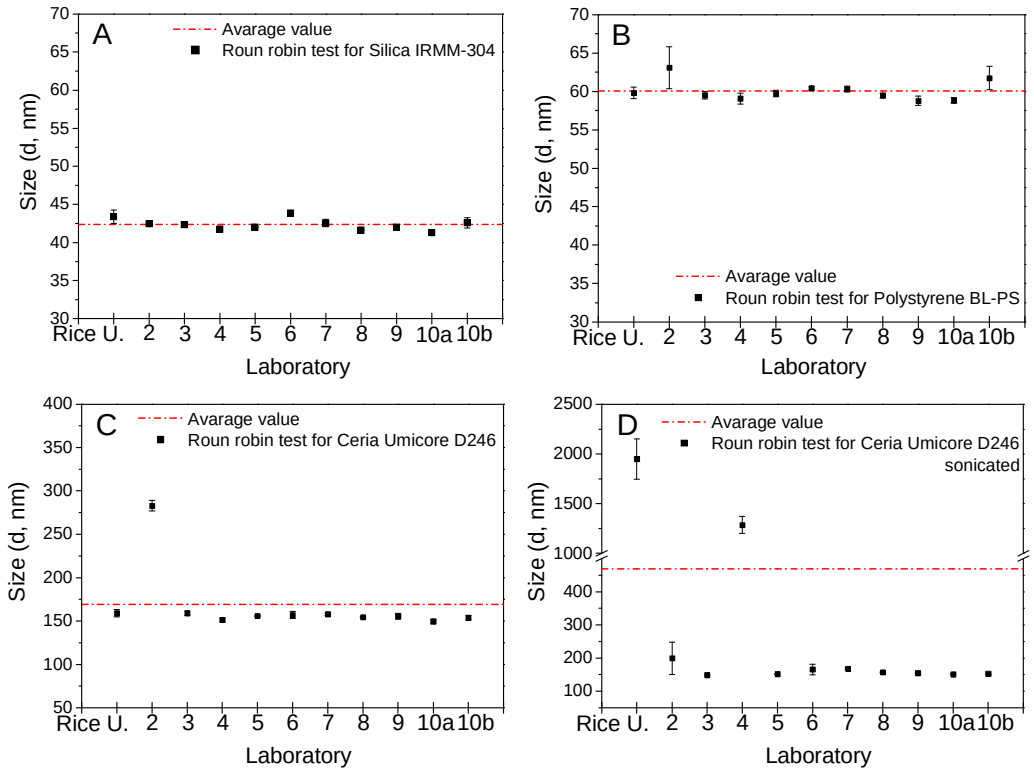

Figure 2.3.7 Hydrodynamic diameters (d) measured for Silica IRMM-304 (A), Polystyrene BL-PS (B), Ceria Umicore D246 (C) and Ceria Umicore D246-sonicated (D). Round robin test participants are listed as Rice U. for CBEN at Rice University and Laboratory 2 – 10 a, b for other participants.

All laboratories reported zeta potential values above + 30 mV for Polystyrene BL-PS indicating stable suspension. However, there was a significant difference of 23 %

between round robin participants in reported data (see Figure 2.3.8). The origin of these variations is not well understood. The zeta potential measurements accuracy for other samples (Silica IRMM-304 and Ceria Umicore D246) was even lower [158]. Rice University did not report values of zeta potential for these samples due to poor data quality. Some laboratories that participated in zeta potential measurements for ceria nanoparticles reported negative zeta potential values, which was opposite of normally expected results. Moreover, one laboratory reported a change form positive to negative values of zeta potential for Ceria Umicore D246 after sonication [158]. This round robin test results revealed important conclusion, about necessity to improve protocol for zeta potential measurement.

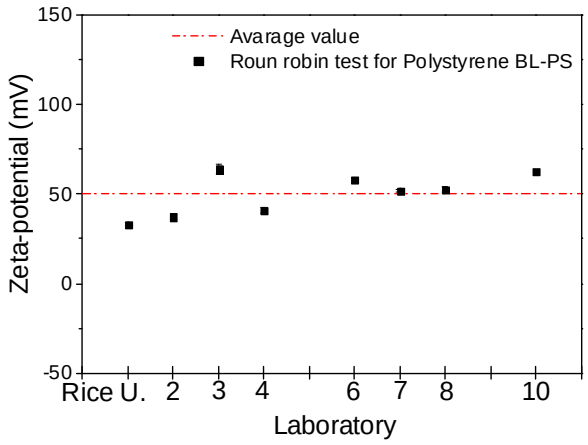

Figure 2.3.8 Zeta potential measurements obtained on Polystyrene BL-PS

The measurement protocol was prepared and tested by ten laboratories. This round robin test revealed that if the protocol is followed, very precise hydrodynamic diameters can be found if samples are homogeneous and non-aggregated. Thus, the IANH protocol for hydrodynamic size measurements using DLS for monodisperse

samples ensures quality data in interlaboratory research. Therefore, it can be used for characterization of nanomaterials for toxicity assessment. Measurement techniques need to be developed for polydispersed and aggregated samples. IANH protocols for zeta potential require further improvement to enable accurate and precise measurements.

Currently, there is a lack of reliable data in nanoparticle characterization because articles often provide insufficient information to allow repetition of the published results and there are no standardized test methods in this area. The IANH-developed protocol that this laboratory helped standardize is a step in the right direction. Still more research is needed to develop tools and testing protocols for nanoparticle physicochemical properties and nanoparticle toxicity. Only then would it be possible to accurately correlate the properties of nanoparticles to their toxicological effects, and ultimately provide schemes for minimizing these effects.

Well-characterized hydrodynamic size and zeta potential of nanoparticle dispersions are imperative for toxicological studies as well as physicochemical properties of engineered nanomaterials in consumer products. There is little research on properties of nanoparticles in consumer products and most research is on the basic nanomaterials [29]. To fully understand the biological effects this requires a complete analysis of the chemical and physical properties of the materials directly recovered from the products. In the following section the shape, size distribution, agglomeration state, crystalline structure, elemental composition and surface area of particles found in eight commercial sunscreens will be presented.

2.4 The structure, composition and dimensions of TiO_2 and ZnO nanomaterials in commercial sunscreens

TiO_2 and ZnO nanomaterials are widely used to block ultraviolet radiation in many skin care products, yet product labels do not specify their actual dimensions, composition, or shape. The lack of this information creates a data gap in the peer-reviewed literature on the effects of nanoparticle exposures which has focused on the study of pure samples of varying types of titania and zinc oxide nanoparticles. We investigated the structural similarity of pigments derived from actual sunscreen products to those commercial nanocrystals which have been the subject of intense scrutiny in the nanotoxicity literature [18]. TiO_2 and ZnO particles were isolated from eight out of nine commercial suncare products using three extraction methods. Their dimension, shape, crystal phase, surface area, and elemental composition were examined using transmission and scanning electron microscopy, x-ray diffraction, BET surface area analysis, energy dispersive x-ray and inductively coupled plasma optical emission spectroscopy.

2.4.1 Materials and methods

Commercial sunscreens and nanoparticle controls

We examined nine commercial sunscreen products with high sun protection factors (SPF, ≥ 30), purchased at local drugstores in Houston, Texas. Eight of them (samples 00 – 05, 07, 08) were primary sunscreens meaning that the primary intention of the product was to protect users from UV radiation. One (sample 06) was a secondary sunscreen that provided UV protection along with moisturizing. We chose one control

(sample 08) that utilized only organic blocking agents for UV protection. Our product set also included an example where TiO_2 was listed as an inactive ingredient (sample 03).

We also analyzed ZnO (Z-Cote) and TiO_2 (T-Avo and T-Eco) particles obtained directly from chemical companies (BASF and EMD Chemicals Inc, respectively). These particles were recommended as inorganic sunscreen UV filters by the manufacturers. Z-Cote particles (ZnO 99.7%) have a mean particle size smaller than 200 nm; T-Avo and T-Eco are about 20 nm TiO_2 particles coated with silica (13.0 – 20.0% SiO_2) and alumina (8.0 – 11.0% Al_2O_3) plus simethicone (1.0 – 3.0% SiO_2), respectively.

Sample preparation

Sunscreens were treated in three different methods to facilitate characterization and identify issues arising from preparation methodologies. The first involved the direct evaporation of sunscreens onto scanning electron microscope specimen holders or glass slides under ambient conditions (termed ‘as-provided’); this is comparable to the skin application process and would have the most minimal impact on materials. Second, sunscreens were diluted with water or ethanol to improve their separation on solid supports and facilitate quantitative imaging (‘diluted’). In detail, 50 mg of sunscreen was shaken with 8 ml of pure water in the case of sample 03 or ethanol (all other samples) prior to evaporation. The third preparation extracted 5 g of the sunscreen emulsion with 30 ml chloroform followed by centrifugation (4500 rpm for 15 min). This operation was repeated three times to get solid particle powders (‘extracted’). We were not able to isolate inorganic material from sample 03 because solvents such as chloroform, hexane

and ethanol led to the formation of a gel. Therefore sample 03 was analyzed only in 'as-provided' and 'diluted' in water forms.

Scanning electron microscopy (SEM)

SEM was used to determine whether nanoscale particles were present in the evaporated residues of sunscreens. 5 mg of cream was introduced onto the stub using a needle applicator. Then, a glass cover slide was placed on the stub and gently pressed to spread the cream; the cover slide was removed from the surface to leave a thin white film (~ 3 mg). The thin sunscreen film was then dried at room temperature in a laboratory hood overnight and analyzed without surface gold coating. SEM images were obtained on an FEI Quanta 400F Field Emission Scope.

Elemental composition

Samples ('as-provided', 'extracted' and inorganic particles obtained from chemical companies) were analyzed for their elemental composition using energy dispersive x-ray spectroscopy (EDS). Materials extracted from lotions and nanopowders obtained from BASF and EMD were mounted on SEM carbon stubs using double-sided adhesive tabs (Ted Pella, Redding, CA) for EDS analysis. The Genesis system from EDAX Inc. was used to reveal the elemental composition. Semi-quantitative analysis was performed using ZAF correction (Z - atomic number, A - absorption, F- fluorescence).

To confirm our EDS analysis of the 'extracted' particles (samples 00-02 and 04-07), related materials were shipped to an independent chemical analysis lab (Galbraith Laboratories Incorporation, Knoxville, TN). These samples were analyzed for five

elements: carbon, titanium, zinc, silicon, and aluminum. Carbon was determined according to the ASTM D5373/D5291 procedure and other elements were measured by Inductively Coupled Plasma Optical Emission Spectroscopy (ICP-OES).

Transmission Electron Microscopy (TEM)

To obtain accurate dimensions of the inorganic pigments, it is critical to identify a clear edge around a particle. The 'as-provided' materials had obscured edges because of the non-volatile organic emulsion components, whereas the 'diluted' sunscreens in water (sample 03) or ethanol (all other samples) were suitable for sizing. TiO_2 and ZnO powders obtained from chemical companies were also mixed with ethanol (by shaking) to make a final concentration of 5 mg/ml. These dispersions were directly applied onto 300-mesh carbon-coated copper grids and then were dried at room temperature in a laboratory hood overnight. The particles were imaged at 30,000x magnification using a JEOL 1230 high contrast TEM, employing an accelerating voltage of 120 kV. For each sample, multiple images were collected to obtain a statistically significant population of more than one hundred particles. The dimensions were defined manually using Image-Pro Plus 5.0 (Media Cybernetics) [127, 128]. In order to resolve the surface characteristics of Z-Cote, T-Avo and T-Eco, high-resolution TEM images were obtained in collaboration with Denise N. Benoit using a JEOL JEM 2100 F transmission electron microscope with a field emission gun (operated at 200 kV).

X-Ray Diffraction Analysis (XRD)

XRD was used to probe the crystal structure of the inorganic sunscreen pigments. It was carried out on a Rigaku D/Max Ultima II Powder Diffractometer equipped with a Cu Kα radiation. Films made by 'as-provided' samples provided sufficient diffraction for phase composition analysis. Z-Cote, T-Avo and T-Eco samples were also directly applied onto glass microscope slides and analyzed. Crystallite sizes were calculated according to procedure described in section 2.2.1 of this thesis. The most intensive diffraction peaks used for crystallite size calculation were (101) for TiO_2 anatase, (110) for TiO_2 rutile and the (002) line of ZnO.

BET Surface Area Analysis

BET surface area analysis was carried out by following the procedure described in details in section 2.2.1 of this thesis. Degassing temperature used to remove surface adsorbed contaminants was 120^{o}C.

2.4.2 Results and discussion

We found nanoscale materials in all sunscreens that listed TiO_2 and ZnO as active ingredients. To begin this anlaysis, we first isolated sunscreen pigments from suncare products purchased at drugstores and grocery stores in Houston, TX. All nine sunscreens had a SPF greater than 30, and two were selected because they did not list inorganic materials as active ingredients. These controls were sample 08, with no labeled inorganic pigments, and sample 03 which listed TiO_2 as an inactive ingredient. Samples 00, 01, 02, 06, 07 offer both UVA and UVB protection. Samples 00 and 02 are marketed for children

and/or babies. Sample 06 is primarily sold as a moisturizer. TiO_2, ZnO, or both may be used as active ingredients; however, only the weight fraction of the pigments was specified on the labels as presented in Table 2.4.1 and Figure 2.4.1. Information about the inorganic pigment size, aggregation level or phase composition was not available on the product label.

Table 2.4.1 Identification of nanoscale pigments in studied sunscreens

Sample	**Inorganic material**	**As-provided**		**Extracted**		
		Labeled (wt %)	**EDS (wt %)**	**Galbraith Laboratory (wt %)**		
		TiO_2 or ZnO	**TiO_2 or ZnO**	**TiO_2 or ZnO**	**Al**	**Si**
00	TiO_2	2.4	15.3	75.1	2.8	0.5
01	TiO_2	9.1	44.1	54.6	2.5	ND
02	TiO_2	1.2	5.3	63.4	3.1	2.2
03[1]	TiO_2	Not specified	6.5	–	–	–
04	ZnO	6.86	52.8	92.2	ND	ND
05	ZnO	6.86	44.1	97.8	ND	ND
06[2]	ZnO	6.0	48.6	96.5	ND	0.9
07	ZnO TiO_2	10.0 5.0	37.8 16.8	95.0 2.5	ND	ND
08	Not detected	Not Listed	Not detected	–	–	–

Notes: [1] Listed TiO_2 as an inactive ingredient; [2] A secondary sunscreen; '–' means not analyzed. The inorganic material was unable to be extracted from the emulsion of sample 03, and sample 08 did not contain TiO_2 or ZnO; hence these two samples were analyzed only in 'as-provided' form by EDS and were not shipped to Galbraith laboratory for chemical analysis.

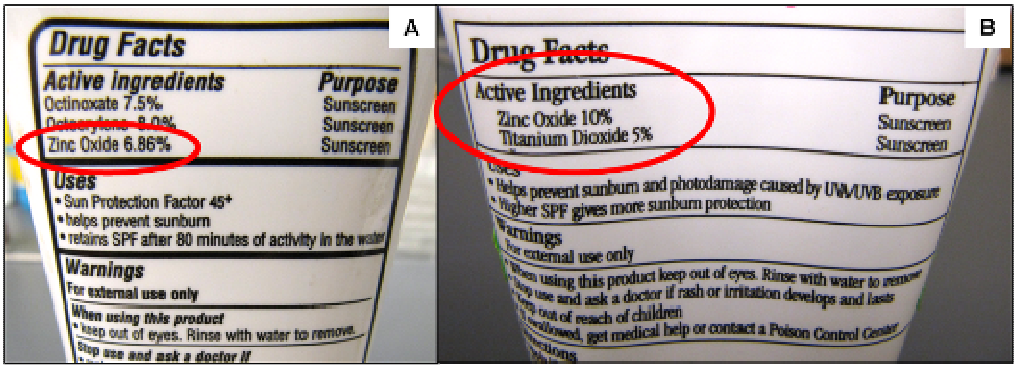

Figure 2.4.1 Photographs of the labels on the sunscreen 05 (A) and 07 (B)

SEM images of pigments derived from sunscreen products revealed nanostructured features were present in eight of the nine products. Figures 2.4.2 A to C show representative micrographs of sunscreens taken with high-resolution SEM. In these 'as-provided' samples the pigment edges were partially obscured by a layer of non-volatile residue; however, agglomerated nanostructures were visible in 8 of the products. In contrast, the control product provided smooth and featureless films presumably because it does not contain any inorganic pigments (Figure 2.4.2 C). Table 2.4.2 summarizes the results from high-resolution SEM for these minimally prepared samples and the corresponding images are provided in Figures 2.4.3 and 2.4.4.

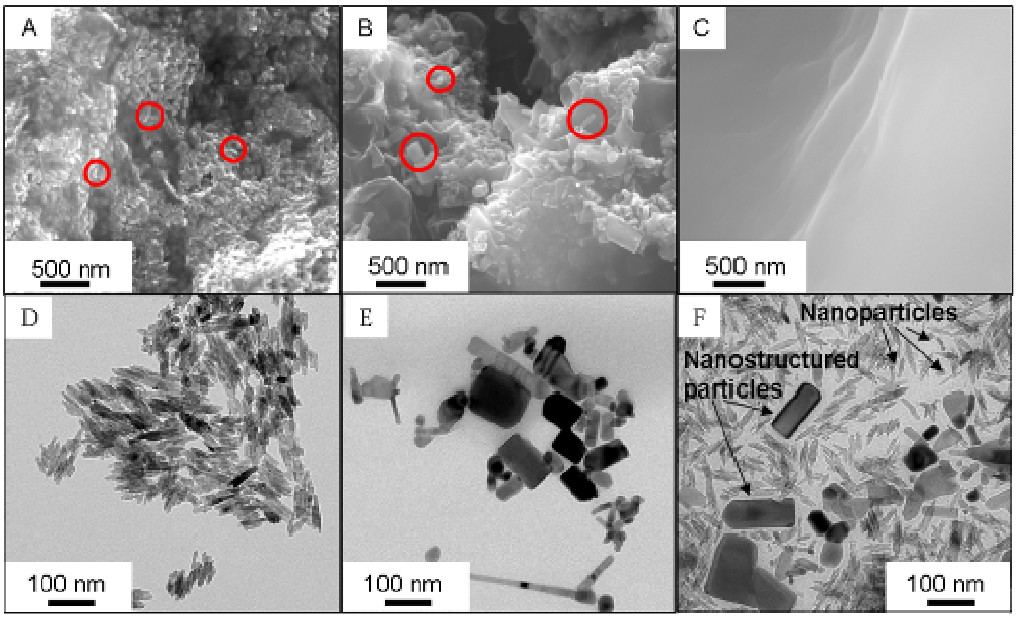

Figure 2.4.2 SEM images of 'as-provided' sunscreens and TEM images of 'diluted' samples. TiO_2 nanoparticles (sample 01) are shown in (A) SEM and (D) TEM images, ZnO nanoparticles and nanostructures (sample 06) in (B) SEM and (E) TEM micrographs; blank sample without nanoscale materials (sample 08) and with both TiO_2 and ZnO nanoparticles and nanostructures (sample 07) are presented in (C) SEM and (F) TEM images, respectively.

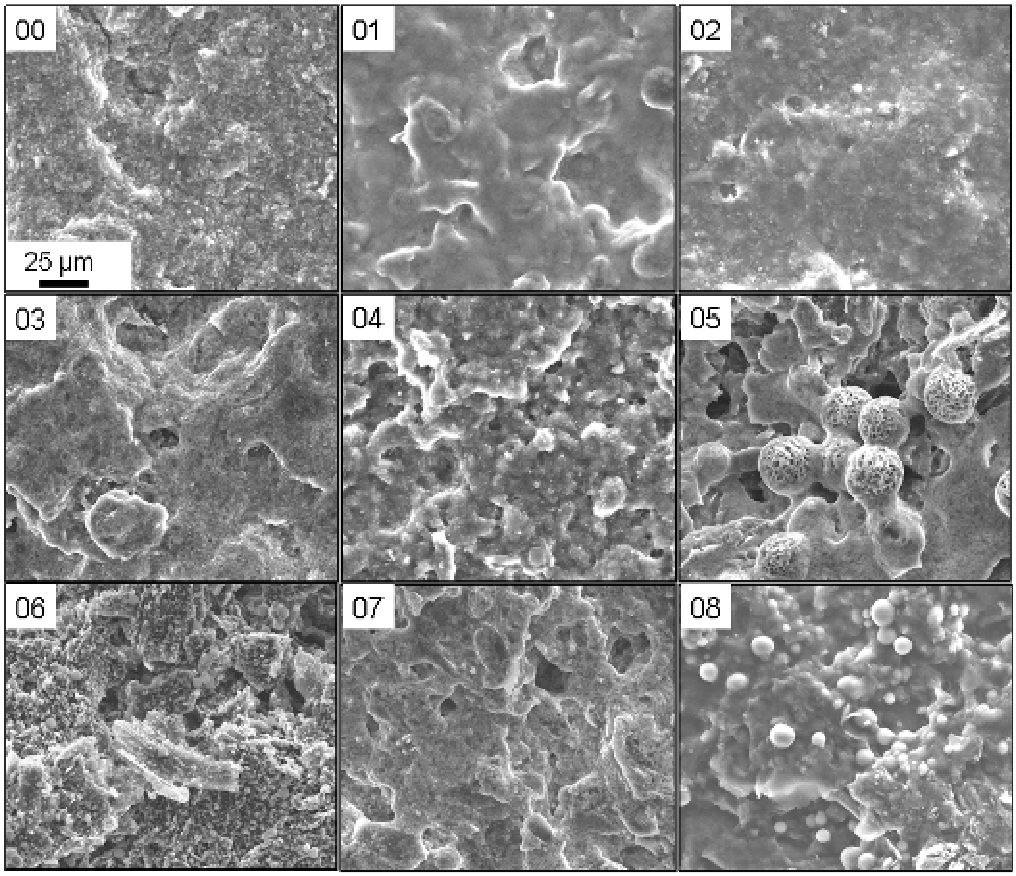

Figure 2.4.3 SEM images at low magnification level (1,000x) for the 'as-provided' samples (00-08). All images have the same scale bar of 25 µm.

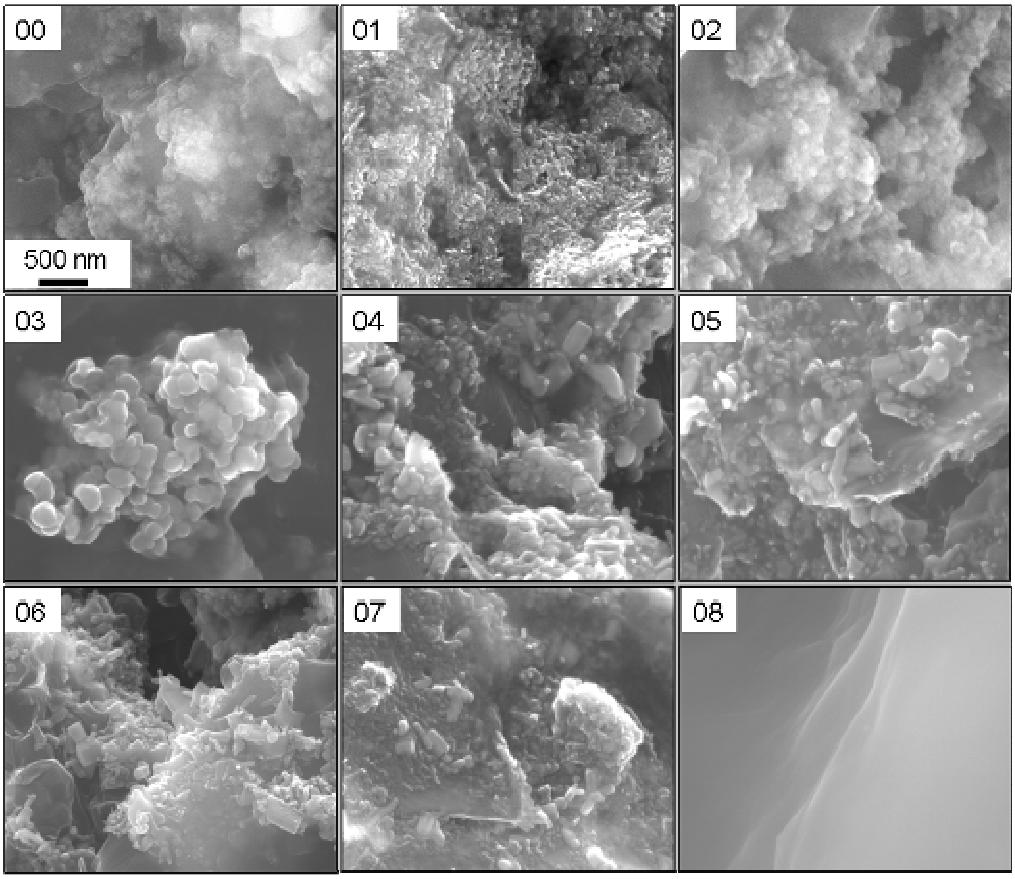

Figure 2.4.4 SEM images at high magnification level (50,000x) for the ‘as-provided’ samples (00-08). All images have the same scale bar of 500 nm.

Table 2.4.2 Characterization of nanoscale pigments

Sample	**Nanoscale pigment**	**Length (nm)**	**Width (nm)**	**Crystal structure**	**Crystallite size (nm)**	**BET (m^2/g)**
00	NP	25.3 ± 8.8	16.0 ± 4.0	Rutile	18.6	25.1
01	NP	24.6 ± 9.9	7.3 ± 1.8	Rutile	18.4	58.2
02	NP	24.9 ± 11.0	10.2 ± 3.9	Rutile	13.3	60.8
03[1]	NP, NS	83.6 ± 71.5	64.7 ± 57.2	Anatase	81.7	–
04	NP, NS	78.5 ± 50.7	40.04 ± 29.7	Wurtzite	72.7	9.1
05	NP, NS	79.9 ± 51.6	33.4 ± 20.3	Wurtzite	75.3	9.3
06[2]	NP, NS	81.3 ± 57.2	38.2 ± 28.7	Wurtzite	67.7	11.2
07	NP, NS	67.0 ± 50.5	27.0 ± 24.1	Rutile, Wurtzite	11.2 64.9	10.1
08	ND	–	–	–	–	–
T-Avo	NP	28.2 ± 8.9	13.8 ± 2.8	Rutile	18.8	57.0
T-Eco	NP	25.2 ± 9.6	7.3 ± 2.3	Rutile	13.6	81.2
Z-Cote	NP, NS	80.6 ± 55.9	39.3 ± 21.7	Wurtzite	64.5	14.7

Notes: [1]Listed TiO_2 as an inactive ingredient; [2]A secondary sunscreen; '–' means not analyzed; 'ND' means not detected; 'NP' means nanoparticles; 'NS' means nanostructures. The inorganic material was unable to be extracted from the emulsion of sample 03; hence the surface area was not analyzed for this sample.

Further analysis of the pigments revealed they were crystalline titania (generally rutile) or zinc oxide. The elemental composition for all 'as-provided' samples was evaluated using energy dispersive x-ray spectroscopy (EDS). TiO_2 and ZnO concentrations found by EDS ranged from 5.3 to 52.8 wt %, as compared to the 1.2 to 9.1 wt % listed in ingredients. This discrepancy arises from the fact that some volatile organic sunscreen components were evaporated before film analysis by EDS thus increasing the relative metal contents. Other inorganic constituents were also found in the sunscreen residues, most notably silicon and aluminum. Silicon exists in the form of silica (SiO_2), and aluminum in the form of alumina (Al_2O_3). These oxides are primarily used as coating agents for TiO_2 [68, 119].

To provide more quantitative assessments of sunscreen particle composition, pigments extracted with chloroform were analyzed both by EDS and inductively coupled plasma optical emission spectroscopy (ICP-OES). Elemental analysis found aluminum in sample 01 and silicon and aluminum in samples 00 and 02 (Table 2.4.1), in addition to titanium. Samples 04, 05, 07 did not contain any other inorganic constituents except zinc. A small amount of silicon, 0.9 wt%, was found in sample 06. However, microscopy revealed that this sample also contained silica microspheres which could account for the measured silicon content.

X-ray diffraction (XRD) studies confirmed the composition of inorganic pigments derived from commercial sunscreens and identified their phase. Figure 2.4.5 shows the diffractograms which reveal that the TiO_2 in samples 00, 01, 02 was rutile whereas the TiO_2 in sample 03 was anatase. Calculation of crystallite size via the diffraction line width found grain sizes that ranged from 11.2 to 18.6 nm for samples 00, 01, 02, 07 and

81.7 for sample 03. These values are in reasonable agreement with those found from electron microscopy. The observed diffraction patterns for ZnO pigments matched well to a hexagonal wurtzite phase (samples 04, 05, 06, 07). The sharp and narrow diffraction lines are indicative of larger crystallite sizes estimated to range from 65 to 75 nanometers.

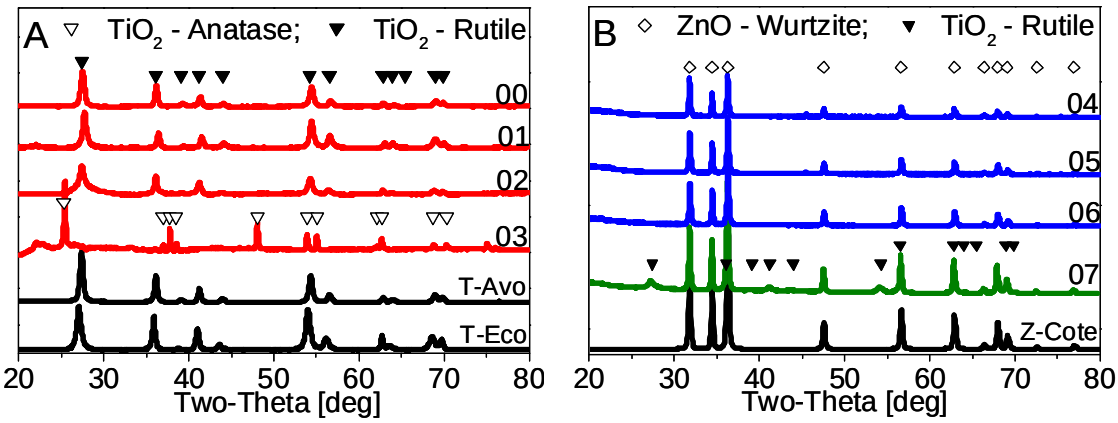

Figure 2.4.5 X-ray diffraction patterns of 'as-provided' sunscreens and industrial nanopowders. Figure 2.4.5 A presents diffraction patterns of TiO_2 nanoscale particles (samples 00, 01, 02, 03, T-Avo, T-Eco) and Figure 2.4.5 B are patterns of ZnO nanoparticles and nanostructures (samples 04, 05, 06, Z-Cote), as well as both ZnO and TiO_2 particles (sample 07).

While the minimally prepared sunscreens clearly contain nanoscale features (Figures 2.4.1 A – C), the presence of the non-volatile organic components makes a quantitative analysis of the pigment dimensions difficult. To acquire better images with clear edge resolution, we diluted sunscreen emulsions with water or ethanol before TEM analysis. These diluted residues were comprised of nanoscale particles whose boundaries

were clearly apparent; this preparation allowed for precise measurement of the size and the corresponding histograms (Figures 2.4.1 D – F). The overall appearance, size and morphology of these pigments were comparable to those presented in Figures 2.4.1 A and B. For this reason, the dilution of the sunscreens by water does not apparently change the morphology of the primary particle sizes. Moreover, the observation suggests that the particles in the evaporated films that appeared to cluster were in fact loose agglomerates. These broke up into discrete nanocrystals after only a mild shaking in water at room temperature.

For environmental release and exposures, sunscreens would be subjected to dilution in diverse aqueous media. The physical signatures of the primary particles are thus of interest as these inorganic oxide materials are likely to remain unchanged in terms of their size after such processes. Two different sizes and forms were observed in the titania and zinc oxide samples. TiO_2 pigments were smaller (except in the control sample 03, see Figure 2.4.6_03) and often were shaped as needles (Figure 2.4.1 D). In contrast, ZnO pigments were much larger with well defined rod-like habits. For sample 07, both TiO_2 and ZnO were present; the distinctive zinc oxide rods were present along with much smaller and agglomerated titania needles (Figure 2.4.1 F). TEM micrographs showed well-defined and isolated primary particles, an ideal sample for quantitative analysis of the primary pigment dimensions.

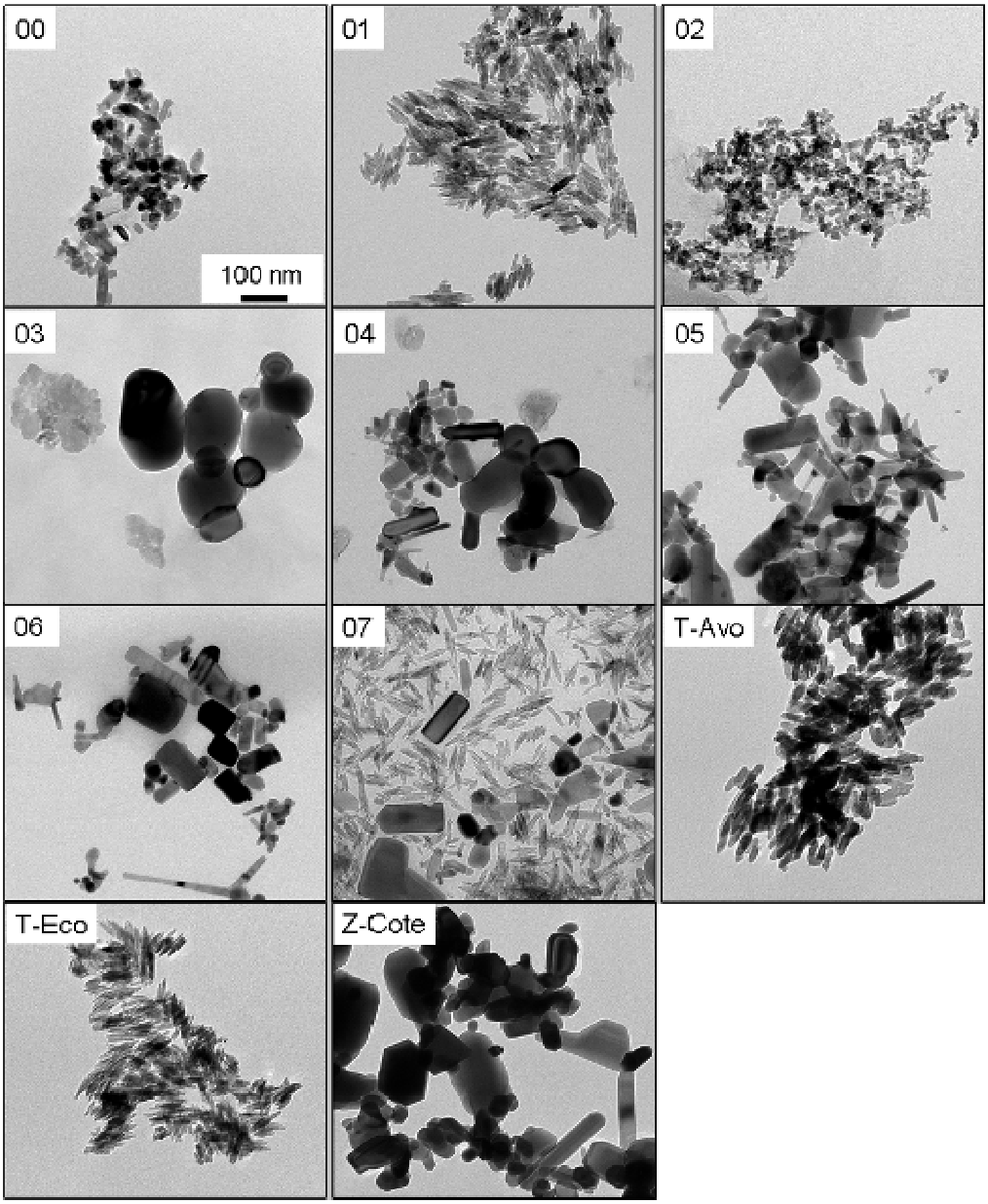

Figure 2.4.6 TEM images of the ‘diluted’ samples (00-07) and the particles obtained from companies (T-Avo, T-Eco, Z-Cote). All images have the same scale bar of 100 nm.

Table 2.4.2 provides the average length and width of particles found in the eight samples with inorganic pigments. In all cases, the pigment diameters were not larger than 100 nm. To further distinguish the different types of sunscreen nanoscale structures, we classified them as either ‘nanostructure’ or ‘nanoparticle’ based on the size and shape, following two terminology standards related to nanotechnology [British Standards Institution [2]and the American Society for Testing and Materials [1]]. Materials are classified as nanoparticles if both their average short and long axes are less than 100 nm; materials are classified as nanostructured if at least one axis is longer than 100 nm (as is the case for sample 03 and all ZnO pigments).

Our analysis revealed that three of the commercial sunscreens contained only TiO_2 nanoparticles (samples 00, 01, 02). The average sizes of TiO_2 varied across the different brands. The average length for samples 00, 01, 02 was 25 nm and the average width was 11 nm; thus they were classified as nanoparticles. Figure 2.4.7 A presents the size distributions in major axis measured for representative sample 02. Sample 03 contained TiO_2 nanoparticles and nanostructures (Figure 2.4.6_03). The label of this sunscreen listed TiO_2 as an inactive ingredient. Both types of nanoscale particles (nanoparticles and nanostructures) were also present in samples 04, 05, 06 and 07. The size distribution for representative sample 04 is presented in Figure 2.4.7 B. The average length of nanoscale pigments for samples 04, 05, 06, which contained only ZnO, was 80 nm; while the average width was 37 nm. ZnO in some cases had long dimensions that exceeded 100 nm with aspect ratios of approximately 2 (Figures 2.4.1 B and 2.4.1 E). Figure 2.4.1 F for sample 07 (containing both TiO_2 and ZnO) shows that there were two populations of shapes: needle and rod-like. Generally ZnO pigments were larger than

TiO_2 with the exception of sample (03). The surface areas of TiO_2 particles were 25 m^2/g for sample 00 and about 60 m^2/g for samples 01 and 02, respectively. All ZnO particles exhibited lower surface area about 10 m^2/g as expected for their larger sizes.

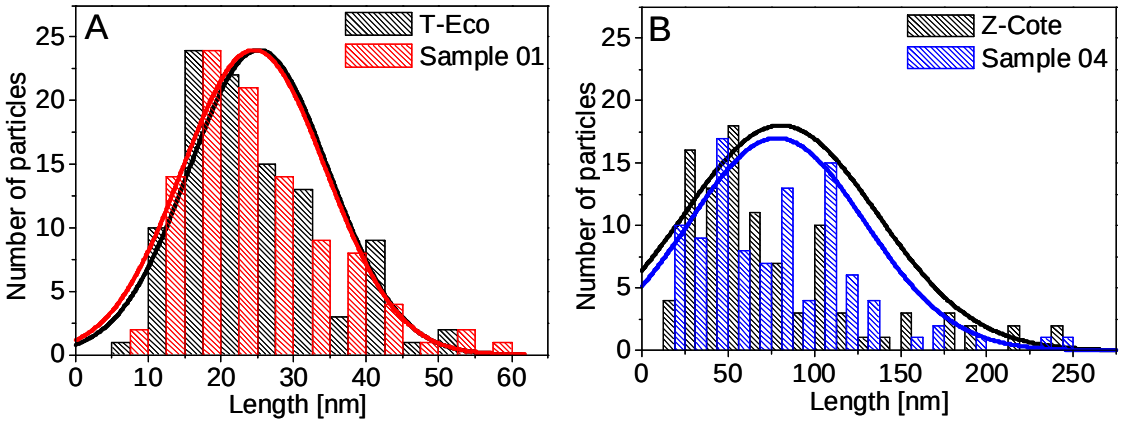

Figure 2.4.7 Particle distribution histograms. Figure 2.4.7 A presents examples of histograms obtained for samples that contained only nanoparticles (samples 01 and T-Eco) and Figure 2.4.7 B if for samples 04 and Z-Cote which contain both nanoparticles and nanostructures.

Comparison of pure TiO_2 and ZnO nanopowders to sunscreen inorganic residues

In many cases, research on the fate and effects of these sunscreen inorganic nanomaterials has relied on commercially available TiO_2 or ZnO nanopowders [116, 165, 166]. There is a wide selection of nanoscale powders available on the industrial market. However, it is not obvious which commercial nanoscale powder is the best representative for the features and structures of those inorganic pigments actually used in commercial suncare products.

We compared the dimension, surface area, shape and elemental composition of several commercial nanomaterial sources, and found that two powders, T-Eco (EMD Chemicals Inc.) and Z-Cote (BASF Company), were excellent matches to the inorganic constituents found in our representative suncare products. Figure 2.4.7 shows the size distributions of these nanomaterials compared to those derived from sunscreens. The match in average size and size distribution was very good in both cases. TiO_2 was found in different crystal structures and sizes among the sunscreens tested (Table 2.4.2). Complete delineation of all relevant TiO_2 surrogates is beyond the scope of this work, but T-Eco does possess the features of at least some sunscreen pigments. Also, like the commercial sunscreen residues, T-Eco has a rutile crystal structure. The ZnO pigment was similar in all of the suncare products examined, and we found Z-Cote is an excellent surrogate for this pigment.

Elemental analysis (EDS and ICP-OES) further provided a useful measure of the similarity between these commercially available and pure nanomaterials and sunscreen pigments. Figure 2.4.8 A shows that the pigment present in sample 02 contains aluminum and silicon, which is similar to T-Eco. Z-Cote does not contain any additional inorganic elements and its elemental composition is similar to samples 04 and 05 (Figure 2.4.8 B).

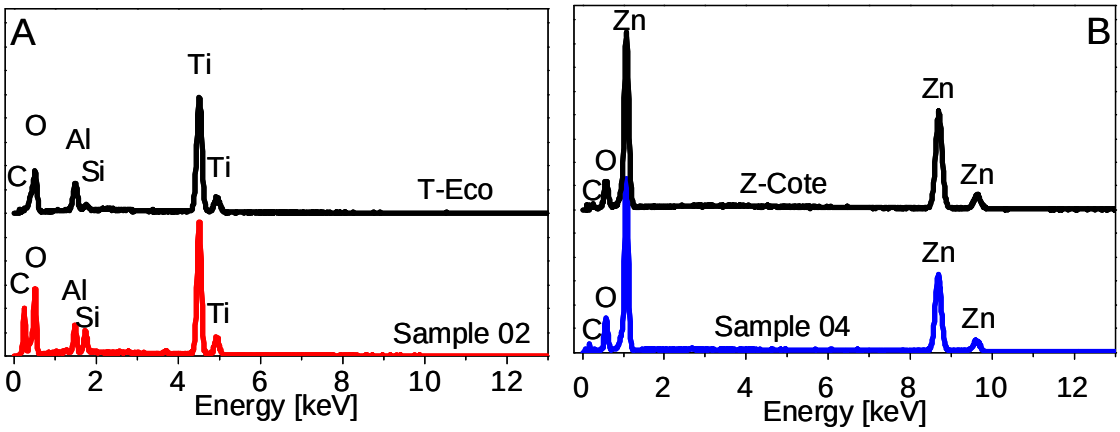

Figure 2.4.8 EDS analysis of TiO_2 pigments 'extracted' from sample 02 and T-Eco (A), and ZnO pigments 'extracted' from sample 04 and Z-Cote (B)

High-resolution TEM of these materials highlights the importance of the surface coating in the nanoscale pigment characterization. The manufacturer, for example, details that T-Avo has a silica coating. This coating is apparent in the TEM image as an amorphous, poorly defined coating on TiO_2 core particles of approximately 2 nm thickness (Figure 2.4.9 A). In contrast, T-Eco uses both alumina and simethicone coating; a low electron dense, somewhat patchy layer can be seen around the TiO_2 particles (Figure 2.4.9 B). ZnO particles are generally not coated. Figure 2.4.9 C shows clear crystal lattice and smooth and uncoated Z-Cote particle surface. However, the similarity between these commercial nanomaterials and sunscreen residues suggests that in the case of TiO_2 the particles are surface coated to reduce their UV photoactivity. Coating layers can block particle surface access to the surrounding environment and limit the formation of the reactive oxygen species [119].

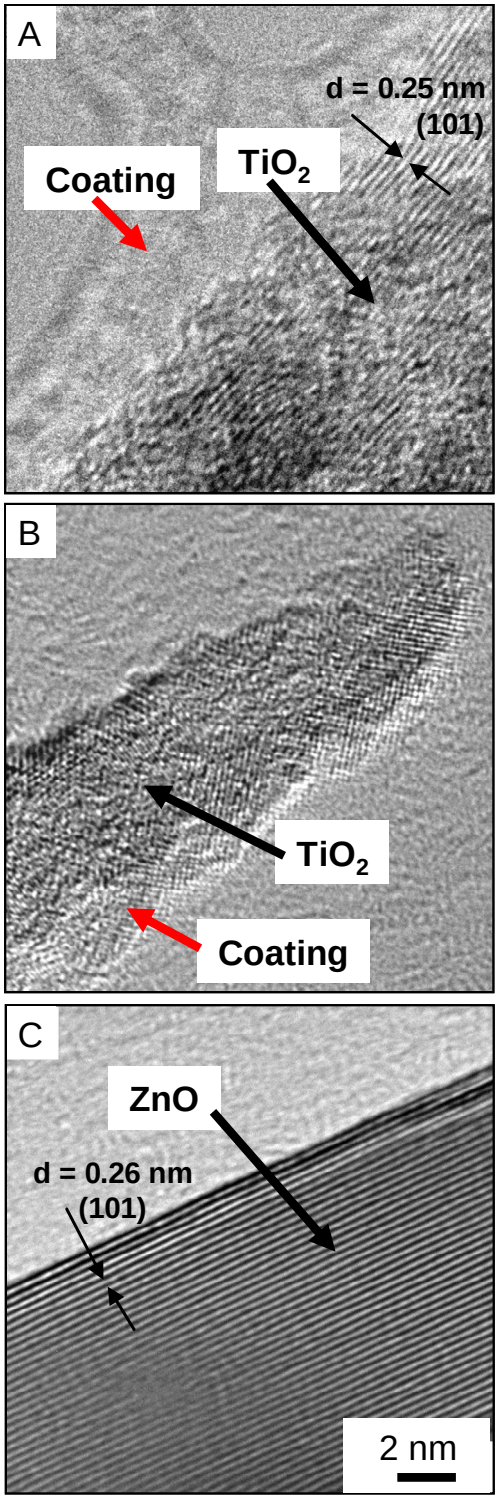

Figure 2.4.9 High resolution TEM images of coated TiO_2 (T-Avo, A and T-Eco, B) and uncoated ZnO (Z-Cote, C) nanopowders

2.4.3 Conclusion

Nanoscale, engineered materials are present in eight of nine commercial suncare products that list titania and zinc oxide as ingredients. Elemental analysis of the non-volatile inorganic residues reveals that they are comprised of TiO_2 and/or ZnO. All the sunscreen inorganic pigments (TiO_2 and ZnO) are crystalline materials whose dimensions are on the nanoscale (e.g. less than 100 nm). In some cases aluminum and silicon are also detected; they are in most cases used as coating materials (possibly Al_2O_3 or SiO_2) to minimize the photochemical activity of TiO_2. This observation underscores the need for studies of nanoscale titatnia containing different types of inorganic coatings. We also compared the characterization data from extracted sunscreen pigments to commercially available, pure nanoscale materials and identified two sources (T-Eco and Z-Cote) that are highly similar to materials derived from commercial sunscreens. Chapter 3 of this thesis presents the results from the photoactivity tests of eight sunscreens as well as commercially available, pure nanoscale materials.

Chapter 3 The photochemical behavior of sunscreen pigments

In the last chapter, characterization of commercial sunscreens established that in most products that use inorganic ingredients these pigments are of nanoscale dimensions. While the pigment's small size offers transparency and a smoother application feel, it can also, in the case of TiO_2 and ZnO, yield materials that may catalytically produce reactive oxygen species (ROS) upon UV illumination. Such a property can be of great value for environmental remediation technologies, but a serious deficiency in a topical sunscreen designed to protect against ROS generation by light.

Here, we describe photochemical studies of nine commercially available sunscreens that contain TiO_2 and ZnO materials, the inorganic particles derived from these sunscreens, and several commercial TiO_2 and ZnO nanopowders. Redundant and complementary assays for detecting reactive oxygen species produced by these samples included dichlorofluorescein fluorescence, luminol chemiluminescence, and the decolorization of dyes (Congo red and Rose Bengal). A more quantitative measurement of ROS generation using POBN and DMPO spin trap electron paramagnetic resonant spectroscopy was applied to materials extracted from sunscreens and commercial powders. The results indicate that nanotitania in sunscreens is relatively inactive; as indicated in the last chapter, manufacturers can use inert oxide coatings such as alumina and silica to coat pigments and render their surfaces non-reactive. In contrast, ZnO in sunscreens can produce substantial amounts of ROS upon UVA illumination; comparatively, these materials are roughly one quarter as active as the standard titania photocatalysts. The photocatalytic activity of ZnO on the nanoscale suggests that more effective suncare products would employ strategies to mitigate this photochemistry.

3.1 Materials and methods

The commercial sunscreens and nanoparticle controls used here were the same materials as used in the previous study (see section 2.4.1). In addition, we also tested P25 and Z-Ald nanopowders obtained from Evonik Degussa Corporation and Sigma Aldrich chemical companies. The size distribution, surface area and the phase composition of Z-Ald and P25 samples were analyzed according to previously described methods (2.4.1 section).

We used ‘as-provided’ samples (sunscreens 00-08) in the dichlorofluorescein and luminol tests. The term ‘extracted’ describes sunscreen particles used in spin trap electron paramagnetic resonance spectroscopy and the decolorization of Congo red dye; extraction methods are described in the previous chapter. Commercial powders were evaluated by spin trap electron paramagnetic resonance spectroscopy to quantify the generation of hydroxyl radicals. Three additional standards (P25, Z-Cote and Z-Ald) were used in comparative investigation of photostability and photocatalytic properties of TiO_2 and ZnO nanoscale materials; specifically, they were evaluated in the photodegradation of Rose Bengal. The summary of all the samples and test types preformed in photoactivity studies are presented in Table 3.1.1.

Table 3.1.1 Types of tests and samples used in photoactivity study

Sample	DCFH	Luminol	Spin trap EPR	Congo red dye	Rose Bengal dye
00					
01					
02					
03					
04					
05					
05					
06					
07					
08					
T-Avo					
T-Eco					
Z-Cote					
Z-Ald					
P25					

Color in the boxes indicate where a test was performed; Orange – 'as-provided' samples, Blue –'extracted' samples and Green – standard samples; DCFH – dichlorofluorescein fluorescence test; Luminol – chemiluminescence experiment

3.1.1 Dichlorofluorescein fluorescence

To examine the ROS generation by commercial sunscreen products we used a slightly modified method described by Lu et al. [167]. First, 0.5 ml of 2',7'-dichlorofluorescein diacetate (DCFH-DA) in dimethyl sulfoxide (DMSO, ≥99.9%, 1 mM) was chemically hydrolyzed to 2',7'-dichlorofluorescein (DCFH) with 2 ml of 0.01 N NaOH in the dark for 30 min at room temperature. The reaction was stopped by adding 10 ml of the phosphate buffer (PBS, 25 mM, pH 7.2). The stock solution of DCFH was wrapped by aluminum foil and kept on ice before use. Next, 50 µl of commercially available sunscreen ('as-provided' sample) and 130 µl of PBS buffer were introduced into the wells of a Costar 96-well plate in triplicates. Then, the 96-well plate was placed

under a 365 nm UV lamp for 5 min (UV lamp Blak-Ray Model B 100 AP/R, 365 nm, 10 mW cm^{-2}). Immediately after the irradiation, 20 µl of horseradish peroxidase (HRP, 0.2 U/ml) and 50 µl of the stock solution of DCFH were added into the wells. The final concentration of DCFH in the wells was 10 µM. The fluorescence generated by the DCFH oxidation was measured after 45 minutes using a SpectraMAX microplate reader (Molecular Devices). The excitation and emission wavelengths were 485 and 530 nm, respectively. Hydrogen peroxide (H_2O_2) and a solution without sunscreen (i.e. a mixture of 130 µl of PBS buffer, 20 µl of HRP and 50 µl of DCFH) were used as positive and negative controls, respectively.

3.1.2 Luminol chemiluminescence

For a chemiluminescent reaction experiment, 50 µl of sunscreen emulsion ('as-provided' samples 00 – 08) was introduced into the wells of a Costar 96-well plate in triplicate. Then, 140 µl of Tris-HCl buffer (pH = 10, adjusted with 0.1 N NaOH) was added. Right after the addition of the buffer, the sample was irradiated with UVA (UV lamp Blak-Ray Model B 100 AP/R, 365 nm, 10 mW cm^{-2}) for 5 min. Immediately after the irradiation, 50 µl of 3 % $K_3Fe(CN)_6$ (potassium ferricyanide) and 10 µl of luminol (5-amino-2,3-dihydrophthalazine-1,4-dione) stock solution (0.01 M in Tris-HCl buffer, pH = 10) were added to the irradiated sunscreen [168, 169]. Within about 10 seconds of the luminol addition, the light intensity at λ = 485 nm was measured using a SpectraMAX microplate reader to detect the photogenerated ROS. Each sunscreen sample was analyzed before UV radiation as well. Moreover, the background, which is the intensity of the blank solution (a mixture of 140 µl of Tris-HCl buffer, 50 µl of 3 % $K_3Fe(CN)_6$

and 10 µl of 0.01 M luminol) and gradient concentrations of H_2O_2 in the range of 0.1µM – 1 mM (control) were also recorded. All the solutions were freshly prepared and used on the same day of the experiment.

3.1.3 POBN and DMPO electron paramagnetic resonance spectroscopy

Two different EPR approaches with high purity POBN (99%) and DMPO (99%) spin traps were used to examine the photogeneration of hydroxyl radicals. First, inorganic materials extracted from sunscreens ('extracted' samples 00-02 and 04-07) were tested with a POBN spin trap and the EPR spectra recorded. Second, a DMPO spin trap was used to confirm the results obtained from EPR analysis with POBN and to quantify the amount of hydroxyl radicals present in each 'extracted' sample. To confirm the origin of the DMPO-OH adduct, ethanol was added as a hydroxyl radical scavenger. In addition to the extracted sunscreen powders, five samples obtained from chemical companies (T-Avo, T-Eco, Z-Cote, Z-Ald, and P25) were also analyzed with POBN and DMPO spin traps. These served as benchmarks to evaluate the magnitude of the radical production.

Specifically, EPR experiments began by mixing TiO_2 and ZnO suspensions prepared by dispersing 10 mg of powder in 1 ml of PBS buffer (pH = 6.0, concentration = 0.05 M, ionic strength = 0.14) with POBN or DMPO spin trap stock solutions (0.2 M, prepared on the same day of experiment). The final concentration of the spin traps in the EPR sample was 0.01 M. These sample suspensions were freshly prepared just before the irradiation with UV light (see conditions above). For the ethanol (200 proof, Decon Laboratories Inc.) quenching experiments, the final concentration of ethanol was 0.82 M.

The reactions were conducted in 4 ml Wheaton 800 soda-lime clear glass vials (top open) placed on a magnetic stirring device under the 365 nm UV lamp. This type of glass allows about 90% of wavelengths longer than 365 nm to pass through [170]. The sample volume in the vial was kept constant at 1 ml. Following irradiation with the UV light (1 and 5 min), samples were immediately transferred to a glass capillary (75 µl, Fisher Scientific, Pittsburgh, PA) and placed in the cavity of an EPR spectrometer. The EPR spectra were collected in less than 5 min from UV irradiation, at room temperature with a Varian E-6 spectrometer equipped with E231 multi purpose cavity and operated in TE102 mode. The EPR spectrometer settings in all the photochemical experiments were: microwave frequency 9.225 GHz, microwave power 10 mW, center field 3285, scan length 100, gain 1.25 x 10^4 (3.2 x 10^4 for some experiments with P25), modulation amplitude 1.6 G (0.08 G for some experiments with P25), scan time 4 min, and time constant 1.

The EPR experiment was repeated twice. For all samples that EPR signals were above the limit of quantification (LOQ = 10σ), the concentration of DMPO-OH adduct was calculated. The calculation of DMPO-OH concentration included double integration of EPR spectra using the Origin 6.0 program and the verification of spin adduct concentration based on the calibration curve obtained for 4-hydroxy-2,2,6,6-tetramethyl-1-piperidinyloxy (TEMPOL) [171]. For the LOQ set at 10σ, the relative uncertainty would be ± 20 % (at a 95 % confidence level) of the true value [172]. The limit of detection (LOD) was defined as an EPR signal that is three times the standard deviation (3σ) of the baseline spectra [173]. The baseline spectra were the EPR spectra that fell outside of the peak sections. Signals below 3σ were reported as ‘not detected’ (ND).

3.1.4 Congo red decolorization

Decolorization of Congo red dye (CR) was used to relate the photoactivity of 'extracted' samples to their ability to degrade chemical molecules. Samples for the dye decolorization test were prepared by dispersing 10 mg of extracted powder into 10 ml of water and vortexing for 30 sec. Then 2.5 ml of Congo red stock solution was added to the nanoparticle dispersion to achieve the final concentration of 30 µM.

The photocatalytic reactions were conducted in Fisher brand 20 ml borosilicate glass vials that allow about 90% of wavelengths greater than 350 nm to pass through, inside a Luzchem 4-V photoreactor equipped with a magnetic stirrer and UVA lamps (350 nm, 3.5 mW cm^{-2}) [170]. First, the reaction dispersion was magnetically stirred in dark for one hour to establish the adsorption/desorption equilibrium of the dye on the catalyst surface. Then, it was placed inside the photoreactor. At given irradiation time intervals, 0.8 ml of the solution was taken and centrifuged (14.5 krpm) for 3 min to separate the particles. The disappearance of Congo red was monitored using the absorbance feature at 496 nm as a function of irradiation time [174]. A Cary 5000 UV-Vis-NIR Spectrophotometer (Varian Incorporation, Walnut Creek, CA) was used for absorption measurements. The photoactivity of tested samples was quantified as a Congo red half-life, which is the amount of time required for degradation of 50 % of the dye. It is expressed on a unit mass basis of TiO_2 and/or ZnO materials ($t_{1/2}$).

3.1.5 Comparative investigation of photocatalytic properties of ZnO and TiO_2 materials

Photostability of TiO_2 and ZnO nanoscale materials

The photostability of ZnO (Z-Ald, Z-Cote) and TiO_2 (P25) nanopowders were examined by inductively coupled plasma spectrometer (ICP-OES, Optima 4300 DV, Perkin Elmer). The suspensions of 1 mg/ml ZnO and TiO_2 nanopowders in 10 ml distilled water were kept in the dark at room temperature as well as were exposed to the UV light in the Luzchem 4-V photoreactor and stirred for 24, 48, 72, 96 and 120 h. The nanoparticles were then separated from the suspension with an inorganic membrane filter (Whatman, 0.02 µm). Next, samples were digested by concentrate nitric acid and analyzed for their Zn and Ti contents with ICP-OES.

Photocatalytic efficiency of TiO_2 and ZnO nanoscale materials

For the photocatalytic activity test of P25, Z-Ald and Z-Cote samples towards Rose Bengal degradation, 20 mg of powder was suspended in water and were vortexed for 30 sec. Then Rose Bengal stock solution was added into the nanoparticle solution to achieve a dye concentration of 15 µM, which given the RB molecular weight of 973 gm/mole corresponds to 14.6 mg/ml of dye. The final concentration of the nanoparticles was 1 mg/ml. The suspension was stirred in the dark for 1 h to reach adsorption equilibrium. Then, the dispersion was placed inside the Luzchem 4-V photoreactor with stirring. At given irradiation time intervals, 1 mL of the suspension was collected and centrifuged (14.5 krpm) for 3 min to remove the photocatalyst. The degraded solution was analyzed by the Cary 5000 UV-Vis-NIR spectrophotometer, and the absorption peak at 550 nm was monitored until the absorbance reached zero. Nanoparticles were recycled

and reused five times in the decomposition of Rose Bengal to test the photocatalytic stability. The photocatalytic efficiency of each sample was quantified as Rose Bengal half-life time expressed on a unit mass basis of TiO_2 and/or ZnO materials ($t_{1/2}$).

3.2 Results and discussion

3.2.1 Dichlorofluorescein and luminol tests: evaluation of ROS production by sunscreen emulsions

We first applied two very sensitive chemical tests for ROS generation to sunscreen emulsions, sunscreen pigments and various benchmark materials. These methods are commonly applied in biological studies focused on ROS-mediated toxicity; they are very sensitive to ROS generation but provide less quantitation than corresponding photodegradation studies typical in the photocatalysis literature. The first approach uses a fluorescent probe, 2',7'-dichlorofluorescin diacetate (DCFH), that increases in its intensity in the presence of superoxide ($O_2\cdot$), hydrogen peroxide (H_2O_2), nitric oxide (NO), hydrogen peroxide ($OH\cdot$) species [175, 176]. The second uses an increase in Luminol chemiluminscence due to catalyst activation by superoxide H_2O_2, $O_2\cdot$ and/or $OH\cdot$ to indirectly detect the presence of this specie [169, 177].

Both of these highly sensitive tests revealed that most ZnO and TiO_2 containing sunscreens have some level of ROS generation after UV illumination. This result was universal for ZnO-containing sunscreens which showed both increased fluorescence from DCFH and increased chemiluminescence from Luminol (Figures 3.2.1 A, B). When irradiated with UVA, all ZnO sunscreens had strong chemiluminesence (above 0.50 a.u.). The magnitude of their ROS generation measured by both techniques was also higher for

ZnO containing sunscreens and materials. Sunscreens formulated without ZnO has low chemiluminescence intensity after the luminol test (~ 0.07 a.u. for sample 00) or no detectable signal (samples 01, 02, 03, 08). DCFH was slightly more sensitive than the luminol, but also found no appreciable ROS generation for the TiO_2-containing sunscreens (Figure 3.2.1 A). These particular products also contained substantial amounts of silica and alumina, possibly due to the presence of a surface coating on the titania pigments similar to that seen in Figures 2.4.9 A and B.

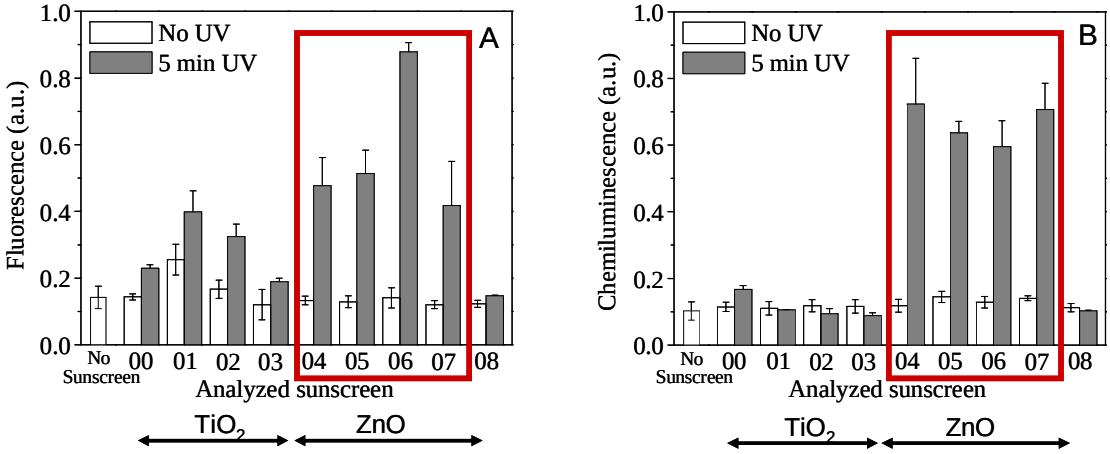

Figure 3.2.1 DCFH fluorescence (A) and luminol chemiluminescence (B) of sunscreen emulsions before and after 5 min of UVA irradiation (λ = 365 nm, intensity = 10 mW cm^{-2}). Values are means ± σ from three independent experiments. Significance versus blank control (no sunscreen): ** $p < 0.01$, # $p < 0.001$. The red box indicates sunscreens that contained ZnO materials.

The data shown in Figure 3.2.1 is particularly interesting because it finds that for some products there can be ROS generation even in neat suncare products. Sunscreens

are applied to the skin as a lotion, and there are a myriad of potential interactions between the photoactive pigments and various organic additives. However, for ZnO-containing sunscreens the emulsion materials themselves do not fully quench the photochemical behavior.

As noted earlier, these tests have many limitations that should be recognized in interpreting the data. Most notably, DCFH and luminol fluorescence and chemiluminescence have not generally been applied as methods to quantitate ROS generation. This is partly due to the fact that the tests are not linear in their response to ROS concentration; at higher concentrations the signals do not continue to increase linearly for example. Also, each method requires several chemical species to participate in electron transfer and/or adduct formation; spectator ions, emulsion components or the pigments themselves may interfere with any one of these steps as a reductant/oxidant, catalyst, or adsorption agent [176, 178-181]. While we compare both the DCFH and luminol tests to account for possible interferences, this possibility limits their broad interpretation. Finally, while sensitive these tests are broadly sensitive to ROS generation.

To examine in more detail the quantitative generation of ROS and pure pigments we used electron paramagnetic resonance or EPR. While this technique can resolve the types of ROS species, and provide quantification of their concentration, the interaction of spin traps with the many different organic constituents in the full sunscreen emulsions precludes its use with unpurified products. For this reason, EPR experiments were completed on the nanoscale pigments extracted from the emulsions.

3.2.2 Spin trapping of hydroxyl radicals

Spin trap EPR experiment revealed that 'extracted' samples which contain ZnO particles (samples 04, 05, 06, 07) have more intense EPR signals upon illumination as compared to EPR signals of POBN-OH and DMPO-OH spin adducts for samples that contained TiO_2 particles (samples 00, 01 and 02). Both POBN and DMPO are known to be efficient spin traps for the detection of hydroxyl radicals [79, 82, 182]. Therefore, these spin traps were employed in order to verify the presence of hydroxyl radicals (OH·) generated from sunscreen inorganic filters under UV irradiation.

Spin trapping with POBN of OH· upon irradiation of 'extracted' samples

Spin trapping experiments with POBN resulted in two EPR spectra (Figure 3.2.2). The first one (marked by '^') shows a triplet of doublets with hyperfine splitting constants (hfsc) of A_N = 14.8 G and A_H = 1.8 G related to POBN-OH. This spectrum was observed for all samples, except for 00 and 01 which had no detectable signals. The second spectrum (marked by 'x') consisted of a quartet with line intensities of 1:2:2:1 and $A_N = A_H$ = 14.5 G. This tert-butyl hydroaminoxyl radical is a decomposition product of the POBN-OH adduct, as well as POBN spin trap [183]. The intensity of the POBN-OH signal (after 5 min of UV irradiation) was lower for sample 02 (containing TiO_2) as compared to samples 04, 05, 06 and 07 (containing ZnO). This trend corresponds to a greater signal for samples with ZnO. No POBN-OH signal could be detected for samples 00 and 01.

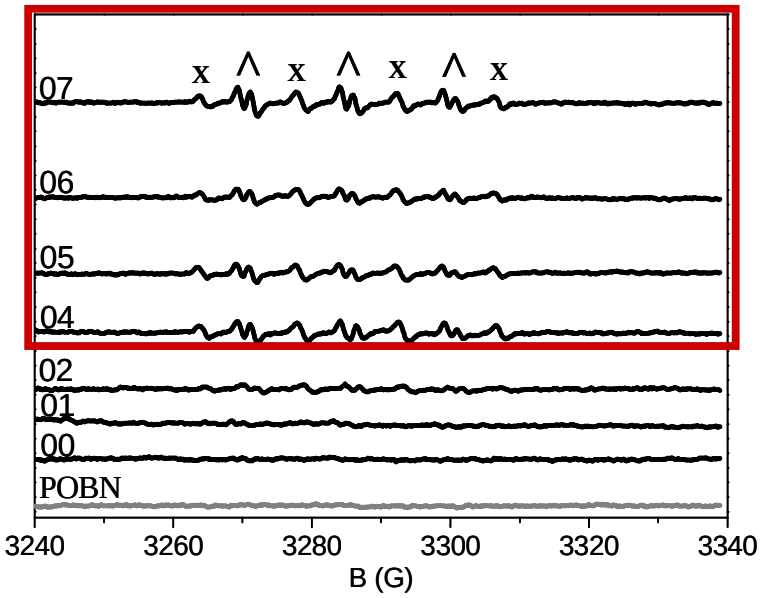

Figure 3.2.2 The EPR spectra of spin trapped radicals obtained by 5 min UVA irradiation of samples 00, 01, 02, 04, 05, 06, 07 dispersions containing POBN. No EPR signals were detected when buffer solutions of the spin trap were irradiated for 5 min; there were also no EPR signals found when nanoparticles were irradiated without the spin trap. The red box indicates sunscreens that contained ZnO materials.

Spin trapping with DMPO of OH· upon irradiation of sunscreen extracts

EPR experiments with DMPO spin trap confirmed the results obtained with POBN: samples containing ZnO particles (samples 04, 05, 06, 07) had more intense EPR signals upon illumination than samples containing TiO_2 (00, 01, 02) (Figure 3.2.3).

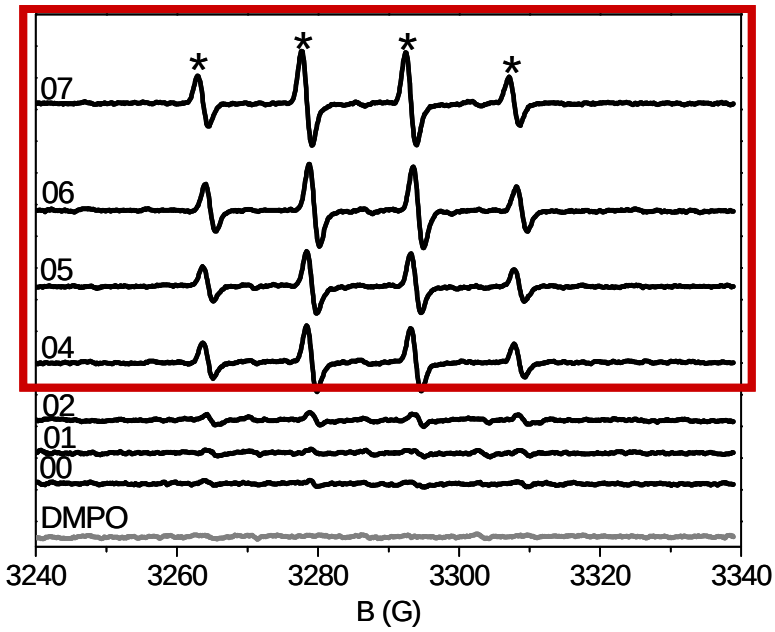

Figure 3.2.3 The EPR spectra of spin trapped radicals obtained by 5 min UV irradiation of extracted inorganic particles from sunscreen samples 00, 01, 02, 03, 04, 05, 06, 07. The DMPO-OH adduct is marked by '*'. No EPR signals were detected when buffer solutions of the DMPO spin trap were irradiated for 5 min; there were also no EPR signals found when nanoparticles were irradiated without the spin trap. The red box indicates sunscreens that contained ZnO materials.

EPR signals recorded in the presence of the DMPO spin trap were composed of four peaks with intensities 1:2:2:1 and $A_N = A_H = 14.8$ G (marked by '*') which were assigned to the DMPO-OH adduct (Figure 3.2.3). However, in order to confirm that the DMPO-OH adduct originated from trapped OH· radicals rather than from the decomposition of DMPO-OOH, ethanol was added as a hydroxyl radical scavenger. Trapped hydroxyl radicals resulted in the disappearance of the DMPO-OH and the

appearance of a new six-line (#) DMPO-$CH(CH)_3OH$ (see Figure 3.2.4), which confirmed that DMPO-OH detected in the original experiments was due to OH· radicals [184].

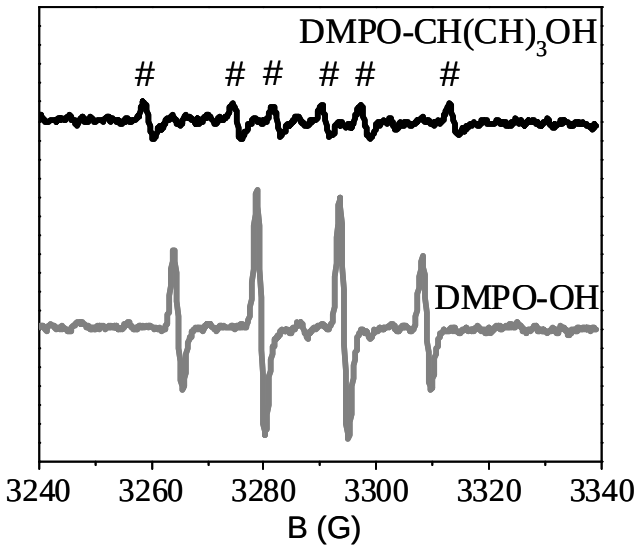

Figure 3.2.4 The EPR spectra of spin trapped radicals obtained by irradiation (5 min) of sample 06 dispersion containing DMPO (lower spectrum), and DMPO/EtOH (upper spectrum)

While Figures 3.2.2 and 3.2.3 seems to suggest that ZnO pigments are more effective at generating ROS than TiO_2, it is not conclusive because this data was collected on identical masses of extracted pigments not identical masses of titania or zinc oxide. Elemental analysis performed by Galbraith Laboratories Incorporation (Knoxville, TN) of sunscreen extracts revealed that samples 00, 01 and 02 contained a lower amount of TiO_2 and a higher amount of organic matter compared to the ZnO-containing samples (04, 05, 06, 07) [18]. The generation of radicals depends on the concentration of the semiconductor particles [79]. Therefore, in order to compare the

activity of analyzed materials, the amount of generated spin adduct presented in the irradiated (5 min) sample was quantified and normalized based on the mass of TiO_2 or ZnO. The mass was calculated from Ti and Zn elemental analysis of the 'extracted' particles (samples 00-02 and 04-07), measured by Inductively Coupled Plasma Optical Emission Spectroscopy (ICP-OES) and performed by an independent chemical analysis lab (Galbraith Laboratories Incorporation, Knoxville, TN).

Moreover, DMPO is efficient at trapping hydroxyl radicals and the chemical stability of DMPO-OH makes it applicable for quantifying analysis. DMPO characterizes high reaction rate with OH· (3.4×10^9 M^{-1} s^{-1}) and relatively long half-lifetime of the DMPO-OH adduct ($t_{1/2}$ = 2.6 h at pH 7.4) [183, 184]. The amount of spin adduct was assessed using an aqueous solution of TEMPOL as standard [171]. EPR spectra of samples and TEMPOL solutions were recorded at the same EPR spectrometer settings and first-derivative EPR spectra were double integrated to obtain the area intensity; then, the concentration of spin adduct in the sample was calculated using the ratio of these areas.

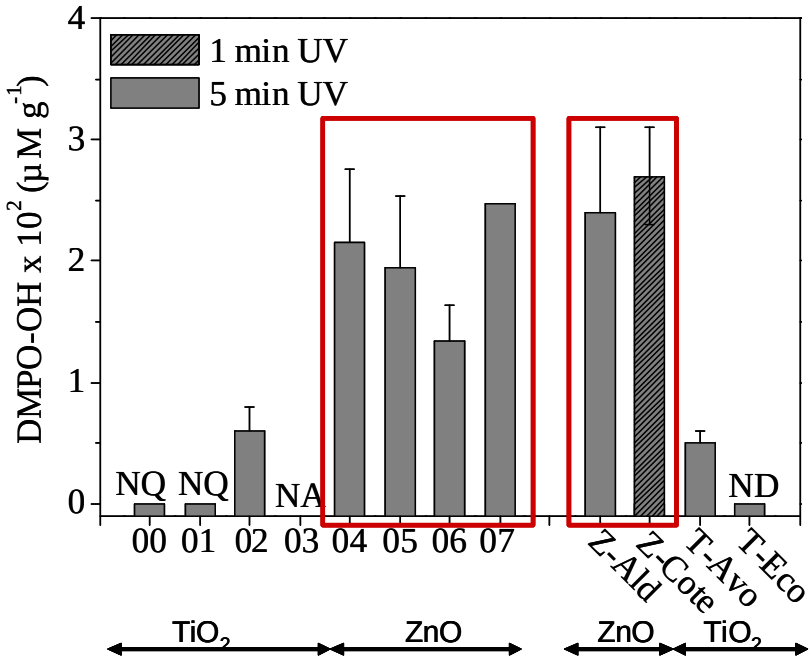

Figure 3.2.5 Concentration of DMPO-OH adduct generated during 1 (P25 and Z-Cote) and 5 min (all other samples) of UVA irradiation, normalized to the active ingredient weight (TiO_2 or ZnO). Values are means ± σ from two independent experiments. Abbreviations: NQ, below limit of quantification (< 10σ); ND, below limit of detection (< 3σ); NA, not analyzed. The red box indicates sunscreens that contained ZnO materials.

All ZnO particles (samples 04, 05, 06, 07) formed a large amount of DMPO-OH spin adduct that ranged from 134 – 247 $\mu M \cdot g^{-1}$ (Figure 3.2.5). Moreover, DMPO is a more efficient trap for OH· as compared to POBN. As a result, samples 00 and 01 which had no signal with POBN had EPR peaks with DMPO above the limit of detection (EPR signal intensity for LOD was 0.3 a.u.; the intensity of the EPR peak for sample 02 after 5 min UV irradiation was 1.2 a.u. which was close to the limit of quantification (EPR signal intensity for LOQ was 1 a.u.) and corresponded to a spin adduct concentration of 60 $\mu M \cdot g^{-1}$.

Extracted samples may contain impurities associated with various components employed in the sunscreen emulsions. These impurities may affect surface chemistry of nanoparticles and influence ROS generation test results, for example by blocking access to the solution environment, quenching radical species or enhance radical formation. Therefore we compared the photoactivity of sunscreen derived metal oxide particles with standard samples obtained directly from manufacturers.

The results obtained for standard samples were in agreement with those presented earlier for extracted particles (see Figure 3.2.5). From three standard samples, recommended by manufacturers for sunscreen applications, ZnO nanopowder (Z-Cote) was the most active as compared to less active silica coated TiO_2 particles (T-Avo) and photoinactive Al_2O_3 and simethicone coated TiO_2 (T-Eco). We also studied a well-known photocatalyst P25 (TiO_2) and a ZnO nanopowder Z-Ald from Sigma-Aldrich that physicochemical properties are presented in Table 3.2.1.

As expected, among all the materials analyzed in this study, P25 was the most active catalyst (DMPO-OH ~ 8.8 x 10^2 $\mu M \cdot g^{-1}$). For P25, the high amount of photogenerated hydroxyl radicals caused strong oxidation of the POBN and DMPO spin traps. As a consequence, there was a reduction in the signal intensities of the POBN-OH and DMPO-OH adducts after a few minutes of irradiation. Similar behavior for P25 in the presence of POBN was reported by Brezova et al. [79]. We also found a decrease of DMPO-OH formation after 1 min of UV irradiation for Z-Cote, which was the second most active sample (DMPO-OH ~ 2.7 x 10^2 $\mu M \cdot g^{-1}$).

Table 3.2.1 Particle characterization and their properties in Rose Bengal degradation

Particle	Crystal structure	Length (nm)	Width (nm)	Crystallite size (nm)	SSA (m^2/g)	$t_{1/2}$ (min)
Z-Cote	Wurtzite	80.6 ± 55.9	39.3 ± 21.7	64.5	14.7	0.15 ± 0.01
Z-Ald	Wurtzite	78.7 ± 44.8	42.2 ± 17.9	70.3	12.1	0.14 ± 0.01
P25	Anatase, Rutile	20.1 ± 5.8	16.7 ± 5.2	20.6	58.5	0.08 ± 0.02

Abbreviations: SSA, specific surface area; $t_{1/2}$, half-life time of Rose Bengal (averaged from five cycles and normalized to the mass of TiO_2 or ZnO).

Surprisingly, Z-Ald (pure ZnO nanopowder from Sigma-Aldrich) presented a lower activity toward OH· generation (DMPO-OH ~ 2.4×10^2 $\mu M \cdot g^{-1}$ after 5 min of UV irradiation) than Z-Cote. We also examined two TiO_2 materials, T-Avo and T-Eco. T-Avo was photoactive and generated ~ 0.5×10^2 $\mu M \cdot g^{-1}$ of DMPO-OH, while T-Eco was inactive. Spin trap EPR confirms that TiO_2 nanoparticles obtained directly from manufacturers with surface coatings do have lower photoactivities. The silica coating of TiO_2 particles (T-Avo) can reduce the generation of hydroxyl radicals; however, it was not able to completely prevent the generation of free radicals. T-Eco gave the best results in the deactivation of the TiO_2 surface, probably due to the Al_2O_3 and simethicone coating. All samples, the photoinactive T-Eco, the less active T-Avo, and the active Z-Cote, are recommended by manufacturers for sunscreen pigments. Each of these varies greatly with regards to their efficiency at generating radicals after ultraviolet illumination. Also notable is the similarity in photochemical behavior between materials derived from

suncare products, and the pure nanocrystalline oxides. The hydroxyl radicals generated by all of the samples (excluding P25) were greatest for ZnO nanoparticles (04, 05, 06, 07, Z-Ald, and Z-Cote). This is also in good agreement with both the luminol and DCFH tests.

While EPR is highly quantitative and specific in the ROS species that it measures, it is not the standard method for characterizing photocatalysts. In particular, it cannot easily confirm a catalytic process or evaluate under conditions of continual illumination how much ROS a particular species may generate. For this question, the materials community often uses the decolorization of the dye molecules by photochemically activated to measure the net activity of a nanoscale photocatalyst. The next section describes such studies with two common dyes, Rose Bengal and Congo red.

3.2.3 Congo red dye decolorization test

The decolorization of dye e.g., Congo red (CR) to evaluate the photoactivity of nanoscale particles is a simple and fast test that requires inexpensive equipment. The results of Congo red (CR) decolorization test confirmed the previous results of sunscreen nanoparticles photoactivity. Congo red dye has an aromatic molecular structure which makes it stable and difficult to be degraded [185]. At a concentration of 30 µM, CR was stable for two hours under UV irradiation. This guarantees that the change of the Congo red absorbance is due to the existence of a photocatalyst, not a self-decomposition. The photogeneration of reactive species (e.g., hydroxyl radicals) by nanoparticles results in quick oxidation of organic compounds and degradation of the dye which can be observed as color disappearance (Figure 3.2.6). In addition, by analyzing the solution absorption

spectra of the dye, the photoactivity of nanoparticles can also be quickly and easily quantified by the dye half-life time expressed on a unit mass basis ($t_{1/2}$).

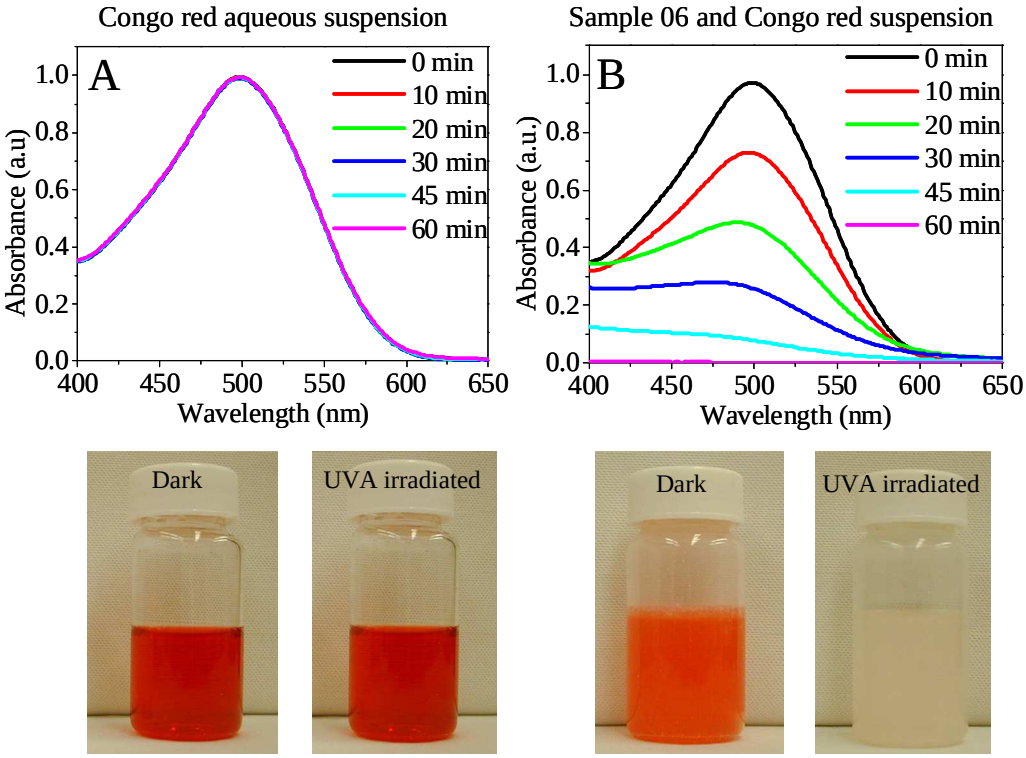

Figure 3.2.6 UV-Vis absorption spectra of (A) Congo red aqueous solution and (B) sample 06 and Congo red aqueous suspension monitored during a 60-min UVA irradiation time. Bottom pictures show the color change of the solutions before and after the 60-min illumination.

The ZnO pigments (04, 05 and 06) lead to more rapid decolorization of Congo red that the apparently inert samples 00 and 01 that contain only TiO_2 nanoparticles Figure 3.2.7. All the ZnO pigments rapidly degraded CR ($t_{1/2}$ ~ 0.20 min) while sunscreens 01 and 00 were much less photoactive and their $t_{1/2}$ was ~ 1.05 min. Sample 07 contained both TiO_2 and ZnO; it was the second most active sunscreen sample with $t_{1/2}$ = 0.16 min.

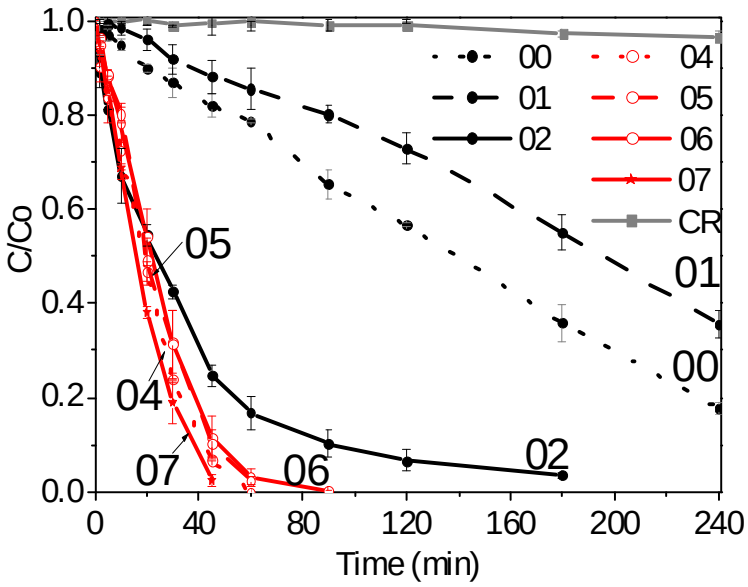

Figure 3.2.7 Experimental data of decolorization of Congo red (CR) dye in the presence of sunscreen extracts (samples 00-02, 04-07), where C_0 is initial dye concentration and C is the dye concentration at irradiation time. The red lines indicate samples that contain ZnO material.

It is interesting to note that sample 02 (containing TiO_2) decolorized CR quickly ($t_{1/2}$ = 0.15 min) while its generation of hydroxyl radicals was lower than other ZnO-containing sunscreen samples (Figure 3.2.5). Therefore, we can assume that other reaction routes may be involved such as the direct oxidation due to positive holes [174, 186]. These holes are created when electrons of a semiconductor (e.g., TiO_2 or ZnO) are excited to the conduction band, leaving positive holes in the valence band. Excitation occurs upon absorption of light energy equal to or greater than the band gap energy of the semiconductor. The positive holes can directly oxidize species that are bound to the surface; they may also react with electron donors like water or hydroxide ions to form hydroxyl radicals which are also potential oxidants. While the Congo red decolorization test itself obfuscates the reaction mechanism, it offers information that is quite important for assessing the overall chemical activity.

The Congo red decolorization test was performed in an unbuffered aqueous solution in the presence of sunscreen extracts or standard control powders; one confounding issue is that to evaluate the dye degradation, the nanoparticles had to be removed by centrifugation or filtration. If the dye itself binds to the nanoparticles, then it can be removed simply due to a physical association with the particles instead of ROS degradation. To evaluate this, pigments were exposed to the dyes without illumination for one hour and the absorbance evaluated. While for the titania samples this control resulted in virtually no change in the absorbance, a different behavior was observed for Z-Cote and Z-Ald samples. Within a few minutes Congo red strongly adsorbed (decrease of the absorbance >80%) on the surface of pure ZnO nanopowders obtained directly from manufacturers.

The different behavior of titania and zinc oxide in relation to the adsorption of Congo red can be explained by the surface properties, particularly the point of zero charge (PZC) which for pure zinc oxide is 9.0 [187]. ZnO nanoparticle surfaces are positively charged in this experiment and as a result CR can strongly adsorb on the surface through the two oxygen atoms of the sulfonate group of the dye molecule [187].

To evaluate the photocatalytic activities of Z-Cote and Z-Ald we chose a different dye - Rose Bengal that did not show significant adsorption to zinc oxide. Using Rose Bengal we could investigate the photocatalytic efficiency of ZnO standard samples in comparison to a P25 titania photocatalyst. Moreover, these two standard ZnO samples are effective sunscreen particle surrogates. They have similar features such as dimension, shape, crystal phase, surface area, elemental composition and hydroxyl radical generation amount to ZnO particles extracted from commercial sunscreens 04, 05, 06 and 07.

3.2.4 ZnO vs. TiO_2 – comparative investigation of photocatalytic properties

Using Rose Bengal, it is possible then to compare the relative catalytic behavior of ZnO sunscreen particle surrogates (Z-Cote and Z-Ald) to TiO_2 (P25) commercial photocatalysts. While prior studies made clear that ZnO can generate ROS species upon UV illumination, these experiments can determine how much ROS a certain mass of pigment can generate. Generally, if the amount of dye that can be decolorized as many times larger than the amount of added pigment, the material is considered to generate ROS in a catalytic fashion. Briefly, after the surface of the particle produces a ROS species, a donor from the solution slowly returns the surface to its fully oxidized state.

ZnO pigments sold for sunscreens, Z-Cote and Z-Ald, at a concentration of 1 mg/ml were able to degrade 225 mg of Rose Bengal in five separate cycles without an apparent loss of activity. This kind of behavior is the hallmark of a photocatalyst which can turn over many reactants, while still retaining activity (Figure 3.2.8). The photocatalytic activity of P25 was greater ($t_{1/2}$ = 0.08 min) than that of ZnO materials ($t_{1/2m}$ = 0.14 min for Z-Ald and $t_{1/2}$ = 0.15 min for Z-Cote). However, as is apparent the level of activity for this experiment both in terms of efficiency (e.g. time of degradation) and turnover (e.g. net amount degraded) are comparable.

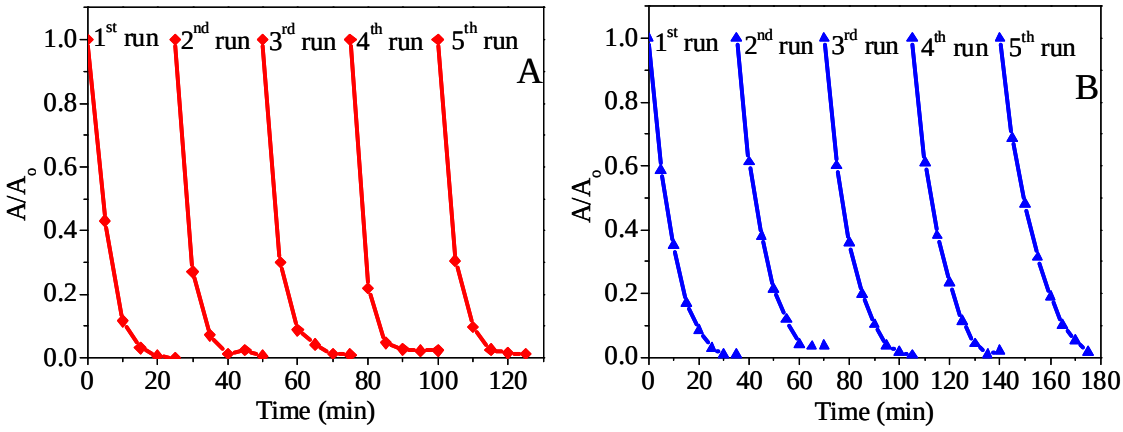

Figure 3.2.8 Photodegradation of Rose Bengal under UVA irradiation for five cycles: (A) Z-Cote, (B) P25 commercial powders. A_o was the initial absorbance measured at λ = 550 nm and A was the absorbance measured during the UV irradiation.

One important difference between zinc oxide and titania that may have importance in evaluating the overall hazard of these materials is the chemical stability of the pigments. The data shown in Figure 3.2.8 was taken over two hours, and while there

was no observable decline in the activity of the zinc oxide materials they are known to dissolve slowly under UV illumination; in contrast, TiO_2 is very stable hence it is generally preferred for industrial applications where photocatalysts may last for months.

To investigate this issue in the context of sunscreen pigments, the chemical stability of Z-Cote, Z-Ald and P25 was investigated in both the dark and under prolonged exposure to UV light in unbuffered aqueous solutions. At different time intervals, the particles were separated from the solution via centrifugation and the Zn and Ti ion content in solution was measured (Figure 3.2.9). The commercial pure P25 titania was insoluble under these conditions; no titanium could be detected in the supernatants. In contrast, after five days without irradiation the zinc concentration in solution was 2.4 ppm for both Z-Ald and Z-Cote. After exposure to UV light for 5 days, the zinc concentration increased to about 24 ppm. While this data confirms that the zinc oxide pigments are more prone to photocorrosion than the titania, they are only marginally different over the several days studied here. Even after five days of continual illumination only 3% of the zinc oxide pigments had dissolved.

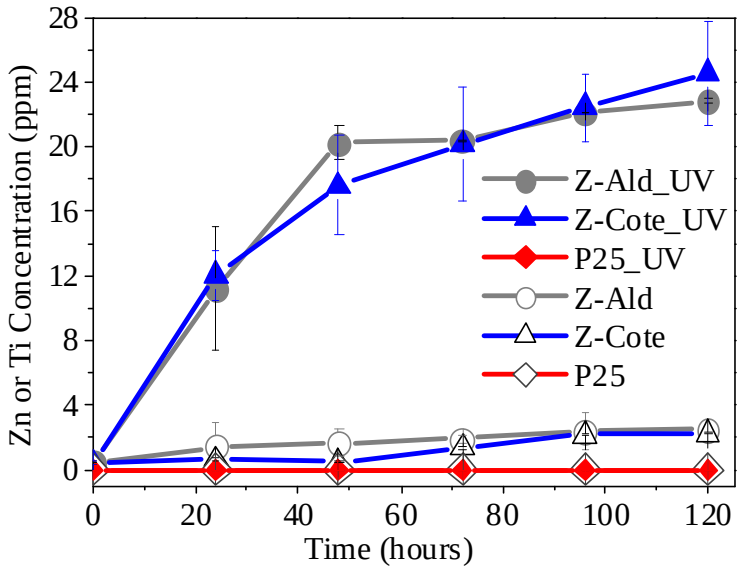

Figure 3.2.7 Photostability of Z-Cote and P25 nanopowders

3.3 Conclusion

The photoactivity of eight commercial sunscreen products containing TiO_2 and/or ZnO inorganic UV filters, as well as the inorganic materials extracted from these sunscreens were examined using a number of assays designed to measure ROS generation efficiency and capacity. All methods revealed that the nanoscale materials presented in commercial sunscreens can generate ROS species under UV illumination. Table 3.2.2 summarizes all of the photoactivity testes. Remarkably consistent behavior is observed among each type of material. For example, Sample 07 demonstrated high activity in all four tests (Luminol CL, DCFH fluorescence, spin trap EPR and CR decolorization).

Table 3.2.2 Output of ROS for the sunscreen samples

Sunscreen sample	ROS Detected by different method			
	DCFH fluorescence (a.u.)	Luminol chemiluminescence (a.u.)	Spin trap EPR ($\mu M \cdot g^{-1}$)	Congo red $t_{1/2}$ (min)
00	0.09 ± 0.01	0.07 ± 0.01	NQ	1.04 ± 0.05
01	0.26 ± 0.06	0.00	NQ	1.07 ± 0.06
02	0.18 ± 0.04	0.00	60 ± 20	0.15 ± 0.01
03	0.05 ± 0.01	0.00	−	−
04	0.34 ± 0.08	0.62 ± 0.14	216 ± 60	0.18 ± 0.02
05	0.37 ± 0.07	0.54 ± 0.03	194 ± 60	0.20 ± 0.03
06	0.74 ± 0.03	0.50 ± 0.08	134 ± 30	0.21 ± 0.04
07	0.28 ± 0.13	0.61 ± 0.08	247	0.16
08	0.00	0.00	−	−

Abbreviations: −, not analyzed; NQ, not quantified. Data are expressed as mean ± σ (n = 3 for luminol and DCFH; n = 2 for EPR and CR) and background values (no sunscreen) in DCFH and luminol assays were subtracted; $t_{1/2}$, half-life time of CR (normalized to the mass of TiO_2 and/or ZnO).

Sunscreen pigments extracted from products showed comparable activity to standard titania and zinc oxide powders. Quantitative measures of ROS concentration revealed that only T-Eco sample, which is TiO_2 coated with alumina and simethicone, did not photogenerate ROS.

One surprising finding from this work is the high level of photoactivity found for both ZnO-containing sunscreens, ZnO nanoparticles extracted from sunscreens, and model ZnO powders obtained from commercial sources. Zinc oxide can generate ROS in much the same way as titania photocatalysts, however, when used in sunscreens they are apparently never coated to limit this intrinsic property. This is in contrast to the titania which is often coated by an inert layer of silica or alumina precisely to reduce the unwanted generation of ROS when UV light is absorbed.

Suncare products are one of many applications of nanoscale materials that offer great benefit to society. As illustrated in this and the last chapter, evaluating the physio-chemical nature and photochemical properties of nanoscale is critical for determining whether the risk of the product outweighs its benefits. The next part of the thesis turns to more conventional nanotechnology in that it centers of developing an application and defining the benefits of working with materials with controlled nanoscale features.

Chapter 4 The optical properties and existing fabrication methods for ring and crescent-shaped nanostructures

Nanostructured materials may exhibit novel properties relative to bulk materials due to their small dimensions. For example, semiconductor nanoparticles such as titanium dioxide and zinc oxide can by virtue of their high surface areas and underdoped metal surface atoms generate reactive oxygen species during ultraviolet illumination; the bulk crystals of these same materials are relatively inert photochemically. Other examples include the size-dependent magnetization of iron oxides or the quantum confinement of optical excitations in quantum dots.

This chapter centers on the review of the properties and fabrication methods for primarily metallic nanostructures. When noble metals are produced with small size, here defined as below 100 nm or ideally even below 5 nm, external electromagnetic fields can induce oscillation in the free conduction electrons [188, 189]. While such excitations are well known in bulk metals as plasmons; however, when they occur in very small particles they generate resonances, or localized surface plasmons, which for gold, silver and copper occur at visible frequencies [188]. The features of these resonances depend sensitively on both the particle size and shape as well as the dielectric properties of the surrounding media [190-192]. Not only does this tunability create great potential for tailored optical filters and coatings, but the excitations of these small particles also can lead to strong field enhancements near the surface or edges of nanoparticles. This latter feature has made these materials of great interest in sensing applications as well as non-linear optics [193-197].

4.1 Optical properties of gold nanorings and nanocrescents

There exist two distinct but complementary approaches to the design and development of metallic nanostructures for optical applications. The first is derived from the decades-old studies of gold nanoparticles; the area of plasmonics views the properties of noble metal nanostructures as derived from bulk plasmons modified by the shape and size of the metal to form localized surface plasmons. The second is of somewhat more recent vintage though its underlying intellectual foundation harkens back nearly a century to microwave antenna design. The designation of materials as 'metamaterials' recognizes that by controlling the size and shape of any dielectric, conductive or otherwise, it is possible to create unique and tunable changes to the permittivity and dielectric response. Metallic structures, particularly c-shaped features, are of special interest to this community. In the following sections, the state of the art in both areas is presented along with their basic approach to material design and application.

4.1.1 Plasmonics as a way of understanding nanorings and nanocrescents

Noble metal nanorings exhibit localized surface plasmon resonances (LSPR) in the visible to near-infrared spectral region; the exact position of the resonance can be tuned by varying the ratio of the ring width to ring outer diameter [197-200]. This tunable resonance arises from oscillations of charges with the same sign at the inner and outer surfaces of the nanoring wall – a feature known as a symmetric dipolar resonance [198, 200]. The antisymmetric dipolar resonance results from charges of opposite sign oscillating at each edge but in gold this particular resonance is absent due to strong damping by the interband transitions [198, 200]. Antisymmetric dipolar resonances can

be observed in silver for which interband transitions start at higher energy region (~3.8 eV) as compared to gold [201]. In addition to these fundamental transitions, Hao et al. demonstrated that for light incident from the side of the nanostructure multipolar resonances of the ring could be excited [200].

Once the incoming light has excited these resonances whether in particles or rings it is possible to obtain electromagnetic field enhancement near the nanostructures [202]. In the case of nanorings, a uniform field enhancement of ten times was observed inside the ring cavity by Aizputua et al. (see Figure 4.1.1) [198]. Tunable resonances and controlled field enhancement of noble metal nanorings offer the ability to manipulate with great precision the fundamental optical properties of these materials.

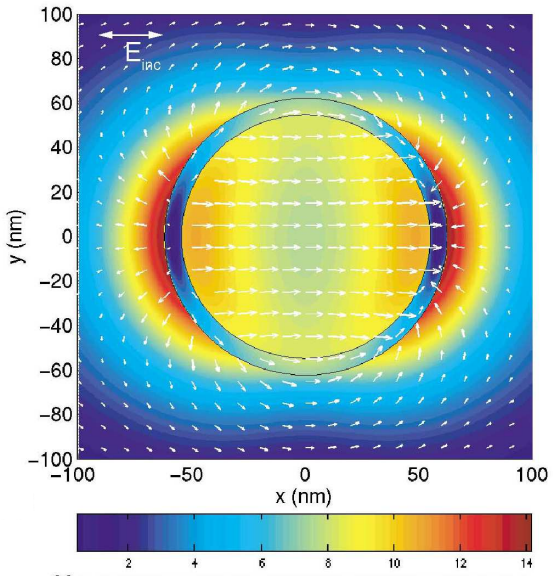

Figure 4.1.1 Simulated local-electric field amplitude distribution of a nanoring of 60 nm radius, adapted from [198]

Noble metal nanoring structures indicate a variety of potential applications due to their unique optical and electrical properties. Of great interest has been the specific case of surface-enhanced Raman scattering (SERS), in which the Raman scattering of molecules is enhanced as compared with free molecules [203]. A similar effect occurs in surface-enhanced infrared absorption (SEIRA), where molecules on metal surfaces show more intense infrared absorption than would be expected from conventional measurements without the metal [204].

Nanorings can also be used for chemical and biological sensing where the cavity of the ring is filled with an analyte [193, 194, 196, 197, 205]. Then, the shift of the resonance due to the small refractive index changes provides a sensitive measurement of the molecules. The detection sensitivity of LSPR sensors based on nanorings is more significant (691 nm per RIU – refractive index unit) as compared to nanospheres, nanoshells, nanowells, nanoholes, and nanoslits (161 to 575 nm per RIU) [194]. Other possible applications suggested for nanorings include fluorescence enhancement [206], highly efficient antennas [207], wave guiding [208, 209], optical data storage [210] and quantum computation [211].

One interesting case of nanorings is the changes in optical properties that occur when the ring symmetry is broken; specifically, these structures appear as c-shapes or more commonly as crescents. Nanocrescents enhance the local electromagnetic field dramatically at their sharp tips, which in turn magnifies the response in SERS [196, 212]. The enhanced electromagnetic field is a result of LSPR that in nanocrescents is polarization sensitive [213-220]. When the incoming light is polarized along the crescent's long axis the charge is distributed at the two arms of the crescent (see Figure

4.1.2 A). Then, field along the plane perpendicular to the crescent is also generated due to current in the crescent. The crescent shows a behavior similar to a magnetic dipole with a magnetic moment. If we treat the gap and gold area as a capacitor (with capacitance C) and inductor (with inductance L), respectively, the fundamental plasmon mode (termed in this thesis as c1) will occur approximately at a frequency $\omega = (LC)^{-1/2}$ predicted by the electrical LC theory [216, 217, 221].

Multiple higher-order plasmon resonances can also be excited for nanocrescents. The charge distribution of the first three resonances of metal nanocrescents is presented in Figure 4.1.2. Rochholz et al. discussed a simple model for understanding multiple plasmonic resonances of crescent-shaped nanoparticles with no interacting ends [215]. They considered the crescent as a rectangular slab and interpreted its resonances as '*standing waves along the rod formed by a superposition of a forward and backward propagating mode of an infinitely extended stripe*'. According to model equation $n \cdot \lambda/2 = L$ multiple resonances are possible and depend on the length of the rod (n – order of the resonance, λ – the wavelength of the resonance, L – the length of the metal structure). The even modes (n = 2, 4 …) correspond to modes excited with light polarized vertically to the tips of the crescent. It is interesting to note that even modes can only be excited for crescent-shaped structures or bent rods. When the rod is straight, or the rings are fully symmetric, the dipole moments cancel out and the even modes are not excited.

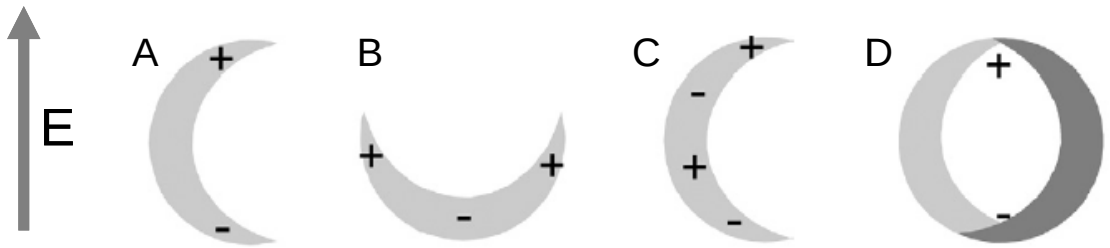

Figure 4.1.2 Sketch of the charge distribution of the first three resonances of metal nanocrescents (A-C) and the closed ring (D), adapted form [215].

The nanocrescents can be modeled as rectangular slabs only in a case of large gap openings, when their tips are separated by a large distance and in effect are non-interacting. When the gap decreases the electric field between the tips increases and the LC resonance moves towards longer wavelengths (see Figure 4.1.3). In effect this trend represents the fact that by decreasing the distance of the plates of the capacitor (e.g. the tips), the capacitance increases and the resonance wavelength increases. Also, the smaller the gap becomes the more pronounced the third order mode (c2) [215, 222]. The position of the second order resonance (u1) is less sensitive to the changes of the gap opening. It shifts slightly to the shorter wavelengths for smaller gaps. When the gap is closed and a nanoring forms only one peak for each polarization is observed due to dipolar resonance on ring structures as described previously.

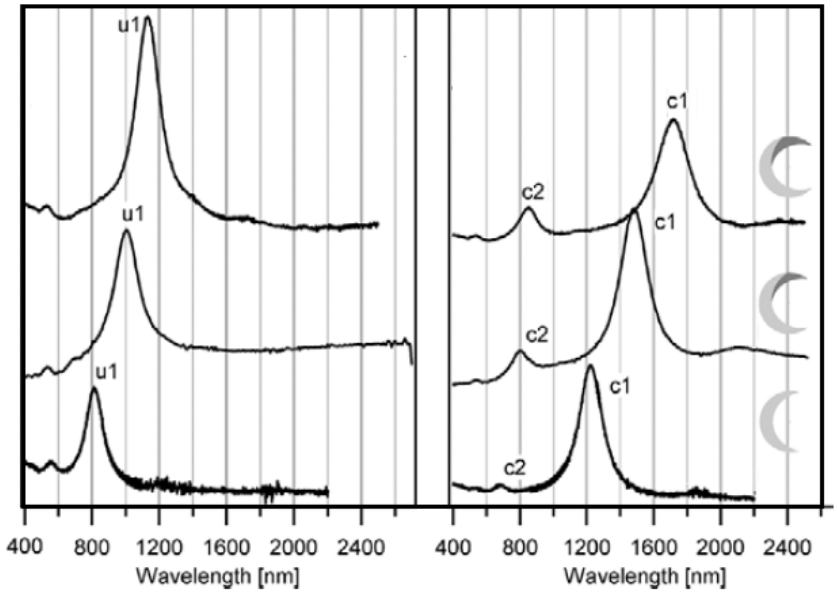

Figure 4.1.3 Extinction spectra for varying crescent opening where c1, u1 and c2 are first, second and third order modes, respectively. Data are adapted from [215]

It has been shown that crescent resonances can be tuned from the visible to the infrared by changing the gap opening as well as the diameter of these nanostructures [215, 219, 222]. Resonances of smaller diameter nanocrescents can shift to the shorter wavelengths. Clark et al fabricated 75 nm radius gold crescents and demonstrated their responses in the visible portion of the spectrum. These size- and shape-dependent optical properties of nanocrescents are of great importance to their applications in surface-enhanced spectroscopy. At resonance, the electric field at the tips of the crescent is strongly enhanced, resulting in molecules in the vicinity exhibiting enhanced absorption and Raman scattering [219].

Highly tunable near-infrared resonances and strong field enhancement at the tips make also nanocrescents ideal candidates for elements of Localized Surface Plasmon

Resonance (LSPR) sensors for detection of chemicals and biomolecules. Nanocrescents array have been used for sensing pH changes of 0.045 pH unit by filling the gaps with a pH responsive hydrogel [223]. Unger et al. demonstrated another example of sensitive detection where LSPR shifts of single gold nanocrescent occurred upon attachment of 60 nm dielectric spheres [224]. Crescent-shaped split ring resonators have also been discussed in the context of metamaterials, a topic further discussed in the next section [217, 222].

4.1.2 The case of metamaterials

The original metamaterial proposal centered on the creation of a substance comprised of artificial atoms that can be tuned to provide virtually any electric and magnetic response to electromagnetic radiation [225]. Additionally, the origin of this tunability is not diffractive; in metamaterial constructions the size and spacing of the 'atoms' needs to be much smaller than the wavelengths of light that they interact with. Under these conditions incident radiation interacts with an effectively homogeneous medium with non-distinguishable artificial atoms.

Of the many properties that such a mythical substance could exhibit, it is the potential to create negative refractive indices that have received the most attention. Generally the responses of materials to electromagnetic fields can be described by material parameters known as dielectric permittivity (ε) and magnetic permeability (μ). In an ordinary transparent dielectrics such as glass and water ε and μ are both positive (region $\varepsilon > 0$ and $\mu > 0$ in Figure 4.1.4). Materials with either negative ε or negative μ rarely occur in nature. Negative permittivity is observed in plasmas at frequencies below

the plasma frequency e.g. for metals (e.g. silver, gold) it is at optical frequencies [226, 227]. Negative permeability can be found in resonant ferromagnetic or antiferromagnetic systems usually in THz and infrared regions [226]. However, at these frequencies these materials are opaque to electromagnetic radiation. Materials with both negative ε and μ and some transparency do not occur naturally [225, 226].

However, in part motivated by the metamaterial discussions, Russian physicist Victor Vesalgo theoretically evaluated the optical properties of a material with simultaneously negative ε and μ. He found that when a material has $\varepsilon < 0$ and $\mu < 0$, the refractive index, derived from $n^2 = \varepsilon \cdot \mu$ has a negative sign $n = -(\varepsilon \cdot \mu)^{1/2}$ [225, 226, 228]. The consequences of $n < 0$ would be that light is refracted negatively at the interface between such a material and a normal material ($n > 0$) [229, 230].

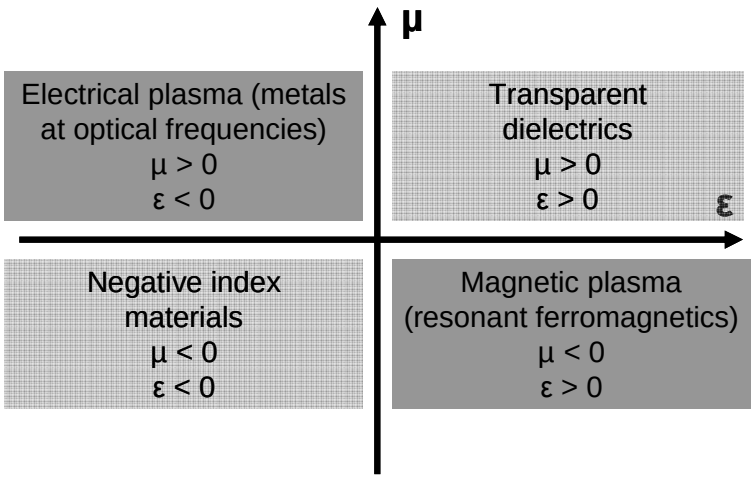

Figure 4.1.4 Dielectric permittivity and magnetic permeability diagram

Snell's law: $n_1 \cdot \sin\theta_1 = n_2 \cdot \sin\theta_2$, where n_1 and n_2 are the refractive indices of the materials and θ_1 and θ_2 are the angles from the normal of the incident and refracted

waves, predicts the direction of the refracted wave. When $n_1 > 0$ and $n_2 > 0$ (Figure 4.1.4 A) refraction is referred to as positive and this is a well known phenomenon. For example, the angle of refraction θ_2 is less than the angle of incidence θ_1 when refraction of light is occurring at the interface between two media of different refractive indices, with $n_2 > n_1$. On the other hand, a negative index of refraction leads to unusual effect which is the bending of light backwards as it passes through the material with a negative refractive index (Figure 4.1.5 B). Such materials with the effective permittivity and the effective permeability both simultaneously negative are called double negative index metamaterials (or left handed) and may be used for enabling perfect lenses that permit overcoming the classical resolution limit [231] or covering ordinary materials in order to cloak them [232].

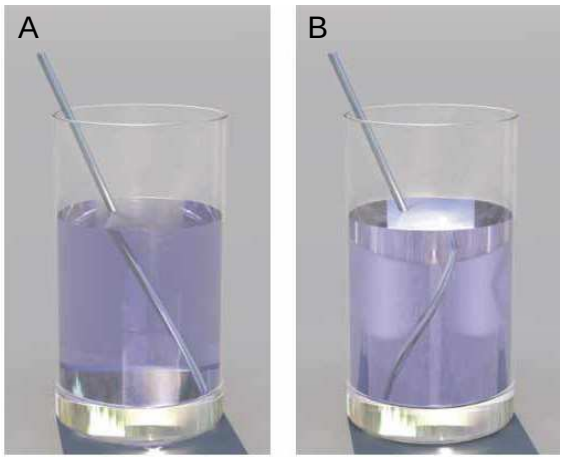

Figure 4.1.5 Calculated images of a metal rod in the glass filled with liquid of n =1.3 (A) and the liquid with a negative refractive index of n = −1.3 (B), adapted from [233]

4.1.3 Metamaterials designs

Microwave frequency metamaterials

There is enormous excitement about the potential of metamaterials, and specifically the many bizarre properties and applications of negative refractive index materials. The central challenge, however, is to design and fabricate a material with ε and μ simultaneously negative. In 2001 Shelby et al. showed negative refraction at microwave frequencies with a material made by unit cells of copper strips and split-ring resonators (see Figure 4.1.6) [234].

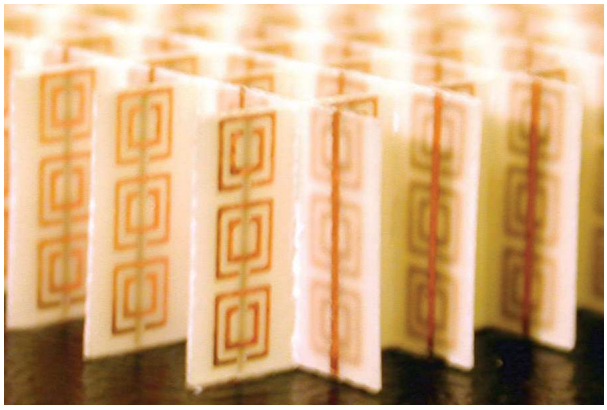

Figure 4.1.6 Microwave frequency metamaterial that consists of a two-dimensional periodic array of copper split ring resonators and wires, fabricated by a shadow mask/etching technique on glass circuit board, adapted from [234]

To build metamaterials with negative refractive index in microwave frequency range, Shelby et al. used ideas presented by Pendry et al. about double split ring resonators to produce negative magnetic permeability (Figure 4.1.7 A) and the wire

system to create negative electric permittivity (Figure 4.1.7 B) in an overlapping frequency regions [235, 236].

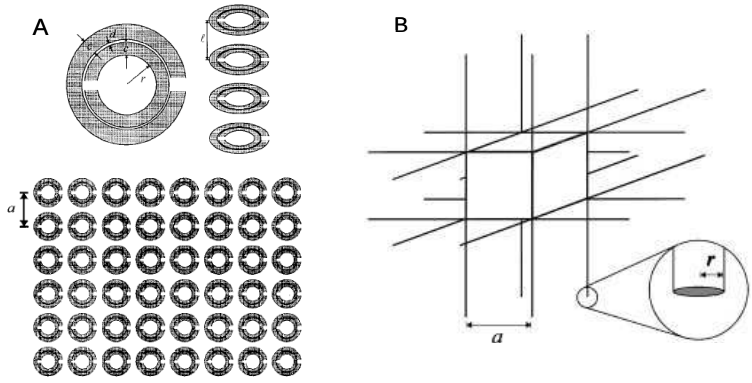

Figure 4.1.7 Metamaterials with $\mu < 0$ (A) and $\varepsilon < 0$ (B); a periodic structures composed of split ring resonators (A) and thin infinite wires (B); adapted from [235, 236]

The effective permittivity of the composite structure such as thin wire array is determined by the following equation $\varepsilon_{eff} = 1 - \frac{\omega_p^2}{\omega}$, where ω_p is the plasma frequency; ω is the frequency of the incident electromagnetic wave. Therefore, the negative permittivity effect in the metal wire array occurs when ω is less than ω_p. Pendry demonstrated that the metal array shifted down the plasma frequency (ω_p) to the low frequency region of the electromagnetic spectrum as compared to the bulk metal and generated negative permittivity in the microwave frequencies. This frequency shift was a result of a decrease in the electron density (n_{eff}) and an increase of the effective mass of electrons (m_{eff}). After detailed calculations the plasma frequency for a thin metallic array

of wires was predicted as a function of the radius of the wires and periodicity of the wire medium $\omega_p^2 = \frac{n_{eff} e^2}{\varepsilon_0 m_{eff}} = \frac{2\pi c_0^2}{a^2 \ln(a/r)}$,

where $n_{eff} = \frac{n\pi r^2}{a^2}$ and $m_{eff} = \frac{\mu_0 e^2 \pi r^2 n}{2\pi} \ln(a/r)$ [227]

- ω_p – the plasma frequency of the thin metallic wires
- n_{eff} – the average density of electrons
- n – the density of electrons in the wires
- e - charge
- m_{eff} – the effective mass of electrons
- c_0 – speed of light
- a – the wire spacing
- r – the wire radius
- ε_0 and μ_0 are vacuum permittivity and permeability, respectively

Below the plasma frequency, the permittivity for the thin metallic wires array became negative. However, with metallic wires it was not possible to obtain negative permeability because these structures did not give any response to magnetic fields. Pendry et al. [236] also suggested a design for artificial magnetic atoms – split ring resonators with negative magnetic permeability (Figure 4.1.7 A). In Pendry's design there were two rings, one inside the other, both having a split. The split rings were situated oppositely and had a small gap in between. Each split ring, composed of a magnetic coil with inductance L and a capacitor with capacitance C (the split), acted as circuit with resonant frequency $\omega = (LC)^{-1/2}$. The small gap between the rings enabled additional capacitance to be formed. Such structures resulted in negative permeability because

incident light coupled to the LC resonance via the magnetic field component. Normal to the SRR plane component of the magnetic field induced a circulating electric current in the SRR coil. Then, the magnetic dipole moment which worked against external magnetic field was created by the current and lead to an effective negative magnetic permeability. A generic function for the effective permeability (μ_{eff}) was described as:

$$\mu_{eff} = 1 - \frac{F\omega^2}{\omega^2 - \omega_0^2 + i\Gamma\omega} \quad [237]$$

- F –the fractional area of the unit cell occupied by the interior of the split ring (a geometrical factor)
- ω_0 – the resonance frequency
- Γ – the dissipation factor

Shelby et al. experimentally proved both Pendry's ideas of SRRs and wires by building metamaterials with negative refractive index in microwave frequency range [234].

Then, Houck et al. and Parazzoli et al. eliminated any doubts about whether a material with negative refractive index can be made by using a similar design and improving the basic optical tests [238, 239].

Towards visible frequency metamaterials

For microwave radiation, the metamaterial structures (e.g. split ring resonators) were on the order of several millimeters. However, in order to manipulate light at optical frequencies it requires photonic metamaterials at the scale of nanometers. By miniaturizing dimensions of SRRs the operation frequencies were further extended [240]. Double split ring resonators with 1 THz (300 μm) magnetic response were presented by

Yen et al [241]. Their square SRR structures with the length of the bottom arm that ranged from 36µm to 26 µm were constructed by a self-aligned microfabrication process. Nanofabrication technique such as electron-beam lithography was used to create single split ring resonators with magnetic response at 100 THz (3 µm) [242]. Linden et al. demonstrated that negative permeability could be obtained in single SRR when light at normal incidence and horizontal polarization couple to the capacitance via the electric field component. The electric field induced a circulating current in the coil, which lead to an oscillatory magnetic dipole moment perpendicular to the SRR plane and a resonant enhancement of the local magnetic fields (Figure 4.1.8).

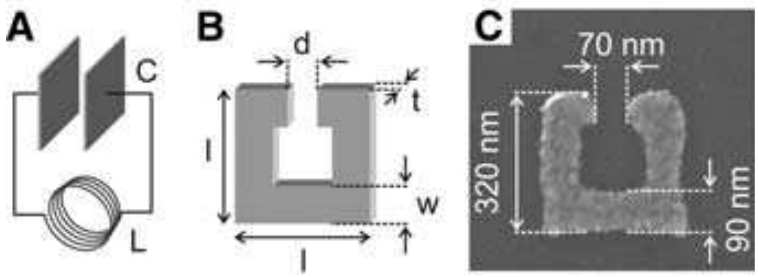

Figure 4.1.8 Illustration of the analogy between a conventional LC circuit (A) and the single SRRs (B). (C) An electron micrograph of a typical SRR fabricated by electron-beam lithography. Adapted from [242] For normal incidence, the electric field vector of the light has a component parallel to the capacitor and leads to the coupling to the LC circuit.

Next, Enkrich et al. pushed SRRs responses to telecommunication wavelength of 1.5 µm (200 THz) by using standard electron-beam lithography and simplifying the nanofabrication. They eliminated the upper arms of the SRR, leading to more U-shaped

structures [243]. The magnetic resonance at 900 nm (333 THz) was reached for gold single-split SRR with the length of the bottom arm of about 110 nm [244]. Then Klein et al. concluded that further miniaturization of single-split SRR dimensions made from gold would not significantly increase the magnetic resonance frequencies due to the increase in losses of the metallic element as its dimensions are shrunk [244-246]. Introducing gain materials into the SRR structure may compensate for loss [247, 248]. Using low loss dielectric substrates, metals with high conductivity (e.g. superconductors) or optimizing geometric design might also allow for resonances with $\mu < 0$ in the visible range [249]. Various methods for reducing losses of the metallic meta-atoms were discussed in paper [249]. These included also designs of negative refractive index metamaterials e.g. cut-wire pairs [250] and fishnet structures [251-255]. The origin of a negative refractive index in a metamaterial built with paired nanorods and nanostrips can be found in [225]. A summary of the progress in 2D metamaterials and their operating frequencies over the past decade is presented in Figure 4.1.9 [195].

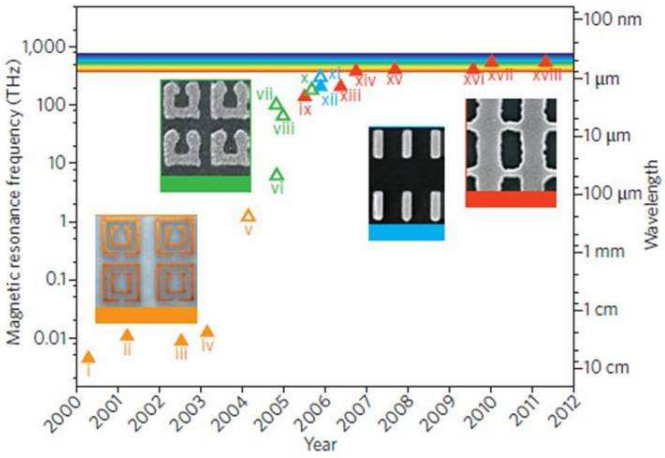

Figure 4.1.9 Progress in metamaterial operating frequency over the past decade, adapted from [195]

4.1.4 Techniques for metamaterials fabrication

Electron beam lithography (EBL) and focused ion beam (FIB) milling are the standard methods for producing 2D near-infrared or visible metamaterials, including SRRs, cut-wire pairs and fishnet structures [256]. Theses lithography processes generate patterns by focusing a beam of electrons or ions onto a substrate and scanning over the desired shapes following a pre-set pattern. In the case of EBL, the substrate is first covered by a resist that is modified chemically by the electron beam. After chemical treatment, exposed areas may be removed leaving a mask that can define areas suitable for subsequent etching or metal deposition. Finally patterns are produced after the lift-off process that removes the unexposed resist [256-259]. Focused ion beam milling creates patterns directly on the surfaces of the substrates by sputtering.

Although, EBL and FIB are capable of resolving nanometer-sized features with a variety of shapes, they have serious limitations in high-volume manufacturing. The instruments for these lithography processes are expensive (over $1 million each) [260]. Moreover, both EBL and FIB are limited by their slow speed; for example, to mill a 16 µm x 16 µm SRR array with FIB takes twenty minutes [261]. Full coverage of centimeters or more would require weeks or even days, at great cost and complexity.

In response to the obvious challenges in scaling up FIB and EBL, other methodologies have been proposed. Interference lithography has been used for structuring larger nanostructured arrays ($1cm^2$) in a reasonable timeframe [256]. In this method the interference patterns (e.g. arrays of lines or dots), generated from multiple coherent beams of laser radiation are transferred onto a photoresist, which after development forms a mask for metal deposition or etching. Interference patterns can be

designed by setting the parameters of the laser beams e.g. directions, polarizations and phases. However, interference lithography is limited in the designs it can produce. It has been most successful in forming wire pairs [262] and fishnet structures [263] rather than more complicated structures like SRRs.

Also on the horizon for metamaterial fabrication is the transition away from two dimensional films. Bulk three-dimensional (3D) infrared and visible negative index materials remain only a theory at infrared and visible frequencies [195]. In the microwave range 3D metamaterials were built by simply stacking printed circuit boards [234, 264]. Negative μ in terahertz [265, 266] and optical frequencies [267] was obtained for multilayers of SSRs fabricated by electron beam lithography. Recently, Garcia-Meca et al. experimentally demonstrated multilayered fishnet structure metamaterial fabricated by focused ion-beam milling, which exhibited a double-negative refractive index in the visible spectral range covering a wavelength region between 620 and 806 nm [251]. Examples of 3D metamaterial structures, which include other than SSR and fishnet designs e.g. chiral, hyperbolic and coaxial structures fabricated by direct-laser writing and electroplatining were recently reviewed in [195, 249, 268]. The 3D metamaterials have so far shown little promise in applications due to their low volume and high cost of fabrication.

Large-scale production of negative index metamaterials in the visible and near-infrared spectral domain requires the development of cheaper and faster nanofabrication techniques. Moreover, these techniques should be able to do patterning in three dimensions. Self-assembly sometimes referred to as ‘bottoms-up’ approaches to metamaterial fabrication are vital (see a review paper [249]). Some structures have been

reported but were often only randomly arranged and lacked experimental confirmation of special metamaterial feature. The effects of disorder may introduce effective losses into these systems and make them not suitable for practical use. The split-ring resonators, however, are particularly interesting candidates for bottoms-up metamaterials. They are identical to nanocrescents and may be amenable to soft lithographic approaches that offer efficient and low cost fabrication strategies. A review of this work is described in the following section.

4.2 Nanosphere lithography for the production of nanorings and nanocrescents arrays

Colloidal lithography makes use of dense arrays of polystyrene or silica nanospheres that form on substrates; such close-packed arrays create a natural mask for either material deposition or etching [269]. The hexagonal closed-packed (hcp) lattice film is the most favorable crystal structure formed by colloidal particles [270, 271]. Monolayer films can be produced by diverse methods including dip-coating, transfer from floating interfacial films, electrophoretic deposition, physical and chemical template-guided self-assembly as well as spin coating [272, 273]. Nanospheres can be assembled into a single layer, double layer or multilayers by varying assembly parameters. Each of these methods is both inexpensive and relatively fast. Moreover, these masks cover large area substrates (of dimensions > 1 cm^2).

Once a nanosphere mask is generated, material can be deposited into the holes between the spheres by sputtering, thermal evaporation or electron beam evaporation. After material deposition, the nanosphere mask is removed – often by simple techniques

such as tape stripping - leaving behind a pattern of material that reflects the holes in the nanosphere array as presented in Figure 4.2.1.

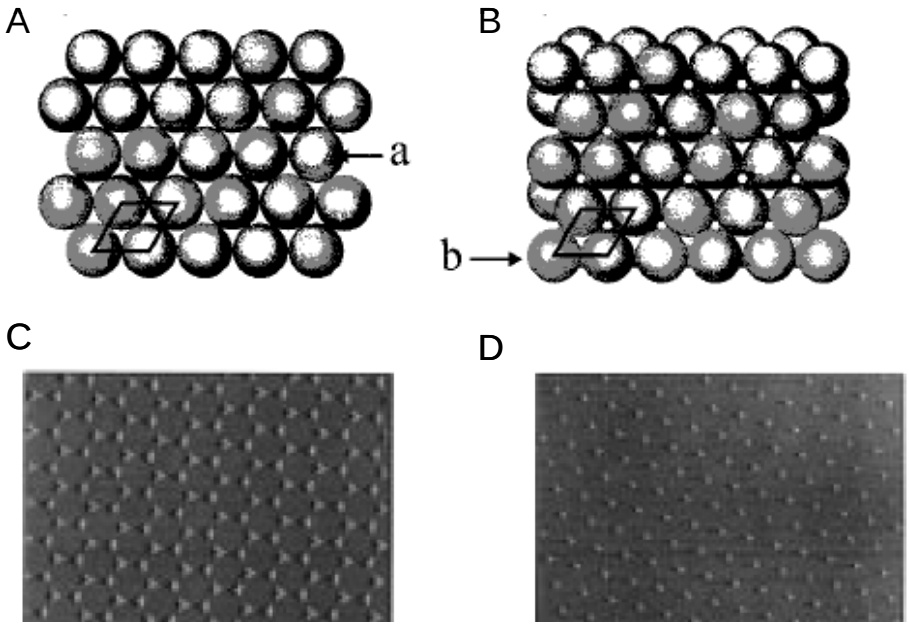

Figure 4.2.1 Schematic diagrams of single-layer (A) and double-layer (B) nanosphere masks and the corresponding nanoparticles arrays (C and D), adapted from [274]

When material is deposited through the single layer mask, an array of triangularly shaped nanoparticles is created Figure 4.2.1A. This is the simplest nanosphere lithography scenario. However, nanoparticle size, shape, and arrangement can be significantly changed to provide a greater range of possible patterns. Some strategies for this include material deposition through multilayers (Figure 4.2.1B), modifications to the deposition technique (angle and/or rotary deposition) as well as presented in Figure 4.2.2 alterations of the nanosphere mask (etching and/or annealing of the spheres).

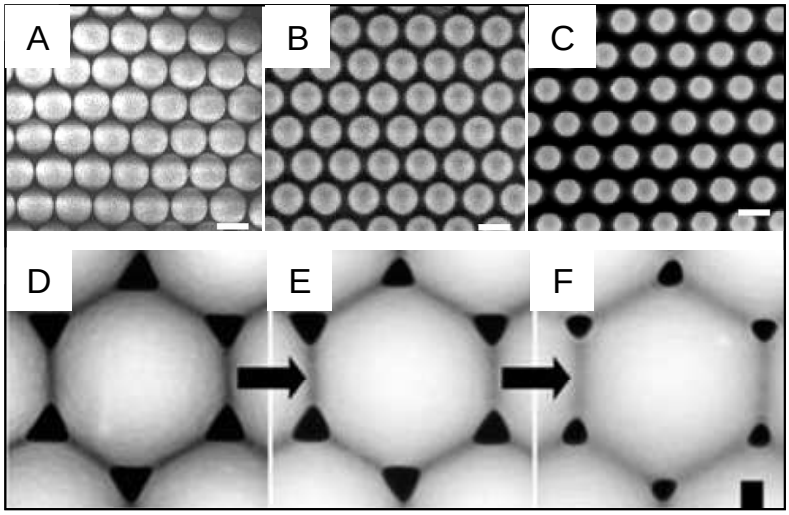

Figure 4.2.2 Changes in the mask morphology obtained by deforming the colloid particles by RIE etching (A-C) for 6 min (A) 14 min (B), and 20 min (C); and annealing (D-F) via 1, 2, 4 microwave exposures, adapted from [275, 276]

Using annealed spheres presented in Figure 4.2.2 D-F Kasiorek et al. fabricated rings, rods, and dots [276]. Nanorings were achieved by using modified evaporation system and evaporating metal with controlled evaporation angle and the sample rotation at the same time. Gwinner et al. used similar nanosphere lithography approach to fabricate nanocrescents arrays [277]. The mask was annealed by thermal treatment on a hot plate isolated from the environment by a glass case; this treatment shrinks the apertures between the spheres. Then the substrate was both tilted and rotated with a custom stage during electron beam evaporation to yield either nanorings or nanocrescents (e.g. split ring resonators). The gap of SRRs was generated by incomplete revolutions during evaporation. These structures were highly uniform and had optical features consistent with either a plasmonic or metamaterial understanding.

Another strategy for nanocrescents fabrication involved carrying metal film deposition with tilted incidence through etched colloidal mask, followed by ion beam milling [221, 278]. Fabricated by Retsch et al. and Vogel et al. crescent-shaped structures showed LC resonances consistent with split ring resonators in the infrared region at about 1.5 μm. However, their approach for nanorings and nanocrescents fabrication is limited by its reliance on ion beam milling, which is slow and expensive, and limited in its ability to rapidly form structures over large areas. Other researchers have reported metallic nanorings and nanocrescents arrays formed from nanospheres, but either demonstrated random arrangements of nanostructures[198, 214, 220, 279] or did not fully characterize their optical responses [280-283].

In Chapter 5 of this thesis an alternative approach for fabrication of well ordered, large area metal nanorings and nanocrescents arrays is presented. The strategy includes the self-assembly of polystyrene spheres; plasma etching of the arrays; metal deposition at normal incidence and finally plasma etching of portions of the exposed metal. This approach reduces the cost and time associated with the fabrication of metal nanoring and nanocrescent arrays. These nanostructures present unusual properties that could be applied in various fields including detection of chemical and biological molecules, surface enhanced spectroscopy or as metamaterials. It may also be possible to vertically stack crescents structures, to enable three-dimensional materials [221, 278]. Furthermore, intensive research and development in technique for production of metal nanorings and nanocrescents arrays led us to new nanosphere lithography approach to fabricate polystyrene nanodoughnuts arrays (Chapter 6).

4.3 Polystyrene nanodoughnuts arrays fabricated by nanosphere lithography

In nanosphere lithography process for the production of periodic triangular-shaped nanoparticle array formation of small nanorings around the points of contact between a sphere and the substrate was reported by Winzer et al., Jia et al. and Boneberg et al. [284-286]. However, there was an inconsistency in their conclusions concerning the nanorings elemental composition. Winzer et al. and Jia et al. did not perform any elemental analysis measurements; however, claimed that fabricated nanometer scale rings were made from gold. Boneberg et al. performed Kelvin mode measurement for surface potential detection and showed contrast difference between nanotriangles and nanorings that were formed on the substrate, which indicated that rings consisted of material different from the triangles. In our nanosphere lithography process for the production of nanocrescents arrays, we observed similar small nanorings around the point where polystyrene particles touched the surface of the substrate. After repeated experimental tests under different conditions we came to a conclusion that changes of the polystyrene spheres composition occurred during plasma etching and solvent treatment of these modified particles resulted in formation of regular nanoring shaped polystyrene residue on the substrate surface. Therefore, from nanosphere lithography a completely undesired outcome may result and it is always necessary to confirm the elemental composition of the fabricated nanostructures. Further research on this unexpected result developed new technique for fabricating polystyrene nanodoughnuts arrays that was described in Chapter 6 of this thesis.

For the successful growth of nanotechnology new and unconventional fabrication methods are needed for making nanostructures inexpensively. Our approach is a

promising method to produce an ordered polystyrene nanodoughnuts because of the simplicity and low cost of all the fabrication steps that include self-assembling of colloidal polystyrene particles on silicon wafer, argon plasma etching and solvent treatment. Conventional methods of polymer nanorings fabrication (soft molding and electron beam lithography) have relatively high cost and low throughput [287, 288]. Presented earlier approaches based on nanosphere lithography involve (i) capillary forces that drive material underneath the spheres that form nanorings around colloidal particles [289, 290], (ii) chemical etching of nanoholes in colloidal spheres [291-293] or (iii) formation of aminosilane protection film around parts of the colloidal particles, which retards the dissolution of the outer portions of the spheres that is in contact with substrate [294]. Nanorings obtained according to the last procedure were used for the attachment of gold or DNA-capped gold nanoparticles and development of substrates for localized surface plasmon resonance based biosensors.

In Chapter 6 we are going to show an alternative approach for producing nanodoughnuts arrays using a modified nanosphere lithography procedure that also can be decorated with nanoparticles made from noble metals (Au or Ag) or ferromagnetic (Co) materials and present optical excitations or act as nanomagnets. These structures can have several other applications as well. For example, they can be used as a mask for the patterning silicon nanorings, which coated with magnetic layer (e.g. Cu/Co/Cu) may act as magnetic nanorings. It has been reported previously that one of the methods to achieve magnetic nanoring arrays is directly depositing the magnetic layer onto a prepatterned substrate [295]. Nanorings made from ferromagnetic materials characterize existence of simple and well-defined magnetic states, the vortex state, in which the

magnetization runs around the ring, either clockwise or counterclockwise and the onion state, which corresponds to opposite circulation of magnetization in each of half of the ring [295-297]. Therefore, the ring shape nanomagnets are promising as elements of high-density magnetic random access memory (MRAM) or other magnetoelectronic devices [298, 299]. The following sections of this thesis (Chapter 5 and Chapter 6) will describe procedures used to fabricate both metal ring-shaped nanostructures arrays and polystyrene nanodoughnuts arrays.

Chapter 5 Fabrication of two-dimensional gold nanostructures arrays by shaped nanosphere lithography

In this chapter fabrication methods based on nanosphere lithography are applied to produce gold nanostructures arrays of various shapes such as triangles, spherical particles, holes, nanorings and nanocrescents. Of particular interest is the fabrication of nanorings and nanocrescents arrays over large areas (>1cm^2). This novel process, termed here 'shaped nanosphere lithography', uses polystyrene spheres to prepare widely spaced arrays of mushroom-shaped spheres. The deposition of gold via sputtering or evaporation results in a continuous metallic film around the shaped spheres; however, the metal builds up a thick layer at the edge of the mushroom structures and subsequent plasma etching leaves only this thicker ring on the silicon substrate. By applying a solid mask to one side of the substrate, it is possible to preferentially etch from one direction more than the other yielding nanocrescents. Because the process relies on a soft lithography, areas as large as a centimeter can be prepared in only a few minutes. The physical characteristics of the rings and crescents, including diameter, wall thickness and gap size, can be tuned over a wide range of dimensions. Specifically, the optical properties of gold nanorings and nanocrescents with outer diameters ranging from 300 to 350 nm were measured and compared with numerical simulations.

5.1 Materials and methods

5.1.1 Substrate preparation and monolayer of polystyrene spheres formation

The first step in a nanosphere lithography process is the formation of a monolayer of polystyrene spheres on a substrate; either a clean piece of single side polished silicon wafer or glass microscope slide (~1 cm^2) can be used for this purpose. Close-packed layers with minimal defects are formed using polystyrene spheres dispersions with reported sizes 400 and 250 nm, purchased from Bangs Laboratories Inc. (Fishers, IN). These materials were passed through 0.8 µm pore size Whatman syringe filter. Silicon or glass wafers were cut using a diamond knife into roughly 1 cm square samples and cleaned using a standard RCA1 solution (1:1:5 NH_4OH : H_2O_2 : H_2O at 75^oC for 10 min). The filtered 400 or 250 nm colloidal particles were spread onto wafers using either a spin-coating technique, drop drying or liquid surface assembly. Generally, spin coating was preferred and we used speeds of 3000 and 5000 rpm for 30 seconds. This treatment formed a large monolayer during the evaporation of the solvent [271].

The other approaches to forming polystyrene arrays included both drop drying and liquid surface self-assembly. For drop drying, 30 µl of 400 nm unmodified polystyrene spheres solution was placed onto a pre-cleaned silicon wafer; after evaporation overnight a residue of spheres was visible. The liquid surface self-assembly method was performed according to the method of Zhang et al. [300].

5.1.2 The shaping of polystyrene sphere form and diameter

After assembly of polystyrene beads on the substrate, the sphere diameters and morphology were altered using either thermal annealing or argon/oxygen (Ar/O_2) reactive ion etching process. During the annealing process, the sample was placed inside Blue-M Inert Gas Clean Room Oven at 105^{o}C on a glass petri dish without a cover. Annealing periods were in the range of 30 – 60 min and resulted in decrease of the void spaces between the spheres.

An etching process was carried out by Ar/O_2 reactive ion etching (RIE) using a Minilock-Phantom III plasma RIE system from Trion Technologies, which picture is presented in Figure 5.1.1. First, the samples were placed on 8" silicon carrier wafer into a Minilock-Phantom III RIE load-lock chamber. After a rough rotary pump, they were transferred to reaction chamber for etching. Argon and oxygen were introduced into the reaction chamber through a showerhead in the upper electrode. The Ar/O_2 flow rate ratio was 25/20 sccm (standard cubic centimeters per minute); this was ideal for the conversion of the spheres into mushrooms. The plasma was activated by 13.56 MHz RF power supply at 60 W. The pressure was controlled at 60 mTorr and the etching time ranged from 10 to 75 sec. During the etching the sphere diameters were reduced and the void spaces between the spheres were increased. Moreover, the spherical morphologies of the spheres were altered into mushroom-type structures.

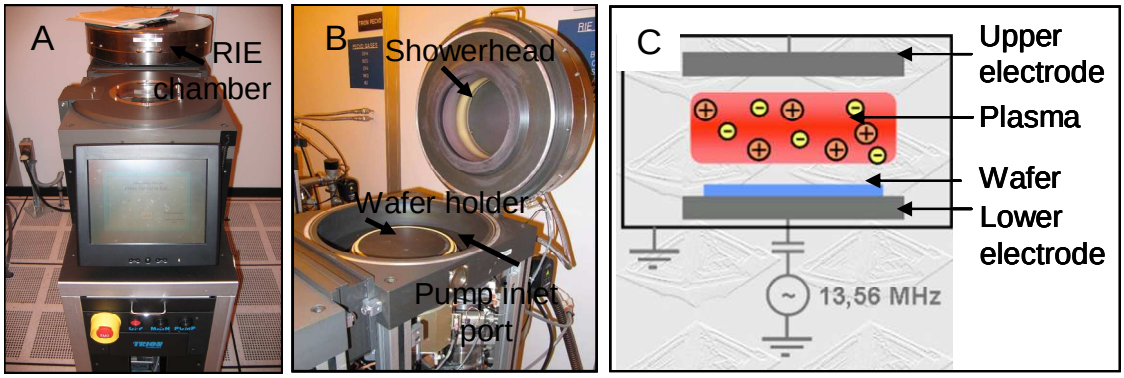

Figure 5.1.1 Digital pictures of Minilock-Phantom III plasma RIE system from Trion Technologies with closed (A) and open (B) RIE chamber and schematic representation of RIE process in the chamber, which was adapted from [301].

5.1.3 Formation of gold nanostructures

The mushroom shaped polystyrene structures became the masks for the formation of gold nanoparticles arrays. Typically, a layer of gold (from 20 to 60 nm thick) was deposited using either a CRC-150 sputter coater or e-beam evaporator (Sharon Vacuum, Brockton, MA). Prior to Au deposition a 4 nm Cr film was sputtered or Ti film was evaporated for a better adhesion of the Au film on the silicon wafer. Depending on the polystyrene spheres mask pattern nanostructures of different shapes were fabricated. Gold nanostructures arrays were achieved when polystyrene beads were removed from the substrates mechanically by using a piece of adhesive tape (Scotch Matte Finish Magic Tape, 19 mm x 7.62 mm) just after metal deposition.

The fabrication of nanorings and nanocrescents arrays involved an additional etching step after metal deposition. After gold evaporation or sputtering, the materials were argon plasma etched using Minilock-Phantom III RIE system, the same one that was used for shaping of polystyrene spheres, with conditions of Ar 40 sccm, 400 W, 12

mTorr for 60 – 150 sec. Finally the polystyrene spheres were mechanically removed from the substrates via a simple tape stripping process.

Alternatively, the array of shape-controlled nanostructures (either nanocrescents or nanorings) could be obtained when the sample was argon plasma etched in the presence of the solid mask. This mask was either a piece of silicon wafer or glass microscope slide of thickness t = 0.4 or t = 2 mm, respectively. It was placed on top of the sample after its conversion to mushroom structures and then used during metal deposition. The configuration is presented in Figures 5.1.2 B and C. In the first case, a single-side solid mask was positioned on one side of the sample, and this covered about 30 % of the total area. In the second experiment, the double-side solid mask covered about 60 % of the total sample at two opposite sides and formed nanorings in the middle part of the sample.

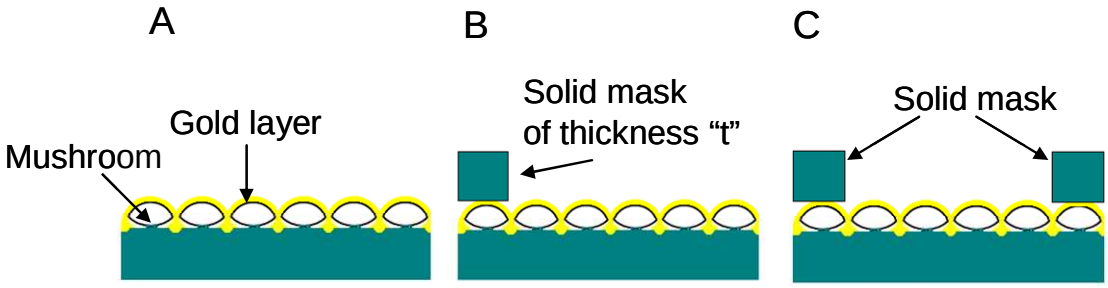

Figures 5.1.2 Schematic view of the sample without the solid mask (A), with one-side solid mask (B) and double-side solid mask (C)

5.1.4 Characterization methods

Hydrodynamic diameters of the purchased polystyrene spheres were obtained from dynamic light scattering (DLS) using a Zetasizer Nano ZS from Malvern Instruments. For a preliminary investigation of the polystyrene sphere films, optical images were taken by using a Nikon Eclipse ME 600L microscope equipped with lenses, covering a magnification range from 5x to 200x and a Nikon DXM1200F camera. Monolayers of polystyrene sphere assemble and arrays of nanostructures on silicon substrate were characterized with scanning electron microscope (SEM) (FEI Quanta 400F field emission scope) equipped with secondary electron (SE) and a liquid nitrogen cooled energy dispersive x-ray spectroscopy (EDS) detector (EDAX Genesis) at a working distance of 10 mm and spot size setting of 3 and beam voltages between 20 and 30 kV. Non-conductive samples were sputter coated with a 10 nm thick gold film, which minimizes charging from the electron beam. EDS elemental maps were collected for primary emission lines of silicon and gold elements.

For structural determination of nanorings and nanocrescents imaging techniques of scanning electron and atomic force microscopy were used. Additionally, UV-VIS-NIR and FTIR spectra were measured to determine the optical properties of nanoring and nanocrescent arrays. Images acquired using the SEM evaluated geometrical parameters of the resulting gold nanostructures arrays, which are schematically presented in Figure 5.1.3. Dimensions were determined by measuring at least one hundred nanostructures manually and compiling the statistics using Image-Pro Plus 5.0 software (Media Cybernetics). A Nanoscope III atomic force microscope (AFM) was used to verify the height of nanostructures. Non-polarized extinction spectra of the nanorings arrays

fabricated on glass microscope slides were recorded with a UV-VIS-NIR Carry 5000 spectrophotometer in transmission mode. Spectra of the nanocrescents arrays were evaluated using a Jasco FTIR 660 Fourier Transform Infrared (FTIR) spectrometer in transmission mode at normal incidence in collaboration with Zhang Qi (from Dr. J. Kono's group at Rice Unibersity) and Nicolet FTIR Microscope in the reflection mode at normal incidence. In transmission mode, the extinction signal represented light that was not being transmitted. This included light that was absorbed and light that was scattered in all directions except for the collection angle of the detector. In reflection mode, the reflectance spectrum showed a peak for where the plasmonic structure scattered light into the collection angle of the objective. The sampling area for FTIR microscopy analysis was 100 x 100 µm.

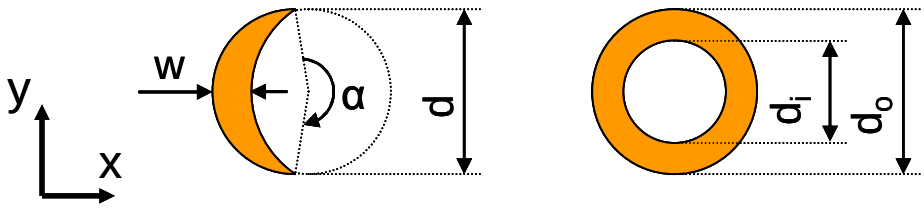

Figure 5.1.3 Sketch of the gold nanostructures geometry indicating the diameter 'd' of the mushroom, the gap opening 'α' of the nanocrescents, the maximum nanostructure width 'w', outer 'd_o' and inner 'd_i' diameters of the nanorings

5.1.5 A simulation study of nanorings and nanocrescents arrays

The optical properties of nanorings and nanocrescents were also calculated from finite difference time domain (FDTD) method [302] using commercial FDTD software (Lumerical Solutions Inc., Canada). This work was done in collaboration with Peter Nordlander's group at Rice University and three-dimensional simulations were performed by Yang Li.

A perfectly matched layer (PML) was used as radiation boundary condition to truncate the simulation domain. Auto non-uniform meshes were applied to the computation domain. A uniformly meshed region with a grid size of 2 nm was used to mesh the nanostructures. In order to better describe the curved edges of the ring structures, conformal meshes were applied to the metallic nanostructures to reduce the possible staircase effects. The whole simulation region was set with a background index of 1 (air) and the refractive index of the glass substrate was taken as 1.5. Lumerical's multi-coefficient model was applied to fit the empirical Cr, Ti and silicon dioxide data. Drude fitted dielectric function $\varepsilon = \varepsilon_\infty - \frac{\omega_B^2}{\omega^2 + i\gamma\omega}$ with the following values was employed to model the gold nanostructures: background dielectric constant $\varepsilon_\infty = 9.5$, bulk plasma frequency $\omega_B = 8.94eV$, and the intrinsic damping parameter $\gamma = 0.069eV$. In the simulation, the nanorings were modeled as concentric rings with inner and outer radius. The crescents were modeled as rings with radius subtracted by another ring of the same radius offset at the center, that was, the width of the structure. To account for the whole array of nanostructures, periodic boundary conditions were applied in the simulation with the periodicity determined from the experimental SEM images.

5.2 Results and discussion

5.2.1 A close-packed array of polystyrene spheres

Colloidal lithography makes use of the propensity of highly uniform particles to form close-packed arrays on flat surfaces; such arrays offer a mask with holes between the spheres. Hexagonal closed-packed (hcp) lattice films are the most favorable crystal structure formed by close-packing, and thus the mask holes reflect this symmetry. Dynamic light scattering was used to confirm the narrow size distribution of the commercial polystyrene spheres. The hydrodynamic diameters were found to be 388 ± 5 and 250 ± 2 nm in good agreement with the sizes reported by Bangs Laboratories (see Figure 5.2.2). These spheres formed hexagonally closed packed layers on both silicon and glass substrates; to minimize defects in the arrays required some attention to both the substrate preparation and solutions themselves. Large agglomerates and impurities found in as purchased suspensions adversely affected the crystalline quality of the monolayers as presented in Figure 5.2.1. Therefore, these clusters and impurities were removed from suspensions by filtration with 0.8 µm pore size syringe filter.

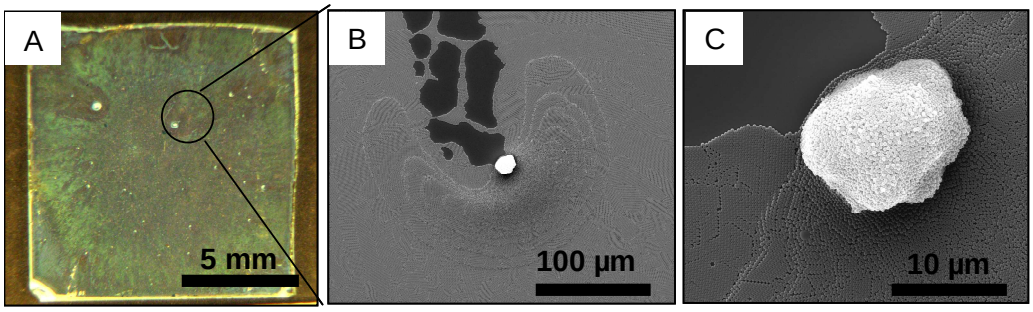

Figure 5.2.1 Digital picture of polystyrene spheres assembled onto glass substrate (A) and SEM images obtained at 5,000x (B) and 20,000x (C) magnification levels of defects in

polystyrene monolayer such as blank spots and multilayers caused by cluster of polystyrene particles. The solution was not filtered before applying to the substrate.

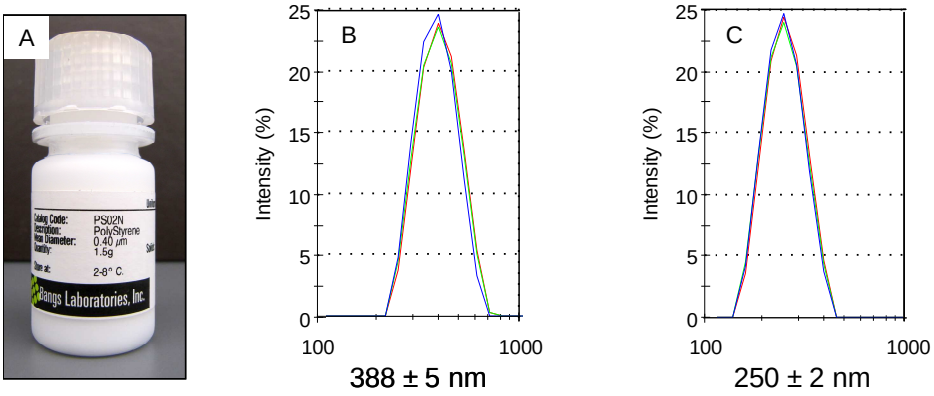

Figure 5.2.2 The aqueous colloidal solution of polystyrene spheres obtained from Bangs Laboratories (A) and DLS analysis of the polystyrene beads obtained from this company and labeled as (B) 400 nm and (C) 250 nm

The quality of the polystyrene spheres film depends not only on the purity and uniformity of the colloid but also the hydrophobicity of the surface. Therefore, before assembling polystyrene particles on the substrates we cleaned the silicon and glass pieces using RCA1 procedure that rendered the surface hydrophilic and allowed the drop (30 µl) of suspension of polystyrene spheres to spread uniformly over the full area of the substrate with lower contact angle as depicted in Figure 5.2.3.

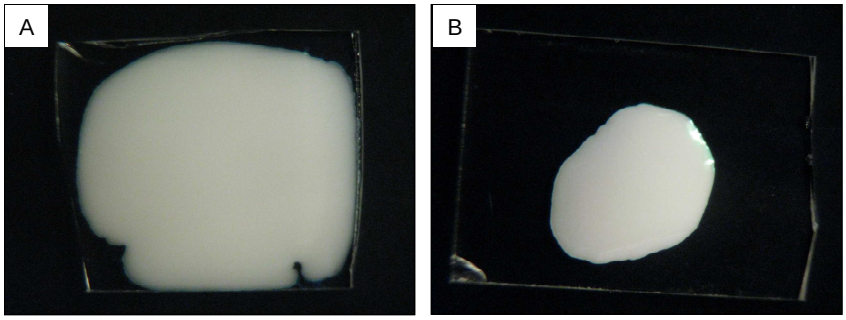

Figure 5.2.3 Digital pictures of 30µl drop of suspension of 400 nm polystyrene spheres on RCA1 cleaned (A) and untreated (B) glass substrates. RCA1 procedure led to a low contact angle, which permitted droplet of polystyrene spheres solution to assume a flatter shape and cover the full area of the substrate.

Once the materials and the surfaces are optimized there are a variety of approaches that can be used to form a colloid assembly: drop drying, dip-coating, floating on an interface (Langmuir–Blodgett), electrophoretic deposition, physical and chemical template-guided self-assembly and spin coating [272]. We evaluated the efficacy of three methods for self assembly: drop drying, floating on an interface and spin coating, which are schematically represented in Figure 5.2.4. Processes were compared based on ease of use, quality of the layer and reproducibility.

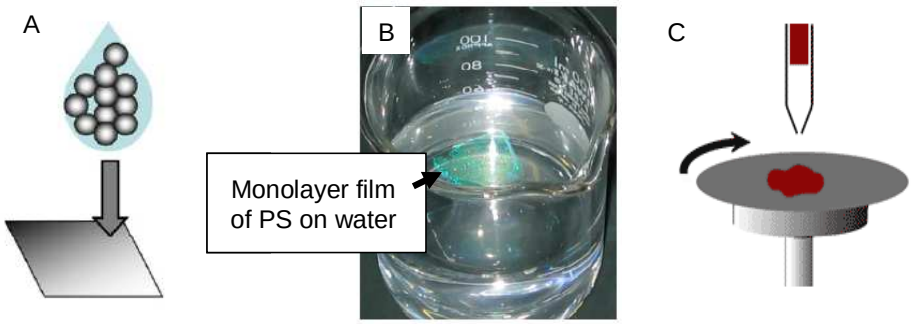

Figure 5.2.4 Schematic representations of drop drying (A), floating on an interface (B) and spin coating (C) methods of assemble of polystyrene spheres (PS). Schematics (A) and (B) were adapted from [303] and (C) from [304]

Drop drying was the simplest way to a obtain film of polystyrene spheres. The film formed as the solvent evaporated leaving spheres adhered to one another due to the forces between neighboring particles. The morphology of the drop drying deposited polystyrene layer and the results are presented in Figure 5.2.5 (A-C). While the technique was simple there were issues of inconsistent layers due to drying coffee-stain-like rings of material [305]. Large areas of monolayers formed with some holes and domains of closed packed polystyrene particles but they were only in the middle, while multilayers were observed on the edge of the ring. SEM images in Figure 5.2.5 A-C revealed that the polystyrene spheres inside one domain formed a close-packed arrangement, wherein each sphere was surrounded by 6 others in the same layer.

The second method, presented by Rybczynski et al and [306] termed in this thesis as ‘floating on an interface’, required more steps:

(i) Treating pieces of silicon wafer with dodecylsodiumsulfate (DSS) solution for 24 h

(ii) Applying a drop of polystyrene spheres solution onto the surface of DSS treated silicon wafer

(iii) Forming an unordered monolayer of polystyrene spheres on the water surface by immersing silicon wafer with polystyrene particles in the glass vessel filled with water

(iv) Forming an ordered monolayer of polystyrene sphere by adding DSS, which changed the water tension and consolidated the particles

(v) Lifting off the monolayer from the water surface using DSS treated silicon wafer

Monolayers obtained by floating on an interface method resulted with smaller voids between domains of closed packed polystyrene particles. However, the domains, which are presented in Figure 5.2.5 D-F were often small (much below 100 μm^2).

Finally, the best results were found via spin coating (see Figure 5.2.5 G-I). During the spin coating process the centrifugal force spreads the solution evenly onto the substrate while the solvent is evaporating. This can lead to rapid monolayer formation and nicely packed arrays with few defects or voids. Large areas of array monolayers (1 cm^2) could be formed within 30 seconds by this approach. For this method, the thickness of the particle layer was controlled by adjusting the spin speed (Figure 5.2.6). Uniform monolayers over large areas were obtained with spin rates of 3000 and 5000 rpm for the polystyrene particles with hydrodynamic diameters 388 ± 5 and 250 ± 2 nm, respectively. Despite the presence of point defects due to spheres of different diameter (see Figure 5.2.6 C), the uniform color exhibited by these colloidal crystals in Figure 5.2.6 D demonstrated their high quality.

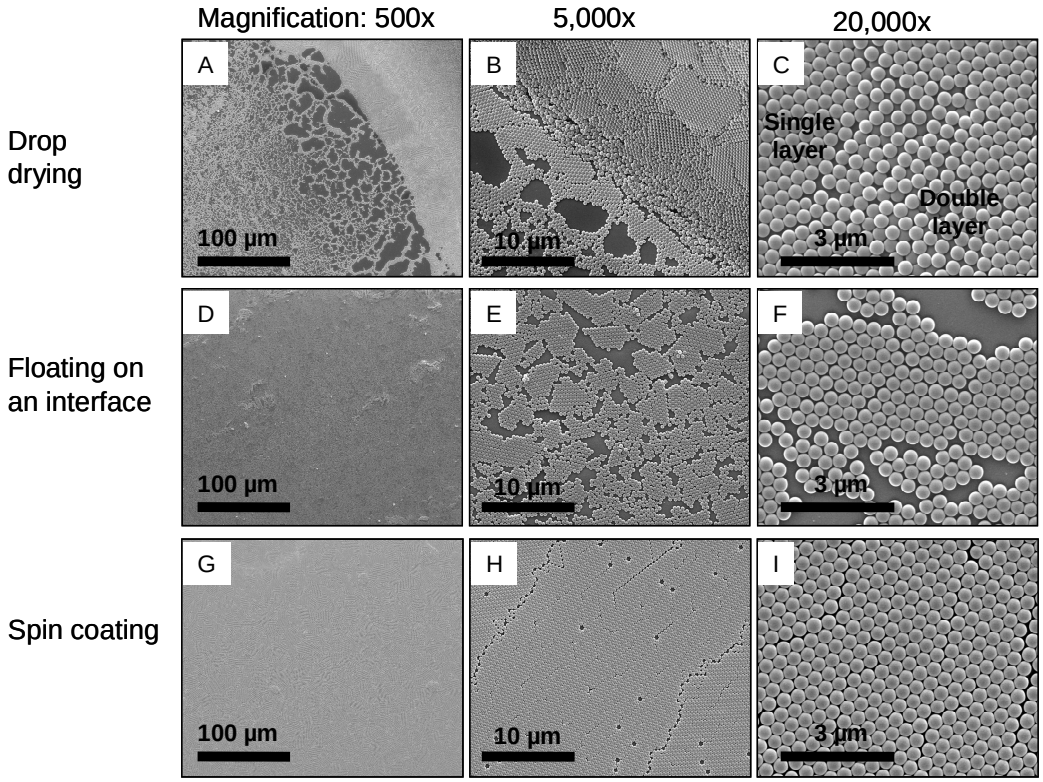

Figure 5.2.5 SEM images obtained at 500x (A, D, G), 5,000x (B, E, H), and 20,000x (C, F, I) magnification levels of polystyrene spheres assembled onto substrates by drop drying (A-C), floating on an interface (D-F) and spin coating (G-I) methods

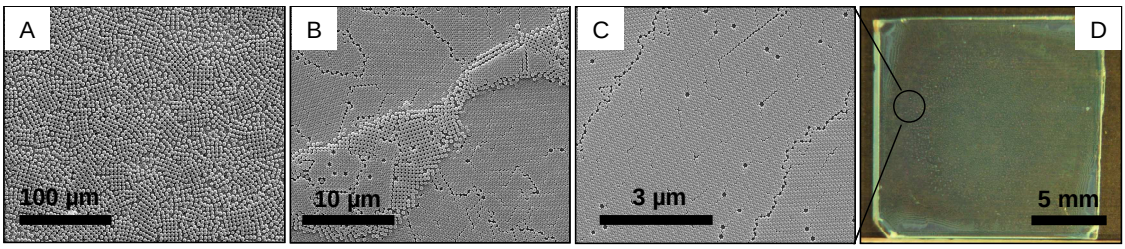

Figure 5.2.6 SEM images of polystyrene spheres patterns obtained by spin coating method at 1,000 (A), 2,000 (B) and 3,000 rpm (C) and digital image of the substrate covered by uniform polystyrene spheres monolayer

SEM microscopy performed in the middle section of the substrate revealed that the deposited material formed monolayers composed of domains of 100 μm^2 with a high degree of crystallinity (Figure 5.2.5 C). However, at the outer edges of the wafer the build-up of spheres led to the formation of multilayers at the corners and edges of the substrate (see Figure 5.2.7 C-D). The edge bead effect is likely due to the properties of the colloid, which is coating the wafer and the substrate geometry. Surface tension dictated a contact angle at the solid-liquid-gas interface and prevented the flow of the fluid outward form the edge of the wafer. Moreover, during the spin coating of square substrates, the higher air flow and an increased evaporation rate at the corners of the wafer resulted in a preferential flow over the dry layer of polystyrene beads resulting in more corner material [307, 308]. However, these defects only occurred over a small edge area and large domains of usable monolayers covered most of the sample.

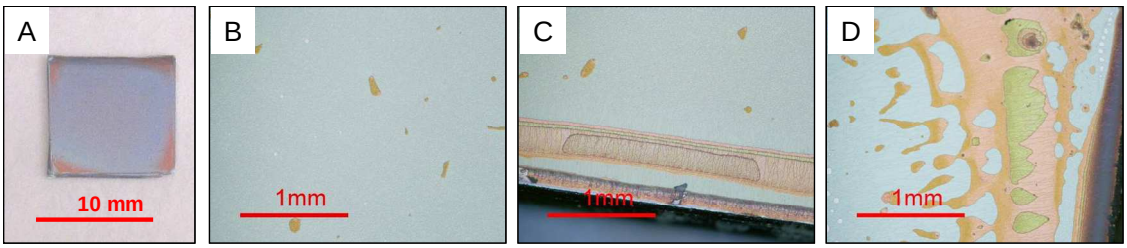

Figure 5.2.7 A digital image of 1 cm^2 silicon wafer piece covered by polystyrene beads (A) and digital optical microscope images of polystyrene beads assembly in the middle part of the sample (B) at the sample edge (C) and the corner (D). Hexagonally closed packed monolayer of 400 nm polystyrene beads on Si wafer appeared in bright blue color in reflected light optical microscopy under white light illumination. Darker areas in the images indicate multilayers.

5.2.2 Annealed and etched polystyrene masks

The samples with monolayers of polystyrene particles in the middle were then exposed to thermal annealing or a reactive ion Ar/O_2 plasma mixture in order etch the mask; initially the treatment was designed to simply widen the area between the spheres so as to make a continuous film after metal deposition. Thermal annealing at 105^{o}C of polystyrene spheres monolayer reduced apertures between the beads as presented in Figure 5.2.8. Upon heating, spaces between spheres got smaller and finally formed a continuous set of windows [276, 309] . It was possible to control the aperture size by choosing the appropriate temperature and time of annealing (see Figure 5.2.8). Unfortunately, the width of the cracks in close-packed monolayers increased with annealing time as well, which can be observed in Figure 5.2.8 D-F [309].

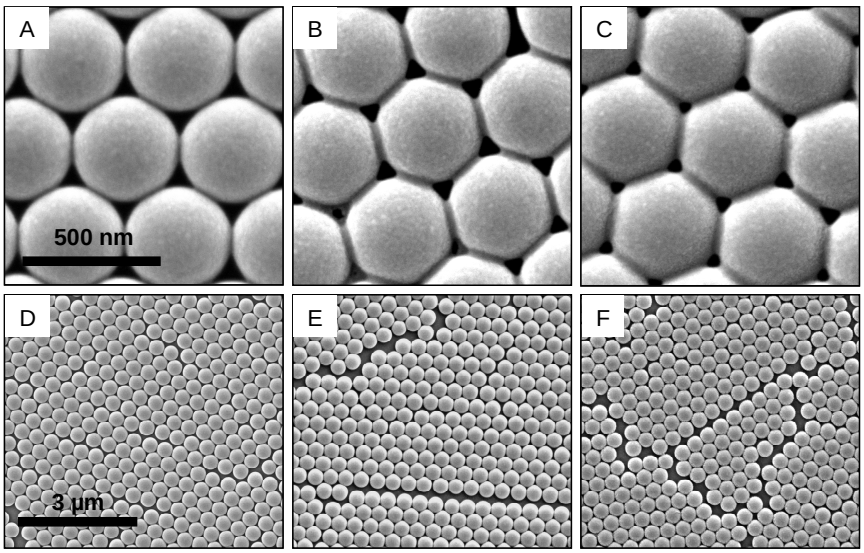

Figure 5.2.8 SEM images of PS 400 nm masks on Si surface before annealing (A, D) and annealed at 105˚C for 30 min (B, E) and 60 min (C, F). Note that cracks present in the crystals before annealing, become larger after sample annealing.

As an alternative, we also pursued etching as a means to widen the mask apertures. In this treatment the array monolayers were exposed to reactive argon and oxygen gases and as a result the aperture sizes increased. The mean particle sizes derived from the SEM images before the etching were 376 ± 11 and 234 ± 5 nm. Reduction of sphere diameter by RIE in a mixture of argon and oxygen gases, within the period of 0 – 60 sec shrunk the diameters of these particles linearly with etching time to 134 ± 5 nm and 217 ± 9 nm, respectively (see Figure 5.2.9). After Ar/O_2 plasma etching the polystyrene bead morphology changed as well forming what resembles a dome or collapsed sphere. As the sizes of the domes decreased, the space between them increased, yet the position remained the same after plasma treatment. Beyond a one minute etch, the surface of the domes changed from smooth to rough. Further plasma processing led to nearly complete removal of the colloids.

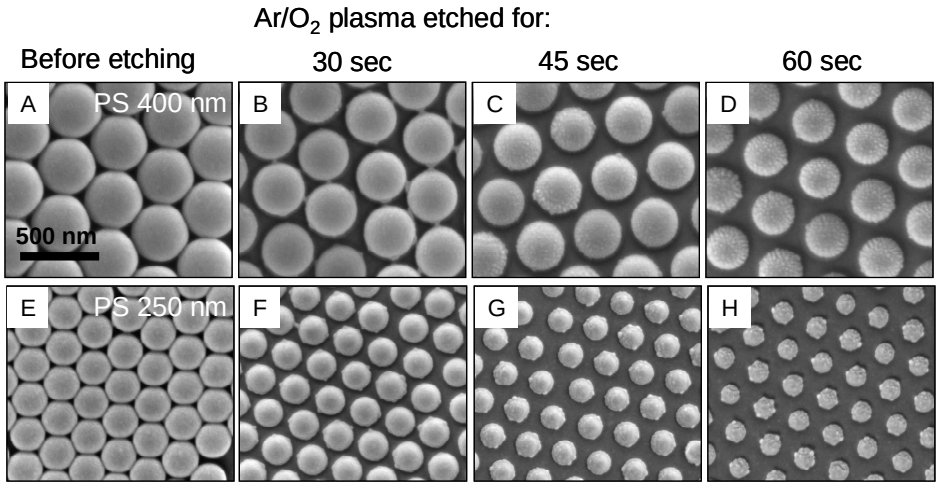

Figure 5.2.9 SEM Images of the polystyrene spheres 400 nm (A-D) and 250 nm (E-H) before (A, E) and after Ar/O_2 plasma etched for 30 sec (B, F), 45 sec (C, G) and 60 sec (D, H)

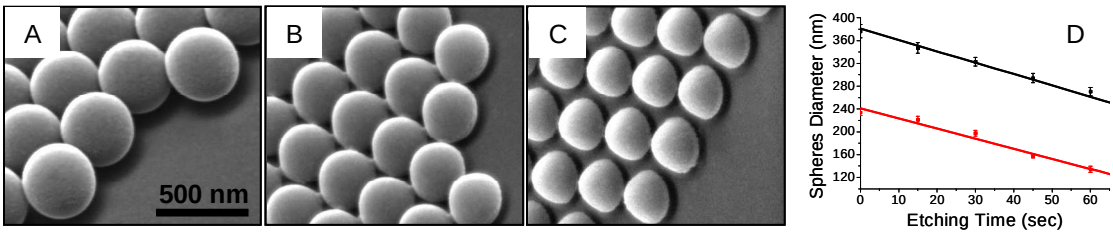

Figure 5.2.10 SEM 45 deg view images of untreated, closely packed polystyrene monolayer (A); 15 sec (B) and 30 sec (C) Ar/O_2 plasma treated monolayer; the dependence of the polystyrene diameter on the Ar/O_2 plasma treatment time for 400 (black line) and 250 nm (red line) polystyrene spheres suspensions purchased from Bangs Laboratories (D); as the plasma treatment time is increased, the diameter of the polystyrene dome decrease linearly. For sizing, the outer diameters of the population of one hundred features were manually measured using Image-Pro Plus 5.0 (Media Cybernetics Inc.).

Moreover, scattered and diffused argon and oxygen ions reached the region shadowed by the domes, attacked the wafer surface and produced a mushroom structure with a gap surrounding the point of contact between the collapsed sphere and the substrate surfaces as it can be observed in 5.2.11 [275].

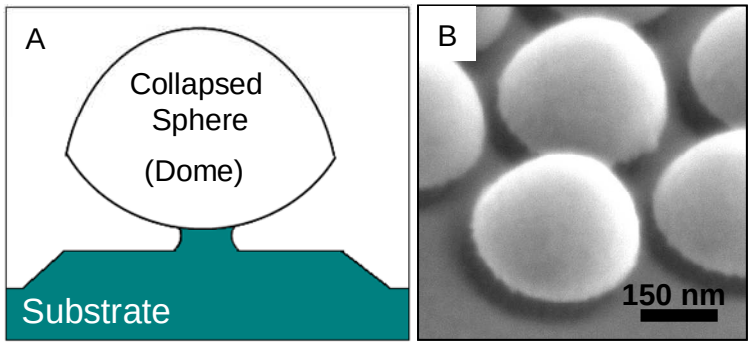

Figure 5.2.11 Schematic side view of the mushroom structure (A) and SEM images obtained at tilt angle of 45 deg of the collapsed spheres formed after 30 sec Ar/O_2 plasma etching of 400 nm polystyrene beads (B)

In addition to material removal apparent in the electron microscopy images, we also found that the etch resulted in chemical changes to the polystyrene itself. Several different methods indicated that the argon/oxygen plasma caused surface oxidation, crosslinking and formation of hydrogenated amorphous carbon [310, 311]. These chemical changes could be correlated with Ar/O_2 plasma power and exposure duration.

In summary, a solution of polystyrene spheres could be assembled into a close packed array by spin coating onto substrates. In the present work, both thermal annealing and Ar/O_2 reactive ion etching were used to widen the apertures between the spheres. Annealing at $105^{o}C$ increased the interstitial voids between the close-packed spheres as expected. The reactive etching also increased aperture sizes, but led to other unanticipated changes to the spheres. The RIE effectively 'shaped' the polystyrene both reducing its diameter and converting the sphere to a mushroom like structure. Chemically the polystyrene also became more oxidized as the RIE effectively made the polymer

matrix more dense. These arrays at various stages of modification were subsequently used as templates for metal deposition as described in the next section.

5.2.3 Structures fabricated by sputtering and electron beam evaporation

Metal deposition through unshaped polystyrene sphere mask

The shapes of metal nanostructures produced by conventional nanosphere lithography, which takes the polystyrene arrays and uses them as masks for metal deposition through sputtering or evaporation were limited to mesh-like structures and triangles [312, 313]. During the sputter deposition, material is ejected from a source by ion or atom bombardment, which is then deposited onto a substrate through the triangular gaps between the hexagonally closed-packed spheres. When 40 nm of gold is sputtered through this single layer of unmodified polystyrene beads, the result is an array of metal nanostructures (Figures 5.2.12 A-C). During sputter deposition, metal atoms undergoing secondary collisions before deposition or, alternatively, metal atoms impacting the surface obliquely can lead to film formation under surface features [312, 313].

In the electron beam evaporation (EBE) process, a block of the material (source) to be deposited was heated by an electron beam to the point where it started to boil and evaporate. The shadowed areas of the substrate blocked by polystyrene spheres were not accessible for gold deposited through electron beam evaporation process because the evaporated material approached the substrate from a single direction perpendicular to the substrate surface. As a consequence more defined triangle-shaped nanoparticles were fabricated by evaporation (Figures 5.2.12 D-F).

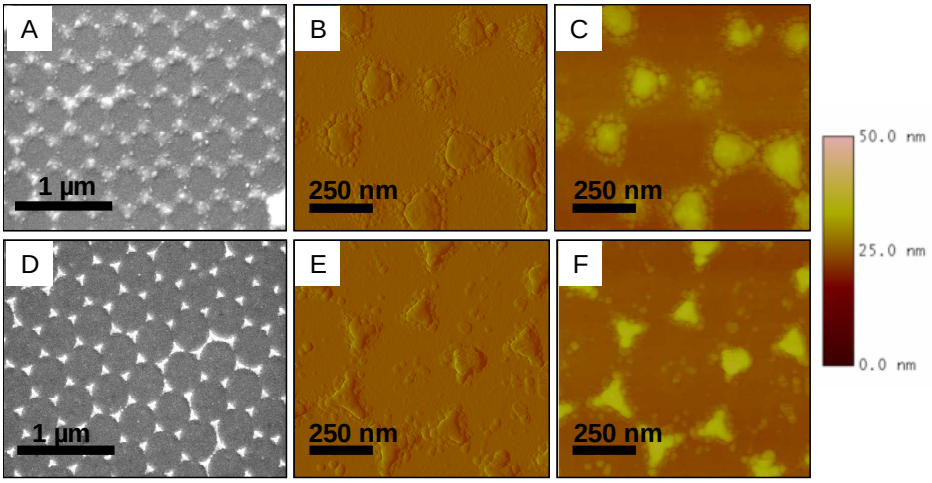

Figure 5.2.12 SEM micrographs (A, D) and AFM amplitude (B, E) and height (C, F) images showing the difference in shape of nanostructures fabricated by sputtering (A-C) and evaporation of 40 nm of gold through 400 nm unmodified polystyrene spheres monolayer

Using double layers of polystyrene spheres, periodic spherical particles were achieved as presented in Figure 5.2.13. We formed double-layer polystyrene sphere masks by spin coating and adjusting the spin speed to 1500 rpm (Figures 5.2.6 A, B). The size and interparticle distance between gold nanoparticles fabricated by nanosphere lithography with single and double layers of unmodified polystyrene spheres could be tuned by using colloids of different diameters. The height of these features could be adjusted by depositing metal to a desired thickness. All presented nanoparticle arrays present excellent ordering and uniformity.

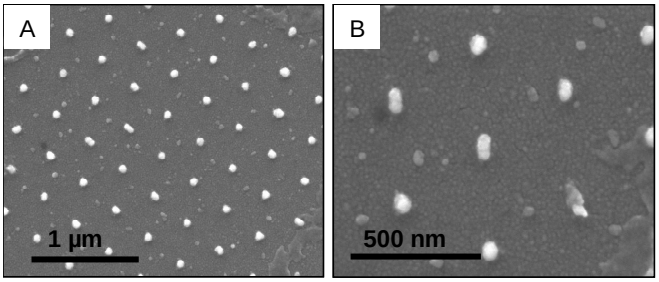

Figures 5.2.13 SEM images obtained at 50,000x (A) and 120,000x (B) magnification levels of gold nanoparticle array formed using a double-layer mask of 400 nm PS.

Metal deposition through shaped nanosphere masks

In nanosphere lithography, the spacing in the polystyrene template tuned either by annealing or etching defines metal nanostructures. First, we compared nanoparticle arrays fabricated by depositing 40 nm Au through unmodified and annealed colloidal masks. Samples consisting of mesh-like structures and triangular nanoparticles on silicon substrates are presented on Figures 5.2.14 A and D. These patterns were fabricated by sputtering (Figure 5.2.14 A-C) and evaporating (Figure 5.2.14 D-F) metal through unmodified 400 nm polystyrene spheres. The use of an annealed mask transformed sputtered mesh-like pattern to triangle shape (Figures 5.2.14 A-C) and evaporated triangular nanoparticles to spherical particles (Figures 5.2.14 D-F). The colloidal mask annealed for 60 min at 105^{o}C formed smaller nanostructures as compared to mask annealed for 30 min due to reduction of mask apertures as described in previous section. Colloidal lithography combined with thermal annealing allows for some control over the nanostructure dimensions. However, rings and crescents were not readily formed.

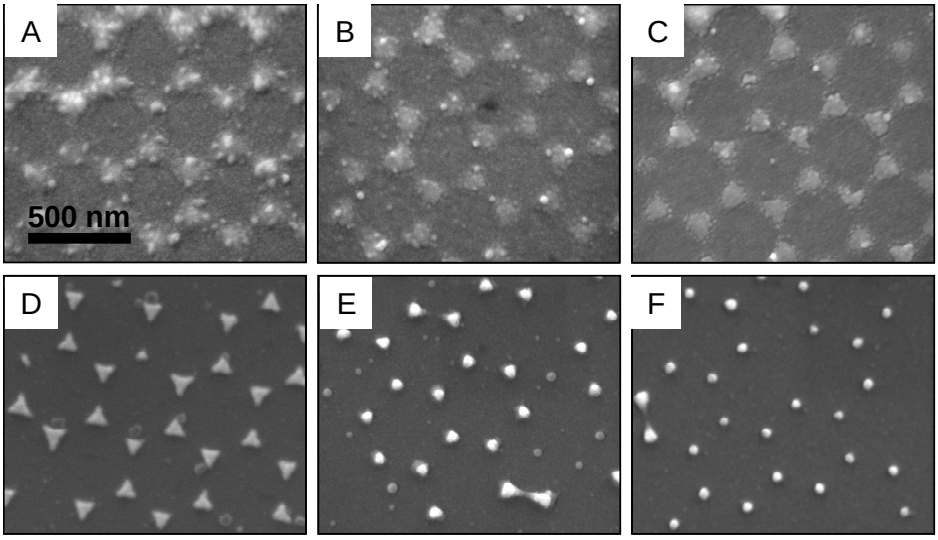

Figure 5.2.14 SEM images of periodic gold nanoparticles arrays formed by sputtering (A-C) and evaporation (D-E) of 40 nm of gold through unmodified masks of 400 nm PS (A-D) and masks annealed for 30 min (B, E) and 60 min (C, F) at 105^{o}C

We observed also that post treatment in form of thermal annealing of triangular nanoparticles resulted in formation of round shape nanoparticles [314]. Gold nanotriangles from Figure 5.2.14 C were annealed at 270ºC for 8 hours in the oven. The transition from triangles to round geometries upon annealing could be observed in Figure 5.2.15 A. The mechanism for the morphology evolution was explained by Sun et al. in [314] as a heating and sintering of ultra-fine gold grains that are deposited on the substrate and form as-prepared triangular nanoparticles. Further heating of the compact grains made the spherical shape due to surface atomic diffusion.

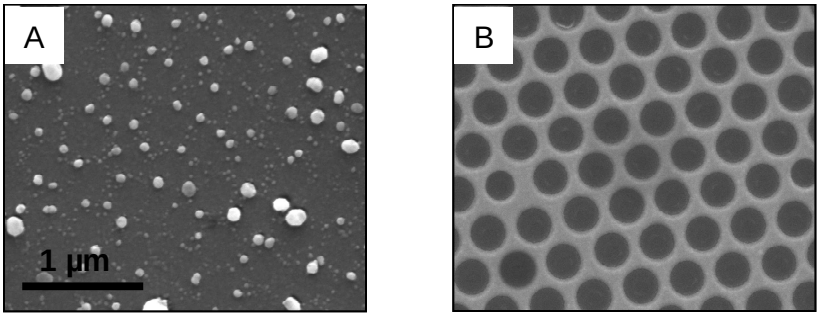

Figure 5.2.15 SEM images of arrays of (A) round nanoparticles with no pattern and (B) nanoholes

When a single layer of polystyrene spheres was Ar/O_2 etched followed by gold deposition onto what was left of the polystyrene spheres, a continuous film of gold formed everywhere except on the collapsed spheres. Metallic nanoholes array was revealed on the substrate after spheres removal (see Figure 5.2.15 B). As discussed earlier, when metal was sputtered the atoms impact the surface with many angles; additionally, the atoms were often moving fast enough to undergo significant secondary scattering off the substrate. For these reasons, sputtering was known to less faithfully reproduce the clean edges of masks because it could build up material under features [312, 313]. In this application, the consequences of non-directional deposition are smaller diameters of nanoholes as compared to sizes of holes fabricated by evaporation.

Summarizing, annealing and RIE were chosen to perform polystyrene sphere mask modifications. Evaporation and sputtering were metal deposition methods. Patterns fabricated by sputtering through PS monolayer had mesh-like structures. Triangles were obtained by evaporation through unshaped mask. Nanostructures manufactured by using an annealed mask had spherical shapes. RIE treatment of PS monolayers led to uniform periodic nanoholes. Such nanosphere lithography methods for fabricating nanotriangles,

spherical nanoparticles and nanoholes arrays are well known [269, 275, 276, 315-317]. A more novel approach to the fabrication of nanostructures arrays by nanosphere lithography requires adding a simple step after the metal deposition as will be shown in the next section. With this addition, nanorings and nanocrescents arrays can be fabricated with simple, economical and rapid methods.

5.2.4 Nanorings and nanocrescents formation

The shaped nanosphere approach to forming nanorings and nanocrescents is presented in Figure 5.2.16. First a close-packed array of uniform polystyrene spheres was formed on a silicon wafer via spin-coating. Then, an argon/oxygen reactive ion etch (RIE) was employed to alter the sphere's shapes and diameters. The etch environment resulted in the collapse of the polystyrene spheres due to chemical oxidation, and their physical conversion into mushroom-like structures. Twenty or forty nanometers of metal were then deposited, either through electron beam evaporation (EBE) or sputtering, onto the array of collapsed mushroom-like spheres. A second argon plasma etch removed all metal except that which was protected under the lips of the mushroom features. What remained of the original polystyrene was then removed by adhesive tape leaving behind metal rings or crescents.

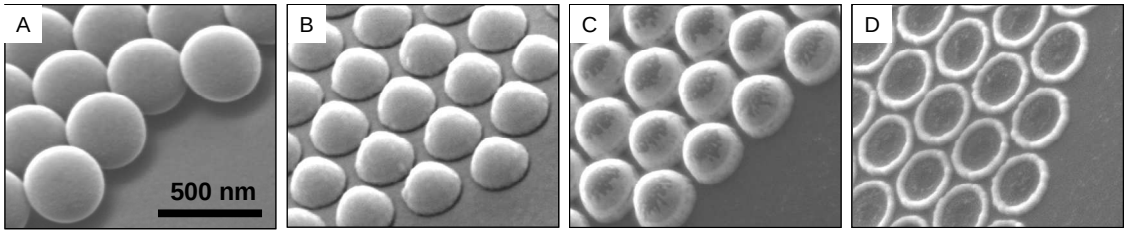

Figure 5.2.16 SEM images obtained at tilt angle of 45 deg showing schematic flow of the fabrication of an array of gold nanorings. (A) is the SEM image of a close-packed polystyrene beads monolayer, (B) covered by sputter deposited metal (Cr 4 nm /Au 40 nm) collapsed spheres, which were formed by Ar/O_2 plasma etching of polystyrene beads, (C) sample after argon plasma etching, (D) the nanorings achieved after polystyrene spheres removal using an adhesive tape.

The second etch in this process uses only argon and thus removes metallic material physically through the collision with incident ions [318]. The forty nanometers of gold located between the mushroom structures was completely removed after only two minutes of treatment (Figure 5.2.16 C). During this etch, redeposition of nonvolatile etch products such as metallic gold is known to occur, and this may have added additional material to the protected area under the collapsed spheres [198, 318]. Subsequent removal of the spheres with tape revealed the metallic residue left behind under the collapsed spheres; its outer diameter matched well to the outer diameter of the spheres but its inner diameter was substantially smaller (see Figure 5.2.17). This latter observation illustrates directly that sputtered metal can be deposited under the collapsed spheres, resulting in feature sizes smaller than the original mask size.

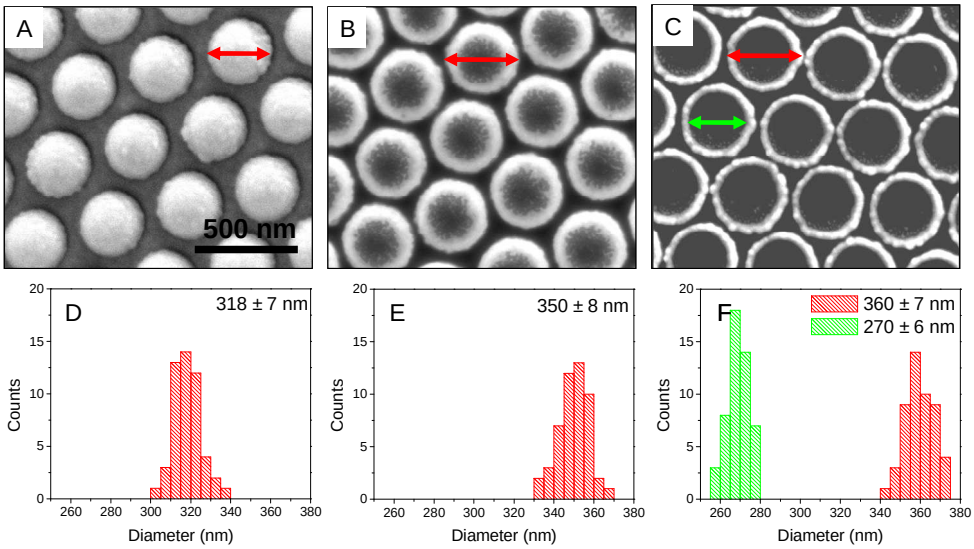

Figure 5.2.17 SEM images and corresponding structure size distribution histograms of collapsed spheres covered with sputter deposited gold film of thickness 40 nm (A and D), sample after 120 sec argon plasma etching (B and E) and the gold nanorings achieved after removal of the spheres by using an adhesive tape (C and F)

Because organic residue may also form in this process, EDS elemental mapping was employed to confirm that the nanostructures were gold as expected (see Figure 5.2.18).

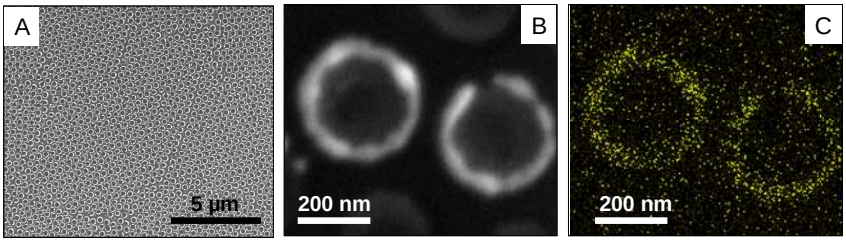

Figure 5.2.18 SEM (A, B) and EDS (C) images of gold nanorings array fabricated by sputter depositing of 20 nm gold film onto a monolayer of collapsed spheres with a diameter of 220 nm and argon plasma etching for 60 sec

One distinct advantage of this methodology for nanoring formation is that it can rapidly produce centimeters of coated substrate; these large sample areas, however, can contain both nanorings and nanocrescents (Figure 5.2.19). SEM images collected from ten to a hundred micron areas revealed nanostructures uniform in size and shape. However, over millimeters variations in the nanostructure form became apparent: in particular, most samples had both nanorings and nanocrescents (Figure 5.2.19 A-C).

The origin of this variation was elusive, and was unrelated to process parameters including sample position in the RIE chamber, reactor configuration, and RIE power and pressure. However, for some nanosphere coated substrates only nanocrescents would form. We reasoned that in these instances the etching processes could have been impacted by the thick nanosphere multilayers at the sample edges (see Figure 5.2.7). These insulating areas could build up charge during the reactive etching, a phenomena that can produce local electric fields which deflect ion and electron trajectories [319-321].

In order to uniformly produce crescent or ring structures, it was vital to cover the substrate edges with a solid mask as schematically presented in Figure 5.1.2. When applied to one side a mask created a preferential direction for reactive ion flow and nanocrescents were the result (Figures 5.2.19 D-F).; when used on opposite sides, there was a more uniform deposition of rings (Figures 5.2.19 G-I) To deflect the ions, and create an anisotropic etch, the sample configuration in the reactive etch step was altered by the addition of a solid mask on one side of the sample (Figure 5.1.2 B) [322]. As anticipated, this mask yielded uniform nanocrescents over a sample area of 0.7 cm^2 (Figures 5.2.19 D-F); the crescent gaps faced away from the solid mask edge. When the solid masks were applied on opposite edges of the sample, nanorings would form in the

center of the substrate. Areas close to one or the other mask did form crescents, but nanorings exclusively formed in the middle over about 0.4 cm^2 (Figures 5.2.19 G-I). These observations suggest that the solid masks build up net charges that change the directionality of the ions in the etch plasma; such a phenomenon has been observed in other studies of reactive etching processes [320, 322, 323].

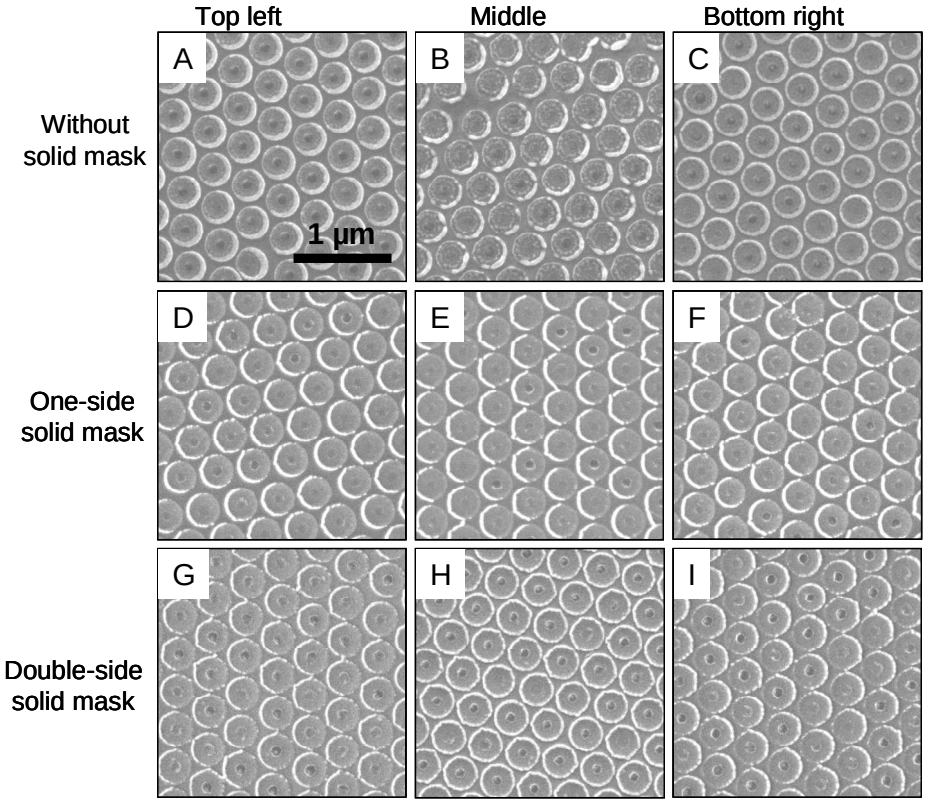

Figure 5.2.19 SEM images presenting uniformity of the samples fabricated by depositing gold film of thickness 40 nm onto a monolayer of the collapsed spheres followed by argon plasma etching without the solid mask (A-B), in a presence of one-side solid mask (D-E) and double-side solid mask (G-I). SEM analysis was carried out at the top left part (A, D, G), in the middle (B, E, H) and at the bottom right part of the sample (C, F, I).

5.2.5 Control over nanorings and nanocrescents features

Outer diameter

With the solid masks, shaped nanosphere lithography approach offers a means to dictate the nanostructure form: from rings to crescents. It also permits control over critical features such as the outer diameter, wall thickness, feature height and, where relevant, the crescent gap size (Figure 5.2.20). The diameter of the polystyrene spheres precisely fixed the outer diameter of both the nanorings and nanocrescents. Figures 5.2.20 A and 5.2.20 B present different nanorings fabricated using 400 nm and 250 nm polystyrene spheres altered to sizes of 300 and 200 nm, respectively.

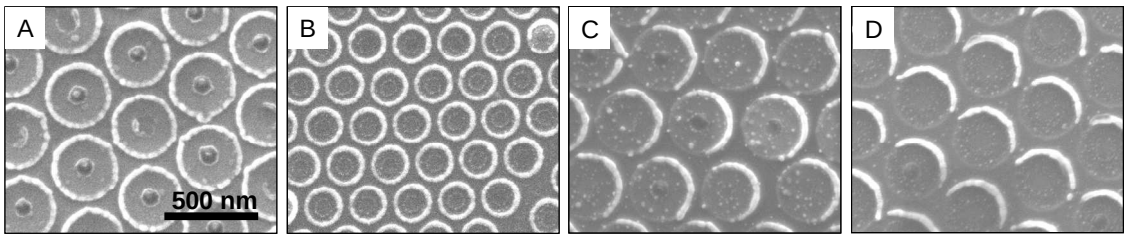

Figure 5.2.20 The dependence of nanostructures dimensions on polystyrene spheres diameters (A and B) and the solid mask thickness (C and D). The nanostructures were fabricated by evaporating a metal film onto a monolayer of collapsed spheres followed by argon plasma etching. The nanorings were achieved using the collapsed spheres with the diameters of 300 nm (A) and 200 nm (B). Nanocrescents with gap openings of 160^{o} (C) and 210^{o} (D) were fabricated using the collapsed spheres with the diameters of about 300 nm and a solid mask of silicon wafer with thickness of 380 µm and two microscope glass slides stuck together with thickness of 2 mm, respectively.

Currently, the dimensions of commercially available polystyrene spheres range from 27 nm to 25 µm [324]. If assembled on silicon substrate and treated as described, such materials should allow for the fabrication of nanorings and nanocrescents well under 50 nm in diameter. One challenge in working with smaller nanospheres is the difficulty with and sphere removal. After depositing 40 nm of gold onto an array of polystyrene particles altered to size of 200 nm, the spheres could not be easily removed after the argon plasma etch (Figure 5.2.21). We speculate that the gold built up underneath the spheres and served to adhere them tightly to the substrate. Other methods of polystyrene sphere removal, such as pure oxygen etching or organic dissolution, could be used to overcome this limitation.

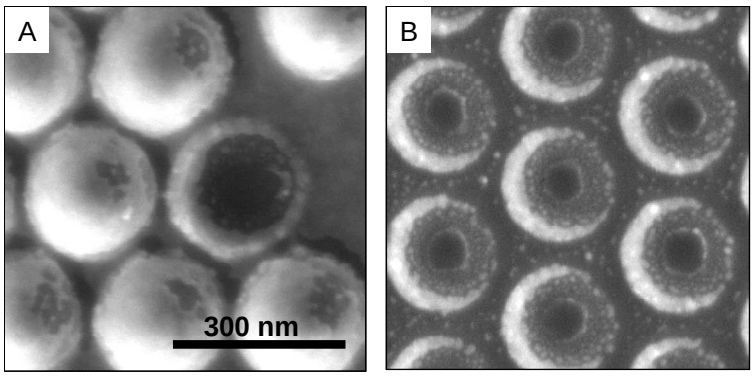

Figure 5.2.21 SEM images of the nanostructures fabricated by sputter depositing of 40 nm (A) and 20 nm (B) gold films onto collapsed spheres with a diameter of 200 nm

Height

While the outer diameter of the nanorings and nanocrescents depended on the diameter of the polystyrene spheres, their height was sensitive to the amount of metal deposited. AFM imaging results showed that nanorings and nanocrescents obtained from

sputtering 40 nm of gold onto a monolayer of collapsed spheres (d = 300 nm) resulted in a maximum feature height of about 50 nm and 60 nm, respectively (Figure 5.2.22). The fact that the height of the features is larger than the thickness of metal deposited on free substrate is further evidence that metal redeposition is responsible for the build-up of material under the collapsed spheres.

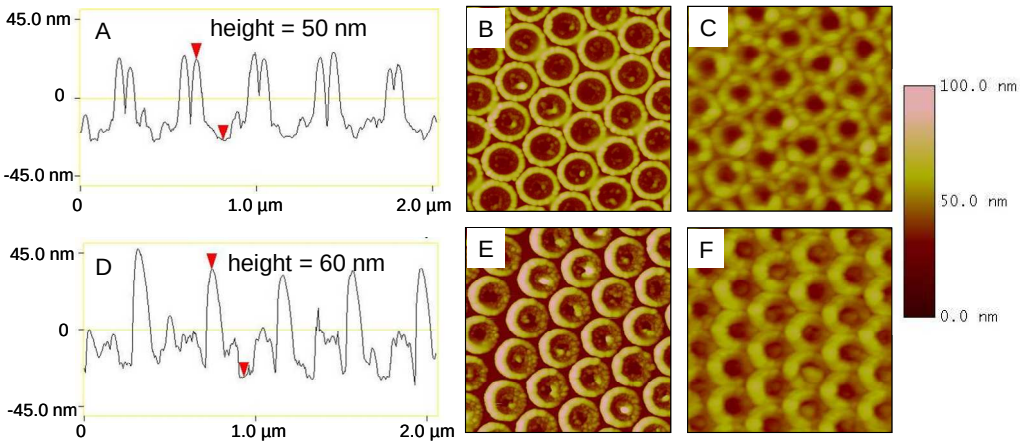

Figure 5.2.22 AFM analysis of the nanorings and the nanocrescent, showing section (A) and height (B) of the nanorings fabricated by sputter depositing 40 nm of gold followed by 120 sec argon plasma etching; height (C) of the nanorings fabricated by sputter depositing 20 nm of gold followed by 60 sec argon plasma etching; section (D) and height (E) of the nanocrescents fabricated by sputter depositing 40 nm of gold followed by 150 sec argon plasma etching and height (F) of the nanocrescents fabricated by sputter depositing 20 nm of gold and 90 sec argon plasma etching. Collapsed spheres with a diameter of 300 nm was used to fabricate these nanostructures

Inner diameter

The inner diameter was most sensitive to the process by which metal was deposited. When sputtering was used to deposit metal the subsequent ring structures were thicker with much smaller inner diameters (typically 15% less) than the collapsed sphere dimensions (Figure 5.2.23). Evaporation yielded thinner rings.

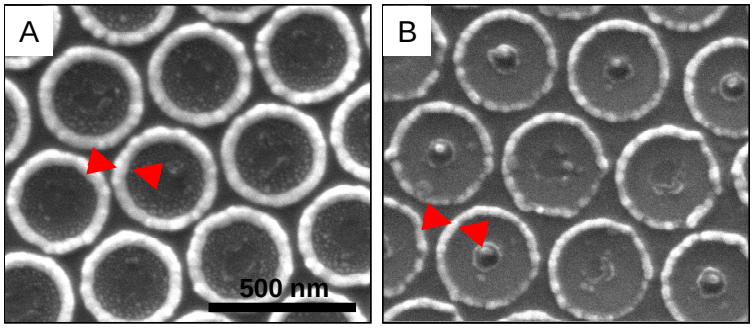

Figure 5.2.23 SEM images of nanorings produced by sputter depositing (A) and evaporating (B) of 40 nm gold film onto a monolayer of collapsed spheres with a diameter of 300 nm. Sputtering made smaller inner diameters and in consequence wider structures then evaporation.

Nanocrescent gap opening

The nanocrescent gap opening was best tuned through adjustments to the solid mask thickness as well as the argon plasma etching time. Figures 5.2.20 C and D present nanocrescents with gap openings of 160^{o} and 210^{o} fabricated using a solid mask of 380 µm silicon wafer and 2 mm of two glass slides respectively. The thicker glass will build up more charge, and lead to more distortion of the ion trajectories resulting in a more pronounced asymmetry to the crescents [322]. This local electric field was large enough

to perturb ion trajectories and affect the etch profiles of nanostructures patterned over a surface area of 1 cm^2 (see Figures 5.2.20 C and D). Also, since the crescents were thinnest near their gap opening, longer argon plasma etching times generally widened the gaps (see Figure 5.2.24). By adjusting the etching time and increasing the solid mask thickness, the bending of argon ion trajectories increased, which resulted in wider gap opening of the nanocrescents.

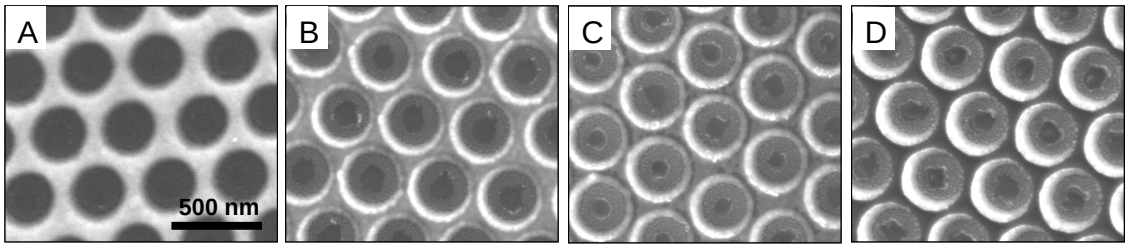

Figure 5.2.24 SEM images of the nanostructures fabricated by sputtering gold film of 40 nm onto a monolayer of collapsed spheres with diameter of 300 nm (A) and etching with argon plasma for 90 sec (B), 120 sec (C) and 150 sec (D)

5.2.6 Optical properties of nanorings and nanocrescents

Experiments

Both metallic nanocrescents and nanorings have been described as optical metamaterials [242, 325]; by virtue of their shape, they possess strongly resonant modes that can be used to manipulate light. The optical properties of nanocrescents and nanorings arrays presented in Figure 5.2.25 were analyzed by using IR microscopy, FTIR and UV-VIS-NIR spectroscopy. Figures 5.2.26 A-C show the extinction spectra of both crescent and ring nanostructures.

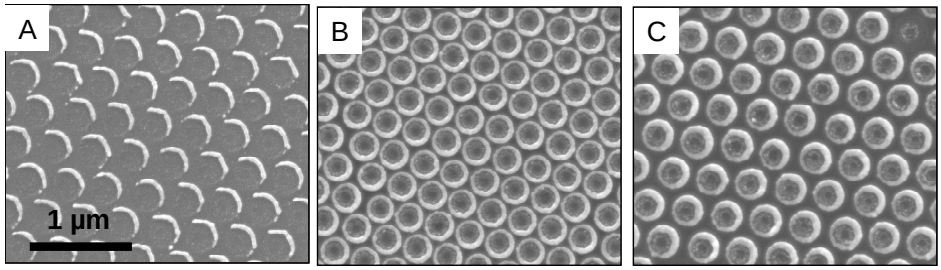

Figure 5.2.25 SEM images of the nanostructures with geometrical parameters as follows: (A) $\alpha = 206 \pm 10^{o}$, $d = 324 \pm 9$ nm, $w = 41 \pm 5$ nm; (B) $d_o = 351 \pm 7$ nm, $d_i = 246 \pm 8$ nm; (C) $d_o = 308 \pm 7$ nm, $d_i = 201 \pm 9$ nm. The geometrical parameters of one hundred nanostructures were manually measured from SEM images to determine the size distribution. The height investigated with AFM was about 40 nm or all presented nanostructures.

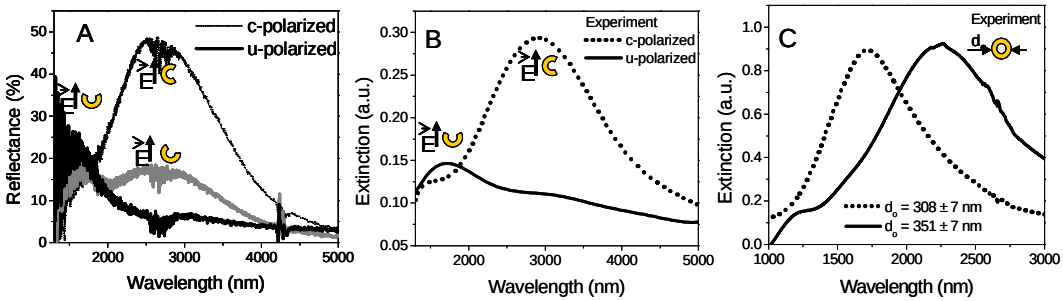

Figure 5.2.26 Experimental measurements performed by using FTIR microscopy (A) and FTIR spectroscopy (B) for nanocrescents array for c-polarized (dotted line) and u-polarized (solid line) beam and measured UV-VIS-NIR extinction spectra of nanorings arrays. SEM images of analyzed nanostructures arrays were presented in Figure 5.2.25.

The polarization dependent optical properties of the nanocrescents compare well with other studies [198, 215, 221, 222, 326, 327]. The nanocrescents show resonances

sensitive to the orientation of the crescents relative to polarization of the incident light beam. These data were collected using a FTIR microscope and spectrometer with a linearly polarized incident beams, normal to the surface of the samples. As shown in Figures 5.2.26 A and B, in the case of polarization parallel to the y-axis (of Figure 5.1.3) termed as c-polarized light, fundamental plasmon mode (c1) at 2925 nm was visible. This resonance disappeared for u-polarized light (polarization parallel to the x-axis of Figure 5.1.3) and a new plasmon resonance at 1695 nm was excited (u1).

The origin of c1 and u1 resonances in gold nanostructures of crescent shape could be understood if the crescent is considered as a bent rod [215, 222, 326]. Then, the resonances can be interpreted as waves which propagate along the rod, reflect at the tips and form standing wave modes. A resonance occurs whenever the resonance condition $n\lambda/2=L$ is fulfilled, n being the order of the resonance, λ the wavelength of the mode and L the length of the metal structure, which in case of crescent structure is $L = d/2(360^{o}–\alpha)$ where d represents the diameter of the collapsed sphere and $(360^{o}–\alpha)$ is the parameter describing the length of a metal structure. In the spectral range of 1300 – 5000 nm and for the crescent with a gap opening of 210^{o} between the two tips we observed the first two resonances (c1 and u1) at 2925 nm and 1695 nm.

It has been reported that when the bending gets stronger and the gap opening decreases to the point where a nanoring is formed, only one characteristic resonance peak for each polarization is found [197, 198, 215]. For this work, a UV-VIS-NIR spectrophotometer with unpolarized light was used to characterize the optical properties of nanoring arrays with feature diameters 351 nm, and 308 nm. The nanorings exhibited infrared resonances with a peak position sensitive to the ring diameter. A red-shift of 45

nm was observed by increasing the outer diameter from 308 nm to 351 nm (see Figure 2.2.26 B). This trend has been observed in other cases where the resonance was found to red-shift as the overall diameter of the ring increased [198, 327].

Simulations

An important feature for applications of metamaterials is the prediction of the resonant peak positions in the extinction spectrum. To examine this issue, we collaborated with Yang Li in Dr. Nodlander's group to simulate the optical response for nanorings and nanocrescents of dimensions presented in Figure 5.2.25 using a finite-difference time-domain (FDTD) method. The peak positions for simulated spectra, were in good agreement with experimental data. The line broadening in experimental spectra (Figure 5.2.26) as compared to simulated results (Figure 5.2.27) was attributed to the size distribution of the nanostructures and other sample imperfections resulted from its fabrication, for example formation of polystyrene spheres multilayers during spin coating process. Further improvement in sample uniformity and processing should result in less variation in nanostructure inner and outer diameter.

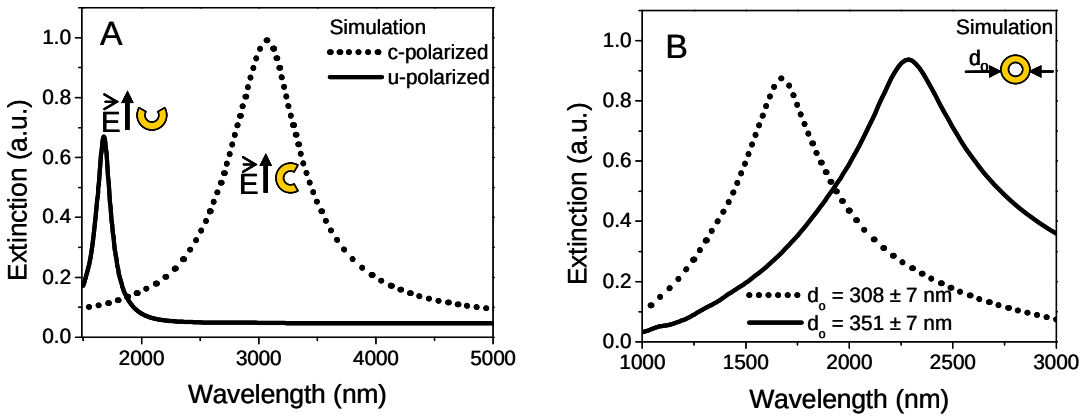

Figure 5.2.27 Numerical simulations for nanocrescents (A) and nanorings (B) arrays which were obtained using the actual parameters of the fabricated nanostructures presented in Figure 5.2.25

Additionally, we simulated influence of the crescent gap size ‘α’ (Figure 5.2.28) and the diameter ‘d’ (Figure 5.2.29) on the extinction resonances for polarization parallel to the crescent gap. The wavelength of fundamental plasmon mode (c1) shifted upon a change of nanocrescent gap opening and diameter.

The position of the c1 resonance red shifted from 3533 nm to 5145 nm with a decrease in the nanocrescent gap opening from 208^{o} to 148^{o}. Moreover, for nanocrescents with α smaller than 198^{o} the higher-order resonance c2 could be observed in analyzed spectral range [215, 222]. Its position was red shifted by 11 % and intensity increased eight times when the nanocrescent gap opening changed from 188^{o} to 148^{o}.

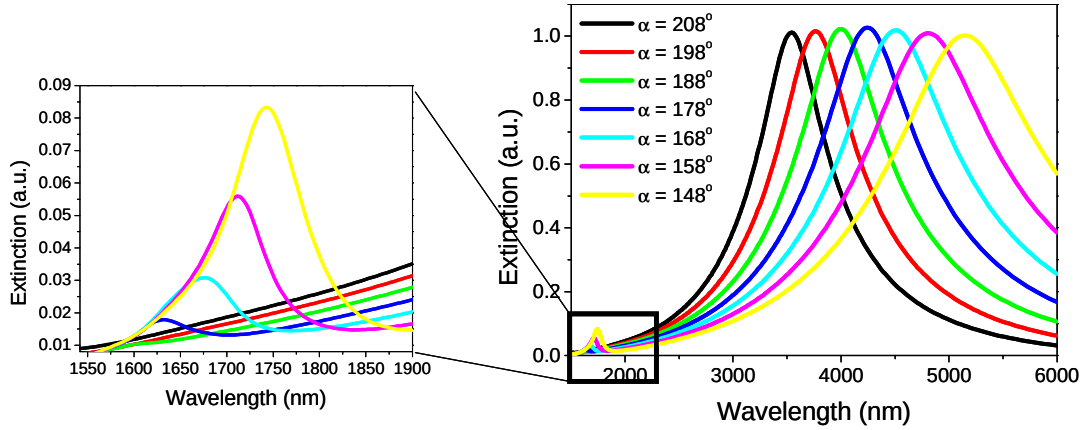

Figure 5.2.28 Gap opening (α) dependent excitation spectra of gold nanocrescents with geometrical parameters: d = 333 nm; w = 46 nm; h = 35 nm

To understand the first order mode resonance frequency, an electrical engineering model of $\omega = 1/(LC)^{1/2}$ can be used [222, 326, 327]. If the crescent is considered as a LC circuit, then the two plates of a capacitor are represented by the two tips of the rod forming a parallel capacitor with capacitance C and the rod forms a coil with inductance L. When the crescent gap opening decreases, according to the equation $C = \varepsilon A/d$, where ε is a relative permeability**,** A is the area of the plates and d is the distance of the plates, the capacitance increases and therefore also the frequency decreases.

Figure 5.2.29 confirmed that for nanocrescents with decreased length of a metal structure (d = 50 nm) and a gap opening of 158° resonance c1 blue shifted to λ = 2136 nm, as compared to λ = 4803 nm for d = 333 nm (see Figure 5.2.28). Resonance c2 blue shifted as well with decreasing crescent diameter [215]. By adjusting the geometries of the nanocrescents a designed electromagnetic response can be obtained. We showed that

fundamental plasmon mode of the nanocrescents with w = 46 nm and h = 35 nm could be tuned in the wavelength regime of 2136 nm and 5127 nm by adjusting crescent gap opening (208^o – 148^o) and crescent diameter (50 – 333 nm). Visible resonances in crescents of w = 46 nm and h = 35 nm may require fabrication of nanostructures with diameter d ~ 50 nm and gap opening $\alpha > 208^o$ on a glass substrate or reduction of energy loss by using silver instead of gold. Future research will examine how best to tune these features to the visible. This may require (a) a reduction in the crescent-shaped nanostructure diameter (b) an increase in the crescent gap opening or (c) fabrication of silver nanocrescents.

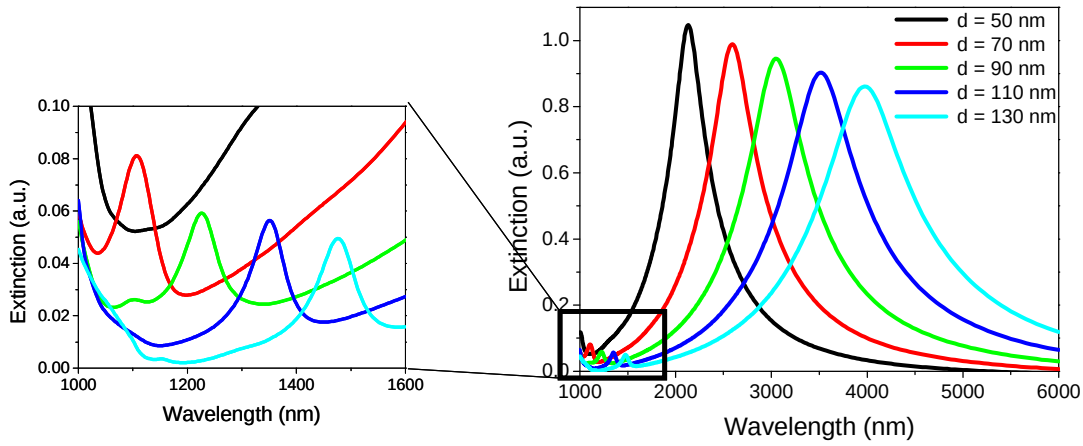

Figure 5.2.29 Diameter (d) dependent excitation spectra of gold nanocrescents with geometrical parameters: $\alpha = 158^o$; w = 46 nm; h = 35 nm

While nanorings and nanocrescents can be formed with great precision using electron beam lithography and ion beam milling, the shaped nanosphere lithography presented here is faster; this makes it possible to form optical metamaterials over sample

areas greater than one centimeter square. Among the drawbacks of ion beam milling are the high cost of the instrument and the long time required for milling the structures [328, 329]; in one study, the milling time of 10 x 5 x 3 μm rectangular area was 10 min, which means that a one centimeter square area would be complete in about 463 days [329]. Electron beam lithography is nearly ten times slower. In contrast, the time needed to remodel a nanosphere sample using argon etch is only 120 seconds. While we demonstrated one square centimeter, in principle the size of substrates is only limited by the dimensions of the RIE chamber. The Minilock-Phantom III RIE system used in this work can process one 8" wafer at a time or many smaller samples which can be etched if mounted on 8" carrier wafers. It may even be possible to apply this process to plastic substrates, as well as curved and deformable surfaces. Therefore, by varying the key parameters of the shaped nanosphere lithography fabrication process, including the mask sphere diameter, the etching time, metal deposition method, the thickness of gold film and the thickness of the solid mask we can effectively design the nanostructure. Moreover, the possibility of controlling nanostructure geometry allows for tuning their optical properties.

5.3 Conclusion

In summary, we have fabricated efficiently and characterized well-ordered arrays of metallic nanorings and nanocrescents over large areas (1 cm^2). Shaped soft lithography process uses ion trajectory distortion in plasma reactor to form crescent shape; hence it overcomes undesirable manufacturing issues such as complex tilted-rotary evaporation and time consuming ion beam milling. Obtained nanocrescents array exhibits an electric

resonance of 1.7 µm and a magnetic resonance of 3µm. Absorption resonances of fabricated nanorings depend on their diameters (d_o) and shift toward shorter wavelengths (λ = 1.7 µm for d_o = 308 nm) as compared to larger rings (λ = 2.2 µm d_o = 351 nm). Shaped soft lithography creates opportunities to generate nanorings and nanocrescents that promise potential application in chemical and biological sensing, as surface enhanced infrared absorption spectroscopy (SEIRA) and in the fields of metamaterials. Nanosphere lithography may also be altered to fabricate arrays of non-conductive elements, namely polystyrene nanodoughnuts. In the next chapter a simple, fast and inexpensive process for the fabrication of large area (1 cm^2) of polystyrene nanodoughnuts with outer diameters ranging from 128 to 242 nm will be presented.

Chapter 6 Fabrication of two-dimensional polymer nanodoughnuts by nanosphere lithography

Here a simple and inexpensive technique to prepare well ordered arrays of polystyrene nanodoughnuts over 1 cm^2 areas on a silicon substrate is presented. The process starts with the formation of a monolayer of polystyrene beads on the silicon; under the appropriate spin coating conditions these beads form close-packed arrays. The spheres are then chemically altered by an argon plasma treatment. X-ray photoelectron and Raman spectroscopy indicate that the polystyrene becomes cross-linked and ultimately graphitized in the plasma; however, the portion of the sphere that is touching the substrate is protected from this plasma treatment. After immersing and sonicating the plasma-treated polystyrene in organic solvents, what remains is a residue of cross-linked polystyrene adhered to the substrate that appears as an ordered array of non-conductive rings. We distinguish them from rings because the width of the edges is typically equal to the dimensions of the interior hole. Scanning electron and atomic force microscopy reveal that the chemical changes brought about by the plasma result in a substantial change in the volume of the spheres; the effectively deflate as the lose mass during the treatment process. The outer diameter of these nanodoughnuts is sensitive to the diameter of the polystyrene beads; smaller beads (e.g. 250 nm) allowed for smaller diameter nanodoughnuts to form (e.g. 128 nm). The width of the interior hole was generally more fixed and was best altered by changing the plasma treatment time. Such nanoscale patterns could provide templates for further deposition of optically or magnetically active nanoparticles, as well as a simple texturing strategy for modifying surface mechanical properties.

6.1 Materials and methods

6.1.1 The formation of nanodoughnuts arrays

Suspensions of polystyrene spheres (PS) with diameter of 250 nm or 400 nm were acquired from Bangs Laboratories Inc. The polystyrene dispersions were the same as those used in previous experiments for gold nanostructures arrays fabrication (see section 5.1.1). The spheres were assembled into a close-packed monolayer on a silicon wafer pre-cleaned with RCA1 solution by a spin coating method described in section 5.1.1.

The monolayer of polystyrene beads was treated with argon plasma in a Minilock-Phantom III RIE chamber from Trion Technology Inc pumped down to a pressure of 12 mTorr. An argon gas of 40 standard cubic centimeters (sccm) was utilized during the etching. Radiofrequency power of 400 W was used to generate the plasma. Treatment times ranging were explored. After plasma, which ranged from 0 to 120 seconds the sample was placed inside a 20 ml glass vial filled with 2 ml of various solvents including water (18.2 MΩ) from Millipore purification system, tetrahydrofuran (certified spectranalyzed), acetone (histological grade) and hexane (99.9 %,) from Fisher Scientific; toluene (99.7 %), chloroform (99.8 %) and methanol (99.8 %) from Alfa Aesar. Samples were exposed in these solutions for up to an hour and ultimately sonicated 5 min using Fisher Scientific batch sonicator to detach the insoluble and collapsed spheres. After sonication, the sample was rinsed with ethanol and gently dried in a flow of nitrogen gas (100.0 %, Matheson).

6.1.2 Characterization methods

Scanning electron and atomic force microscopes were used to image and characterize the polystyrene spheres before and after argon plasma etching. Scanning electron microscopy (SEM) was performed using a FEI Quanta 400 field emission scope. Samples were sputter coated with gold (~ 10 nm thick) to prevent charging effects. SEM images obtained at 50,000x magnification level were used to size the beads and nanodoughnuts. Over one hundred nanostructures were manually measured using Image-Pro Plus 5.0 (Media Cybernetics Inc.) to create histograms and generate statistics about the uniformity of the nanostructure dimensions. Arrays of polystyrene nanodoughnuts were also imaged with a Nanoscope IIIA atomic force microscope (AFM) in tapping mode; this information provided a precise measure of the height and topology of the nanostructures.

Both the chemical nature and the elemental composition of the polystyrene spheres changed as a result of the plasma treatment; the resulting materials were characterized by both X-Ray photoelectron spectroscopy (XPS) and Raman spectroscopy. The settings of a Quantera XPS scanning microprobe that was used to collect the XPS data were described in section 2.2.1 of this thesis. The binding energy in this work was obtained through a reference to the C1s line at 284.8 eV from adventitious hydrocarbon (C-H bond). Raman spectra of polystyrene beads at a variable plasma exposure times (0 to 90 seconds) were collected in collaboration with Christopher Jones using a micro-Raman spectrometer operating at a laser wavelength of 514.5 nm (Renishaw, Gluocestershire, U.K.). The number of scans and integration time were varied to ensure a sufficient signal-to-noise ratio. An optical microscope was used to focus the laser beam

and collect the scattered light. Typical spot sizes for this experiment were on the order of single square microns.

6.2 Results and discussion

Large areas (1 cm^2), of uniform arrays of polystyrene nanodoughnuts can be produced using a simple procedure based on shaped nanosphere lithography. This simple, economical and rapid method shapes nanospheres through chemical modifications introduced by plasma etching. Only the material that is in contact with the substrate is protected, and thus remains insoluble in the organic solvents and sonication used to remove the graphitized polystyrene material. The details of this treatment are outlined in the remainder of this chapter (see Figure 6.2.1).

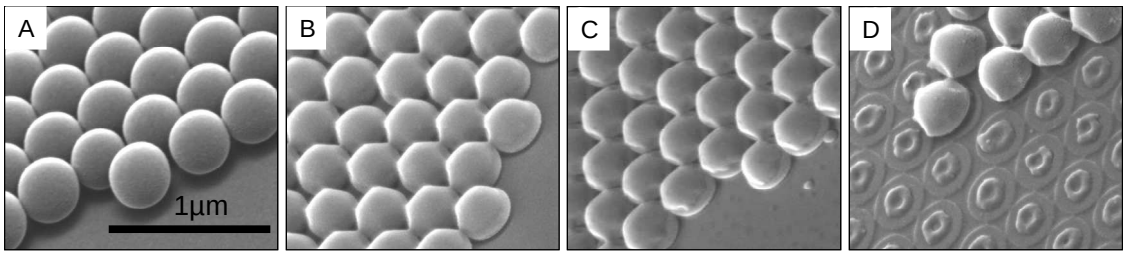

Figure 6.2.1 SEM images obtained at tilt angle of 45 degrees showing the change in morphology of polystyrene spheres after argon plasma etching. (A) SEM image of 400 nm close-packed polystyrene beads monolayer assembled on a silicon wafer, (B) polystyrene beads treated by argon plasma for 90 sec, (C) sample after immersion in tetrahydrofuran for thirty minutes and (D) the same sample after sonication for five minutes.

The production of close-packed arrays of uniform sub-micron spheres is a well established process for nanosphere lithography. Here, we generate the arrays across a centimeter square area of silicon using a spin coating methodology described in the previous sections of this thesis (see 5.1.1 and 5.2.1). The monolayers appear uniformly blue when they are formed correctly, and SEM images of the films confirm that a good quality and dense monlayer (Figures 6.2.2 A and D). The blue color arises from the interference of light reflected by the polystyrene film surface and the underlying silicon substrate which for 400 nm diameter spheres appears blue [330]. Darker areas in the image indicate multilayers such as edge beads at the wafer corners and spin coating conditions were optimized so as to avoid this geometry [307, 308].

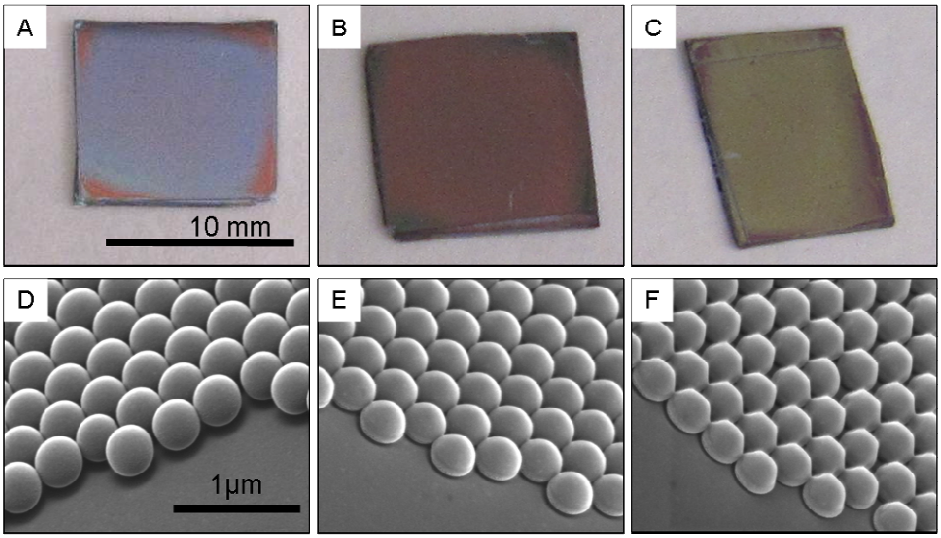

Figures 6.2.2 Digital images (A-C) and SEM images (D-F) of 1 cm^2 silicon wafer pieces covered by 400 nm polystyrene spheres (A, D) and samples after argon plasma etching for 60 sec (B, E) and 90 sec (C, F)

The nanosphere arrays were then etched by argon plasma for roughly a minute. The changes to the films were visibly apparent as shown in Figure 6.2.2; specifically the sample changed from blue (untreated sample) to red and ultimately brown as etching time increased (Figures 6.2.2 A-C). These color changes suggest the plasma etching may be changing both the diameter as well as the refractive index of the polystyrene spheres [330]. SEM analysis (Figures 6.2.1 B and 6.2.2 E-F) showed that the etching does affect significant changes on the dimensions and morphology of the spheres. Material is lost from the spheres, and they apparently collapse into mushroom-like structures. A schematic illustration of these changes are presented in Figure 5.2.11 in Chapter 5 however in that case the etching included some oxygen [275]. While it is difficult to visualize in these images, there exists an overhang of polystyrene above the silicon substrate. The etched spheres do not apparently fully lift off the surface in spite of their massive volume change; the original point of contact between the sphere and the substrate surface remains. Moreover, because this polystyrene was more protected from the etch that the surrounding sphere material it remains adhered to the substrate.

Once plasma-treated the array material was very different chemically that the original polystyrene. Most notably, organic solvents such as THF, toluene and chloroform could not dissolve the spheres even after immersion for 30 minutes. In contrast, bulk polystyrene dissolves readily in one minute in these solvents. For example, a 1 cm^2 piece of polystyrene readily dissolved in THF, toluene, and chloroform, but is unaffected by water, acetone, methanol and hexanes. We confirmed that the polystyrene arrays prior to plasma etching showed similar behavior to bulk polystyrene; films could be readily dissolved from the silicon substrate when immersed in THF, toluene and

chloroform but remained on the wafer when placed in water, acetone, hexane and methanol. These data suggest the plasma treated polystyrene has changed its chemical composition as a result of its brief exposure to argon plasma.

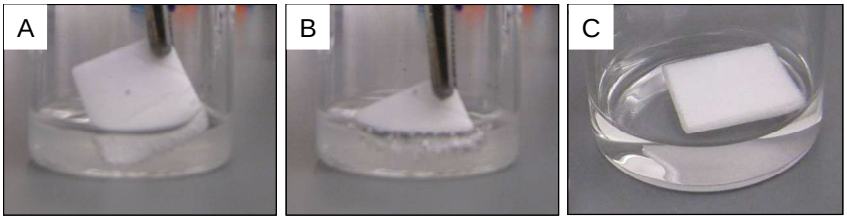

Figure 6.2.3 Effect of solvent treatment on bulk polystyrene. Digital images of piece of polystyrene foam food container introduced into tetrahydrofuran (A), after 2 sec in tetrahydrofuran (B) after 10 min in methanol (C).

Completely different dissolution behavior was observed for the plasma etched mushroomed materials. The collapsed spheres remained on the substrate even after 30 minutes in THF (Figure 6.2.4). Also important is that the mushroom morphology and size was apparently unaffected by immersion in organic solvents (see Figures 6.2.2 and 6.2.4).

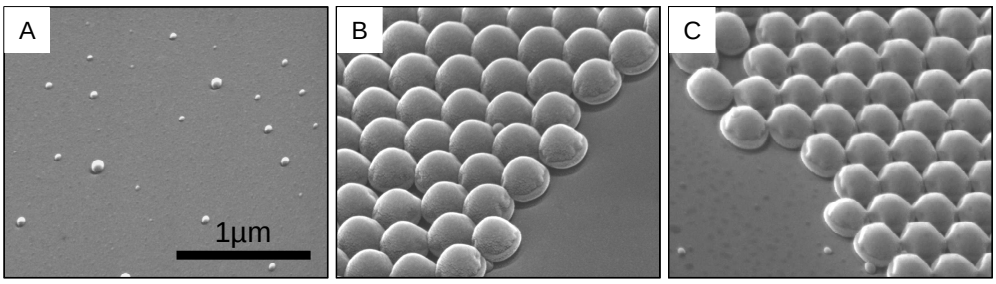

Figure 6.2.4 SEM images obtained at a tilt angle of 45 deg and 50,000 magnification levels of (A) untreated, (B) 60 sec and (C) 90 sec plasma treated polystyrene beads immersed in tetrahydrofuran for 30 min

The only way to remove the plasma-treated material was to combine the immersion in solvents with a mild sonication. It was after this step that a doughnut-shaped residue was observed. These structures were found after sonication for a variety of solvent immersions including THF (Figure 6.2.5 A), toluene (Figure 6.2.5 B) and chloroform. The residues were not apparent after immersion in water, acetone, hexane or methanol (Figure 6.2.5 C). In these cases, only a hexagonally close-packed pattern was observed that results from the mild differential etching of the underlying silicon substrate caused by the presence of the nanospheres.

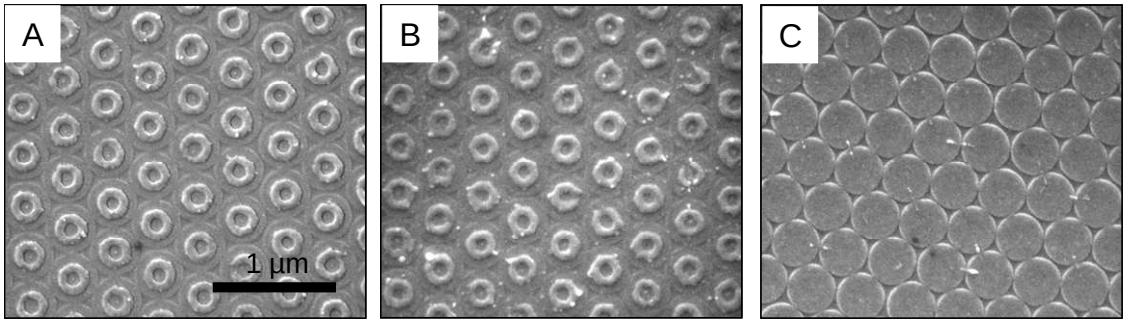

Figure 6.2.5 SEM studies on the effect of solvent on formation of polystyrene nanodoughnuts. SEM images of samples after immersion in tetrahydrofuran (A), toluene (B) and methanol (C)

While it is perhaps intuitive that the points of contacts for the nanospheres would be protected during etching, it is less obvious why when this material remains as a residue it appears as a doughnut rather than a disk. To gain insight into the mechanism we first turned towards microscopy. The plasma-treated polystyrene was tape stripped off and its underside imaged using SEM. This data reveals that after lengthy plasma

etching the spheres are not only mushrooms, but they are also hollow shells (Figure 6.2.6B). The interior diameter of the deflated sphere matches to the outer diameter of the doughnuts (Figure 6.2.6 A-B). We hypothesized that the inner ring of material in the collapsed sphere remains protected from the etching reaction as it is contacting the substrate and fully adhered (Figure 6.2.6 C). When the treated material is removed, this shell remains and lacks a center due to the deflation of the sphere material.

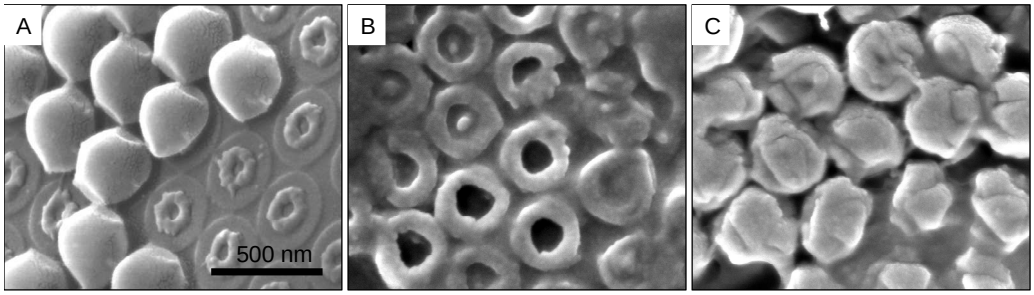

Figure 6.2.6 Tilted-view SEM image (A) of nanodoughnuts array with some undetached domes and top-view SEM images (B and C) of underside of the domes, shaped after exposure of 400 nm PS to argon plasma for 90 sec (B) and 30 sec (C) followed by immersion in THF for 30 min. Panel B shows the domes under which nanodoughnuts array formed, that are clearly hollow (shells with holes in their surfaces) while panel C shows spheres not yet fully collapsed. Such structures do not produce nanoscale doughnuts.

To better understand the morphological changes in the films, we employed both XPS and vibrational spectroscopies. First, as expected we found that doughnut residues have the same chemical composition as the original, untreated polystyrene spheres (Figures 6.2.7). The XPS 1S carbon feature exhibits a shake-up satellite at 291.4 eV

characteristics of the styrene aromatic ring (Figures 6.2.7 F). This is consistent with our expectation that the residue material is to some extent protected from the argon etch.

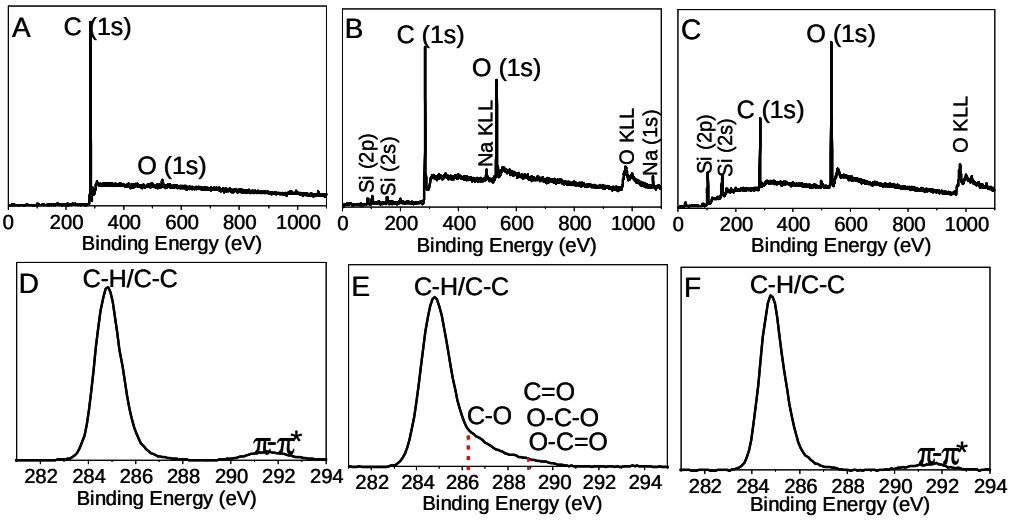

Figure 6.2.7 XPS survey scans and C 1s spectra of untreated and argon plasma treated polystyrene beads assembled on silicon wafer as well as nanodoughnuts array. Survey scans: (A) untreated and (B) 60 sec argon plasma treated beads and (C) nanodoughnuts array; C (1s) spectra: (D) untreated and (E) 60 sec argon plasma treated beads and (F) nanodoughnuts array. Sodium detected by XPS may come from sodium dodecyl sulfate , which was added into the polystyrene nanospheres solution by Bangs Laboratory Inc.

While nanodoughnuts had the same chemical composition as untreated polystyrene spheres, we found that the plasma-etched arrays had very different chemical composition (Figure 6.2.7). Argon plasma etching of polystyrene spheres altered the carbon-oxygen functionalities and removed the shake-up satellite peak from the aromatic ring. These effects increased with increasing plasma treatment time and can best be described as an oxidation. Initially the surface of untreated polystyrene spheres was free

of oxygen (Figure 6.2.7 A), with aromatic character demonstrated by the C 1s shake-up satellite at 291.4 eV (Figure 6.2.7 C) [311]. Samples exposed to argon plasma for 30 sec, 60 sec, 90 sec and 120 sec showed that the level of surface oxidation increased from 24.0 to 35.4 at % with the increased etch duration. Furthermore, XPS analysis of the C 1s spectra, presented in Figure 6.2.7 D, revealed that this increasing oxidation resulted in a wide range of funcationality with new C−O (peak at 286.2 eV) and C=O, O−C−O O−C=O (peak at 289.0 eV) increasing with etching time. The rings themselves change also as the signatures of aromaticity diminish [311, 331, 332]. The greater oxygen content of the films would make them less soluble than polystyrene in more organic media in agreement with our prior observations.

Argon plasma etching of bulk polystyrene films has been studied and similar oxidation has been observed. While no oxygen was introduced into the etch chamber, the native oxygen from air is enough to cause substantial oxidation chemistry. Grant et al. in particular observed oxidized structures at the surface of polystyrene. He suggested that argon ion bombardment produces carbon radicals that become rapidly oxidized by oxygen available from the ambient residual atmosphere [311].

Raman spectroscopy of both treated and untreated films supports the general findings of polymer oxidation during the plasma etch, and provides further information about the nature of the etched nanosphere arrays. Most notably, plasma etched samples have substantial graphitic character which increases with increasing etch time. Figure 6.2.8 shows a typical Raman spectrum; there are characteristic silicon lines at 979–943 (overlaid peaks), 826, 672 and 622 cm^{-1} for all samples. However, the Raman spectra of untreated and mildly etched polystyrene monolayers are quite distinctive. The original

array had lines at 1605, 1586, 1452, 1201, 1184, 1157, 1033, 1003, 797 and 623 cm^{-1}, which correspond to polystyrene [333]. In contrast, longer plasma treated samples (60 and 90 sec) have very intense and broad Raman features at 1543 and 1384 cm^{-1} in addition to the original polystyrene features. These are signatures of various graphitic structures [333]. At intermediate etch times, such as thirty seconds, films have both polystyrene and graphitic character which suggests some parts of the sample remain unmodified. These findings were in a good agreement with previously published results concerning the effects of plasma on polystyrene films. With an increasing time, argon plasma treatment resulted in material loss and chemical modifications including crosslinking and formation of graphitic carbon on the surface [310, 311, 333, 334].

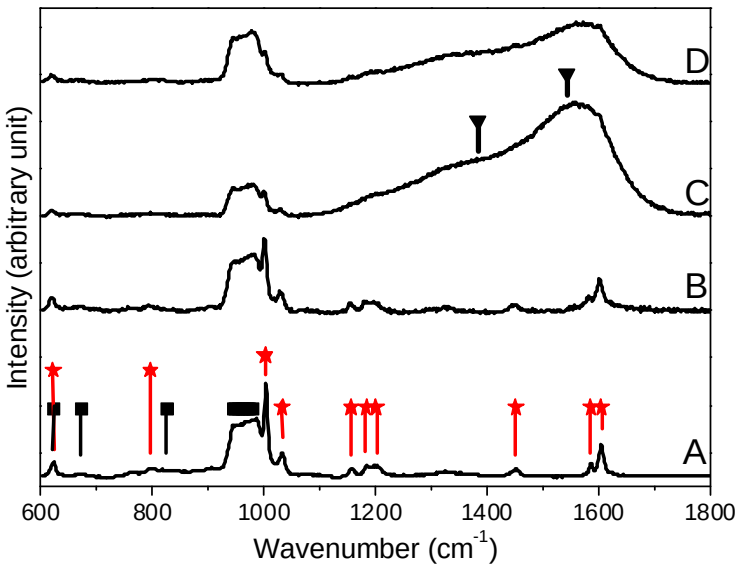

Figure 6.2.8 Raman spectra from (A) 400 nm spin coated polystyrene beads on a silicon substrate; (B), (C), (D) polystyrene beads etched with argon plasma for 30, 60 and 90 sec, respectively. The peaks that correspond to polystyrene material are labeled with red stars and silicon and graphitic structures with black squares and triangles, respectively.

Taken together, the chemical analysis and microscopy suggests that the etch process has profound impact on the polystyrene sphere morphology as well as its chemistry. The plasma etching serves to oxidize the polymer starting at its surface; these oxygen functionalities may result in increased cross-linking and eventually the formation graphitic carbon and substantial loss of material. Once etched, the materials are more stiff and are not able to swell or dissolve in solvents that typically dissolve the starting polystyrene [333, 335, 336].

Furthermore, Zhang et al speculated that there is less swelling of the material under the stiff layer [335]. However, we concluded that plasma treated polystyrene particles consisted of the stiff shell of graphitic carbon on the surface and two underlayers: a strong crosslinked layer in the upper part and minimally altered or even untouched polystyrene at the core [333]. Expanded polystyrene adheres strongly to the substrate in the area around the point of contact due to structural defects created by the ion bombardment that increased adhesive bonding in that area [337]. The unaltered polystyrene material in the core readily dissolves in the solvent and freely flows out leaving an empty space behind, which corresponds to nanodoughnut hole. Mechanical detachment of the stiff shell, which is now hollow leaves behind nanodoughnuts on the substrate.

This approach is a simple method to produce large areas arrays of polystyrene nanodoughnuts with dimensions that are sensitive to the diameter of the initial polystyrene spheres. To illustrate the tunability of the method, Figure 6.2.9 presents the nanostructures fabricated on pre-cleaned silicon wafer ($1cm^2$) starting with spin coating

of 400 nm polystyrene particles, which were argon plasma etched for 60 sec, then soaked for 30 min and sonicated for 5 min in THF. The resulting doughnuts shown in Figure 6.2.9 and 6.2.10 A-B had high uniformity with an average outer diameter (d_o) of 242 ± 6 nm, width (w) 68 ± 8 nm (SEM analysis of N = 100) and height ~ 25 nm. Smaller polystyrene nanodoughnuts are shown in Figure 6.2.10 C with d_o = 128 ± 12 nm and w = 28 ± 5 nm. These were formed with 250 nm polystyrene particles assembled on the silicon wafer, following the same procedure.

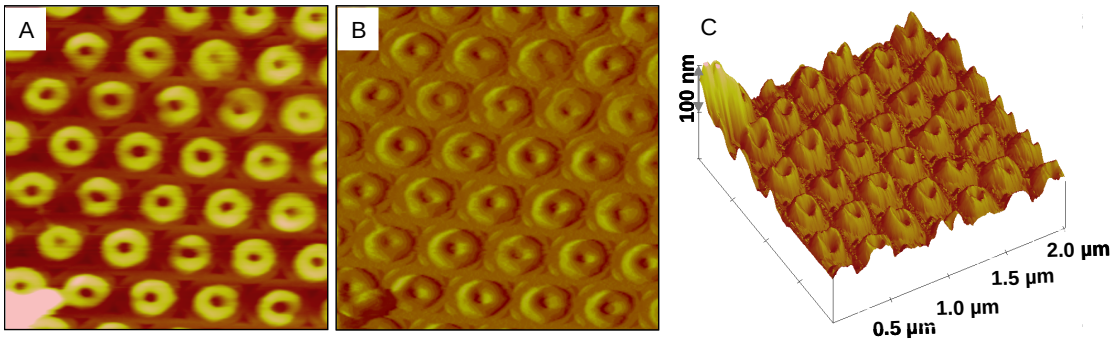

Figure 6.2.9 AFM analysis of the polystyrene nanodoughnuts array on silicon substrate fabricated using 400 nm polystyrene beads, showing phase (A), amplitude (B) and topography (C) with a scan size of 2 x 2 µm

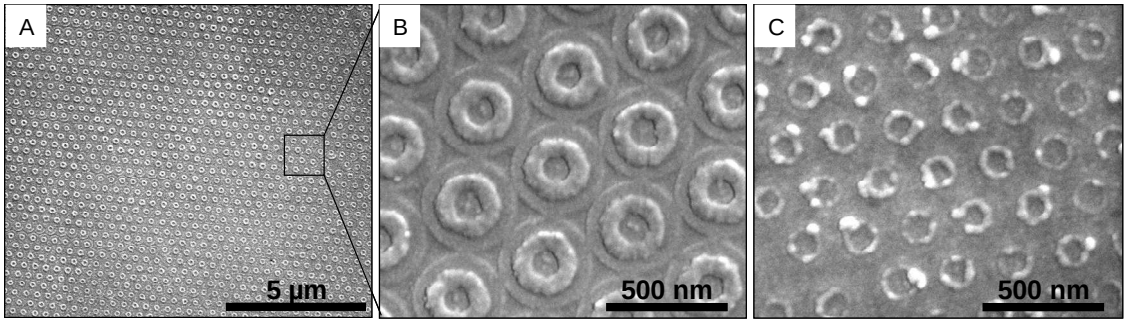

Figure 6.2.10 SEM images of nanodoughnuts arrays fabricated using 400 nm (A, B) and 250 nm polystyrene beads (C). SEM imaged were obtained at 10,000x (A) and 100,000x (B, C) magnification levels.

Presented here is a method for fabricating well ordered, large area (1 cm^2), polystyrene nanodoughnuts arrays which is easy to perform and much faster than conventional electron beam lithography [287, 328, 329]. These nanodoughnuts were fabricated using techniques like: spin coating, argon plasma etching, solvent soaking and sonicating. Therefore, this process is free of design factors such as monomer and surfactant concentration, surfactant chain length, polymerization time and temperature, and solution ionic strength, which have to be controlled for dielectric nanodoughnuts formation by capillary forces to drive polymer under the spheres [289, 290]. The other advantage of this approach is that it does not require the assistance of an etching mask because no chemical etching process is used to form the doughnuts. Instead of drilling holes in polystyrene spheres by chemical etching with reactive gases only neutral argon plasma is used to make the polystyrene spheres surface more resistant against dissolution in solvent [291-293]. Argon plasma treatment could be performed in any argon plasma system including for example reactive ion etching (RIE), inductively coupled plasma (ICP), sputtering or evaporating systems equipped with argon etching device for surface

cleaning. Therefore, presented here polystyrene nanodoughnuts arrays are fabricated over large areas by using only low cost and simple fabrication techniques.

6.3 Conclusion

Large area arrays (1 cm^2) of polystyrene nanodonuts with outer diameters ranging from 128 to 242 nm were fabricated using low cost and simple fabrication techniques. A combination of nanosphere lithography, argon plasma treatment, immersion in organic solvents and sonication resulted in formation of thick polystyrene rings. These rings developed around the spots where modified by argon plasma polystyrene beads contacted a surface. Their diameters were generally two times smaller than the beads dimensions. Scanning electron and atomic force microscopy revealed that the argon ions etched polystyrene spheres into non-spherical particles, referred to herein as domes. Moreover, X-ray photoelectron and Raman spectroscopy found that the argon plasma changed the composition of the polystyrene spheres surface by forming graphitic materials, which may act as a stiff skin that thickness depends on ion penetration depth. Under this hard surface there were crosslinked polystyrene macromolecules that in the solvent may change conformation and form thick nanorings. The arrays of nanodoughnuts are feasible as templates for silicon nanorings, which coated with magnetic layers (e.g. Cu/Co/Cu) will have application in magnetic devices. Nanodonuts can also be doped with nanoparticles made, for example from noble metals (Au or Ag) and present optical resonances.

Conclusion

The objectives of this PhD work were twofold: to perform physicochemical characterization of commercial nanomaterials for environmental and health studies; and to find a cost-effective fabrication method for metal nanostructures arrays over large areas (> 1 cm^2).

First, the characterization set that included parameters identified by toxicologists as responsible for nanomaterial toxicity was performed on three forms of nanoscale materials. Various nanoparticle properties in dry powders, dispersions and incorporated into the consumer's products including primary particle size and size distribution, shape, aggregation state, specific surface area, porosity, crystal structure, crystallite size, overall and surface elemental compositions, were measured using the major academic research techniques for characterization of nanoscale particles. These results revealed that information provided by manufacturers of nanoscale materials can be incomplete and/or wrong due to, for example nanoparticle batch-to-batch variability or lack of measurement protocols. Therefore, it is recommended to choose a variety of techniques that provide complementary information about nanoparticles before in vitro or in vivo testing of these materials. Moreover, standardized tests and protocols for nanoparticle characterization need to be established for accurate assessment of their properties.

The characterization set of TiO_2 and ZnO nanoparticles was extended by additional photochemical data, because these materials are known to generate reactive oxygen species (ROS), which may be a key factor in their toxicity. The photochemical properties of sunscreens that contained TiO_2 and ZnO materials, the inorganic particles derived from these sunscreens, and several commercial TiO_2 and ZnO nanopowders were

examined toward the production of reactive oxygen species using multiple simple and quick cell free assays. The results of the physicochemical analysis revealed that ZnO nanoparticles in sunscreens either did not have coatings or the coating layer was insufficient to prevent ROS generation. On the other hand, the coating layer attached to the surface of the TiO_2 particles reduced their photoactivity. Since both types of nanoscale materials (photoactive ZnO and inactive TiO_2) are used in sunscreens, nanotechnology-based consumer products require that nanoscale components be promptly investigated first by in vitro and then by in vivo testing to avoid health and environmental hazards from manufacturing, using and disposing of these products.

In the second part of the project a novel approach based on shaped nanosphere lithography to the fabrication of nanorings and nanocrescents arrays over centimeters was presented. Gold nanorings and nanocrescents with outer diameters ranging from 300 to 350 nm were produced and their optical properties were measured and compared with numerical simulations. Shaped nanosphere lithography does not require complex tilted-rotary evaporation system and time consuming ion beam milling processes, which are necessary in other known nanosphere lithography approaches for ring-shaped nanostructures arrays fabrication. This method generates nanorings and nanocrescents that may have potential application in surface enhanced spectroscopy and in the fields of metamaterials.

Finally, a novel method based on nanosphere lithography for the fabrication of polystyrene nanodoughnuts arrays was described. Large area arrays (1 cm^2) of polystyrene nanodoughnuts with outer diameters ranging from 128 to 242 nm were

fabricated using low cost and simple fabrication techniques such argon plasma treatment, immersion in organic solvents and sonication.

References

1. ASTM. Terminology for Nanotechnology. E2456-06. 2006 [cited 7 February 2011]; Available from: http://www.astm.org/Standards/E2456.htm.

2. BSI. Terminology for nanomaterials. PAS 136:2007. 2007 [cited 15 February 2010]; Available from: www.bsigroup.com.

3. Krug, H.F. and P. Wick. 2011. Nanotoxicology: An Interdisciplinary Challenge. Angewandte Chemie-International Edition 50(6):1260-1278.

4. Maynard, A.D. 2007. Nanotechnology: The next big thing, or much ado about nothing? Annals of Occupational Hygiene 51(1):1-12.

5. Oberdorster, G., E. Oberdorster, and J. Oberdorster. 2005. Nanotoxicology: An emerging discipline evolving from studies of ultrafine particles. Environmental Health Perspectives 113(7):823-839.

6. Wigginton, N.S., K.L. Haus, and M.F. Hochella. 2007. Aquatic environmental nanoparticles. Journal of Environmental Monitoring 9(12):1306-1316.

7. Rossetti, R., S. Nakahara, and L.E. Brus. 1983. Quantum Size Effects in the Redox Potentials, Resonance Raman-Spectra, and Electronic-Spectra of Cds Crystallites in Aqueous-Solution. Journal of Chemical Physics 79(2):1086-1088.

8. Schutz-Sikma, E.A., et al. 2011. Probing the Chemical Stability of Mixed Ferrites: Implications for Magnetic Resonance Contrast Agent Design. Chemistry of Materials 23(10):2657-2664.

9. Hansen, S.F., et al. 2008. Categorization framework to aid exposure assessment of nanomaterials in consumer products. Ecotoxicology 17(5):438-447.

10. PEN. The Project on Emerging Nanotechnologies; Analysis. 2009 [cited 08 February 2011]; Available from: www.nanotechproject.org.

11. Kessler, R. 2011. Engineered nanoparticles in consumer products: understanding a new ingredient. Environmental health perspectives 119(3):a120-5.

12. Maynard, A.D., et al. 2006. Safe handling of nanotechnology. Nature 444(7117):267-269.

13. Nielsen, E., *Human Health and Nanomaterials in Consumer Products*, in *Literature Review for the Region of Peel's Public Health Unit*. 2008.

14. Simko, M. and M.O. Mattsson. 2010. Risks from accidental exposures to engineered nanoparticles and neurological health effects: A critical review. Particle and Fibre Toxicology 7.

15. Borm, P.J.A., et al. 2006. The potential risks of nanomaterials: a review carried out for ECETOC. Part Fibre Toxicol 3:11.

16. ICON. Nano-EHS Database Analysis Tool. 2012 [cited March 05 2012]; Available from: http://icon.rice.edu/report.cfm.

17. Peralta-Videa, J.R., et al. 2011. Nanomaterials and the environment: A review for the biennium 2008-2010. Journal of Hazardous Materials 186(1):1-15.

18. Lewicka, Z.A., et al. 2011. The Structure, Composition and Dimensions of TiO2 and ZnO Nanomaterials in Commercial Sunscreens. Journal of Nanoparticle Research 12(4):3607-3617.

19. More, B.D. 2007. Physical sunscreens: On the comeback trail. Indian Journal of Dermatology Venereology & Leprology 73(2):80-85.

20. Popov, A.P., et al. 2005. The effect of nanometer particles of titanium oxide on the protective properties of skin in the UV region. J Opt Technol 73:208-211.

21. Hendren, C.Z., et al. 2011. Estimating Production Data for Five Engineered Nanomaterials As a Basis for Exposure Assessment. Environmen. Sci. Technol.(45):2562-2568.

22. Nowack, B. and T.D. Bucheli. 2007. Occurrence, behavior and effects of nanoparticles in the environment. Environmental Pollution 150:5-22.

23. Musee, N. 2011. Nanowastes and the environment: Potential new waste management paradigm. Environment International 37(1):112-128.

24. Kiser, M.A., et al. 2009. Titanium Nanomaterial Removal and Release from Wastewater Treatment Plants. Environmental Science & Technology 43(17):6757-6763.

25. Gottschalk, F., et al. 2010. Possibilities and Limitations of Modeling Environmental Exposure to Engineered Nanomaterials by Probabilistic Material Flow Analysis. Environmental Toxicology and Chemistry 29(5):1036-1048.

26. Gottschalk, F., et al. 2009. Modeled Environmental Concentrations of Engineered Nanomaterials (TiO2, ZnO, Ag, CNT, Fullerenes) for Different Regions. Environmental Science & Technology 43(24):9216-9222.

27. Stone, V., et al. 2010. Nanomaterials for environmental studies: Classification, reference material issues, and strategies for physico-chemical characterisation. Science of the Total Environment 408(7):1745-1754.

28. Brar, S.K., et al. 2010. Engineered nanoparticles in wastewater and wastewater sludge - Evidence and impacts. Waste Management 30(3):504-520.

29. McCall, M.J. 2011. Environmental, Health and Safety Issues; Nanoparticles in the real world. Nature Nanotechnology 6(10):613-614.

30. Guzman, K.A.D., M.P. Finnegan, and J.F. Banfield. 2006. Influence of surface potential on aggregation and transport of titania nanoparticles. Environmental Science & Technology 40(24):7688-7693.

31. Labille, J., et al. 2010. Aging of TiO2 nanocomposites used in sunscreen. Dispersion and fate of the degradation products in aqueous environment. Environmental Pollution 158(12):3482-3489.

32. Zhu, X.S., Y. Chang, and Y.S. Chen. 2010. Toxicity and bioaccumulation of TiO2 nanoparticle aggregates in Daphnia magna. Chemosphere 78(3):V-215.

33. Zhu, X.S., et al. 2008. Comparative toxicity of several metal oxide nanoparticle aqueous suspensions to Zebrafish (Danio rerio) early developmental stage. Journal of Environmental Science and Health Part a-Toxic/Hazardous Substances & Environmental Engineering 43(3):278-284.

34. Adams, L.K., D.Y. Lyon, and P.J.J. Alvarez. 2006. Comparative eco-toxicity of nanoscale TiO2, SiO2, and ZnO water suspensions. Water Research 40(19):3527-3532.

35. Bai, W., et al. 2010. Toxicity of zinc oxide nanoparticles to zebrafish embryo: a physicochemical study of toxicity mechanism. Journal of Nanoparticle Research 12(5):1645-1654.

36. Franklin, N.M., et al. 2007. Comparative toxicity of nanoparticulate ZnO, bulk ZnO, and ZnCl2 to a freshwater microalga (Pseudokirchneriella subcapitata): The importance of particle solubility. Environmental Science & Technology 41(24):8484-8490.

37. Crane, M., et al. 2008. Ecotoxicity test methods and environmental hazard assessment for engineered nanoparticles. Ecotoxicology 17(5):421-437.

38. Roh, J.-Y., et al. 2010. Ecotoxicological investigation of CeO2 and TiO2 nanoparticles on the soil nematode Caenorhabditis elegans using gene expression, growth, fertility, and survival as endpoints. Environmental Toxicology and Pharmacology 29(2):167-172.

39. Wang, H.H., R.L. Wick, and B.S. Xing. 2009. Toxicity of nanoparticulate and bulk ZnO, Al2O3 and TiO2 to the nematode Caenorhabditis elegans. Environmental Pollution 157(4):1171-1177.

40. Sharma, V.K. 2009. Aggregation and toxicity of titanium dioxide nanoparticles in aquatic environment-A Review. Journal of Environmental Science and Health Part a-Toxic/Hazardous Substances & Environmental Engineering 44(14):1485-1495.

41. Yang, W., J.I. Peters, and R.O. Williams. 2008. Inhaled nanoparticles - A current review. International Journal of Pharmaceutics 356(1-2):239-247.

42. Kreyling, W.G., et al. 2002. Translocation of ultrafine insoluble iridium particles from lung epithelium to extrapulmonary organs is size dependent but very low. Journal of Toxicology and Environmental Health-Part A 65(20):1513-1530.

43. Oberdorster, G., et al. 2004. Translocation of inhaled ultrafine particles to the brain. Inhalation Toxicology 16(6-7):437-445.

44. Wang, J.X., et al. 2008. Time-dependent translocation and potential impairment on central nervous system by intranasally instilled TiO2 nanoparticles. Toxicology 254(1-2):82-90.

45. Smijs, T.G.M. and J.A. Bouwstra. 2010. Focus on Skin as a Possible Port of Entry for Solid Nanoparticles and the Toxicological Impact. Journal of Biomedical Nanotechnology 6(5):469-484.

46. Lu, M., et al. 2010. Physiologically Based Pharmacokinetic Modeling of Nanoparticles. Acs Nano 4(11):6303-6317.

47. Bartneck, M., et al. 2010. Phagocytosis Independent Extracellular Nanoparticle Clearance by Human Immune Cells. Nano Letters 10(1):59-63.

48. Stone, V., H. Johnston, and R.P.F. Schins. 2009. Development of in vitro systems for nanotoxicology: methodological considerations. Critical Reviews in Toxicology 39(7):613-626.

49. Rivera Gil, P., et al. 2010. Correlating Physico-Chemical with Toxicological Properties of Nanoparticles: The Present and the Future. Acs Nano 4(10):5527-5531.

50. Lewinski, N., V. Colvin, and R. Drezek. 2008. Cytotoxicity of nanoparticles. Small 4(1):26-49.

51. Khlebtsov, N. and L. Dykman. 2010. Biodistribution and toxicity of engineered gold nanoparticles: a review of in vitro and in vivo studies. Chemical Society Reviews 40(3):1647-1671.

52. Landsiedel, R., et al. 2010. Testing Metal-Oxide Nanomaterials for Human Safety. Advanced Materials 22(24):2601-2627.

53. Nel, A., et al. 2006. Toxic potential of materials at the nanolevel. Science 311(5761):622-627.

54. Seaton, A., et al. 2011. Nanoparticles, human health hazard and regulation. Journal of the Royal Society Interface 7:S119-S129.

55. Pulskamp, K., S. Diabate, and H.F. Krug. 2007. Carbon nanotubes show no sign of acute toxicity but induce intracellular reactive oxygen species in dependence on contaminants. Toxicology Letters 168(1):58-74.

56. Chlopek, J., et al. 2006. In vitro studies of carbon nanotubes biocompatibility. Carbon 44(6):1106-1111.

57. Thomas, C.R., et al. 2011. Nanomaterials in the Environment: From Materials to High-Throughput Screening to Organisms. Acs Nano 5(1):13-20.

58. Warheit, D.B. 2008. How meaningful are the results of nanotoxicity studies in the absence of adequate material characterization? Toxicological Sciences 101(2):183-185.

59. Oberdorster, G. 2009. Safety assessment for nanotechnology and nanomedicine: concepts of nanotoxicology. Journal of Internal Medicine 267(1):89-105.

60. Grieger, K.D., A. Baun, and R. Owen. 2010. Redefining risk research priorities for nanomaterials. Journal of Nanoparticle Research 12(2):383-392.

61. Card, J.W. and B.A. Magnuson. 2011. A Method to Assess the Quality of Studies That Examine the Toxicity of Engineered Nanomaterials. International Journal of Toxicology 29(4):402-410.

62. Boverhof, D.R. and R.M. David. 2010. Nanomaterial characterization: considerations and needs for hazard assessment and safety evaluation. Analytical and Bioanalytical Chemistry 396(3):953-961.

63. ISO. International Standards for Business, Government and Society. [cited 18 May 2011]; Available from: http://www.iso.org/iso/iso_technical_committee?commid=381983.

64. MINChar. Recommended Minimum Physical and Chemical Parameters for Characterizing Nanomaterials on Toxicology Studies. 2008 [cited 21 May 2011]; Available from: http://characterizationmatters.org/parameters/.

65. Maynard, A.D., D.B. Warheit, and M.A. Philbert. 2011. The New Toxicology of Sophisticated Materials: Nanotoxicology and Beyond. Toxicological Sciences 120:S109-S129.

66. Powers, K.W., et al. 2006. Research strategies for safety evaluation of nanomaterials. Part VI. Characterization of nanoscale particles for toxicological evaluation. Toxicological Sciences 90(2):296-303.

67. Fairhurst, D. and M.A. Mitchnick, *Particulate Sun Blocks: General Principles*, in *Sunscreens, development, evaluation, and regulatory aspects (Lowe NJ, Shaath NA, Pathak MA). New York: Marcel Dekker, 313.* 1997.

68. Serpone, N., D. Dondi, and A. Albini. 2007. Inorganic and organic UV filters: Their role and efficacy in sunscreens and suncare product. Inorganica Chimica Acta 360(3):794-802.

69. Stamatakis, P., et al. 1990. Optimum Particle-Size of Titanium-Dioxide and Zinc-Oxide for Attenuation of Ultraviolet-Radiation. Journal of Coatings Technology 62(789):95-98.

70. FDA. 1999. Sunscreen Drug Products For Over-The-Counter Human Use, Final Monograph, Federal Register /Vol. 48, No. 98. U.S. Food and Drug Administration.

71. Sayes, C.M., et al. 2006. Correlating Nanoscale Titania Structure with Toxicity: A Cytotoxicity and Inflammatory Response Study with Human Dermal Fibroblasts and Human Lung Epithelial Cells. Toxicological Sciences 92:174–185.

72. Cunningham, J. and P. Sedlak. 1994. Interrelationships between Pollutant Concentration, Extent of Adsorption, Tio2-Sensitized Removal, Photon Flux and Levels of Electron or Hole Trapping Additives .1. Aqueous Monochlorophenol-Tio2(P25) Suspensions. Journal of Photochemistry and Photobiology a-Chemistry 77(2-3):255-263.

73. Doliveira, J.C., G. Alsayyed, and P. Pichat. 1990. Photodegradation of 2-Chlorophenol and 3-Chlorophenol in TiO2 Aqueous Suspensions. Environmental Science & Technology 24(7):990-996.

74. Linsebigler, A.L., G.Q. Lu, and J.T. Yates. 1995. Photocatalysis on Tio2 Surfaces - Principles, Mechanisms, and Selected Results. Chemical Reviews 95(3):735-758.

75. Mills, G. and M.R. Hoffmann. 1993. Photocatalytic Degradation of Pentachlorophenol on Tio2 Particles - Identification of Intermediates and Mechanism of Reaction. Environmental Science & Technology 27(8):1681-1689.

76. Stafford, U., K.A. Gray, and P.V. Kamat. 1994. Radiolytic and Tio2-Assisted Photocatalytic Degradation of 4-Chlorophenol - a Comparative-Study. Journal of Physical Chemistry 98(25):6343-6351.

77. Jiang, J., et al. 2008. Does nanoparticle activity depend upon size and crystal phase? Nanotoxicology 2(1):33-42.

78. Powers, K.W., et al. 2007. Characterization of the size, shape, and state of dispersion of nanoparticles for toxicological studies. Nanotoxicology 1(1):42-51.

79. Brezova, V., D. Dvoranova, and A. Stasko. 2007. Characterization of titanium dioxide photoactivity following the formation of radicals by EPR spectroscopy. Research on Chemical Intermediates 33(3-5):251-268.

80. Brezova, V., et al. 2005. Reactive oxygen species produced upon photoexcitation of sunscreens containing titanium dioxide (an EPR study). Journal of Photochemistry and Photobiology B-Biology 79(2):121-134.

81. Hoffmann, M.R., et al. 1995. Environmental Applications of Semiconductor Photocatalysis. Chemical Reviews 95(1):69-96.

82. Riegel, G. and J.R. Bolton. 1995. Photocatalytic Efficiency Variability in Tio2 Particles. Journal of Physical Chemistry 99(12):4215-4224.

83. Daneshvar, N., D. Salari, and A.R. Khataee. 2004. Photocatalytic degradation of azo dye acid red 14 in water on ZnO as an alternative catalyst to TiO2. Journal of Photochemistry and Photobiology a-Chemistry 162(2-3):317-322.

84. Gouvea, C.A.K., et al. 2000. Semiconductor-assisted photocatalytic degradation of reactive dyes in aqueous solution. Chemosphere 40(4):433-440.

85. Harbour, J.R. and M.L. Hair. 1979. Radical Intermediates in the Photosynthetic Generation of H2O2 with Aqueous Zno Dispersions. Journal of Physical Chemistry 83(6):652-656.

86. Kandavelu, V., H. Kastien, and K.R. Thampi. 2004. Photocatalytic degradation of isothiazolin-3-ones in water and emulsion paints containing nanocrystalline TiO2 and ZnO catalysts. Applied Catalysis B-Environmental 48(2):101-111.

87. Kormann, C., D.W. Bahnemann, and M.R. Hoffmann. 1988. Photocatalytic Production of H2O2 and Organic Peroxides in Aqueous Suspensions of TiO2, ZnO, and Desert Sand. Environmental Science & Technology 22(7):798-806.

88. Lipovsky, A., et al. 2009. EPR Study of Visible Light-Induced ROS Generation by Nanoparticles of ZnO. Journal of Physical Chemistry C 113(36):15997-16001.

89. Shafaei, A., M. Nikazar, and M. Arami. 2010. Photocatalytic degradation of terephthalic acid using titania and zinc oxide photocatalysts: Comparative study. Desalination 252(1-3):8-16.

90. Villasenor, J., P. Reyes, and G. Pecchi. 1998. Photodegradation of pentachlorophenol on ZnO. Journal of Chemical Technology and Biotechnology 72(2):105-110.

91. Balasubramanian, B., W.K. Pogozelski, and T.D. Tullius. 1998. DNA strand breaking by the hydroxyl radical is governed by the accessible surface areas of the hydrogen atoms of the DNA backbone. Proceedings of the National Academy of Sciences of the United States of America 95(17):9738-9743.

92. Davies, K.J.A. 1987. Protein Damage and Degradation by Oxygen Radicals .1. General-Aspects. Journal of Biological Chemistry 262(20):9895-9901.

93. Kruk, I. 1998. Environmental Toxicology and Chemistry of Oxyden Species. In The Handbook of Environmental Chemistry 2.1. Springer-Verlag Berlin Heidelberg.

94. Nakagawa, Y., et al. 1997. The photogenotoxicity of titanium dioxide particles. Mutation Research-Genetic Toxicology and Environmental Mutagenesis 394(1-3):125-132.

95. Reeves, J.F., et al. 2008. Hydroxyl radicals ((OH)-O-center dot) are associated with titanium dioxide (TiO2) nanoparticle-induced cytotoxicity and oxidative DNA damage in fish cells. Mutation Research-Fundamental and Molecular Mechanisms of Mutagenesis 640(1-2):113-122.

96. Uchino, T., et al. 2002. Quantitative determination of OH radical generation and its cytotoxicity induced by TiO2-UVA treatment. Toxicology in Vitro 16(5):629-635.

97. Wang, C., et al. 2011. Induction of cytotoxicity by photoexcitation of TiO(2) can prolong survival in glioma-bearing mice. Molecular Biology Reports 38(1):523-530.

98. Petkovic, J., et al. 2011. Pre-irradiation of anatase TiO(2) particles with UV enhances their cytotoxic and genotoxic potential in human hepatoma HepG2 cells. Journal of Hazardous Materials 196:145-152.

99. Gopalan, R.C., et al. 2009. The effect of zinc oxide and titanium dioxide nanoparticles in the Comet assay with UVA photoactivation of human sperm and lymphocytes. Nanotoxicology 3(1):33-39.

100. Hirakawa, K., et al. 2004. Photo-irradiated titanium dioxide catalyzes site specific DNA damage via generation of hydrogen peroxide. Free Radical Research 38(5):439-447.

101. Hidaka, H., et al. 2006. DNA Damage Photoinduced by Cosmetic Pigments and Sunscreen Agents under Solar Exposure and Artifical UV Illumination. J. Oleo Sci 55:205–1212.

102. TGA. A review of the scientific literature on the safety of nanoparticulate titanium dioxide or zinc oxide in sunscreens. 2009 [cited 12 September 2010]; Available from: www.tga.gov.au.

103. Tran, D.T. and R. Salmon. 2010. Potential photocarcinogenic effects of nanoparticle sunscreens. Australasian Journal of Dermatology.

104. Crosera, M., et al. 2009. Nanoparticle dermal absorption and toxicity: a review of the literature. International Archives of Occupational and Environmental Health 82(9):1043-1055.

105. Newman, M.D., M. Stotland, and J.I. Ellis. 2009. The safety of nanosized particles in titanium dioxide- and zinc oxide-based sunscreens. Journal of the American Academy of Dermatology 61(4):685-692.

106. Nohynek, G.J., et al. 2009. Safety assessment of personal care products/cosmetics and their ingredients. Toxicology and Applied Pharmacology 243(2):239-259.

107. Nohynek, G.J., et al. 2007. Grey goo on the skin? Nanotechnology, cosmetic and sunscreen safety. Critical Reviews in Toxicology 37(3):251-277.

108. Osmond, M.J. and M.J. McCall. 2010. Zinc oxide nanoparticles in modern sunscreens: An analysis of potential exposure and hazard. Nanotoxicology 4(1):15-41.

109. Sadrieh, N., et al. 2010. Lack of Significant Dermal Penetration of Titanium Dioxide from Sunscreen Formulations Containing Nano- and Submicron-Size TiO2 Particles. Toxicological Sciences 115(1):156-166.

110. Baroli, B. 2009. Penetration of Nanoplarticles and Nanomaterials in the Skin: Fiction or Reality? Journal of Pharmaceutical Sciences 99(1):21-50.

111. Mortensen, L.J., et al. 2008. In Vivo Skin Penetration of Quantum Dot Nanoparticles in the Murine Model: The Effect of UVR. Nano Lett 8(9):2779-87.

112. Rouse, J.G., et al. 2007. Effects of Mechanical Flexion on the Penetration of Fullerene Amino Acid-Derivatized Peptide Nanoparticles through Skin. Nano Lett 7:155-160.

113. Tinkle, S.S., et al. 2003. Skin as a Route of Exposure and Sensitization in Chronic Beryllium Disease. Environ Health Perspect 111:1202–1208.

114. Egerton, T.A., et al. 2008. Interaction of TiO2 nano-particles with organic UV absorbers. Journal of Photochemistry and Photobiology a-Chemistry 193(1):10-17.

115. Sayes, C.M., et al. 2006. Correlating nanoscale titania structure with toxicity: A cytotoxicity and inflammatory response study with human dermal fibroblasts and human lung epithelial cells. Toxicological Sciences 92(1):174-185.

116. Carlotti, M.E., et al. 2009. Role of particle coating in controlling skin damage photoinduced by titania nanoparticles. Free Radical Research 43(3):312-322.

117. Hakim, L.F., et al. 2007. Nanoparticle coating for advanced optical, mechanical and rheological properties. Advanced Functional Materials 17:3175-3181.

118. Rampaul, A., I.P. Parkin, and L.P. Cramer. 2007. Damaging and protective properties of inorganic components of sunscreens applied to cultured human skin cells. Journal of Photochemistry and Photobiology a-Chemistry 191(2-3):138-148.

119. Wakefield, G., et al. 2004. Modified titania nanomaterials for sunscreen applications - reducing free radical generation and DNA damage. Materials Science and Technology 20(8):985-988.

120. Wakefield, G., et al. 2004. The effects of manganese doping on UVA absorption and free radical generation of micronised titanium dioxide and its consequences for the photostability of UVA absorbing organic sunscreen components. Photochemical & Photobiological Sciences 3(7):648-652.

121. Johnston, H.J., et al. 2009. Identification of the mechanisms that drive the toxicity of TiO2 particulates: the contribution of physicochemical characteristics. Particle and Fibre Toxicology 6.

122. Schilling, K., et al. 2010. Human safety review of "nano" titanium dioxide and zinc oxide. Photochemical & Photobiological Sciences 9(4):495-509.

123. Dunford, R., et al. 1997. Chemical oxidation and DNA damage catalysed by inorganic sunscreen ingredients. FEBS Letters 418:87-90.

124. Buchalska, M., et al. 2010. Singlet oxygen generation in the presence of titanium dioxide materials used as sunscreens in suntan lotions. Journal of Photochemistry and Photobiology a-Chemistry 213(2-3):158-163.

125. Barker, P.J. and A. Branch. 2008. The interaction of modern sunscreen formulations with surface coatings. Progress in Organic Coatings 62(3):313-320.

126. Vigneau, E., et al. 2000. Number of particles for the determination of size distribution from microscopic images. Powder Technology 107(3):243-250.

127. Yu, W.W., et al. 2004. Preparation and characterization of monodisperse PbSe semiconductor nanocrystals in a noncoordinating solvent. Chemistry of Materials 16(17):3318-3322.

128. Yu, W.W., et al. 2004. Synthesis of monodisperse iron oxide nanocrystals by thermal decomposition of iron carboxylate salts. Chemical Communications(20):2306-2307.

129. Ishihara. Photocatalytic Titanium Dioxide ST-01. [cited 28 April 2011]; Available from: http://www20.inetba.com/ishiharacorpusa/item416089.ctlg.

130. EMD. Eusolex T-Avo. [cited 28 April 2011]; Available from: http://www.omnipur.info/usa/eusolex-t-avo/EMD_CHEM-1.05335/p_tCib.s1LbBgAAAEWzeAfVhTl.

131. Umicore. Your NanoMaterials solutions partner. Nanograin [cited 28 April 2011]; Available from: http://www.umicore.jp/ja/productsUmsj/nanoMaterialsFuelCells/nanoMaterials/show_nanoGrain.pdf.

132. Sigma-Aldrich. Iron(II,III) oxide. [cited 28 April 2011]; Available from: http://www.sigmaaldrich.com.

133. Nichols, G., et al. 2002. A review of the terms agglomerate and aggregate with a recommendation for nomenclature used in powder and particle characterization. Journal of Pharmaceutical Sciences 91(10):2103-2109.

134. Paine, A.J. 1993. Error-Estimates in the Sampling from Particle-Size Distributions. Particle & Particle Systems Characterization 10(1):26-32.

135. Montes-Burgos, I., et al. 2010. Characterisation of nanoparticle size and state prior to nanotoxicological studies. Journal of Nanoparticle Research 12(1):47-53.

136. Stoeger, T., et al. 2006. Instillation of six different ultrafine carbon particles indicates a surface area threshold dose for acute lung inflammation in mice. Environmental Health Perspectives 114(3):328-333.

137. Brown, D.M., et al. 2001. Size-dependent proinflammatory effects of ultrafine polystyrene particles: A role for surface area and oxidative stress in the enhanced activity of ultrafines. Toxicology and Applied Pharmacology 175(3):191-199.

138. Duffin, R., et al. 2007. Proinflammogenic effects of low-toxicity and metal nanoparticles in vivo and in vitro: Highlighting the role of particle surface area and surface reactivity. Inhalation Toxicology 19(10):849-856.

139. Napierska, D., et al. 2009. Size-Dependent Cytotoxicity of Monodisperse Silica Nanoparticles in Human Endothelial Cells. Small 5(7):846-853.

140. Maurer-Jones, M.A., Y.S. Lin, and C.L. Haynes. 2010. Functional Assessment of Metal Oxide Nanoparticle Toxicity in Immune Cells. Acs Nano 4(6):3363-3373.

141. Lanone, S., et al. 2009. Comparative toxicity of 24 manufactured nanoparticles in human alveolar epithelial and macrophage cell lines. Particle and Fibre Toxicology 6.

142. Ortiz, A.L., et al. 2008. Crystallite sizes of LiH before and after ball milling and thermal exposure. Journal of Alloys and Compounds 454(1-2):297-305.

143. Naskar, M.K. 2010. Soft Solution Processing for the Synthesis of Alumina Nanoparticles in the Presence of Glucose. Journal of the American Ceramic Society 93(5):1260-1263.

144. Saiah, F.B.D., B.L. Su, and N. Bettahar. 2009. Nickel-iron layered double hydroxide (LDH): Textural properties upon hydrothermal treatments and application on dye sorption. Journal of Hazardous Materials 165(1-3):206-217.

145. Bouras, P., E. Stathatos, and P. Lianos. 2007. Pure versus metal-ion-doped nanocrystalline titania for photocatalysis. Applied Catalysis B-Environmental 73(1-2):51-59.

146. Wang, S.G., et al. 2008. Challenge in understanding size and shape dependent toxicity of gold nanomaterials in human skin keratinocytes. Chemical Physics Letters 463(1-3):145-149.

147. Warheit, D.B., et al. 2005. Comparative pulmonary toxicity inhalation and instillation studies with different TiO2 particle formulations: Impact of surface treatments on particle toxicity. Toxicological Sciences 88(2):514-524.

148. Otterstedt, J.-E. and D.A. Brandreth. 1998. Pigments. In: Small Particles Technology. Plenum Publishing Corporation. New York and London 270-405.

149. Song, D., J. Hrbek, and R. Osgood. 2005. Formation of TiO2 nanoparticles by reactive-layer-assisted deposition and characterization by XPS and STM. Nano Letters 5(7):1327-1332.

150. Dong, F., W.R. Zhao, and Z.B. Wu. 2008. Characterization and photocatalytic activities of C, N and S co-doped TiO2 with 1D nanostructure prepared by the nano-confinement effect. Nanotechnology 19(36).

151. Zhang, F., et al. 2004. Cerium oxidation state in ceria nanoparticles studied with X-ray photoelectron spectroscopy and absorption near edge spectroscopy. Surface Science 563(1-3):74-82.

152. Yamashita, T. and P. Hayes. 2008. Analysis of XPS spectra of Fe2+ and Fe3+ ions in oxide materials. Applied Surface Science 254(8):2441-2449.

153. NIST, *National Institute of Standards and Technology (NIST) X-ray Photoelectron Spectroscopy Database* in *NIST Standard Reference Database 20, Version 3.5* 2003.

154. Liu, Z.L., et al. 2005. Preparation and characterization of cerium oxide doped TiO2 nanoparticles. Journal of Physics and Chemistry of Solids 66(1):161-167.

155. Lin, Z.A., et al. 2010. Synthesis of magnetic nanoparticles with immobilized aminophenylboronic acid for selective capture of glycoproteins. Journal of Materials Chemistry 21(2):518-524.

156. Li, L., et al. 2009. Preparation of Core-shell Magnetic Molecularly Imprinted Polymer Nanoparticles for Recognition of Bovine Hemoglobin. Chemistry-an Asian Journal 4(2):286-293.

157. Yin, H., H.P. Too, and G.M. Chow. 2005. The effects of particle size and surface coating on the cytotoxicity of nickel ferrite. Biomaterials 26(29):5818-5826.

158. Roebben, G., et al. 2011. Interlaboratory comparison of size and surface charge measurements on nanoparticles prior to biological impact assessment. Journal of Nanoparticle Research 13(7):2675-2687.

159. IANH. The International Alliance for NanoEHS Harmonization. [cited 14 July 2011]; Available from: www.nanoehsalliance.org.

160. Xia, T., et al. 2008. Cationic polystyrene nanosphere toxicity depends on cell-specific endocytic and mitochondrial injury pathways. Acs Nano 2(1):85-96.

161. IRMM, *Certified Reference Materials 2011*. 2011, Institute for Reference Materials and Measurements.

162. Hackley, V.A. and J.D. Clogston. 2007. Measuring the size of nanoparticles in aqueous media using batch-mode dynamic light scattering. NIST-NCL Joint Assay Protocol PCC-1, National Cancer Institute, Nanotechnology Characterization Laboratory.

163. Malvern. Zeta Potential An Introduction in 30 Minutes Zetasizer Nano Series Technical Note [cited 29 July 2011]; Available from: http://www.nbtc.cornell.edu/facilities/downloads/Zeta%20potential%20-%20An%20introduction%20in%2030%20minutes.pdf.

164. Clogston, J.D. 2009. Measuring Zeta Potential of Nanoparticles. Nanotechnology Characterization Laboratory

165. Tiano, L., et al. 2010. Modified TiO2 particles differentially affect human skin fibroblasts exposed to UVA light. Free Radical Biology and Medicine 49(3):408-415.

166. Wokovich, A., et al. 2009. Particle size determination of sunscreens formulated with various forms of titanium dioxide. Drug Development and Industrial Pharmacy 35(10):1180-1189.

167. Lu, S.L., et al. 2009. Efficacy of Simple Short-Term in Vitro Assays for Predicting the Potential of Metal Oxide Nanoparticles to Cause Pulmonary Inflammation. Environmental Health Perspectives 117(2):241-247.

168. Shevlin, P.B. and H.A. Neufeld. 1970. Mechamism of Ferricyanide-Catalyzed Chemiluminescence of Luminol. Journal of Organic Chemistry 35(7):2178-&.

169. Nosaka, Y., Y. Yamashita, and H. Fukuyama. 1997. Application of chemiluminescent probe to monitoring superoxide radicals and hydrogen peroxide in TiO2 photocatalysis. Journal of Physical Chemistry B 101(30):5822-5827.

170. Sinclair. Optical Transmission Curves. 2009 [cited January 21 2011]; Available from: http://www.sinclairmfg.com/datasheets/optical3.html.

171. Barr, D., J.J. Jiang, and R.T. Weber, *How to Quantitate Nitroxide Spin Adducts Using TEMPOL*, in *Experimental Techniques Note 3.* , EPR Division of Bruker BioSpin Corp, USA. .

172. Artiola, J., I.L. Pepper, and M.L. Brusseau, *Environmental monitoring and characterization*. 2004, San Diego: Elsevier Academic Press.

173. Keith, L.H., et al. 1983. Principles of Environmental-Analysis. Analytical Chemistry 55(14):2210-2218.

174. Wahi, R.K., et al. 2005. Photodegradation of Congo Red catalyzed by nanosized TiO2. Journal of Molecular Catalysis A 242:48–56.

175. Setsukinai, K., et al. 2003. Development of novel fluorescence probes that can reliably detect reactive oxygen species and distinguish specific species. Journal of Biological Chemistry 278(5):3170-3175.

176. Myhre, O., et al. 2003. Evaluation of the probes 2 ',7 '-dichlorofluorescin diacetate, luminol, and lucigenin as indicators of reactive species formation. Biochemical Pharmacology 65(10):1575-1582.

177. Yildiz, G. and A.T. Demiryurek. 1998. Ferrous iron-induced luminol chemiluminescence: A method for hydroxyl radical study. Journal of Pharmacological and Toxicological Methods 39(3):179-184.

178. Duan, C.F., et al. 2007. Size-dependent inhibition and enhancement by gold nanoparticles of luminol-ferricyanide chemiluminescence. Journal of Physical Chemistry C 111(12):4561-4566.

179. Kaneko, M. and I. Okura, *Chemiluminescent Probe for Active Oxygens*, in *Photocatalysis: Science and Technology*. 2002, Springer Berlin Heidelberg.

180. Lu, C., G. Song, and J.M. Lin. 2006. Reactive oxygen species and their chemiluminescence-detection methods. Trac-Trends in Analytical Chemistry 25(10):985-995.

181. Royall, J.A. and H. Ischiropoulos. 1993. Evaluation of 2',7'-Dichlorofluorescin and Dihydrorhodamine 123 as Fluorescent-Probes for Intracellular H2o2 in Cultured Endothelial-Cells. Archives of Biochemistry and Biophysics 302(2):348-355.

182. Jaeger, C.D. and A.J. Bard. 1979. Spin Trapping and Electron-Spin Resonance Detection of Radical Intermediates in the Photo-Decomposition of Water at TiO2 Particulate Systems. Journal of Physical Chemistry 83(24):3146-3152.

183. Janzen, E.G., Y. Kotake, and R.D. Hinton. 1992. Stabilities of Hydroxyl Radical Spin Adducts of PBN-Type Spin Traps. Free Radical Biology and Medicine 12(2):169-173.

184. Finkelstein, E., G.M. Rosen, and E.J. Rauckman. 1980. Spin Trapping of Superoxide and Hydroxyl Radical - Practical Aspects. Archives of Biochemistry and Biophysics 200(1):1-16.

185. Lachheb, H., et al. 2002. Photocatalytic degradation of various types of dyes (Alizarin S, Crocein Orange G, Methyl Red, Congo Red, Methylene Blue) in water by UV-irradiated titania. Applied Catalysis B-Environmental 39(1):75-90.

186. Comparelli, R., et al. 2005. UV-induced photocatalytic degradation of azo dyes by organic-capped ZnO nanocrystals immobilized onto substrates. Applied Catalysis B-Environmental 60(1-2):1-11.

187. Movahedi, M., A.R. Mahjoub, and S. Janitabar-Darzi. 2009. Photodegradation of Congo Red in Aqueous Solution on ZnO as an Alternative Catalyst to TiO2. Journal of the Iranian Chemical Society 6(3):570-577.

188. Jain, P.K., et al. 2007. Review of some interesting surface plasmon resonance-enhanced properties of noble metal nanoparticles and their applications to biosystems. Plasmonics 2(3):107-118.

189. Link, S. and M.A. El-Sayed. 1999. Size and temperature dependence of the plasmon absorption of colloidal gold nanoparticles. Journal of Physical Chemistry B 103(21):4212-4217.

190. El-Sayed, M.A. 2001. Some interesting properties of metals confined in time and nanometer space of different shapes. Accounts of Chemical Research 34(4):257-264.

191. Kelly, K.L., et al. 2003. The optical properties of metal nanoparticles: The influence of size, shape, and dielectric environment. Journal of Physical Chemistry B 107(3):668-677.

192. Jain, P.K., et al. 2006. Calculated absorption and scattering properties of gold nanoparticles of different size, shape, and composition: Applications in biological imaging and biomedicine. Journal of Physical Chemistry B 110(14):7238-7248.

193. Teo, S.L., et al. 2010. Gold nanoring trimers: a versatile structure for infrared sensing. Optics Express 18(21):22271-22282.

194. Tsai, C.Y., et al. 2011. High sensitivity plasmonic index sensor using slablike gold nanoring arrays. Applied Physics Letters 98(15).

195. Soukoulis, C.M. and M. Wegener. 2011. Past achievements and future challenges in the development of three-dimensional photonic metamaterials. Nature Photonics 5(9):523-530.

196. Chung, T., et al., *Plasmonic Nanostructures for Nano-Scale Bio-Sensing*, in *Sensors*. 2011. p. 10907-10929.

197. Larsson, E.M., et al. 2007. Sensing characteristics of NIR localized surface plasmon resonances in gold nanorings for application as ultrasensitive biosensors. Nano Letters 7(5):1256-1263.

198. Aizpurua, J., et al. 2003. Optical properties of gold nanorings. Physical Review Letters 90(5):057401.

199. Nordlander, P. 2009. The Ring: A Leitmotif in Plasmonics. Acs Nano 3(3):488-492.

200. Hao, F., et al. 2008. Shedding light on dark plasmons in gold nanorings. Chemical Physics Letters 458(4-6):262-266.

201. Ye, J., et al. 2009. Observation of plasmonic dipolar anti-bonding mode in silver nanoring structures. Nanotechnology 20(46).

202. Jain, P.K., et al. 2008. Noble Metals on the Nanoscale: Optical and Photothermal Properties and Some Applications in Imaging, Sensing, Biology, and Medicine. Accounts of Chemical Research 41(12):1578-1586.

203. Banaee, M.G. and K.B. Crozier. 2010. Gold nanorings as substrates for surface-enhanced Raman scattering. Optics Letters 35(5):760-762.

204. Le, F., et al. 2008. Metallic nanoparticle arrays: A common substrate for both surface-enhanced Raman scattering and surface-enhanced infrared absorption. Acs Nano 2(4):707-718.

205. Kim, S., et al. 2006. Patterned Arrays of Au rings for localized surface plasmon resonance. Langmuir 22(17):7109-7112.

206. Fischer, J., et al. 2010. Near-Field-Mediated Enhancement of Two-Photon-Induced Fluorescence on Plasmonic Nanostructures. Journal of Physical Chemistry C 114(49):20968-20973.

207. Gong, H.-M., et al. 2009. Illuminating Dark Plasmons of Silver Nanoantenna Rings to Enhance Exciton-Plasmon Interactions. Advanced Functional Materials 19(2):298-303.

208. Jafari, M.R., F. Ebrahimi, and M. Nooshirvani. 2011. Subwavelength electromagnetic energy transport by stack of metallic nanorings. Journal of Applied Physics 108(5).

209. Jung, K.-Y., F.L. Teixeira, and R.M. Reano. 2007. Au/SiO2 nanoring plasmon waveguides at optical communication band. Journal of Lightwave Technology 25(9):2757-2765.

210. Chiu, K.P., K.F. Lai, and D.P. Tsai. 2008. Application of surface polariton coupling between nano recording marks to optical data storage. Optics Express 16(18):13885-13892.

211. Lin, Z.R., et al. 2010. Quantum bus of metal nanoring with surface plasmon polaritons. Physical Review B 82(24).

212. Liu, S.D., Z.S. Zhang, and Q.Q. Wang. 2009. High sensitivity and large field enhancement of symmetry broken Au nanorings: effect of multipolar plasmon resonance and propagation. Optics Express 17(4):2906-2917.

213. Bukasov, R., et al. 2010. Probing the Plasmonic Near-Field of Gold Nanocrescent Antennas. Acs Nano 4(11):6639-6650.

214. Shumaker-Parry, J.S., H. Rochholz, and M. Kreiter. 2005. Fabrication of crescent-shaped optical antennas. Advanced Materials 17(17):2131-+.

215. Rochholz, H., N. Bocchio, and M. Kreiter. 2007. Tuning resonances on crescent-shaped noble-metal nanoparticles. New Journal of Physics 9.

216. Iyer, S., S. Popov, and A.T. Friberg. 2010. Transmission resonances in periodic U-shaped metallic nanostructures. Optics Express 18(17):17719-17728.

217. Okamoto, T., et al. 2011. Visible near-infrared light scattering of single silver split-ring structure made by nanosphere lithography. Optics Express 19(8):7068-7076.

218. Ross, B.M. and L.P. Lee. 2008. Plasmon tuning and local field enhancement maximization of the nanocrescent. Nanotechnology 19(27).

219. Bukasov, R. and J.S. Shumaker-Parry. 2007. Highly tunable infrared extinction properties of gold nanocrescents. Nano Letters 7(5):1113-1118.

220. Fischer, J., et al. 2011. Plasmon hybridization and strong near-field enhancements in opposing nanocrescent dimers with tunable resonances. Nanoscale 3(11):4788-4797.

221. Vogel, N., et al. 2011. Plasmon Hybridization in Stacked Double Crescents Arrays Fabricated by Colloidal Lithography. Nano Letters 11(2):446-454.

222. Clark, A.W., et al. 2007. Tuneable visible resonances in crescent shaped nano-split-ring resonators. Applied Physics Letters 91(9).

223. Jiang, H., J. Markowski, and J. Sabarinathan. 2009. Near-infrared optical response of thin film pH-sensitive hydrogel coated on a gold nanocrescent array. Optics Express 17(24):21802-21807.

224. Unger, A., et al. 2009. Sensitivity of Crescent-Shaped Metal Nanoparticles to Attachment of Dielectric Colloids. Nano Letters 9(6):2311-2315.

225. Noginov, M.A. and V.A. Podolskiy, eds. *Tutorials in Metamaterials*. Nano-Optics and Nanophotonics, ed. S. Kawata and V.M. Shalaev. 2012, CRC Press, Taylor & Francis Group: New York.

226. Pendry, J.B. and D.R. Smith. 2004. Reversing light with negative refraction. Physics Today 57(6):37-43.

227. Pendry, J.B., et al. 1998. Low frequency plasmons in thin-wire structures. Journal of Physics-Condensed Matter 10(22):4785-4809.

228. Veselago, V.G., *The electrodynamics of substances with simultaneously negative values of ε and μ*, in *Sov Phys Uspekhi*. 1968. p. 509-514.

229. Belov, P.A., C.R. Simovski, and P. Ikonen, *Flat lenses formed by photonic and electromagnetic crystals*, in *Handbook of Artificial Materials*, F. Capolino, Editor. 2009, CRC Press LLC.

230. Smith, D.R., J.B. Pendry, and M.C.K. Wiltshire. 2004. Metamaterials and negative refractive index. Science 305(5685):788-792.

231. Pendry, J.B. 2000. Negative refraction makes a perfect lens. Physical Review Letters 85(18):3966-3969.

232. Pendry, J.B., D. Schurig, and D.R. Smith. 2006. Controlling electromagnetic fields. Science 312(5781):1780-1782.

233. Dolling, G., et al. 2006. Photorealistic images of objects in effective negative-index materials. Optics Express 14(5):1842-1849.

234. Shelby, R.A., D.R. Smith, and S. Schultz. 2001. Experimental verification of a negative index of refraction. Science 292(5514):77-79.

235. Pendry, J.B., et al. 1996. Extremely low frequency plasmons in metallic mesostructures. Physical Review Letters 76(25):4773-4776.

236. Pendry, J.B., et al. 1999. Magnetism from conductors and enhanced nonlinear phenomena. Ieee Transactions on Microwave Theory and Techniques 47(11):2075-2084.

237. Smith, D.R., et al. 2000. Composite medium with simultaneously negative permeability and permittivity. Physical Review Letters 84(18):4184-4187.

238. Houck, A.A., J.B. Brock, and I.L. Chuang. 2003. Experimental observations of a left-handed material that obeys Snell's law. Physical Review Letters 90(13).

239. Parazzoli, C.G., et al. 2003. Experimental verification and simulation of negative index of refraction using Snell's law. Physical Review Letters 90(10).

240. Shalaev, V.M. 2007. Optical negative-index metamaterials. Nature Photonics 1(1):41-48.

241. Yen, T.J., et al. 2004. Terahertz magnetic response from artificial materials. Science 303(5663):1494-1496.

242. Linden, S., et al. 2004. Magnetic response of metamaterials at 100 terahertz. Science 306(5700):1351-1353.

243. Enkrich, C., et al. 2005. Magnetic metamaterials at telecommunication and visible frequencies. Physical Review Letters 95(20).

244. Klein, M.W., et al. 2006. Single-slit split-ring resonators at optical frequencies: limits of size scaling. Optics Letters 31(9):1259-1261.

245. Anlage, S.M. 2011. The physics and applications of superconducting metamaterials. Journal of Optics 13(2).

246. Linden, S., et al. 2006. Photonic metamaterials: Magnetism at optical frequencies. Ieee Journal of Selected Topics in Quantum Electronics 12(6):1097-1105.

247. Meinzer, N., et al. 2010. Arrays of Ag split-ring resonators coupled to InGaAs single-quantum-well gain. Optics Express 18(23):24140-24151.

248. Plum, E., et al. 2009. Towards the lasing spaser: controlling metamaterial optical response with semiconductor quantum dots. Optics Express 17(10):8548-8551.

249. Chen, H. 2011. Metamaterials: constitutive parameters, performance, and chemical methods for realization. Journal of Materials Chemistry 21(18):6452-6463.

250. Shalaev, V.M., et al. 2005. Negative index of refraction in optical metamaterials. Optics Letters 30(24):3356-3358.

251. Garcia-Meca, C., et al. 2011. Low-Loss Multilayered Metamaterial Exhibiting a Negative Index of Refraction at Visible Wavelengths. Physical Review Letters 106(6).

252. Garcia-Meca, C., et al. 2009. Double-negative polarization-independent fishnet metamaterial in the visible spectrum. Optics Letters 34(10):1603-1605.

253. Xiao, S., et al. 2009. Yellow-light negative-index metamaterials. Optics Letters 34(22):3478-3480.

254. Chettiar, U.K., et al. 2007. Dual-band negative index metamaterial: double negative at 813nm and single negative at 772nm. Optics Letters 32(12):1671-1673.

255. Dolling, G., et al. 2007. Negative-index metamaterial at 780 nm wavelength. Optics Letters 32(1):53-55.

256. Linden, F. and M. Wegner, *Fabrication and Optical Characterization of Photonic Metamaterials*, in *Applications of Metamaterials*, F. Capolino, Editor. 2009, CRC Press Taylor&Francis Group: New York.

257. Saavedra, H.M., et al. 2010. Hybrid strategies in nanolithography. Reports on Progress in Physics 73(3).

258. Xia, Y.N., et al. 1999. Unconventional methods for fabricating and patterning nanostructures. Chemical Reviews 99(7):1823-1848.

259. Adams, M., *Research and Development of Electron-Beam Lithography Using a Transmission Electron Microscope at 200 kV*, in *PROCESS & CHARACTERIZATION*. 2006. p. 114-115.

260. Open House Held for Newest Core Facility: The Nanofabrication Facility. 2011 [cited 13 February 2012]; Available from: http://www.research.uh.edu/Home/Newsletter--Research-Update/March-April-2011-Newsletter.aspx.

261. Enkrich, C., et al. 2005. Focused-ion-beam nanofabrication of near-infrared magnetic metamaterials. Advanced Materials 17(21):2547-+.

262. Feth, N., et al. 2007. Large-area magnetic metamaterials via compact interference lithography. Optics Express 15(2):501-507.

263. Zhang, S., et al. 2005. Experimental demonstration of near-infrared negative-index metamaterials. Physical Review Letters 95(13).

264. Schurig, D., et al. 2006. Metamaterial electromagnetic cloak at microwave frequencies. Science 314(5801):977-980.

265. Katsarakis, N., et al. 2005. Magnetic response of split-ring resonators in the far-infrared frequency regime. Optics Letters 30(11):1348-1350.

266. Miyamaru, F., et al. 2010. Three-dimensional bulk metamaterials operating in the terahertz range. Applied Physics Letters 96(8).

267. Liu, N., et al. 2008. Three-dimensional photonic metamaterials at optical frequencies. Nature Materials 7(1):31-37.

268. Soukoulis, C.M. and M. Wegener. 2010. Optical Metamaterials-More Bulky and Less Lossy. Science 330(6011):1633-1634.

269. Haynes, C.L. and R.P. Van Duyne. 2001. Nanosphere lithography: A versatile nanofabrication tool for studies of size-dependent nanoparticle optics. Journal of Physical Chemistry B 105(24):5599-5611.

270. Burmeister, F., et al. 1998. From mesoscopic to nanoscopic surface structures: Lithography with colloid monolayers. Advanced Materials 10(6):495-+.

271. Jiang, P., et al. 1999. Single-crystal colloidal multilayers of controlled thickness. Chemistry of Materials 11(8):2132-2140.

272. Yang, S.M., et al. 2006. Nanomachining by colloidal lithography. Small 2(4):458-475.

273. Yang, S. and Y. Lei. 2011. Recent progress on surface pattern fabrications based on monolayer colloidal crystal templates and related applications. Nanoscale 3(7):2768-2782.

274. Hulteen, J.C., et al. 1999. Nanosphere lithography: Size-tunable silver nanoparticle and surface cluster arrays. Journal of Physical Chemistry B 103(19):3854-3863.

275. Tan, B.J.Y., et al. 2004. Fabrication of a two-dimensional periodic non-close-packed array of polystyrene particles. Journal of Physical Chemistry B 108(48):18575-18579.

276. Kosiorek, A., et al. 2005. Fabrication of nanoscale rings, dots, and rods by combining shadow nanosphere lithography and annealed polystyrene nanosphere masks. Small 1(4):439-444.

277. Gwinner, M.C., et al. 2009. Periodic Large-Area Metallic Split-Ring Resonator Metamaterial Fabrication Based on Shadow Nanosphere Lithography. Small 5(3):400-406.

278. Retsch, M., et al. 2009. Parallel Preparation of Densely Packed Arrays of 150-nm Gold-Nanocrescent Resonators in Three Dimensions. Small 5(18):2105-2110.

279. Cataldo, S., et al. 2012. Hole-mask colloidal nanolithography for large-area low-cost metamaterials and antenna-assisted surface-enhanced infrared absorption substrates. ACS nano 6(1):979-85.

280. Hobbs, K.L., et al. 2004. Fabrication of nanoring arrays by sputter redeposition using porous alumina templates. Nano Letters 4(1):167-171.

281. Meng, T., et al. 2008. Fabrication of Metallic Split-Ring Arrays for Metamaterials Using Silica Particle Templates Anchored on a Silicon Substrate. Japanese Journal of Applied Physics 47(10):8109-8112.

282. Sun, Z., et al. 2008. A Universal Approach to Fabricate Various Nanoring Arrays Based on a Colloidal-Crystal-Assisted-Lithography Strategy. Advanced Functional Materials 18(24):4036-4042.

283. Zheng, Y.B., et al. 2006. Fabrication of large area ordered metal nanoring arrays for nanoscale optical sensors. Journal of Non-Crystalline Solids 352(23-25):2532-2535.

284. Boneberg, J., et al. 1997. The formation of nano-dot and nano-ring structures in colloidal monolayer lithography. Langmuir 13(26):7080-7084.

285. Jia, D.D. and A. Goonewardene. 2006. Two-dimensional nanotriangle and nanoring arrays on silicon wafer. Applied Physics Letters 88(5).

286. Winzer, M., et al. 1996. Fabrication of nano-dot- and nano-ring-arrays by nanosphere lithography. Applied Physics a-Materials Science & Processing 63(6):617-619.

287. Brands, M., A. Carl, and G. Dumpich. 2005. Preparation of large area sub-50 nm polymer nanoring arrays. Superlattices and Microstructures 37(6):388-393.

288. Yu, X.H., et al. 2005. Fabrication of structures with tunable morphologies au and sizes by soft molding. Applied Surface Science 252(5):1947-1953.

289. Marquez, M., et al. 2007. Factors affecting the synthesis of polymeric nanostructures from template assisted admicellar polymerization. Langmuir 23:10008-10019.

290. Yan, F. and W.A. Goedel. 2005. The preparation of mesoscopic rings in colloidal crystal templates. Angewandte Chemie-International Edition 44(14):2084-2088.

291. Yan, Q.F., et al. 2006. Drilling nanoholes in colloidal spheres by selective etching. Journal of Materials Chemistry 16(22):2132-2134.

292. Ren, Z.Y., et al. 2009. Building cavities in microspheres and nanospheres. Nanotechnology 20(6).

293. Marczewski, D. and W.A. Goedel. 2005. The preparation of submicrometer-sized rings by embedding and selective etching of spherical silica particles. Nano Letters 5(2):295-299.

294. Wang, Y., et al. 2004. A modified nanosphere lithography for the fabrication of aminosilane/polystyrene nanoring arrays and the subsequent attachment of gold or

DNA-capped gold nanoparticles. Journal of Materials Chemistry 14(24):3488-3494.

295. Klaui, M., et al. 2003. Vortex formation in narrow ferromagnetic rings. Journal of Physics-Condensed Matter 15(21):R985-R1023.

296. Castano, F.J., et al. 2003. Metastable states in magnetic nanorings. Physical Review B 67(18).

297. Zhu, F.Q., et al. 2004. Ultrahigh-Density Arrays of ferromagnetic nanorings on macroscopic areas. Advanced Materials 16(23-24):2155-+.

298. Miller, M.M., et al. 2002. Detection of a micron-sized magnetic sphere using a ring-shaped anisotropic magnetoresistance-based sensor: A model for a magnetoresistance-based biosensor. Applied Physics Letters 81(12):2211-2213.

299. Zhu, J.G., Y.F. Zheng, and G.A. Prinz. 2000. Ultrahigh density vertical magnetoresistive random access memory (invited). Journal of Applied Physics 87(9):6668-6673.

300. Zhang, Y.J., W. Li, and K.J. Chen. 2008. Application of two-dimensional polystyrene arrays in the fabrication of ordered silicon pillars. Journal of Alloys and Compounds 450(1-2):512-516.

301. Trion. Trion Technology; Plasma Technology. [cited 12 January 2012]; Available from: http://www.crystec.com/triplae.htm.

302. Yee, K.S. 1966. Numerical Solution of Initial Boundary Value Problems Involving Maxwells Equations in Isotropic Media. Ieee Transactions on Antennas and Propagation AP14(3):302-&.

303. Nagao, D., et al. 2008. Single- and multi-layered patterns of polystyrene and silica particles assembled with a simple dip-coating. Colloids and Surfaces a-Physicochemical and Engineering Aspects 317(1-3):722-729.

304. Brewer Science, Inc. Spin Coater Theory. [cited 06 January 2012]; Available from: http://www.brewerscience.com/research/processing-theory/spin-coater-theory.

305. Bigioni, T.P., et al. 2006. Kinetically driven self assembly of highly ordered nanoparticle monolayers. Nature Materials 5(4):265-270.

306. Rybczynski, J., U. Ebels, and M. Giersig. 2003. Large-scale, 2D arrays of magnetic nanoparticles. Colloids and Surfaces a-Physicochemical and Engineering Aspects 219(1-3):1-6.

307. Atthi, N., et al. 2009. Study of optimization condition for spin coating of the photoresist film on rectangular substrate by Taguchi design of an experiment. Songklanakarin Journal of Science and Technology 31(3):331-335.

308. Wei, Y. and R.L. Brainard, *Edge bead and backside contamination*, in *Advanced processes for 193-nm immersion lithography*. 2009, Society of Photo-Optical Instrumentation Engineers: Bellingham, Washington.

309. Gigault, C., K. Dalnoki-Veress, and J.R. Dutcher. 2001. Changes in the morphology of self-assembled polystyrene microsphere monolayers produced by annealing. Journal of Colloid and Interface Science 243(1):143-155.

310. Calcagno, L., G. Compagnini, and G. Foti. 1992. Structural Modification of Polymer-Films by Ion Irradiation. Nuclear Instruments & Methods in Physics Research Section B-Beam Interactions with Materials and Atoms 65(1-4):413-422.

311. Grant, J.L., D.S. Dunn, and D.J. McClure. 1988. Argon and Oxygen Sputter Etching of Polystyrene, Polypropylene, and Poly(Ethylene-Terephthalate) Thin-Films. Journal of Vacuum Science & Technology a-Vacuum Surfaces and Films 6(4):2213-2220.

312. Ulmeanu, M., M. Filipescu, and R.V. Medianu. 2008. Fabrication of 2-D nanostructures via metal deposition through a colloidal mask: comparison between thermal evaporation and RF magnetron sputtering. Physica Status Solidi (C) 5(12):3584–3587.

313. Wright, J.P., et al. 2006. Ultraflat ternary nanopatterns fabricated using colloidal lithography. Advanced Materials 18(4):421-+.

314. Sun, F., et al. 2005. Laser morphological manipulation of gold nanoparticles periodically arranged on solid supports. Applied Physics B-Lasers and Optics 81(6):765-768.

315. Hulteen, J.C. and R.P. Vanduyne. 1995. Nanosphere Lithography - a Materials General Fabrication Process for Periodic Particle Array Surfaces. Journal of Vacuum Science & Technology a-Vacuum Surfaces and Films 13(3):1553-1558.

316. Zhang, X., et al. 2006. Advances in contemporary nanosphere lithographic techniques. Journal of Nanoscience and Nanotechnology 6(7):1920-1934.

317. Zhang, J., et al. 2010. Colloidal Self-Assembly Meets Nanofabrication: From Two-Dimensional Colloidal Crystals to Nanostructure Arrays. Advanced Materials 22(38):4249-4269.

318. Stafford, L., et al. 2007. Influence of redeposition on the plasma etching dynamics. Journal of Applied Physics 101(8).

319. Chang, J.P. and J.W. Coburn. 2003. Plasma-surface interactions. Journal of Vacuum Science & Technology A 21(5):S145-S151.

320. Giapis, K.P., G.S. Hwang, and O. Joubert. 2002. The role of mask charging in profile evolution and gate oxide degradation. Microelectronic Engineering 61-2:835-847.

321. Sumiya, M., H. Tamura, and S. Watanabe. 2002. Mechanism of the reduction of electron shading charge build-up using pulsed plasma. Japanese Journal of Applied Physics Part 1-Regular Papers Short Notes & Review Papers 41(2A):856-859.

322. Grigoras, K. and S. Franssila. 2009. "Etching under the corner" - inclined macropores by reactive ion etching. Physica Status Solidi a-Applications and Materials Science 206(6):1245-1249.

323. Madziwa-Nussinov, T.G., D. Amush, and F.F. Chen. 2007. Ion-shading effects during metal etch in plasma processing. Ieee Transactions on Plasma Science 35:1388-1396.

324. BangsLaboratory. Polymer Microspheres. [cited; Available from: http://www.bangslabs.com/products/polymer_microspheres.

325. Zou, S. 2008. Light-driven circular plasmon current in a silver nanoring. Optics Letters 33(18):2113-2115.

326. Rockstuhl, C., et al. 2006. On the reinterpretation of resonances in split-ring-resonators at normal incidence. Optics Express 14(19):8827-8836.

327. Rockstuhl, C., et al. 2006. Resonances of split-ring resonator metamaterials in the near infrared. Applied Physics B-Lasers and Optics 84(1-2):219-227.

328. Hitachi. Hitachi Ion Milling System E-3500. [cited 27 May 2011]; Available from: www.hitachi-hta.com.

329. FEI. Focused ion beam technology, capabilities and applications. [cited 06 December 2010]; Available from: http://www.fei.com/uploadedFiles/Documents/Content/2006_06_FIB_Overview_pb.pdf.

330. Dushkin, C.D., et al. 1993. Colored Multilayers from Transparent Submicrometer Spheres. Langmuir 9(12):3695-3701.

331. Stankovich, S., et al. 2006. Stable aqueous dispersions of graphitic nanoplatelets via the reduction of exfoliated graphite oxide in the presence of poly(sodium 4-styrenesulfonate). Journal of Materials Chemistry 16(2):155-158.

332. Vandencasteele, N. and F. Reniers. 2010. Plasma-modified polymer surfaces: Characterization using XPS. Journal of Electron Spectroscopy and Related Phenomena 178:394-408.

333. Kondyurin, A., et al. 2008. Argon plasma immersion ion implantation of polystyrene films. Nuclear Instruments & Methods in Physics Research Section B-Beam Interactions with Materials and Atoms 266(7):1074-1084.

334. Kondyurin, A., et al. 2006. Etching and structural changes of polystyrene films during plasma immersion ion implantation from argon plasma. Nuclear Instruments & Methods in Physics Research Section B-Beam Interactions with Materials and Atoms 251(2):413-418.

335. Zhang, R., et al. 2008. Swelling of cross-linked polystyrene beads in toluene. Microelectronic Engineering 85(5-6):1261-1264.

336. Zekonyte, J., et al. 2003. Mechanisms of argon ion-beam surface modification of polystyrene. Surface Science 532:1040-1044.

337. Suni, T., et al. 2002. Effects of plasma activation on hydrophilic bonding of Si and SiO2. Journal of the Electrochemical Society 149(6):G348-G351.